Electrochemical and Spectroelectrochemical Studies of Complexes with Multiple Redox Centers

---

A Dissertation

Presented to

the Faculty of the Department of Chemistry

University of Houston

In Partial Fulfillment

of the Requirements for the Degree

Doctor of Philosophy

---

by

Machima Manowong

May 2014

Electrochemical and Spectroelectrochemical Studies of Complexes with Multiple Redox Centers

_____

Machima Manowong

Approved:

_____

Dr. Karl M. Kadish, Chairman

_____

Dr. John L. Bear

_____

Dr. Roman Czernuszewicz

_____

Dr. Shoujun Xu

_____

Dr. James M. Briggs

_____

Dean, College of Natural Sciences and Mathematics

Dedication

This dissertation is dedicated to my parents

for their love, support, and encouragement.

Acknowledgments

I would like to express my deep appreciation to my advisor, Dr. Karl M. Kadish for his support and guidance throughout the research. I am sincerely grateful to all of my committee members, Dr. John L. Bear, Dr. Roman Czernuszewicz, Dr. Shoujun Xu, and Dr. James M. Briggs for their constructive comments.

Particular thanks are given to Dr. Roberto Paolesse, Dr. Tomás Torres, Dr. Baocheng Han, and Dr. Roger Guilard for providing compounds and for their contributions to this dissertation. Financial support provided by the Robert A. Welch Foundation is also gratefully acknowledged.

I would like to thank Dr. Eric Van Caemelbecke, Dr. Ping Chen, Dr. Siyabonga Ngubane, and the past and the present members of the Kadish group. My research would have not been possible without their help.

Finally, I wish to show best of my gratitude to my family and friends for their encouragement, love, and support.

Electrochemical and Spectroelectrochemical Studies of Complexes with Multiple Redox Centers

---

An Abstract of a Dissertation

Presented to

the Faculty of the Department of Chemistry

University of Houston

In Partial Fulfillment

of the Requirements for the Degree

Doctor of Philosophy

---

by

Machima Manowong

May 2014

Abstract

The electrochemical and spectroscopic properties of different types of complexes with multiple redox centers were investigated. Cyclic voltammetry was used as the main electrochemical technique along with thin-layer UV-visible and FTIR spectroelectrochemistry. The primary focus of this work was to elucidate the overall redox behavior of the compounds and to examine the site of electron transfer. Ligand-binding reactions were also monitored by UV-visible spectroscopy and/or electrochemical titration methods. The examined electroactive compounds included: (i) free base corroles with nitro substituents at the *β*-pyrrole positions, (ii) *β*-nitro-substituted iron corroles, (iii) *bis*-[PcRu(CO)][$Ru_2(ap)_4(C \equiv CC_5H_4N)_2$]: a tetraruthenium complex containing two ruthenium(II) phthalocyanines and one metal-metal bonded diruthenium(III,III) unit, (iv) diruthenium complexes containing four symmetrical anionic bridging ligands, and (v) copper(I) complexes with diethoxyphosphoryl-substituted 1,10-phenanthroline ligands.

Table of Contents

List of Abbreviations

Abbreviation	Meaning
ap	2-anilinopyridinate anion
$CHCl_3$	chloroform
CH_2Cl_2	dichloromethane
Corr/C	corrole
CV	cyclic voltammetry
DMF	*N,N′*-dimethylformamide
dpb	diphenylbenzamidinate anion
dpf	*N,N′*-diphenylformamidinate ion
$E_{1/2}$	half-wave potential
E_{pa}	anodic peak potential by cyclic voltammetry
E_{pc}	cathodic peak potential by cyclic voltammetry
ε	molar absorptivity
HOMO	highest occupied molecular orbital
i_{pa}	anodic peak current by cyclic voltammetry
i_{pc}	cathodic peak current by cyclic voltammetry
LUMO	lowest unoccupied molecular orbital
MeOH	methanol
Pc	phthalocyanine
PhCN	benzonitrile
py	pyridine

SCE	saturated calomel electrode
TBABr	tetra-*n*-butylammonium bromide
TBACl	tetra-*n*-butylammonium chloride
TBAF	tetra-*n*-butylammonium fluoride
TBAI	tetra-*n*-butylammonium iodide
TBAP	tetra-*n*-butylammonium perchlorate
$TBAPF_6$	tetra-*n*-butylammonium hexafluorophosphate
TFA	trifluoroacetic acid
TPP	5, 10, 15, 20-tetraphenylporphyrin

List of Figures

List of Schemes and Charts

List of Tables

CHAPTER ONE

Introduction

1.1 Introduction to Dissertation and Scope of Coverage

The main long-term research interest of our laboratory has involved the areas of electrosynthesis, electrochemistry, and chemical reactivity of porphyrins and porphyrin-like macrocycles having different central metal ions. The projects in this dissertation are in line with this interest and thus the overall goal of this dissertation was to study redox properties and electron transfer mechanisms of complexes with multiple redox centers, while characterizing the products or transient intermediates produced during each oxidation/reduction process using basic electrochemical methodologies and thin-layer UV-vis, FTIR, and/or ESR spectroelectrochemistry.

Rather than focus on a single chemical system, we have studied multiple related chemical systems as described on the following pages. Chapter One provides general information about the investigated compounds and techniques used in this work, while experimental details are presented in Chapter Two. Chapters Three and Four focus on free base corroles and iron corroles. Chapters Five to Seven report studies of different types of compounds: a tetraruthenium complex, diruthenium complexes, and copper(I) complexes.

The electrochemical and spectroscopic data on each chemical system are analyzed as a function of solution conditions, metal oxidation state, type of axial ligands, nature of all π ring systems, and the presence of any interaction between electroactive groups on the macrocycle, while also providing supplementary information for applications in the area of chemical catalysis, molecular devices, electrochemical sensors, or as effective photodynamic therapy agents.

1.2 Electrochemical Techniques

Cyclic voltammetry (CV) has been widely used to obtain qualitative and quantitative information on a variety of chemical systems. In addition to evaluating the amount of electroactive material in solution, one can obtain information on reaction mechanisms and kinetics of electron-transfer processes. The technique of CV is based on applying a linear increasing potential at an electrode while monitoring the resultant current which flows during the reduction and oxidation. The potential applied to the working electrode usually varies between +2.0 and -2.0 V *vs* SCE and is the form of a triangular waveform, as shown in Figure 1-1. The forward and reverse potential scan can occur for one full cycle, or a series of cycles can be performed. A "half cycle", from E_{init} to E_{final} can also be applied and is called linear sweep voltammetry. The corresponding plot of current versus potential for one forward and one reverse cycle is called a cyclic voltammogram.

Both reversible and irreversible redox processes are possible. The response of a reversible redox couple is illustrated in Figure 1-2. For example, the oxidized form, represented as O, is reduced at a characteristic potential, $E_{1/2}$ by negative potential scan starting from a value where no reduction occurs. When the applied potential reaches the characteristic potential for the redox process to occur, the cathodic (reduction) current begins to increase. At the switching potential, the scan will be reversed and the reduced form of the molecule, represented as R, is reoxidized back to O and an anodic current flows. For reversible processes, the oxidation and reduction currents are equal to each other and the cathodic and anodic peaks are separated by approximately 60 mV. For irreversible processes, which result from a slow electron transfer, widely separated peaks are observed or no reverse

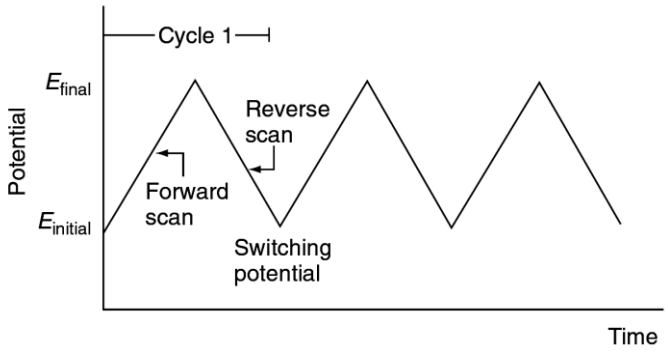

Figure 1-1. Potential-time excitation signal in cyclic voltammetry experiment.

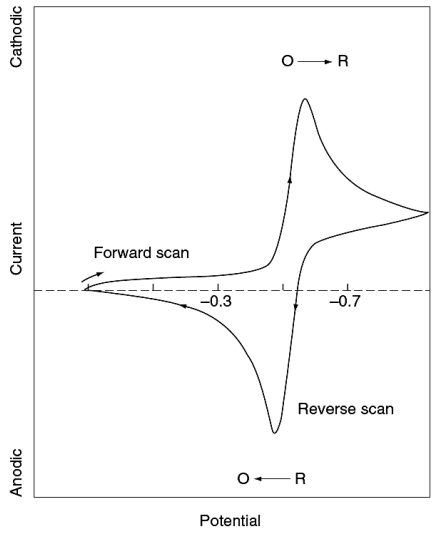

Figure 1-2. Typical cyclic voltammogram for a reversible redox process ($O + ne^- \rightleftarrows R$).

peak at all is detected on the reverse scan. The peak current on the linear scan is still proportional to the concentration, but will be lower in height than for a reversible process.[1,2] Spectroelectrochemistry combines the techniques of electrochemistry and spectroscopy in which *in situ* generated products of redox reactions are monitored by spectroscopic methods as the redox reaction proceeds. Examples in this dissertation are given by thin-layer UV-visible spectroelectrochemistry and IR spectroelectrochemistry. Raman spectroscopy and electron paramagnetic resonance (EPR) can also be combined with electrochemistry.[3,4] The technique of spectroelectrochemistry is a powerful method to study the site of electron transfer or to identify intermediates which are formed during a redox process. In our own lab, spectroelectrochemical methods are routinely used to distinguish metal-centered reactions from ring-centered reactions involving porphyrins, whose core structure is shown in Figure 1-3. For example, a metal-centered reaction of porphyrins is dominated by red or blue shifts of the Soret band which is located between 350 and 450 nm, while a ring-centered reaction of the porphyrin conjugated π ring system leads to a significant decrease in intensity of the Soret band along with the appearance of new broad visible or near IR bands.[5,6]

1.3 Corroles

Corroles are synthetic tetrapyrrolic macrocycles in the porphyrinoid family. The structures of corroles are closely related to porphyrins in that they have an 18 π-electron aromatic system (see Figure 1-3), but there is a direct carbon-carbon bond between two pyrroles in the corrole which leads to a smaller cavity size than in the case of porphyrins.[7,8] The first corrole was synthesized by Johnson and Kay in 1965[9], and since that time corrole chemistry has received much attention because of several interesting and particular

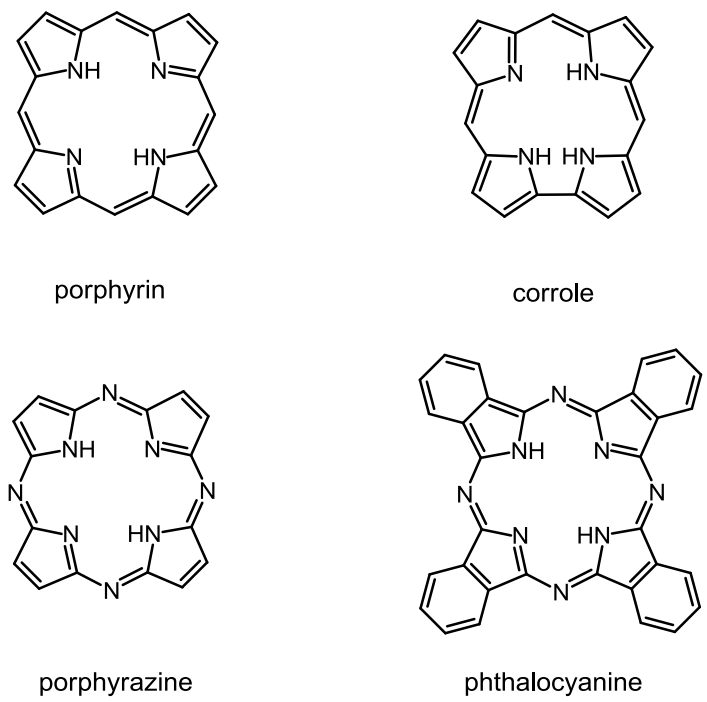

Figure 1-3. Representation of porphyrin and related compounds.

Scheme 1-1

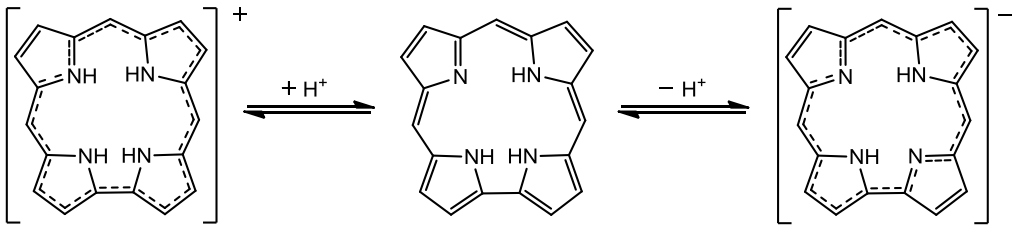

$[(Cor)H_4]^+$ $(Cor)H_3$ $[(Cor)H_2]^-$

properties of the macrocycle.[7,8,10,11] One of these is the corrole's ability to stabilize the central metal ion in a higher oxidation state than for the corresponding porphyrin with a similar set of substituents. This stabilization of the higher metal oxidation state in corroles occurs by virtue of the fact that the corrole macrocycle has a charge of -3 as compared to -2 for the core of the porphyrin. The properties of corroles have allowed for their use in a number of applications, examples being in the area of chemical sensors, catalysts, solar cells, and medicine.[10-13]

Corroles are more acidic than porphyrins and the free-base macrocycle can easily undergo a loss of one proton at the four inner nitrogens. In dilute basic solutions, the free-base corroles can be converted to the monoanionic species $[(Cor)H_2]^-$, whereas in acidic solutions they can also be converted to monocationic derivatives of the form $[(Cor)H_4]^+$ (See Scheme 1-1).

The increased electron density on the corrole macrocycle as compared to porphyrins leads to differences in redox potentials between corroles and porphyrins. Metallocorroles are generally harder to reduce and easier to oxidize than the corresponding metalloporphyrins.[7,8,11] The site of the electron transfer may be assigned on the basis of spectroscopic data or by electrochemical diagnostic criteria, or it may be assigned on the basis of comparison with the known chemistry and electrochemistry of a related compound or series of compounds. Corroles can undergo up to three ring-centered one-electron oxidations to stepwise produce a corrole π-cation radical, a corrole dication and a corrole trication. This compares with the analogous porphyrins where only two ring-centered oxidations can be obtained. The ring-centered reductions of metallocorroles usually occur at potentials close to the negative potential limit of the nonaqueous solvent, e.g., at $E_{1/2}$ = -1.74

V for (OEC)$Sn^{IV}(C_6H_5)$ in CH_2Cl_2, at -1.58 V for (OEC)Mn^{III} in PhCN, and -1.71 V for (OEC)$P^{V}(CH_3)_2$ in PhCN. Also, like in the case of porphyrins, metal-centered reactions of the corroles generally occur at potentials located between $E_{1/2}$ values for formation of the π-cation and π-anion radical.

The electronic spectra of corroles are very similar to those of the analogous porphyrins due to the structural similarity between the two macrocycles. Both macrocycles exhibit an intense Soret band at 410-420 nm and one or two Q-bands at 500-650 nm. The spectral features of metallocorroles and metalloporphyrins both depend on the central metal ion and its oxidation state, as well as on the presence or absence of any coordinating axial ligands. In addition, UV-visible spectra of the corrole and porphyrin π-cation and π-anion radicals are similar to each other in that both show a reduced intensity Soret band as compared with the non-oxidized or non-reduced forms of the compounds.

1.4 Phthalocyanines

Phthalocyanine (Pc) is a macrocycle derived from porphyrin, more exactly from porphyrazine by fusion with four benzene units (Figure 1-3). Its extensively conjugated system leads to an absorption spectrum with an intense Q band between 620-700 nm and a weak Soret band near 350 nm. The latter band is much broader and far less intense than the Soret band in porphyrins.[14,15]

Metallophthalocyanines are well known for their intense color and high thermal stability.[16-18] Moreover, the optical and redox properties of phthalocyanines can be tuned by changing the central metal ion and/or substituents at the peripheral and/or axial positions of the macrocycle.[18,19] Owing to their chemical versatility and their optoelectronic properties, these synthetic porphyrin analogues play a major role in the field of molecular electronics.

They have been used as potential photosensitizers in solar technologies and in the photodynamic treatment of cancer.[20-22] Additional potential applications of phthalocyanines include their use as analytical sensors for industry, environmental studies, and medicine.[20,23]

Ruthenium phthalocyanines (PcRu) have shown a wide range of formal metal oxidation states, but the majority of reported ruthenium phthalocyanines have a Ru(II) metal center. The phthalocyanine macrocycle can be both reduced and oxidized and the stepwise abstraction of two electrons yields $Pc^{\bullet -}$ and Pc^{0}, while the stepwise addition of two electrons leads to Pc^{3-} and Pc^{4-}. Substitution of the periphery and changes of ligands at the axial position of the phthalocyanine macrocycle may have a significant effect on the half-wave potentials for reduction and oxidation. For example, the first oxidation for $[PcRuX_2]^{2-}$, where $X = Cl^-$ or Br^-, is a metal-centered $Ru^{II/III}$ process, while the first oxidation of $[PcRcX(CO)]^-$ is assigned to an electron abstraction from the macrocycle.

1.5 Diruthenium Complexes

A large number of metal-metal bonded diruthenium complexes with anionic bridging ligands have been studied since the first synthesis of a tetracarboxylate diruthenium complex (Figure 1-4) was reported by Stephenson and Wilkinson in 1966.[24] The most common oxidation state of the diruthenium core in this is Ru_2^{5+}, but stable diruthenium derivatives with Ru_2^{4+} or Ru_2^{6+} cores have also been isolated and structurally characterized.[25-29] A few diruthenium complexes in lower oxidation states, Ru_2^{3+} or Ru_2^{2+} have also been *in situ* electrogenerated from the initial Ru_2^{5+} and Ru_2^{4+} complexes after coordination of the dimetal unit with NO or CO.[30-32]

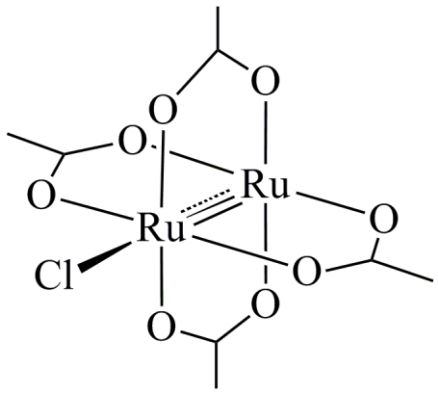

Figure 1-4. Schematic structure of $Ru_2(CO_2CH_3)_4Cl$.

The anionic bridging ligands in diruthenium complexes can be classified into two categories, one of which is symmetrical and the other unsymmetrical. Dimetal complexes bridged by symmetrical bridging ligands are represented by a single structural formula but up to four different isomeric forms are possible for these types of dimetal complexes containing unsymmetrical bridging ligands. These isomers have been represented as (4,0), (3,1), (2,2) trans, or (2,2) cis depending upon the substitution pattern of the ligands with the diruthenium unit.[26,33-36]

The majority of investigated Ru_2^{5+} complexes have contained an axially bound chloride anion and are formulated in their neutral form as Ru_2L_4Cl or $Ru_2(OAc)_x(L)_{4-x}Cl$ (x = 1-4) where L is a symmetrical or unsymmetrical anionic bridging ligands. For these types of diruthenium compounds, two oxidations and two reductions are generally observed in nonaqueous solvents. Half-wave potentials for reduction and oxidation of the diruthenium unit will depend upon the type of anionic bridging ligands as well as the type and number of axial ligands. For example, the $E_{1/2}$ for reduction of $Ru_2(F_2ap)_4Cl$ in CH_2Cl_2 was reported as -0.35 V,[26] where F_5ap = 2-(2,3,4,5,6-pentafluoroanilino)pyridinate anion while $Ru_2(ap)_4Cl$ is reduced at -0.87 V vs SCE[27] under the same solution conditions, a difference of more than 500 mV with changes in substituents on the ap bridging ligands. Likewise, the $E_{1/2}$ for reduction of $Ru_2(ap)_4CN$ is located at -0.73 V while $[Ru_2(ap)_4(CN)_2]^-$ is reduced at -1.24 V in the same solvent.[37]

1.6 Copper(I) Phenanthrolines

1,10-Phenanthroline complexes of transition metals have been extensively studied by researchers working in the area of photochemistry and photophysics,[38] electrochemistry,[39] biochemistry,[40] supramolecular chemistry, and material science.[41] One major interest of these

complexes stems from their relevance to solar energy conversion, sequence-selective DNA cleavage, and fine chemical production by catalytic reactions. The Cu(I) phenanthroline complexes examined in this dissertation are of interest for a number of reasons. They are efficient catalysts for an impressive range of carbon—carbon and carbon—heteroatom bond-forming reactions.[42] Moreover, studies of redox processes involving simple copper(I)–O_2 complexes are useful to mimic the action of Cu-containing metalloenzymes.[43] In addition, their photochemical and photophysical properties have been widely studied.[44,45]

It has been shown that the ligands on the copper phenanthroline complexes are labile and the compounds can undergo ligand exchange reactions in the presence of nucleophiles or coordinating solvents. The substituents on the phenanthroline ring will also have an effect on the structure and electrochemical behavior of the complexes.[46-50] For example, a $Cu^{II/I}$ reduction process of $Cu(phen)_2^+$ is observed at 0.04 V vs SCE in acetonitrile while a $Cu^{II/I}$ reduction process occurs at 0.68 V for $Cu(dap)_2^+$ (phen = 1,10-phenanthroline and dmp = 2,9-dimethyl-1,10-phenanthroline).[50]

1.7 References

1. Wang, J. *Analytical Chemistry*; VCH Publisher, Inc.: New York, **1948**.
2. Bard, A. J.; Faulkner, L. R. *Electrochemical Methods: Fundamentals and Applications (2nd edition)*; John Wiley & Sons, Inc.: New York, **2001**.
3. Kaim, W.; Klein, A. *Spectroelectrochemistry*; Royal Society of Chemistry: Cambridge, **2008**.
4. Kaim, W.; Fiedler, J. *Chemical Society Reviews* **2009**, *38*, 3373-3382.
5. Gouterman, M. *J. Mol. Spectrosc.* **1961**, *6*, 138-63.
6. Fuhrhop, J. H. *Struct. Bonding (Berlin)* **1974**, *18*, 1-67.
7. Erben, C.; Will, S.; Kadish, K. M. In *The Porphyrin Handbook*; Kadish, K. M., Smith, K. M., Guilard, R., Eds.; Acedemic Press: New York, **2000**; Vol. 2, p 233-300.
8. Paolesse, R. In *The Porphyrin Handbook*; Kadish, K. M., Smith, K. M., Guilard, R., Eds.; Academic Press: New York, **2000**; Vol. 2, p 201-232.
9. Johnson, A. W.; Kay, I. T. *J. Chem. Soc.* **1965**, 1620-9.
10. Aviv, I.; Gross, Z. *Chem. Commun. (Cambridge, U. K.)* **2007**, 1987-1999.
11. Aviv-Harel, I.; Gross, Z. *Chem. - Eur. J.* **2009**, *15*, 8382-8394.
12. Paolesse, R.; Di Natale, C.; Macagnano, A.; Sagone, F.; Scarselli, M. A.; Chiaradia, P.; Troitsky, V. I.; Berzina, T. S.; D'Amico, A. *Langmuir* **1999**, *15*, 1268-1274.
13. Aviv-Harel, I.; Gross, Z. *Coord. Chem. Rev.* **2011**, *255*, 717-736.
14. L'Her, M.; Pondaven, A. In *The Porphyrin Handbook*; Kadish, K. M., Smith, K. M., Guilard, R., Eds.; Academic Press: New York, **2003**; Vol. 16, p 117-170.
15. Rawling, T.; McDonagh, A. *Coord. Chem. Rev.* **2007**, *251*, 1128-1157.

16. *The Porphyrin Handbook*; Kadish, K. M.; Smith, K. M.; Guilard, R., Eds.; Acedemic Press: San Diego, CA, **2003**; Vol. 15-20.

17. Rio, Y.; Rodriguez-Morgade, M. S.; Torres, T. *Org. Biomol. Chem.* **2008**, *6*, 1877-1894.

18. Nemykin, V. N.; Lukyanets, E. A. In *Handbook of Porphyrin Science*; Kadish, K. M., Smith, K. M., Guilard, R., Eds.; World Scientific Publishing Co. Pte. Ltd.: Singapore, **2010**; Vol. 3, p 1-323.

19. Li, R.; Zhang, X.; Zhu, P.; Ng, D. K. P.; Kobayashi, N.; Jiang, J. *Inorg. Chem.* **2006**, *45*, 2327-2334.

20. Walter, M. G.; Rudine, A. B.; Wamser, C. C. *J. Porphyrins Phthalocyanines* **2010**, *14*, 759-792.

21. Sergeeva, N. N.; Senge, M. O. In *CRC Handbook of Organic Photochemistry and Photobiology (3rd Edition)* Griesbeck, A., Oelgemöller, M., Ghetti, F., Eds.; CRC Press: Boca Raton, FL, **2012**; Vol. 1, p 831-879.

22. Ragoussi, M.-E.; Ince, M.; Torres, T. *Eur. J. Org. Chem.* **2013**, 6475-6489.

23. Trogler, W. C. *Struct. Bonding (Berlin, Ger.)* **2012**, *142*, 91-118.

24. Stephenson, T. A.; Wilkinson, G. *J. Inorg. Nucl. Chem.* **1966**, *28*, 2285-91.

25. Bear, J. L.; Han, B.; Huang, S.; Kadish, K. M. *Inorg. Chem.* **1996**, *35*, 3012-21.

26. Bear, J. L.; Li, Y.; Han, B.; Van Caemelbecke, E.; Kadish, K. M. *Inorg. Chem.* **1997**, *36*, 5449-5456.

27. Kadish, K. M.; Wang, L.-L.; Thuriere, A.; Van Caemelbecke, E.; Bear, J. L. *Inorg. Chem.* **2003**, *42*, 834-843.

28. Angaridis, P. *Multiple Bonds between Metal Atoms*; 3 ed.; Springer Science and Business Media Inc.: New York, **2005**.

29. Kadish, K. M.; Nguyen, M.; Van Caemelbecke, E.; Bear, J. L. *Inorg. Chem.* **2006**, *45*, 5996-6003.

30. Kadish, K. M.; Han, B.; Shao, J.; Ou, Z.; Bear, J. L. *Inorg. Chem.* **2001**, *40*, 6848-6851.

31. Han, B.; Shao, J.; Ou, Z.; Phan, T. D.; Shen, J.; Bear, J. L.; Kadish, K. M. *Inorg. Chem.* **2004**, *43*, 7741-7751.

32. Kadish, K. M.; Phan, T. D.; Giribabu, L.; Shao, J.; Wang, L.-L.; Thuriere, A.; Van Caemelbecke, E.; Bear, J. L. *Inorg. Chem.* **2004**, *43*, 1012-1020.

33. Chakravarty, A. R.; Cotton, F. A. *Polyhedron* **1985**, *4*, 1957-8.

34. Bear, J. L.; Liu, L. M.; Kadish, K. M. *Inorg. Chem.* **1987**, *26*, 2927-9.

35. Bear, J. L.; Yao, C. L.; Liu, L. M.; Capdevielle, F. J.; Korp, J. D.; Albright, T. A.; Kang, S. K.; Kadish, K. M. *Inorg. Chem.* **1989**, *28*, 1254-62.

36. Bear, J. L.; Wellhoff, J.; Royal, G.; Van Caemelbecke, E.; Eapen, S.; Kadish, K. M. *Inorg. Chem.* **2001**, *40*, 2282-2286.

37. Bear, J. L.; Chen, W.-Z.; Han, B.; Huang, S.; Wang, L.-L.; Thuriere, A.; Van Caemelbecke, E.; Kadish, K. M.; Ren, T. *Inorg. Chem.* **2003**, *42*, 6230-6240.

38. Juris, A.; Balzani, V.; Barigelletti, F.; Campagna, S.; Belser, P.; Von Zelewsky, A. *Coord. Chem. Rev.* **1988**, *84*, 85-277.

39. Sugihara, H.; Hiratani, K. *Coord. Chem. Rev.* **1996**, *148*, 285-299.

40. Bencini, A.; Lippolis, V. *Coord. Chem. Rev.* **2010**, *254*, 2096-2180.

41. Catalano, V. J.; Bennett, B. L.; Yson, R. L.; Noll, B. C. *J. Am. Chem. Soc.* **2000**, *122*, 10056-10062.

42. Gujadhur, R. K.; Bates, C. G.; Venkataraman, D. *Org. Lett.* **2001**, *3*, 4315-4317.

43. Lei, Y.; Anson, F. C. *Inorg. Chem.* **1995**, *34*, 1083-1089.

44. Armaroli, N. *Chem. Soc. Rev.* **2001**, *30*, 113-124.

45. Lavie-Cambot, A.; Cantuel, M.; Leydet, Y.; Jonusauskas, G.; Bassani, D. M.; McClenaghan, N. D. *Coord. Chem. Rev.* **2008**, *252*, 2572-2584.

46. Bush, P. M.; Whitehead, J. P.; Pink, C. C.; Gramm, E. C.; Eglin, J. L.; Watton, S. P.; Pence, L. E. *Inorg. Chem.* **2001**, *40*, 1871-1877.

47. Eggleston, M. K.; McMillin, D. R.; Koenig, K. S.; Pallenberg, A. J. *Inorg. Chem.* **1997**, *36*, 172-176.

48. Scaltrito, D. V.; Thompson, D. W.; O'Callaghan, J. A.; Meyer, G. J. *Coord. Chem. Rev.* **2000**, *208*, 243-266.

49. Yang, P.; Yang, X.-J.; Wu, B. *Eur. J. Inorg. Chem.* **2009**, 2951-2958.

50. Federlin, P.; Kern, J. M.; Rastegar, A.; Dietrich-Buchecker, C.; Marnot, P. A.; Sauvage, J. P. *New J. Chem.* **1990**, *14*, 9-12.

CHAPTER TWO

Experimental and Methods

2.1 Chemicals

2.1.1 Studied Compounds

All compounds investigated in this dissertation were obtained from our collaborators. The free-base and iron corroles were prepared in the laboratory of Dr. Roberto Paolesse at the University of Rome Tor Vergata.[1,2] Ruthenium thalocyanine and the tetraruthenium complex were synthesized in the laboratory of Dr. Tomás Torres at the Autonomous University of Madrid.[3] The diruthenium complexes were prepared by Dr. Baocheng Han at the University of Wisconsin-Whitewater. The copper complexes were obtained from Dr. Roger Guilard at the University of Dijon. The purity of these compounds was verified by comparing UV-visible data obtained in our laboratory with those provided by our collaborators.

2.1.2 Other Chemicals

Solvents were used as received unless otherwise stated. Dichloromethane (99.8%, CH_2Cl_2) was purchased from EMD Chemical Inc. Pyridine (99.8%, Py) was purchased from Aldrich Chemical Co. Reagent plus grade benzonitrile (99%, PhCN) was also purchased from Aldrich Chemical Co. and distilled over P_2O_5 under vacuum prior to use.

Tetra-*n*-butylammonium perchlorate ($TBAClO_4$, Fluka Chemicals Co.); Tetra-*n*-butylammonium hexafluorophosphate ($TBAPF_6$, Sigma Aldrich); Tetra-*n*-butylammonium fluoride (TBAF, Fluka Chemicals Co.); Tetra-*n*-butylammonium chloride (TBACl, Fluka Chemicals Co.); Tetra-*n*-butylammonium iodide (TBAI, Sigma Aldrich); and Tetra-*n*-butylammonium bromide (TBABr, TCI America) were all used as received without further purification.

Ultra high purity grade nitrogen (N_2) and research purity grade carbon monoxide (CO) were purchased from Matheson Tri-gas. N_2 was passed through anhydrous calcium sulfate and sodium hydroxide pellets to eliminate traces of water prior to use while CO was used without further purification.

2.2 Physical Measurements

2.2.1 Electrochemistry

Cyclic voltammetric measurements were performed with a three-electrode system using an EG&G Princeton Applied Research (PAR) Model 173 potentiostat. The cyclic voltammogram set up is illustrated in Figure 2-1. A glassy carbon electrode was used as a working electrode (WE). A Pt wire was used as a counter electrode (CE) and a homemade saturated calomel electrode (SCE) was used as the reference electrode. This electrode was separated from the bulk of the solution by a fritted glass bridge of low porosity containing the solvent/supporting electrolyte mixture. The solvent was saturated with N_2 gas prior to taking measurements. Ferrocene (Fc) was used as an internal standard for some measurements.

2.2.2 UV-visible Spectroelectrochemistry

UV-visible spectroelectrochemical experiments were performed with an optically transparent platinum thin-layer electrode of the type described in the literature.[4] (Figure 2-2). Potentials were applied and monitored with an EG&G Princeton Applied Research (PAR) Model 173 potentiostat. Time-resolved UV-visible spectra were recorded with a Hewlett-Packard Model 8453 diode array rapid-scanning spectrophotometer.

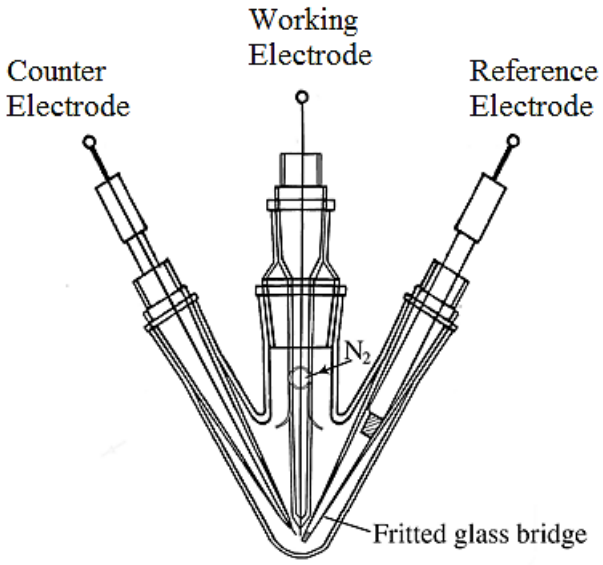

Figure 2-1. Three-electrode electrochemical cell used for cyclic voltammetry measurements.

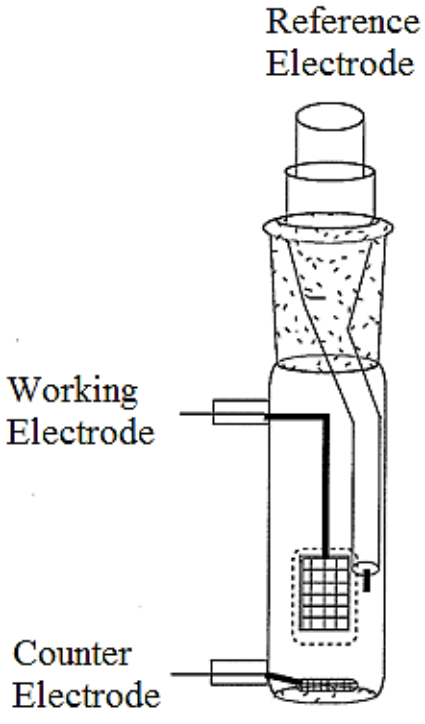

Figure 2-2. Schematic representation of the thin-layer UV-visible spectroelectrochemical cell.

2.2.3 FTIR Spectroelectrochemistry

Thin-layer FTIR spectroelectrochemistry measurements were performed using a Nicolet 6700 FTIR spectrometer along with an EG&G model 173 potentiostat and a specially constructed light-transparent three-electrode cell[5] shown in Figure 2-3.

2.3 Analytical Methods

2.3.1 Measurement of Half-wave Potentials, $E_{1/2}$

Anodic and cathodic peak potentials, E_{pa} and E_{pc} obtained from the cyclic votammograms were used to calculate the half-wave potentials, $E_{1/2}$ according to Eq 2-1.

The anodic and cathodic peak currents, i_{pa} and i_{pc} can be measured. For a reversible redox process, the ratio of $i_{pa}/i_{pc} = 1$. The theoretical peal-to-peak separation is described by Eq 2-2 where n is the number of electrons transferred.

$$(E_{pa} + E_{pc})/2 = E_{1/2} \qquad (2\text{-}1)$$

$$\Delta E_p = E_{pc} - E_{pa} = 0.059/n \qquad (2\text{-}2)$$

2.3.2 Measurement of Formation Constants

Formation constants for ligand binding were calculated using either UV-visible spectroscopy or electrochemistry. A stock solution containing a known concentration of the ligand was quantitatively added to the nonaqueous solvent. Changes in the UV-visible spectra or in the half-wave potentials for reduction or oxidation were monitored during a titration. The methods described below were used to calculate the formation constants.

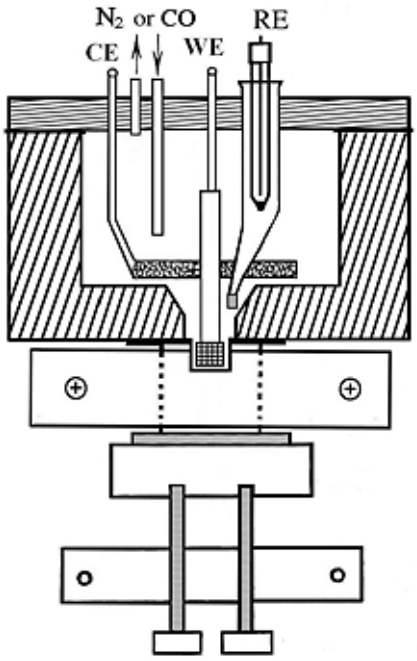

Figure 2-3. Schematic illustration of the *in situ* IR spectroelectrochemical cell (CE = counter electrode, WE = working electrode and RE = reference electrode).

2.3.2.1 Calculation of Formation Constants by Electrochemical Titration Methods[6-8]

For a reversible electron transfer reaction involving ligand binding as shown in Eq 2-3,

$$M + pL + ne \rightleftharpoons (ML_p)^{n-} \qquad (2\text{-}3)$$

the half-wave potentials will shift with a change in the concentration of the ligand according to Eq 2-4,

$$(E_{1/2})_c = (E_{1/2})_s - \frac{RT}{nF}(\log K + p \log[L]) \qquad (2\text{-}4)$$

where $(E_{1/2})_c$ and $(E_{1/2})_s$ are the half-wave potentials for the electron transfer reaction of the ligated and unligated complexes, respectively. *n* is the number of electrons transferred. The term RT/F is equal to 59 mV at 25 °C. The number of ligands bound represented by *p* can be calculated from the plot of $(E_{1/2})_c$ *vs* log[L] and the formation constant (*K*) can be determined from the intercept of the plot.

If both the oxidized and reduced forms of the compound can bind ligands, the electrochemical calculations are more complicated and the relevant equation (at 25 °C) is given by Eq 2-5.

$$(E_{1/2})_c = (E_{1/2})_s - 0.059 \log \frac{K_{ML_p}}{K_{(ML_q)^-}} - (p-q)0.059 \log[L] \qquad (2\text{-}5)$$

In this case, *p* and *q* are equal to the number of ligands bound to the oxidized and reduced forms of the compound, $(E_{1/2})_c$ and $(E_{1/2})_s$ are half-wave potentials for the ligated and unligated compound. K_{ML_p} and $K_{(ML_q)^-}$ are the formation constants of the ML_p and $(ML_q)^-$, respectively. When the ligand concentration is equal to 1.0 M or when $p = q$, the

difference in half-wave potential $(E_{1/2})_c$ and $(E_{1/2})_s$ will give directly the ratio of stability constants for ligand binding to the different forms of the redox couple.

2.3.2.2 Calculation of Formation Constants by UV-vis Spectroscopy[9-11]

For a ligand-binding reaction, $M + pL \rightleftharpoons ML_p$, the relationship between the formation constant (K) and the concentration of the species in solution is given by Eq 2-6

$$\log([ML_p]/[M]) = \log K + p\log[L] \quad (2\text{-}6)$$

where [M] and $[ML_p]$ are the concentrations of the unligated and ligated compound, respectively. [L] is the concentration of the free ligand in solution and p is the number of the coordinated ligands. According to Beer's law, we can write:

$$A_o = \varepsilon_M b C_M \quad (2\text{-}7)$$

$$A_f = \varepsilon_{ML_p} b C_{ML_p} \quad (2\text{-}8)$$

$$A_i = \varepsilon_M b[M] + \varepsilon_{ML_p} b[ML_p] \quad (2\text{-}9)$$

where C_M and C_{ML_p} are the total concentrations of M and ML_p, repectively. ε is the molar absorptivity of each species. b is the path length of the UV-visible cell. A_o and A_f are the initial and final absorbances at a given wavelength (λ_{max}) for the species M and ML_p. A_i is the absorbance at λ_{max} during the titration.

According to the mass balance equation, $C_M = C_{ML_p} = [M] + [ML_p]$, in solution. Equation 2-6 can be simplified and expressed in terms of the absorbances from Eqs 2-7 to 2-9. This will solve for the Hill plot (see Eq 2-10), where the [M] and $[ML_p]$ terms are substituted for by the absorbance terms.

$$\log[(A_i - A_o)/(A_f - A_i)] = \log K + p\log[L] \quad (2\text{-}10)$$

A plot of $\log[(A_i - A_o)/(A_f - A_i)]$ *vs* $\log[L]$ should be a straight line with a slope corresponding to the number of bound ligands (p). The zero intercept of the equation describing in Eq 2-10 can be used to calculate the binding constant.

2.4 References

1. Nardis, S.; Stefanelli, M.; Mohite, P.; Pomarico, G.; Tortora, L.; Manowong, M.; Chen, P.; Kadish, K. M.; Fronczek, F. R.; McCandless, G. T.; Smith, K. M.; Paolesse, R. *Inorg. Chem.* **2012**, *51*, 3910-3920.
2. Stefanelli, M.; Pomarico, G.; Tortora, L.; Nardis, S.; Fronczek, F. R.; McCandless, G. T.; Smith, K. M.; Manowong, M.; Chen, P.; Kadish, K. M.; Rosa, A.; Ricciardi, G.; Paolesse, R. *Inorg. Chem.* **2012**, *51*, 6928-6942.
3. Manowong, M.; Van Caemelbecke, E.; Rodríguez-Morgade, M. S.; Bear, J. L.; Kadish, K. M.; Torres, T. *J. Porphyrins and Phthalocyanines* **2014**, *18*, 1-9.
4. Lin, X. Q.; Kadish, K. M. *Anal. Chem.* **1985**, *57*, 1498-501.
5. Kadish, K. M.; Mu, X. H.; Lin, X. Q. *Electroanalysis (N. Y.)* **1989**, *1*, 35-41.
6. Crow, D. R. In *Polarography of Metal Complexes*; Academic Press: London, **1969**.
7. Kadish, K. M. In *Iron Porphyrins, Part Two*; Lever, A. B. P., Grey, H. B., Eds.; Addison-Wesley: London, **1983**, p 161.
8. Lingane, J. J. *Chem. Rev.* **1941**, *29*, 1-35.
9. Budesinsky, B. W. *Talanta* **1974**, *21*, 323-6.
10. Yoe, J. H.; Jones, A. L. *Ind. Eng. Chem., Anal. Ed.* **1944**, *16*, 111-15.
11. Ellis, P. E., Jr.; Linard, J. E.; Szymanski, T.; Jones, R. D.; Budge, J. R.; Basolo, F. *J. Am. Chem. Soc.* **1980**, *102*, 1889-96.

CHAPTER THREE

β-Nitro-5,10,15-tritolylcorroles

3.1 Introduction

The establishment of efficient synthetic methodologies for the preparation of corrole[1-4] has allowed a more detailed investigation of its chelating properties as a ligand, and of its unique behavior in several reactions.[5] The investigation of corrole functionalization reactions is fundamental for the potential exploitation of this macrocyle in practical uses, since the manipulation of the peripheral positions can deeply affect the corrole properties, as shown by the first seminal examples reported in the literature.[6-8]

Compared with porphyrins, the peripheral functionalization of the corrole macrocycle is possible only in a limited number of cases, but recently some successful substitutions have been reported in the literature.[4,9] In particular, we have been interested in the nitration reaction, because the insertion of one or more -NO_2 groups onto the β-pyrrole positions represents one of the most valuable modifications for researchers interested in functionalization of the corrole skeleton; for example, the potential of the nitro group in activating nucleophilic substitution on the adjacent β-carbons of the pyrrole rings is well-known. Furthermore, it is also interesting to evaluate the influence of the strong electron withdrawing character of the nitro group on the behavior of the corrole ring, which is characterized by high electron density and its noninnocent character as ligand.[10] In this connection, we recently reported the first successful example of a vicarious nucleophilic substitution performed on corrole nitro-derivatives by reacting copper and germanium β-(NO_2) corrolates with 4-amino-4H-1,2,4-triazole.[11] The reaction afforded β-amino-β-nitro derivatives, which can have great synthetic value for the elaboration of new chromophores, as well as extended aromatic β-fused architectures. To date β-nitrocorrole derivatives of copper,[11] germanium,[12] gallium,[13] silver,[14] cobalt,[15] and iron[16] have been prepared by using a

variety of nitrating systems and reaction conditions, while all attempts to nitrate the corrole free-base failed, mainly because of the lability of corroles under these substitution conditions. This was evidenced under a variety of reaction conditions with the formation of isocorrole species. The recent development of demetalation protocols for the effective removal of silver[17] and copper[18-20] from the corresponding corrole complexes has allowed the preparation of nitrocorrole free bases from the application of the reductive DBU/THF system to a silver 3-NO_2 corrolate (3-NO_2TtBuCorrAg), obtained by using a large excess of $AgNO_2$.[17] Although this approach allowed circumvention of the instability of corrole under the nitrating systems tested to date, it opened the way to preparation of otherwise unavailable 3-NO_2 corroles. Such preparations of functionalized free bases in a single step is highly desirable, particularly in the preparation of polynitrated free bases. Prompted by the recent results obtained in the case of nitration of copper corrole complexes[11] carried out with an optimized ratio of silver salt and sodium nitrite mixture as the nitrating system, we decided to apply the same reaction conditions to corrole free bases, surmising that minimizing the oxidant stoichiometry could preserve corrole aromaticity during the reaction, but still allow nucleophilic attack by the NO_2^- ion upon the macrocycle.

We report here the first successful example of nitration of the corrole free base, obtained by reacting 5,10,15-tritolylcorrole ($TTCorrH_3$) with the $AgNO_2/NaNO_2$ system.[21] Variation of the molar ratio of reagents allowed us to obtain 3-nitro- and 3,17- dinitro-derivatives of corrole in satisfying yield, together with traces of other isomers, namely 2-NO_2-, 2,3-$(NO_2)_2$, and 3,12-$(NO_2)_2$ corroles (Chart 3-1). While the substitution pattern of 2-NO_2TTCorrH_3 was established structurally by X-ray crystallography, in the case of 2,3-$(NO_2)_2$TTCorrH_3 and 3,12-$(NO_2)_2$TTCorrH_3 isomers, the substitution pattern was

unambiguously confirmed by preparation of the corresponding Co triphenylphosphine complexes, which were also structurally characterized.

The definition of the synthetic protocols for the preparation of free base nitrocorroles prompted us to study in detail the influence of the introduction of the nitro group at the corrole *β*-positions. This has been accomplished through a detailed UV-visible, electrochemical, and spectroelectrochemical characterization of these functionalized corroles. The changes in the UV-visible spectra and in the first reduction potential following *β*-nitration have been rationalized by density functional theory (DFT) and time-dependent DFT (TDDFT) calculations of the ground and excited states of the $TTCorrH_3$, 2-$NO_2TTCorrH_3$, 3-$NO_2TTCorrH_3$, and 3,17-$(NO_2)_2TTCorrH_3$ series of free base corroles. Taken together, the experimental and theoretical results provide informative details on the behavior of these macrocycles.

Chart 3-1. Molecular structures of *β*-nitrocorroles presented in this dissertation.

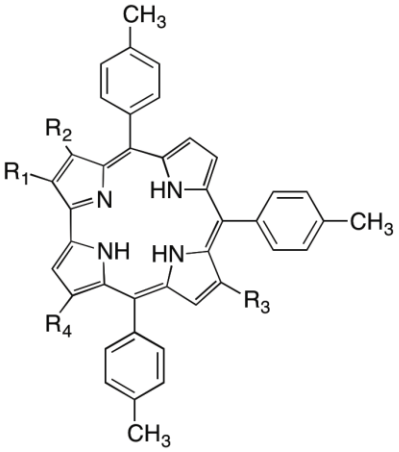

$TTCorrH_3$	$R_1 = R_2 = R_3 = R_4 = H$		
3-$NO_2TTCorrH_3$	$R_1 = R_3 = R_4 = H$	$R_2 = NO_2$	
2-$NO_2TTCorrH_3$	$R_2 = R_3 = R_4 = H$	$R_1 = NO_2$	
3,17-$(NO_2)_2TTCorrH_3$	$R_1 = R_3 = H$	$R_2 = R_4 = NO_2$	
2,3-$(NO_2)_2TTCorrH_3$	$R_3 = R_4 = H$	$R_1 = R_2 = NO_2$	
3,12-$(NO_2)_2TTCorrH_3$	$R_1 = R_4 = H$	$R_2 = R_3 = NO_2$	

3.2 Results and Discussion

3.2.1 Synthesis

In the past few years, we have been particularly interested in the elaboration of synthetic protocols for the synthesis of β-nitrocorrole derivatives. By using different nitrating systems, we have been able to establish diverse methodologies for the convenient preparation of mono- and dinitro-metallocorrolates, starting in most cases from metallocorroles, such as the Cu, Ge, and Fe derivatives. Our attempts to introduce nitro groups directly onto the free base, to obtain the corresponding functionalized corrole failed, since the required β-substitution took place in combination with other structural modifications, thereby precluding the isolation of the pure nitrocorrole free base. For example, using a large excess of $AgNO_2$, both functionalization and metalation of the macrocycle occurred simultaneously, affording the corresponding Ag(III) 3-nitrocorrole as the reaction product.[14] In the case of TFA/$NaNO_2$ or HCl/$NaNO_2$ systems, the formation of β-nitroisocorroles was observed, but these were converted in a second step into the corresponding aromatic corrole complexes by cobalt insertion.[15] Our hypothesis for the nitration reaction mechanism is that the first step requires an oxidant species for the generation of the corrole π-cation radical, which is then attacked by nitrite to afford the final product. However, corrole free bases demonstrate extreme sensitivity under oxidizing reaction conditions, leading to a quite facile conversion of the macrocycle into the corresponding isocorrole species.[11,15,17,22-26] Therefore, the nitration reaction conditions made the preparation of aromatic nitro-compounds difficult, instead favoring the formation of isocorrole derivatives through nucleophile insertion onto a *meso*-carbon position, which was

observed for the 3-NO_2-5-OH-isocorroles.[11,26] Since the oxidation step is crucial for the reaction outcome, we surmised that a careful choice of the oxidant species could potentially drive the reaction pathway toward nitrocorroles, inhibiting the further transformation to isocorroles.

We recently reported that when the nitration reaction is performed on corrole using an equimolar amount of an oxidizing agent, such as chloranil in combination with an excess of $NaNO_2$, the 3-NO_2-5-OH-isocorrole is rapidly obtained as the main reaction product, confirming the regioselectivity of both mononitration and the formation of the single 5-substituted isocorrole isomer.[26] Our attention turned toward other oxidants, and prompted by the results reported recently for nitration of copper corrolates, we tested the $AgNO_2$/$NaNO_2$ system, which allows the preparation of mono- and dinitro-derivatives in good yields just by varying the reagent stoichiometry.[11]

Thus, $TTCorrH_3$ was reacted in refluxing DMF with a mixture of sodium and silver nitrites using a corrole/$AgNO_2$/$NaNO_2$ molar ratio of 1:1:9 (Scheme 3-1) with the intention of achieving mononitration of the corrole. The reaction proceeded very fast and in 10 min complete disappearance of the starting compound was observed by TLC analysis, together with the formation of a green major product. The UV-visible spectrum of the mixture changed rapidly even from the beginning of the reaction and showed at the end the typical spectral features of 3-$NO_2TTCorrH_3$,[17] indicating it as the main product. Chromatographic purification afforded traces of the silver complex of the corrole as the first rose-red band together with a second fraction containing a mixture of brownish and greenish products, inseparable on the column. A third green fraction was the major reaction product and

Scheme 3-1. Synthesis of $(NO_2)_xTTCorrH_3$.

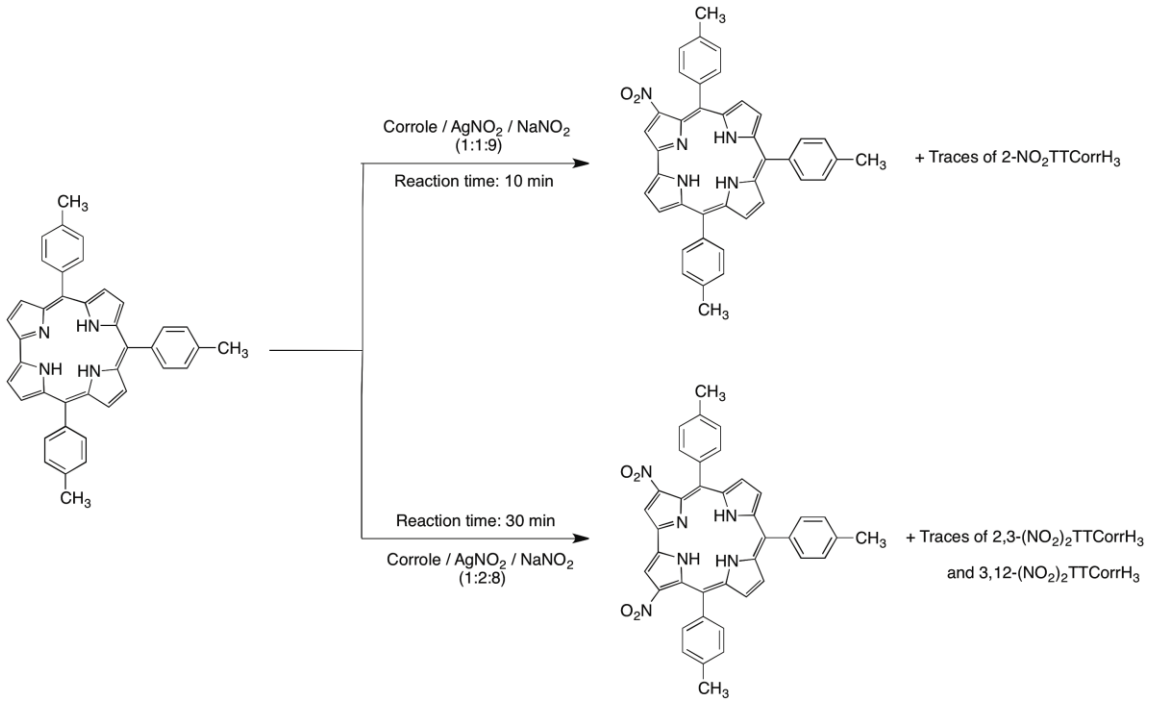

corresponded to 3-NO_2TTCorrH_3, obtained in 52% yield. It is worth mentioning that the formation of the 3-nitro-5-hydroxy-isocorrole was not observed, showing that the amount of silver nitrite was correctly chosen to allow the *β*-functionalization, and to preserve at the same time the integrity of the nitrocorrole free base formed in the reaction medium. The second band was further purified on a preparative silica gel TLC plate, using a mixture of CH_2Cl_2/hexane as eluant. A green band (R_f = 0.52) was isolated in sufficient amount to be characterized using the usual spectroscopic techniques. This fraction showed an unusual UV-visible spectrum, characterized by a split Soret band (of similar intensity) at 408 and 460 nm, a less intense narrow band centered at 588 nm, and a broad band at about 715 nm. The FAB mass spectrum of this compound afforded a molecular peak at *m/z* 613, which is consistent with a mononitrocorrole. The ^{1}H NMR spectrum and integral calculations confirmed it as a

monosubstituted corrole showing a proton singlet at 9.08 ppm. It is noteworthy that the pattern of substitution is clearly different from that of the known 3- $NO_2TTCorrH_3$, showing a pyrrolic doublet more deshielded compared with the singlet, just as observed for the 2-bromocorrole isomer obtained by reacting the $TTCorrH_3$ with EtMgBr.[25] The definitive identification of position C2 as the site of substitution for this compound was afforded by X-ray crystallographic analysis, carried out on a single crystal obtained by slow diffusion of *n*-hexane into a dilute dichloromethane solution. This unambiguously confirmed the new monosubstituted corrole as the 2-$NO_2TTCorrH_3$ isomer (Figure 3-1).

The three protonated N atoms in the interior of the molecule force marked deviations of the corrole system from coplanarity. The mean deviation of its 23 atoms is 0.159 Å, with a maximum of 0.415(4) Å. The nitrated "A" pyrrole and the adjacent "B" pyrrole not directly bonded to it come nearest to being coplanar, forming a dihedral angle of 10.5(6)°. The main distortion of the corrole is a twist, in which the other two pyrroles "C" and "D" tip alternately above and below this plane, forming dihedral angles of 18.1(3) and 20.6(2)° with it and 23.8(3)° with each other. The N atoms of the two alternately tipped pyrroles are somewhat pyramidal, with their H atoms lying 0.14(4) and -0.30(4) Å out of the best planes of their respective pyrroles. The third N−H hydrogen atom is not tipped out of plane, but forms an N−H···N hydrogen bond (N···N 2.623(3) Å; N−H···N 134(3)°). The nitro group lies essentially in the plane of the pyrrole to which it is bonded, with a C1−C2−N−O torsion angle 1.2(4)°. The two directly bonded pyrroles exhibit a N−C1−C19−N twist of 7.6(3)°.

With the aim of driving the reaction toward dinitrocorrole derivatives, we modified the amounts of nitrating agents by altering the corrole/$AgNO_2$ molar ratio to 1:2 (Scheme 3-1). Of course, in this case, we were aware that the increase of the oxidant reagent could induce

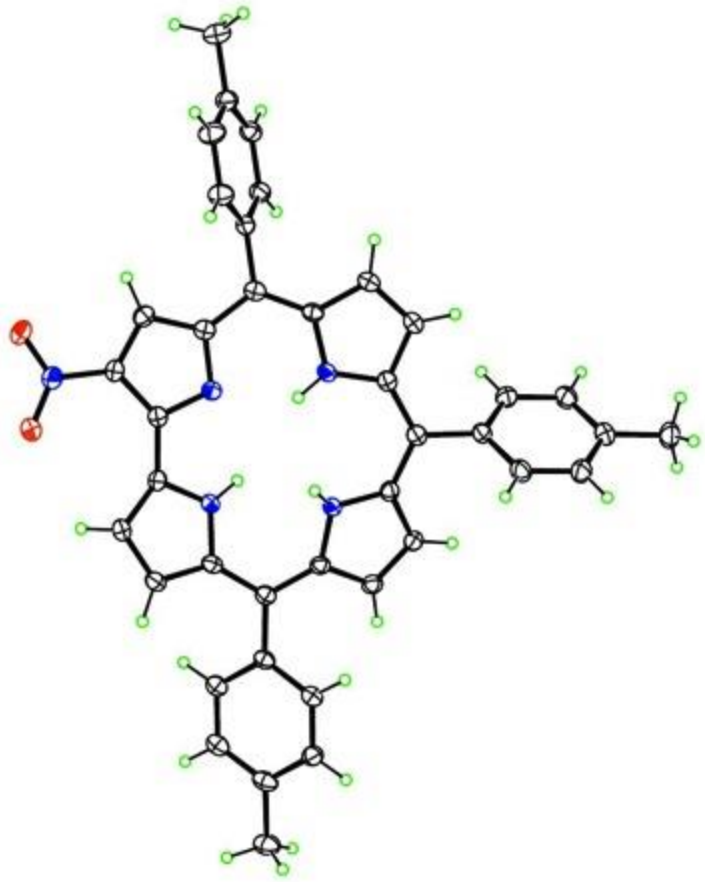

Figure 3-1. Molecular structure of 2-NO_2TTCorrH_3, with 50% ellipsoids (taken from ref 21).

the formation of the isocorrole, instead of forming dinitrocorroles. The reaction of $TTCorrH_3$ with silver and sodium nitrites in a 1:2:8 molar ratio, afforded in 30 min a mixture of compounds observable from the TLC analysis as green and bluish-green bands together with a number of decomposition products.

Chromatographic purification on silica gel using dichloromethane as eluant afforded, after elution of small traces of the silver tritolylcorrolate, a first major fraction consisting of the $3\text{-}NO_2\text{-}5\text{-}OH\text{-}TTisoCorrH_2$, obtained in 9% yield. Afterward, a small quantity of two green fractions was isolated and subjected to spectroscopic identification. The band having the greater R_f value showed a UV-visible spectral profile quite similar to $3\text{-}NO_2TTCorrH_3$, but generally red-shifted, while the second fraction displayed a strongly red-shifted Soret band at 472 nm together with two satellite bands at 613 and 666 nm. The mass spectrometry analysis afforded a molecular peak at *m/z* 658 for both compounds, tentatively identifying them as two different dinitrocorrole isomers. The proton NMR spectra of both compounds were of poor resolution, hampering definitive identification of the sites of substitution by the nitro groups.

The last green fraction obtained by column chromatographic purification was the main reaction product, obtained in 20% yield, and fully characterized as $3,17\text{-}(NO_2)_2TTCorrH_3$. The UV-visible spectrum was unusual, having a split Soret band at 439 and 483 nm and an intense broad absorption at ca. 700 nm.

To allow a more definitive identification of the other dinitrocorrole isomers, we decided to prepare the corresponding Co complexes, by reaction of these products with $Co(OAc)_2$ and PPh_3; the reaction provided cobalt complexes having well resolved ^1H NMR

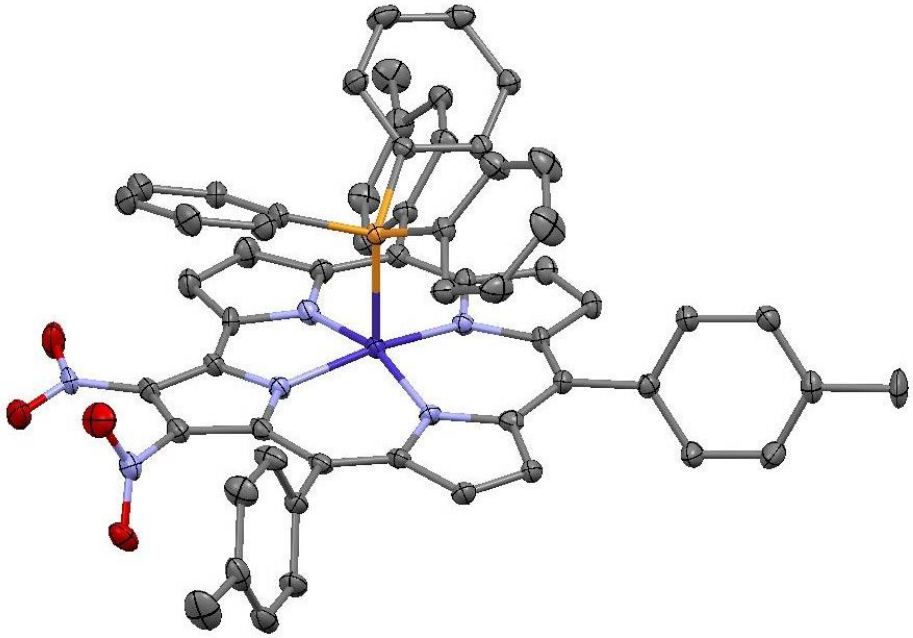

Figure 3-2. Molecular structure of 2,3-$(NO_2)_2$TTCorrCoPPh_3, with 50% ellipsoids and H atoms not shown (taken from ref 21).

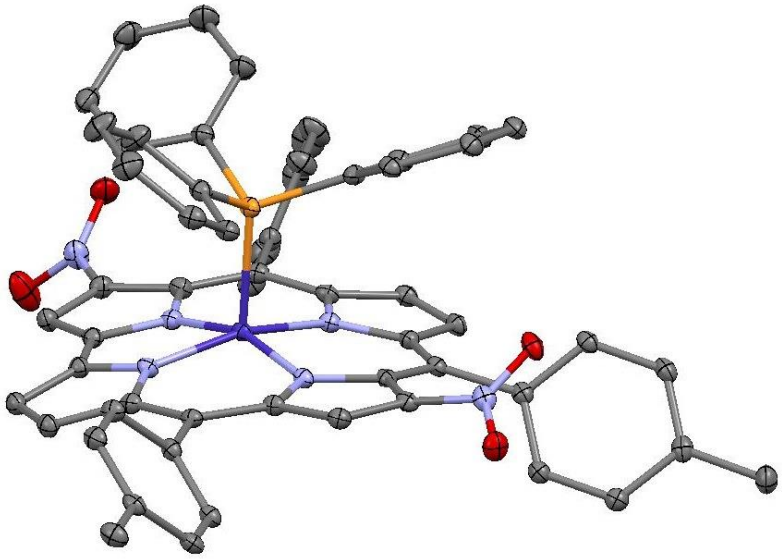

Figure 3-3. Molecular structure of 3,12-$(NO_2)_2$TTCorrCoPPh_3, with 30% ellipsoids and H atoms not shown (taken from ref 21).

spectra. In the case of the first compound, the lack of proton singlets together with the presence of a downfield shifted doublet above 9 ppm, clearly separated from the other five pyrrolic resonances at ca. 8-8.5 ppm, led to the conclusion that for this compound the substitution occurred on the C2 and C3 positions of the corrole macrocycle. We were able to obtain crystals of this isomer suitable for X-ray crystallographic analysis, which helped to elucidate the structure of the corresponding free base as 2,3-$(NO_2)_2$TTCorrH_3.

The structure of 2,3-$(NO_2)_2$TTCorrCoPPh_3 is shown in Figure 3-2. The Co atom has square pyramidal coordination with Co−N distances in the range 1.869(3)-1.886(3) Å (mean 1.880 Å), Co−P distance 2.2321(8) Å, and the Co is 0.2634(13) Å out of the best plane of the four pyrrole N atoms. The 23-atom $C_{19}N_4$ corrole core deviates only slightly from planarity, with an rms deviation 0.059 Å and maximum deviation 0.119(3) Å for C7. The small distortion from planarity is a slight saddle. One nitro group lies nearly in the corrole best plane, with C1−C2−N−O torsion angle -6.9(5)°, while the other is more nearly orthogonal to the corrole, with C2−C3−N−O torsion angle -73.1(4)°.

The second Co complex showed two proton singlets at 8.98 and 8.67 ppm, respectively, and three different proton signals of equal intensity at 2.62, 2.57, and 2.54 ppm, indicating it to be an asymmetric product. Also in this case, the X-ray crystallographic characterization (Figure 3-3) led to identification of 3,12-$(NO_2)_2$TTCorrCoPPh_3, confirming the corresponding corrole free base as the 3,12-$(NO_2)_2$TTCorrH_3 isomer. It is interesting to note that this isomer is, to the best of our knowledge, the first example of a disubstituted corrole where pyrroles A and C are functionalized, instead the usual A and D pattern.

The structure of 3,12-$(NO_2)_2$TTCorrCoPPh_3 is illustrated in Figure 3-3 and is quite similar to that of 2,3-$(NO_2)_2$TTCorrCoPPh_3, with a somewhat more nonplanar corrole core.

The Co atom has square pyramidal coordination with Co−N distances in the range 1.873(3)-1.892(3) Å (mean 1.878 Å), Co−P distance 2.2113(11) Å, and the Co is 0.2734(15) Å out of the best plane of the four pyrrole N atoms. The 23-atom $C_{19}N_4$ corrole core is approximately three times more distorted from planarity than that of 2,3-$(NO_2)_2$TTCorrCoPPh_3, having an rms deviation of 0.159 Å and maximum deviation 0.339(4) Å for C8. The distortion is best described as a saddle, although all four N atoms lie on the same side of the 23-atom best plane by a mean distance of 0.118 Å. The two nitro groups are twisted out of the corrole best plane by similar amounts, forming torsion angles: C4−C3−N−O, -40.0 (6)° and C11−C12−N−O, 29.2 (5)°.

It is worth mentioning that in all cases the use of the $AgNO_2$/$NaNO_2$ system allowed the *β*-functionalization of the macrocycle, without inducing the concomitant metalation, which occurs when the reaction is carried out with an excess of silver nitrite. In this case the $AgNO_2$ acts only as oxidant, and the proper amount chosen prevented the metalation of the macrocycle. The transient formation of the silver corrole complex, then demetalated by the final addition of hydrazine can be safely excluded, because hydrazine is unable to promote silver corrole demetalation and because the same products were again obtained when the nitration reaction was carried out avoiding the addition of this reagent.

3.2.2 Electrochemistry and Spectroelectrochemistry in Nonaqueous Media

The redox behavior of free base corroles is complicated in nonaqueous media by the facile gain or loss of protons, which can give in solution a mixture of the neutral corrole along with either its protonated $[CorrH_4]^+$ or deprotonated $[CorrH_2]^-$ form. To investigate the effect of nitration and the solvent on both the overall oxidation/reduction mechanism and the electrochemically initiated protonation/deprotonation process, a series of three corroles,

$TTCorrH_3$, 3-$NO_2TTCorrH_3$, and 3,17-$(NO_2)_2TTCorrH_3$, were selected for electrochemical and spectroelectrochemical characterization in pyridine, benzonitrile (PhCN), and dichloromethane (CH_2Cl_2).

We earlier reported the electrochemistry and spectroelectrochemistry of several meso-substituted corroles in PhCN and pyridine, including $TTCorrH_3$.[27,28] It was demonstrated that the electroactive species in PhCN was the neutral corrole $CorrH_3$, while in pyridine, the monoanion $[CorrH_2]^-$ is the prevalent species,[27,28] the deprotonation process being almost complete. A similar solvent effect on deprotonation is seen for the currently investigated corroles, as seen by the cyclic voltammograms in Figure 3-4 for $TTCorrH_3$ in CH_2Cl_2, PhCN, and pyridine.

The first reduction of $TTCorrH_3$ is irreversible in all three solvents and located at E_p = −1.33 to -1.40 V for a scan rate of 0.1 V/s. Only a residual amount of neutral $CorrH_3$ is present in the basic pyridine solvent and a small peak current is seen for reduction of the fully protonated corrole. This contrasts with CH_2Cl_2, where $CorrH_3$ is the main electroactive species in solution and the peak current is much higher for the first reduction. Sweeping the potential from -0.40 to values beyond the first reduction in PhCN or pyridine drives to completion the deprotonation of $TTCorrH_3$, after which the deprotonated $[TTCorrH_2]^-$ product undergoes a reversible one-electron ring-reduction, which is located at $E_{1/2}$ = -1.90 V in PhCN and -1.88 V in pyridine.

As indicated above, $TTCorrH_3$ undergoes deprotonation in both CH_2Cl_2 and PhCN after the first one-electron reduction and this then generates $[CorrH_2]^-$. As a result, when reversing the scan at potential negative of the first reduction and then scanning in a positive

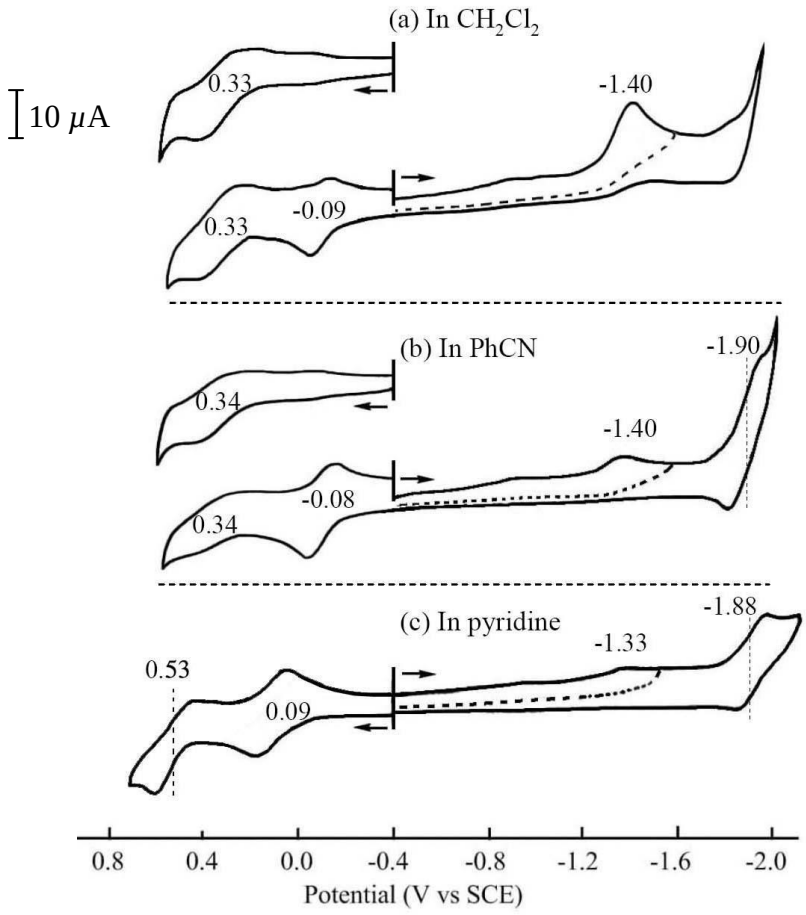

Figure 3-4. Cyclic voltammograms of $TTCorrH_3$ in (a) CH_2Cl_2, (b) PhCN and (c) pyridine containing 0.1 M TBAP.

direction, a new redox couple assigned to $[(Corr)H_2]^-/[(^{\bullet}Corr)H_2]$ can be seen in CH_2Cl_2 and PhCN. This process is located at $E_{1/2}$ = -0.09 to -0.08 V and it is not observed in CH_2Cl_2 or PhCN, when sweeping the potential toward more positive values from the initial potential of -0.4 V. This oxidation of $[(Corr)H_2]^-$ is however seen in pyridine on all scans, in a positive or negative direction ($E_{1/2}$ = 0.09 V).

To investigate the effect of nitration on both the overall oxidation/reduction mechanism and the protonation/deprotonation processes, 3-NO_2TTCorrH_3 and 3,17-$(NO_2)_2$TTCorrH_3 were also characterized electrochemically and spectroelectrochemically in pyridine, PhCN, and CH_2Cl_2.

The addition of one or two nitro substituents to the β-pyrrole positions of the macrocycle leads to a positive shift in $E_{1/2}$ for each oxidation or reduction of the nitro-substituted free base corroles, as compared to measured half-wave potentials for the oxidation or reduction of TTCorrH_3. This is as expected, due to the strong electron withdrawing character of the NO_2 substituents, with the magnitude of the positive shift in $E_{1/2}$ varying as a function of both the number of the nitro groups on the macrocycle (0, 1, or 2), as well as the specific electrode reaction.

A summary of redox potentials for of TTCorrH_3, 3-NO_2TTCorrH_3, and 3,17-$(NO_2)_2$TTCorrH_3 in the different solvents is given in Table 3-1, while typical cyclic voltammograms are shown in Figure 3-5 for the three corroles in pyridine, containing 0.1 M TBAP. As shown in this figure, the addition of one or two nitro substituents to the β-pyrrole positions of the macrocycle leads to similar positive shifts in $E_{1/2}$ for the first two oxidations. A positive shift in $E_{1/2}$ of 130-160 mV for each additional nitro group is at the 3 and 17

Table 3-1. Half-wave or Peak Potentials (V vs SCE) for the Different Forms of $(NO_2)_xTTCorrH_3$ in Solvents Containing 0.1 M TBAP.

solvent	cpd	oxidation			reduction		
		2nd	1st		1st	2nd	3rd
pyridine	$TTCorrH_3$	0.56[a]	0.09		-1.33[a]	-1.88	
	$3\text{-}NO_2TTCorrH_3$	0.70[a]	0.25		-0.87[a]	-1.34	-1.71
	$3,17\text{-}(NO_2)_2TTCorrH_3$	0.83[a]	0.41		-0.75[a]	-1.05	-1.40
CH_2Cl_2	$TTCorrH_3$		0.33	-0.09[b]	-1.40[a]		
	$3\text{-}NO_2TTCorrH_3$		0.50[a]	0.16[b]	-0.84[a]	-1.42[a]	-1.60[a]
	$3,17\text{-}(NO_2)_2TTCorrH_3$			0.33[b]	-0.62[a]	-1.06	-1.39
PhCN	$TTCorrH_3$		0.34	-0.08[b]	-1.40[a]	-1.90	
	$3\text{-}NO_2TTCorrH_3$			0.14[b]	-0.84[a]	-1.39	-1.76[a]
	$3,17\text{-}(NO_2)_2TTCorrH_3$		0.94	0.35[b]	-0.62[a]	-1.08	-1.38

[a] Peak potential at a scan rate of 0.1 V/s.
[b] This redox couple can only be seen on the second positive potential sweep after scanning through the first reduction.

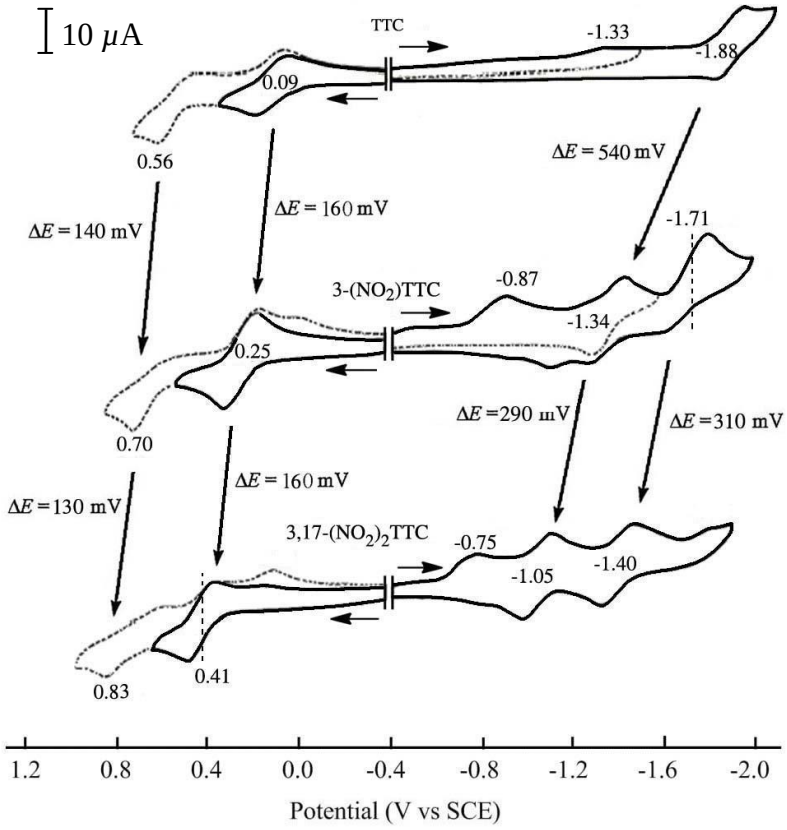

Figure 3-5. Cyclic voltammograms of $TTCorrH_3$**,** 3-$NO_2TTCorrH_3$ and 3,17-$(NO_2)_2TTCorrH_3$ in pyridine containing 0.1 M TBAP.

positions of the macrocycle. For example, the $[CorrH_2]^-/[^{\bullet}CorrH_2]$ reaction in pyridine is located at $E_{1/2}$ = 0.09 V for $TTCorrH_3$ (with no NO_2 group), while 3-$NO_2$$TTCorrH_3$ (with one NO_2 group) is oxidized at $E_{1/2}$ = 0.25 V and 3,17-$(NO_2)_2$$TTCorrH_3$ (with two NO_2 groups) is oxidized at $E_{1/2}$ = 0.41 V. It is also worth mentioning that a much larger substituent effect of the nitro group is observed for the reductions than for the oxidations. For example, a 540 mV shift in $E_{1/2}$ for the second reduction is seen upon going from $TTCorrH_3$ to 3-$NO_2$$TTCorrH_3$. Although the magnitude of the shift in $E_{1/2}$ for the second and third reductions is reduced to 290 and 310 mV respectively, upon going from 3-$NO_2$$TTCorrH_3$ to 3,17-$(NO_2)_2$$TTCorrH_3$, the effect of NO_2 on these processes is still much larger than that observed for the first oxidation. This trend in substituent effects was also observed for β-NO_2 substituted Fe(III), Cu(III), and Ge(IV) corroles having similar structures[11,12,29] and fits with the major effect of the nitro group being to lower the energy of the lowest unoccupied molecular orbital (LUMO), *vide infra*.

As mentioned above, the first reduction of the investigated corroles is irreversible in pyridine, as well as in CH_2Cl_2 and PhCN (see Table 3-1). In all three solvents, the reduction leads to formation of the deprotonated $[CorrH_2]^-$ species as the final product. An example of the thin-layer UV-visible spectral changes observed during the first one-electron reduction of 3-$NO_2$$TTCorrH_3$ in CH_2Cl_2 are shown in Figure 3-6a. As seen in this figure, the initial spectrum of 3-$NO_2$$TTCorrH_3$ is characterized by three separated Soret bands at 396, 438, and 464 nm and two visible Q-like bands at 589 and 667 nm. Controlled potential reduction at −0.95 V in the thin-layer cell leads to a decreased intensity of the 396 and 464 nm bands, as well as to a complete disappearance of the 438 nm band, while the two initially separated

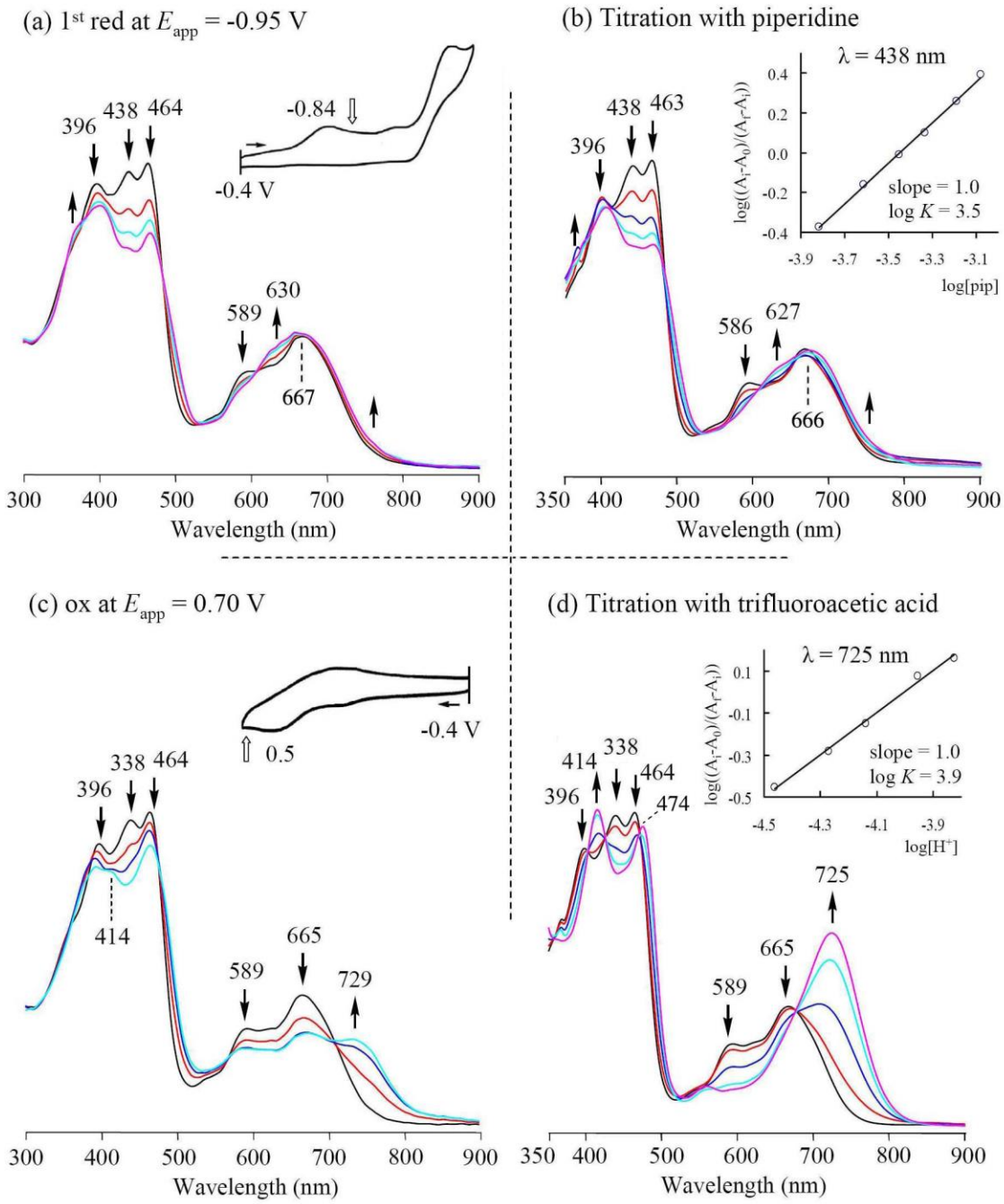

Figure 3-6. UV-visible spectral changes of 3-NO_2TTCorrH_3 in CH_2Cl_2 during (a) the controlled reduction at -0.95 V, (b) successive addition of piperidine (inset shows the Hill plot), (c) the controlled oxidation at 0.70 V, and (d) with successive additions of TFA (inset shows the Hill plot).

visible bands become merged into a single peak at 630-667 nm (Figure 3-6a). These spectral changes match perfectly spectral changes observed in the same solvent during a titration of 3-NO_2TTCorrH_3 with piperidine (Figure 3-6b) and gives further evidence for formation of the deprotonated species in the electrochemical reaction, where $[CorrH_2]^-$ is characterized by absorption bands at 396, 463 and 666 nm. The diagnostic log-log plot of the titration data is shown in the inset of Figure 3-6b and has a slope of 1.0 with a log K = 3.5 for dissociation of one proton under the given solution condition.

As shown by the cyclic voltammogram insert in Figure 3-6c, 3-NO_2TTCorrH_3 undergoes an irreversible to quasi-reversible one-electron oxidation at E_p = 0.50 V in CH_2Cl_2 at scan rate of 0.1 V/s. Similar irreversible oxidations have been observed for some free-base porphyrins, where the product of the first electron abstraction involves a protonation process,[30,31] although in the case of free-base corroles the oxidation mechanism seems to be more complicated. Our previous studies[27] suggest that the one-electron oxidation of triarylcorroles initially gives the corrole radical cation, $[CorrH_3]^+$, which then rapidly loses a proton after reaction with another molecule of the neutral corrole in solution to generate a mixture of the free-base neutral corrole radical, $CorrH_2$, and the corrole monocation, $[CorrH_4]^+$. In Figure 3-6c and d, it is possible to compare the spectral changes observed for 3-NO_2TTCorrH_3, when a controlled potential oxidation at 0.70 V was carried out (see Figure 3-6c), and when the same macrocycle was titrated with successive additions of TFA in CH_2Cl_2 solution. The final UV-visible spectra under these two conditions are quite similar to each other.

As expected, the introduction of one or two nitro groups at the β-positions of the corrole macrocycle influences the corresponding acid-base properties of the molecule.

Spectral changes of the type reported in Figure 3-6b and d for 3-NO_2TTCorrH_3 were exploited to obtain equilibrium constants for deprotonation (log K_a) and protonation (log K_b) processes of the three investigated free-base corroles in CH_2Cl_2, and the corresponding protonation-deprotonation constants are reported in Table 3-2. The equilibrium constant for proton dissociation increased upon going from TTCorrH_3 (log K_a = 1.1) to 3-NO_2TTCorrH_3 (log K_a = 3.5) and then to 3,17-$(NO_2)_2$TTCorrH_3 (log K_a = 4.9), while for log K_b, a reverse trend is obtained (see Table 3-2), indicating that the acidity of free-base corroles increases, while the basicity decreases upon increasing the number of peripheral nitro substituents. It is interesting to note that the effect of the nitro groups is higher for the increase of the acidity constants than that observed for the corresponding K_b.

3.2.3 Theoretical Studies

To rationalize the effects of introducing nitro groups at the periphery of TTCorrH_3, the structural, electronic, optical, and electrochemical properties of TTCorrH_3 and its nitro derivatives were theoretically investigated using DFT and TDDFT methods.

(a) Molecular Structures. In metal-free corroles the inner hydrogen atoms can be distributed in different ways among the four nitrogen atoms,[32-34] which results in the formation of tautomers. In this study only one tautomeric form of TTCorrH_3, 2-NO_2TTCorrH_3, 3-NO_2TTCorrH_3, and 3,17-$(NO_2)_2$TTCorrH_3 was examined theoretically. In the choice of the tautomers of TTCorrH_3 and its nitro derivatives, we have been guided by the X-ray structural data available for TPCorrH_3 (TPCorrH_3 = 5,10,15-triphenylcorrole)[34] and 2-NO_2TTCorrH_3, respectively. In both compounds the inner hydrogen atoms are located on B, C, and D pyrrole rings. The structural analysis was performed in the gas-phase and in

Table 3-2. Equilibrium Constants for Deprotonation (log K_a) and Protonation (log K_b) of $(NO_2)_xTTCorrH_3$ in CH_2Cl_2.

cpd	log K_a	log K_b
	reacting with piperidine	reacting with trifluoroacetic acid
$TTCorrH_3$	1.1	4.5
3-$NO_2TTCorrH_3$	3.5	3.9
3,17-$(NO_2)_2TTCorrH_3$	4.9	3.3

dichloromethane solution, using both BP86 and B3LYP functionals. The optimized structures showed very little sensitivity to the used functional and solvation effects. Table 3-3 collects the relevant structural parameters computed at the B3LYP level, in the gas-phase, for $TTCorrH_3$, 2-NO_2-$TTCorrH_3$, 3-$NO_2TTCorrH_3$, and 3,17-$(NO_2)_2TTCorrH_3$. For 2-$NO_2TTCorrH_3$, comparison is made between the theoretical and experimental data.

As observed in other metal-free triarylcorroles,[34-37] in $TTCorrH_3$ the macrocycle exhibits a significant distortion from planarity to minimize the steric hindrance between the inner protons. The macrocycle adopts a puckered conformation in which the pyrrole rings turn either slightly up or down. According to the computed twist angle between the pyrrole mean planes, *θ1*, the pyrrolenine ring A and the adjacent pyrrole not directly bonded to it, B, are close to be coplanar, mostly due to the presence of an intramolecular hydrogen bond between the N_2−H group and the iminic N_1 atom (N_1−N_2 = 2.621 Å, ∠N_2−H_2···N_1 = 132.2°). The D and C rings are tipped up and down with respect to the 23 atom mean plane forming a dihedral angle (*θ3*) of 22.2° with each other. The two directly bonded pyrroles, A and D, show a N−C−C−N twist angle (*φ1*) of 10.3°. Comparison of the structural parameters of 2-$NO_2TTCorrH_3$ with those of $TTCorrH_3$ shows that the introduction of a nitro group at the C_2 position has very little impact on the geometry of the corrole macrocycle. As indicated by the C_1−C_2−N_5−O_1 angle (*φ2*), the NO_2 group is substantially coplanar with the pyrrolenine ring A. This, together with a relatively short C_2−N_5 bond length (1.430 Å), suggests conjugation between the corrole and the nitro substituent. The geometrical data listed in Table 3-3 for 2-$NO_2TTCorrH_3$ show agreement between theory and experiment, thus confirming that the puckering of the corrole macrocycle is dictated by intrinsic electronic factors. Because of

Table 3-3. Selected Bond Lengths (Å), Bond Angles (deg) and Metrical Parameters Calculated for $TTCorrH_3$ and its Nitro Derivatives, 2-$NO_2TTCorrH_3$, 3-$NO_2TTCorrH_3$, and 3,17-$(NO_2)_2TTCorrH_3$ (data taken from ref 21).

	$TTCorrH_3$	2-$NO_2TTCorrH_3$[a]	3-$NO_2TTCorrH_3$	3,17-$(NO_2)_2TTCorrH_3$
$C–N_{(nitro)}$[b]		1.430/*1.421(3)*	1.445	1.447/1.441
$N_1–N_2$	2.621	2.639/*2.623(3)*	2.623	2.627
$N_2–H_2\cdots N_1$	132.2	131.5/*134(3)*	130.4	129.8
θ_1[c]	10.2	9.4/*10.5(6)*	12.4	13.7
θ_3[d]	22.2	22.4/*23.8(3)*	23.6	27.9
φ_1[e]	10.3	11.0/*7.3(3)*	12.1	14.4
φ_2[f]		2.8/*1.2(4)*	31.4	32.9/20.0

[a]Experimental values (this work) in italics. [b]$C_2–N_5$, $C_3–N_5$, and $C_3–N_5/C_{17}–N_6$ bond lengths for 2-$NO_2TTCorrH_3$, 3-$NO_2TTCorrH_3$, and 3,17-$(NO_2)_2TTCorrH_3$, respectively. [c]Dihedral angle between the B and A pyrrole mean planes. [d]Dihedral angle between the C and D pyrrole mean planes. [e]$N_1–C_5–C_{19}–N_4$ torsional angle. [f]$C_1–C_2–N_5–O_1$, $C_4–C_3–N_5–O_1$, $C_4–C_3–N_5–O_1/C_{16}–C_{17}–N_6–O_3$ torsional angles for 2-$NO_2TTCorrH_3$, 3-$NO_2TTCorrH_3$, and 3,17-$(NO_2)_2TTCorrH_3$, respectively.

steric hindrance with the adjacent phenyl ring, the nitro group in 3-NO_2TTCorrH_3 is no longer coplanar with the pyrrolenine ring A, the C_4−C_3−N_5−O_1 angle amounting to 31.4°. This results in decreased conjugation between the nitro group and the corrole macrocycle, as confirmed by the elongation of the C−N bond. In turn, the phenyl ring on the 5 position tilts toward the bipyrrolic block by 50.2°. This is reflected in a slight increase of macrocycle puckering. In 3,17-$(NO_2)_2$TTCorrH_3, the puckering of the corrole macrocycle is further enhanced relative to the mononitrated corroles, due to the cooperative effects of the nitro substituents. It is worth noting, however, that while the twisting of the nitro group on the 3 position is very much the same as in 3-NO_2TTCorrH_3 (32.9° vs 31.4°), that of the nitro group on the 17 position is only 20.0°, leading to a more effective conjugation with the pertinent pyrrole.

(b) Ground-State Electronic Structure and Optical Spectra. To provide an interpretation of the UV/vis spectral changes accompanying the nitration of TTCorrH_3, TDDFT calculations of the electronic absorption spectra in dichloromethane solution were performed for 2-NO_2TTCorrH_3, 3-NO_2TTCorrH_3, 3,17-$(NO_2)_2$TTCorrH_3, and the parent TTCorrH_3. Before dealing with the excited states, we briefly discuss the ground-state electronic structure of the investigated metal-free corroles. To highlight the electronic effects of the nitro groups, the electronic structure of the unsubstituted freebase is taken as a reference. An energy level scheme of the highest occupied and lowest unoccupied Kohn−Sham orbitals of TTCorrH_3 and its nitro derivatives is shown in Figure 3-7.

The plots of the two highest occupied and of the two lowest unoccupied MOs of these compounds are displayed in Figure 3-8. The HOMO−1 and HOMO of TTCorrH_3 resemble

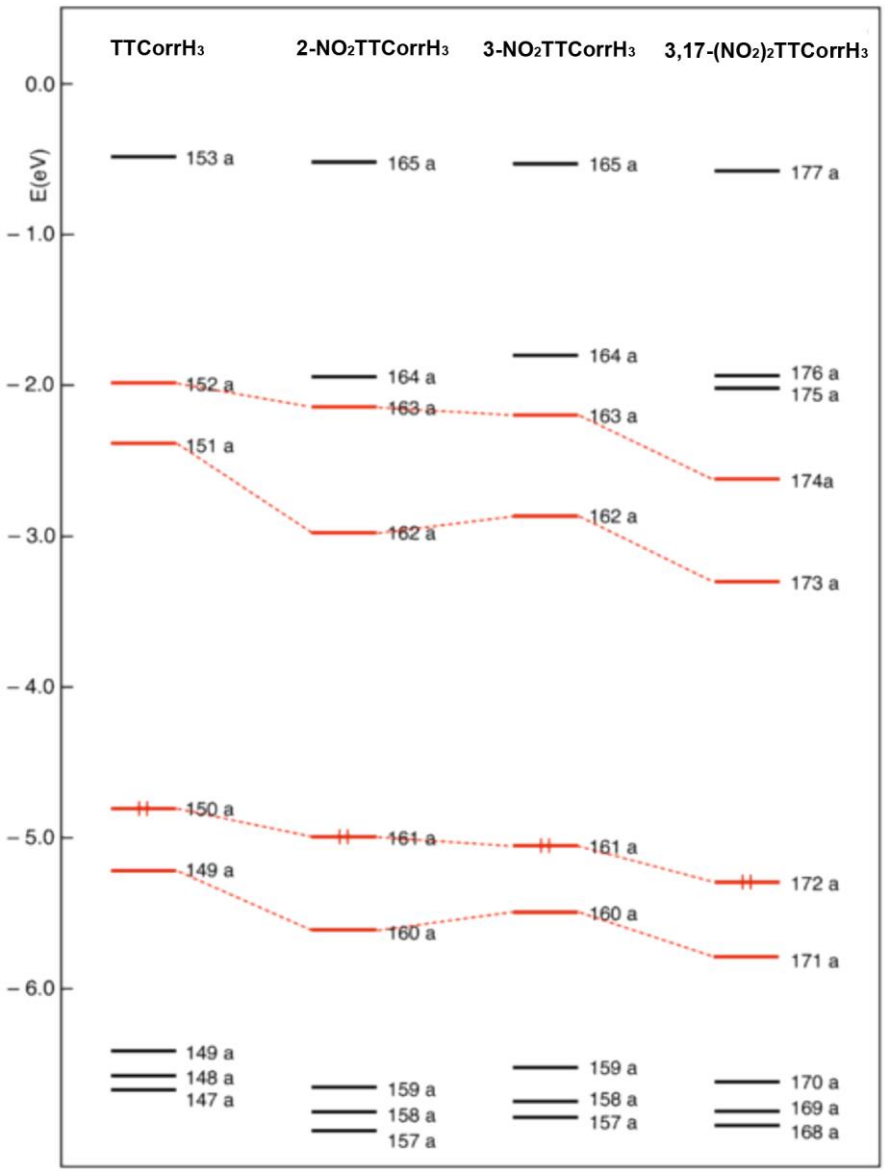

Figure 3-7. Energy level scheme for $TTCorrH_3$ and its nitro derivatives. The Gouterman-derived MOs are indicated with red lines (taken from ref 21).

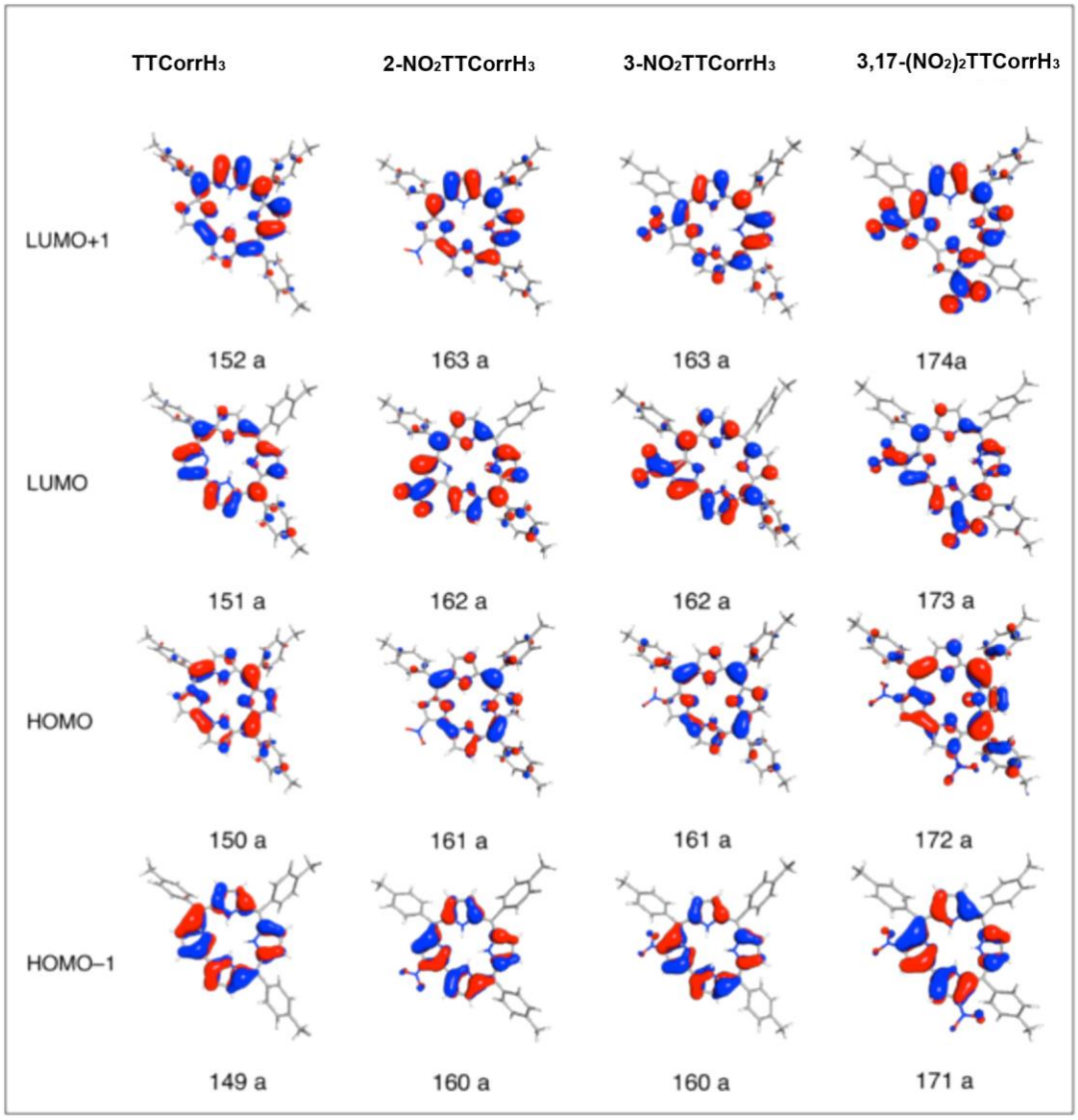

Figure 3-8. Plots of the frontier orbitals of $TTCorrH_3$ and its nitro derivatives (taken from ref 21).

the HOMO−1(a_u) and HOMO(b_{1u}) of $TPPH_2$ (D_{2h} symmetry).[38] Less pronounced is the similarity between the LUMO and LUMO+1 of $TTCorrH_3$ and the LUMO(b_{2g}) and LUMO+1(b_{3g}) of $TPPH_2$ (D_{2h} symmetry).[38] In the nitro derivatives and in the parent $TTCorrH_3$, a quite large energy gap separates the HOMO−1 from the lower lying MOs, which are largely localized on the aryl groups and on the pyrrolenine ring. In the nitro derivatives, one or two MOs having some amplitude on the nitro groups interpose between the LUMO+1 and the highlying set of π-phenyl orbitals. According to the level scheme of Figure 3-7, the outstanding effect of introducing nitro groups into $TTCorrH_3$ is the stabilization of the LUMO and, to a lesser extent, of the HOMO−1. As a result, the LUMO/LUMO+1 splitting increases dramatically on going from $TTCorrH_3$ to the nitro derivatives. The large stabilization of the LUMO moving from $TTCorrH_3$ to the nitro derivatives is due to the $C-N_{(nitro)}$ *π-bonding* character of this orbital well visible in the plots displayed in Figure 3-8. In 3-$NO_2TTCorrH_3$ the LUMO is slightly less stabilized than in 2-$NO_2TTCorrH_3$ because the nitro group is rotated by 31.4° with respect to the pertinent pyrrole plane and hence the overlap between the C3 and N5 $2p_z$ orbitals is less effective than in 2-$NO_2TTCorrH_3$ where the nitro group is almost coplanar with the pertinent pyrrole. In the dinitro derivative both the LUMO and LUMO+1 experience a significant downward shift as compared to the parent $TTCorrH_3$. This is because both these MOs have $C-N_{(nitro)}$ π-bonding character. Due to the presence of two $C-N_{(nitro)}$ π-bonding interactions, the stabilization of the LUMO and LUMO+1 is quite large in 3,17-$(NO_2)_2$-$TTCorrH_3$. However, it should be noted that, for overlap reasons, the $C-N_{(nitro)}$ π-bonding interaction involving the nitro group on the 3 position is somewhat less effective than that involving the nitro group on

the 17 position. As pointed out earlier, the nitro groups on the 3 and 17 positions are rotated with respect to the plane of the pertinent pyrrole by 32.9° and 20.0°, respectively.

In summary, comparison between the one-electron levels of the nitro corroles and those of the parent free-base reveals that the most striking differences are the increased LUMO/LUMO+1 splitting and the diminished HOMO/LUMO energy gap, which are mainly due to the downshift of the LUMO in the nitro derivatives.

We see now how the previously discussed electronic structure changes accompanying the nitration of the corrole macrocycle reflect on the UV-visible spectroscopic properties of the investigated nitrocorroles. The excitation energies and oscillator strengths calculated for the lowest singlet excited states of $TTCorrH_3$ and its nitro derivatives are reported in Tables 3-4 to 3-7 together with the major one-electron transitions contributing to the excited-state solution vectors.

In Figure 3-9, the computed and experimental absorption spectra of these compounds in CH_2Cl_2 are compared. Considering first $TTCorrH_3$ as point of reference for the nitro derivatives, only two excited states are computed in the energy regime of the four Q bands, the 1^1A and 2^1A. As found in $TPPH_2$,[39] these states originate from out-of-phase combination of the Gouterman transitions. However, due to the lifting of the LUMO/LUMO+1 degeneracy induced by the appreciable distortion of the macrocycle in $TTCorrH_3$, the mixing coefficients of the Gouterman transitions change significantly relative to $TPPH_2$. As a matter of fact, the 1^1A excited state in $TTCorrH_3$ is mostly described by the HOMO → LUMO transition, the transition out of the HOMO−1 into the LUMO+1 entering in this state with only a minor (15%) weight. The 2^1A is instead a nearly 50:50 mixture of the HOMO →

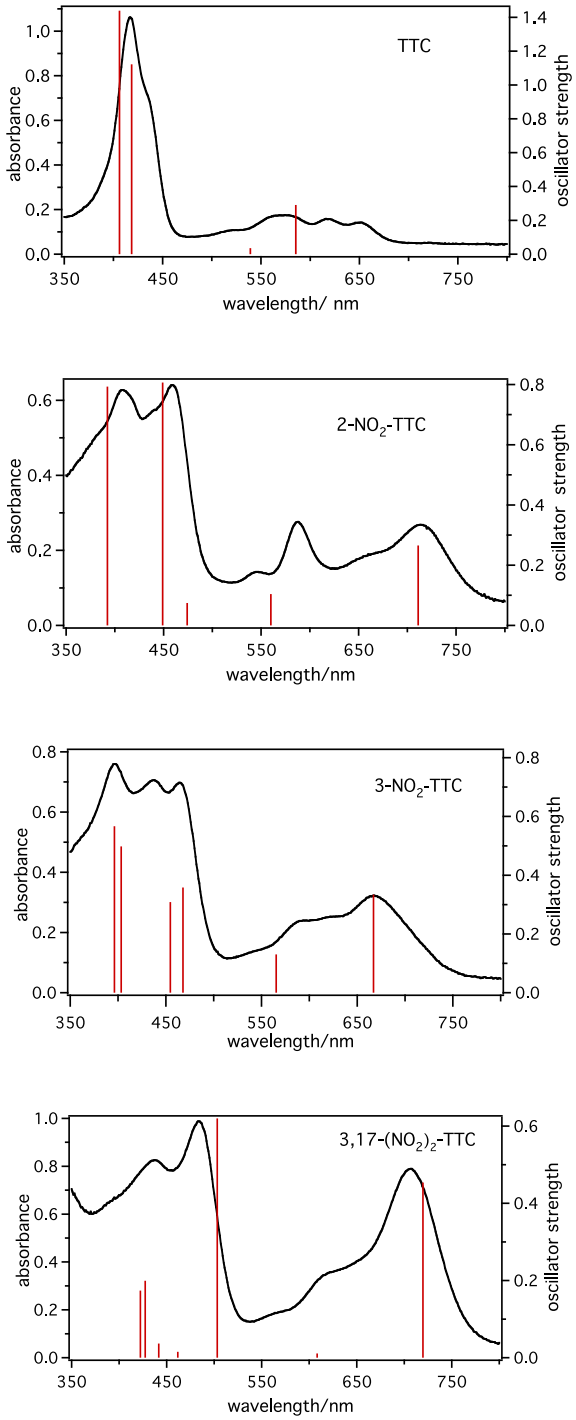

Figure 3-9. Comparison between computed (TDDFT/B3LYP) and experimental absorption spectra of TTCorrH_3 and its nitro derivatives in CH_2Cl_2 (taken from ref 21).

LUMO+1 and HOMO−1 → LUMO transitions. Due to a less effective mixing of the contributing transitions and, hence, to a less effective cancellation of their large dipole moments, the oscillator strength computed for the 1^1A state is significantly larger than that of the 2^1A. By analogy with the assignment previously proposed for $TPPH_2$,[39] the Q bands observed in the CH_2Cl_2 absorption spectrum of $TTCorrH_3$ at 652 and 574 nm are assigned to the 1^1A and 2^1A states, respectively, although the computed absorption wavelengths are somewhat blue-shifted with respect to the experimental values. According to the TDDFT calculations, the Q bands at 616 and 465 nm are identified as vibrational in origin. The B band profile of $TTCorrH_3$ is nicely accounted for by the nearly degenerate 3^1A and 4^1A excited states. These originate from inphase combinations of the Gouterman type transitions and, hence, have large oscillator strength (see Table 3-4).

Coming to the nitrocorroles, in the energy regime of the Q bands, TDDFT calculations predict, just as for the parent $TTCorrH_3$, only two excited states, the 1^1A and 2^1A. As can be inferred from the composition of these states in Tables 3-4 to 3-7 for all three nitro derivatives, the 1^1A is a nearly pure (>90%) HOMO → LUMO state and the 2^1A is a mixture of the HOMO → LUMO+1 and HOMO−1 → LUMO transitions. The lowest excited state nicely accounts for the energy and intensity of the longest wavelength Q-band. The 2^1A excited state is responsible for the higher energy Q-band appearing as a distinct peak at 588 nm in the UV-visible spectrum of 2-$NO_2TTCorrH_3$ and as a broad feature at around 600 nm in the spectra of the other nitro derivatives. The calculations also account for the observed red shift of this band on going from $TTCorrH_3$ to the nitro derivatives. Distinct from $TTCorrH_3$, the nitro corroles exhibit a complex B band system characterized by several

Table 3-4. Composition, Vertical Excitation Energies, *E* (eV/nm), and Oscillator Strengths, *f*, for the Lowest Optically Allowed Excited States of $TTCorrH_3$ in CH_2Cl_2 (data taken from ref 21).

state	composition (%)	*E*	*f*
1^1A	150a→151a (78) 149a→152a (15)	2.12/585	0.2905
2^1A	150a→152a (47) 149a→151a (46)	2.30/539	0.03580
3^1A	149a→151a (48) 150a→152a (47)	2.96/418	1.122
4^1A	149a→152a (80) 150a→151a (14)	3.05/406	1.439

Table 3-5. Composition, Vertical Excitation Energies, *E* (eV/nm), and Oscillator Strengths, *f*, for the Lowest Optically Allowed Excited States of 2-NO_2TTCorrH_3 in CH_2Cl_2 (data taken from ref 21).

state	composition (%)	*E*	*f*
1^1A	161a→162a (94)	1.74/711	0.2655
2^1A	160a→162a (72) 161a→163a (25)	2.21/560	0.1042
3^1A	161a→164a (82) 160a→163a (16)	2.61/474	0.07460
4^1A	161a→163a (59) 160a→162a (20) 160a→164a (16)	2.76/449	0.8068
5^1A	160a→163a (49) 159a→162a (31)	3.16/392	0.7931

Table 3-6. Composition, Vertical Excitation Energies, *E* (eV/nm), and Oscillator Strengths, *f*, for the Lowest Optically Allowed Excited States of 3-NO_2TTCorrH_3 in CH_2Cl_2 (data taken from ref 21).

state	composition (%)	*E*	*f*
1^1A	161a→162a (91)	1.86/667	0.3338
2^1A	160a→162a (69) 161a→163a (27)	2.19/565	0.1304
3^1A	161a→164a (38) 161a→163a (37) 160a→162a (14)	2.65/468	0.3584
4^1A	160a→163a (32) 161a→164a (27) 161a→163a (23)	2.73/455	0.3085
5^1A	159a→162a (54) 161a→164a (17) 160a→163a (14)	3.07/403	0.4981
6^1A	159a→162a (36) 160a→163a (33) 161a→164a (14)	3.13/396	0.5669

Table 3-7. Composition, Vertical Excitation Energies, *E* (eV/nm), and Oscillator Strengths, *f*, for the Lowest Optically Allowed Excited States of 3,17-$(NO_2)_2$TTCorrH_3 in CH_2Cl_2 (data taken from ref 21).

state	composition (%)	*E*	*f*
1^1A	172a→173a (96)	1.72/720	0.4537
2^1A	171a→173a (59) 172a→174a (40)	2.04/608	0.01098
3^1A	172a→174a (54) 171a→173a (35)	2.46/503	0.6455
4^1A	171a→174a (71) 172a→176a (20)	2.69/462	0.01524
5^1A	170a→173a (68) 172a→175a (24)	2.81/442	0.03678
6^1A	172a→176a (47) 170a→173a (16) 171a→175a (14)	2.90/427	0.1994
7^1A	172a→175a (37) 170a→173a (20) 171a→174a (16)	2.93/422	0.1740

overlapping features. The increased complexity of the B band system in nitrocorroles is related to the involvement of non-Gouterman transitions in the excited states accounting for this spectral region. The calculations indicate that the Gouterman-type transitions, which account for the nearly degenerate B bands of $TTCorrH_3$, mix to a variable extent with transitions out of the HOMO−2 (a MO largely localized on the aryl groups and on the pyrrolenine ring) into the LUMO, or with transitions out of the HOMO into the LUMO+2 (a MO with sizable amplitude on the nitro groups). As for 2-$NO_2TTCorrH_3$, the two prominent B bands are well accounted for by the 4^1A and 5^1A excited states computed at 449 and 392 nm and with oscillator strength of 0.8068 and 0.7931, respectively. According to their composition (see Table 3-5), these states are largely composed of the Gouterman-type transitions with the above-mentioned non-Gouterman transitions entering with a minor, although not negligible, weight. Four intense excited states are computed in the energy regime of the three B band system of 3-$NO_2TTCorrH_3$. On the basis of their energy, the 3^1A and 4^1A are assigned to the lowest energy features at 465 and 438 nm, respectively, and the nearly degenerate 5^1A and 6^1A states to the most prominent feature at 397 nm.

The B band system of the dinitrocorrole is characterized by an intense, sharp feature at 483 nm followed to the blue by a broad, less intense feature. The energy and oscillator strength computed for the 3^1A excited state leaves no doubt about the assignment of the longer wavelength B band to this state. It is noteworthy that the 3^1A state consists of the same Gouterman transitions as the 2^1A, HOMO−1 → LUMO and HOMO → LUMO+1, with approximately reversed weights. The large transition dipoles of these transitions reinforce in the 3^1A and cancel in the 2^1A state with the result that the former is by far more intense than the latter.

In the energy regime of the broad B feature, the calculations predict four excited states, two of which, the nearly degenerate 6^1A and 7^1A, account for most of the intensity of this band.

(c) Reduction Potentials. The redox behavior of metal-free corroles is rather complex owing to the proton transfer equilibrium reaction $CorrH_3 \rightleftharpoons [CorrH_2]^-$. As seen in the previous section, the reduction potentials of the three-protonated species, $CorrH_3$, positively shifts when one or two nitro groups are introduced at the β-position of the macrocycle. Also the addition of a second nitro group to the macrocycle decreases the effect of nitration on the reduction potentials under the same experimental conditions. To rationalize the observed trend, we have computed the first reduction potential of 2-NO_2TTCorrH_3, 3-NO_2TTCorrH_3, 3,17-$(NO_2)_2$TTCorrH_3, and the parent TTCorrH_3 in dichloromethane solution, using a DFT/COSMO model.

The standard reduction potential, $E°_{ox/red}$, for the reaction

$$CorrH_3(CH_2Cl_2) + e^-(g) \rightarrow [CorrH_3]^-(CH_2Cl_2) \qquad (3\text{-}1)$$

is related to the standard free energy change relative to the standard hydrogen electrode (SHE) through the equation:

$$E°_{ox/red} = -(\Delta G°_{ox/red} - \Delta G°_{SHE})/nF \qquad (3\text{-}2)$$

In Eq 3-2, n is the number of electrons consumed in the reduction reaction, 1 in the present case, and F is a constant. If the free energies are expressed in molar units, F is the Faraday constant (the negative of the charge on one mole of electrons), but if energies are expressed in electron volts per molecule, as in the present study, then F is equal to the unit

charge e^-. $\Delta G°_{ox/red}$ is the free energy change associated with reaction 3-1, whereas $\Delta G°_{SHE}$ is the free energy change of the following reaction

$$H^+_{(aq)} + e^-(g) \rightarrow ½\ H_2(g) \qquad (3\text{-}3)$$

$\Delta G°_{SHE}$ has been established in literature to be -4.28 eV.[40]

As the experimental half-wave potentials of the investigated metal-free corroles were measured using SCE as the reference electrode, the theoretical reduction potentials obtained from Eq 3-2 were converted to SCE referenced potentials by subtracting 0.09 V, which was obtained by taking the literature value of the reduction potential of aqueous SCE relative to SHE at 298 K (0.24 V)[41] and correcting it to its corresponding value in dichloromethane solution using the literature value of the liquid junction potential (ljp) for dichloromethane-water (0.15 V).[42,43] The corrected one-electron reduction potentials of $TTCorrH_3$, 2-$NO_2TTCorrH_3$, 3-$NO_2TTCorrH_3$, and 3,17-$(NO_2)_2TTCorrH_3$ are compared with the experimental halfwave potentials in Table 3-8 where the thermodynamic parameters computed for the one-electron reduction process in Eq 3-1 are also reported. The data in Table 3-8 indicate that there is an excellent agreement between the theoretically predicted one-electron reduction potentials and the available experimental values. The thermodynamic data reveal that the one-electron reduction process is energetically controlled by enthalpic factors, the entropic factors playing a negligible role. The ΔE_{solv} values indicate that the energetic contribution of solvation to the enthalpic term, though relevant, is substantially constant along the series. Thus, the $\Delta H°_{ox/red}$ trend is primarily determined by the electronic enthalpy that favors energetically the reduced form over the oxidized one in the order $TTCorrH_3 \ll$ 2-$NO_2TTCorrH_3 \cong$ 3-$NO_2TTCorrH3 <$ 3,17-$(NO_2)_2TTCorrH_3$. In nitrocorrole

Table 3-8. Thermodynamic Parameters (eV) for the One-electron Reduction Reaction 3-1, and One-electron Reduction Potentials (V) for $TTCorrH_3$, 2-$NO_2TTCorrH_3$, 3-$NO_2TTCorrH_3$, and 3,17-$(NO_2)_2TTCorrH_3$ (data taken from ref 21).

	$\Delta H°_{ox/red}$	$-T\Delta S°_{ox/red}$	ΔE_{solv} [a]	$\Delta G°_{ox/red}$	$E°_{ox/red}$ *vs* SCE	$E_{1/2}$ [b] *vs* SCE
$TTCorrH_3$	–2.93	0.02	–1.41	–2.91	–1.46	–1.40
2-$(NO_2)TTCorrH_3$	–3.49	0.03	–1.50	–3.52	–0.85	–
3-$(NO_2)TTCorrH_3$	–3.44	0.03	–1.47	–3.47	–0.90	–0.84
3,17-$(NO_2)_2TTCorrH_3$	–3.78	0.04	–1.31	–3.82	–0.55	–0.62

[a] ΔE_{solv} is the difference between the dielectric energy of the reduced species and the dielectric energy of the oxidized species. [b] Experimental values in dichloromethane solution, this work.

the one-electron reduced form is much more stable than the oxidized form as compared to $TTCorrH_3$, and this is consistent with the added electron entering a MO with $C{-}N_{(nitro)}$ π-bonding character in the former, as witnessed by the significant shortening of the $C{-}N_{(nitro)}$ bond. In 2-NO_2TTCorrH_3 and 3-NO_2TTCorrH_3, the $C{-}N_{(nitro)}$ bond shortens by 0.027 and 0.033 Å, respectively. In the dinitro derivative, the two $C{-}N_{(nitro)}$ bonds shorten, on the average, by 0.025 Å.

3.3 Summary

We have reported the first example of efficient insertion of nitro groups into the β-pyrrole positions of corrole free bases, effectively overcoming the formation of isocorrole by controlling the amount and the nature of the oxidant used for the reaction. The regioselectivity usually observed in the functionalization of corrole ring is also demonstrated for the nitration reaction, producing the 3-nitro- and the 3,17-dinitrocorroles as the main reaction products of mono- and disubstitution; we have also been able to characterize some other minor regioisomers, such as the 2-nitro, 2,3-, and the 3,12-dinitro derivatives. It is interesting to note that this last regioisomer is the first example of antipodal functionalization of corrole ring.

The introduction of nitro substituents at the β-pyrrole positions of the corrole ring strongly influence the chemical and spectroscopic behavior of the macrocycle. The strong electron withdrawing character of the nitro group leads to a positive shift of the $E_{1/2}$ of the redox processes of corrole and to an increase of the macrocycle acidity. It is noteworthy that the introduction of the first nitro group is more effective than the second substituent in changing the properties of the functionalized macrocycle. Optical absorption spectra of β-

nitrocorroles are strongly influenced by the peripheral nitro groups, which increase the number of bands, characterized also by a significant red shift.

The theoretical results on these β-nitrocorrole derivatives also afforded significant information, closely matching the experimental observations. It was found that the β-NO_2 substituents conjugate with the π-aromatic system of the macrocycle, which initiates significant changes in both the spectroscopic and redox properties of the so functionalized corroles. This effect is more pronounced when the nitro group is introduced at the 2-position, because in this case the conjugation is, for steric reasons, more efficient than in the 3-nitro isomer.

3.4 References

1 Paolesse, R. In *The Porphyrin Handbook*; Kadish, K. M., Smith, K. M., Guilard, R., Eds.; Academic Press: New York, **2000**; Vol. 2, p 201-232.

2. Nardis, S.; Monti, D.; Paolesse, R. *Mini-Rev. Org. Chem.* **2005**, *2*, 355-374.

3. Gryko, D. T. *J. Porphyrins Phthalocyanines* **2008**, *12*, 906-917.

4. Paolesse, R. *Synlett* **2008**, 2215-2230.

5. Aviv-Harel, I.; Gross, Z. *Coord. Chem. Rev.* **2011**, *255*, 717-736.

6. Gross, Z.; Aviv-Harel, I. *Chem. Eur. J.* **2009**, *15*, 8382-8394.

7. Kanamori, A.; Catrinescu, M.-M.; Mahammed, A.; Gross, Z.; Levin, L. A. *J. Neurochem.* **2010**, *114*, 488-498.

8. Kupershmidt, L.; Okun, Z.; Amit, T.; Mandel, S.; Saltsman, I.; Mahammed, A.; Bar-Am, O.; Gross, Z.; Youdim, M. B. H. *J. Neurochem.* **2010**, *113*, 363-373.

9. Lemon, C. M.; Brothers, P. J. *J. Porphyrins Phthalocyanines* **2011**, *15*, 809-834.

10. Walker, F. A.; Licoccia, S.; Paolesse, R. *J. Inorg. Biochem.* **2006**, *100*, 810-837.

11. Stefanelli, M.; Mandoj, F.; Mastroianni, M.; Nardis, S.; Mohite, P.; Fronczek, F. R.; Smith, K. M.; Kadish, K. M.; Xiao, X.; Ou, Z.; Chen, P.; Paolesse, R. *Inorg. Chem.* **2011**, *50*, 8281-8292.

12. Mastroianni, M.; Zhu, W.; Stefanelli, M.; Nardis, S.; Fronczek, F. R.; Smith, K. M.; Ou, Z.; Kadish, K. M.; Paolesse, R. *Inorg. Chem.* **2008**, *47*, 11680-11687.

13. Saltsman, I.; Mahammed, A.; Goldberg, I.; Tkachenko, E.; Botoshansky, M.; Gross, Z. *J. Am. Chem. Soc.* **2002**, *124*, 7411-7420.

14. Stefanelli, M.; Mastroianni, M.; Nardis, S.; Licoccia, S.; Fronczek, F. R.; Smith, K. M.; Zhu, W.; Ou, Z.; Kadish, K. M.; Paolesse, R. *Inorg. Chem.* **2007**, *46*, 10791-10799.

15. Pomarico, G.; Fronczek, F. R.; Nardis, S.; Smith, K. M.; Paolesse, R. *J. Porphyrins and Phthalocyanines* **2011**, *15*, 1085-1092.

16. Stefanelli, M.; Nardis, S.; Tortora, L.; Fronczek, F. R.; Smith, K. M.; Licoccia, S.; Paolesse, R. *Chem. Commun.* **2011**, *47*, 4255-4257.

17. Stefanelli, M.; Shen, J.; Zhu, W.; Mastroianni, M.; Mandoj, F.; Nardis, S.; Ou, Z.; Kadish, K. M.; Fronczek, F. R.; Smith, K. M.; Paolesse, R. *Inorg. Chem.* **2009**, *48*, 6879-6887.

18. Capar, C.; Thomas, K. E.; Ghosh, A. *J. Porphyrins Phthalocyanines* **2008**, *12*, 964-967.

19. Mandoj, F.; Nardis, S.; Pomarico, G.; Paolesse, R. *J. Porphyrins Phthalocyanines* **2008**, *12*, 19-26.

20. Ngo, T. H.; Van Rossom, W.; Dehaen, W.; Maes, W. *Org. Biomol. Chem.* **2009**, *7*, 439-443.

21. Stefanelli, M.; Pomarico, G.; Tortora, L.; Nardis, S.; Fronczek, F. R.; McCandless, G. T.; Smith, K. M.; Manowong, M.; Chen, P.; Kadish, K. M.; Rosa, A.; Ricciardi, G.; Paolesse, R. *Inorg. Chem.* **2012**, *51*, 6928-6942.

22. Setsune, J.-i.; Tsukajima, A.; Watanabe, J. *Tetrahedron Lett.* **2006**, *47*, 1817-1820.

23. Nardis, S.; Pomarico, G.; Fronczek, F. R.; Vicente, M. G. H.; Paolesse, R. *Tetrahedron Lett.* **2007**, *48*, 8643-8646.

24. Flint, D. L.; Fowler, R. L.; LeSaulnier, T. D.; Long, A. C.; O'Brien, A. Y.; Geier, G. R., III *J. Org. Chem.* **2010**, *75*, 553-563.

25. Nardis, S.; Pomarico, G.; Mandoj, F.; Fronczek, F. R.; Smith, K. M.; Paolesse, R. *J. Porphyrins and Phthalocyanines* **2010**, *14*, 752-757.

26. Tortora, L.; Nardis, S.; Fronczek, F. R.; Smith, K. M.; Paolesse, R. *Chem. Commun. (Cambridge, U. K.)* **2011**, *47*, 4243-4245.

27. Shen, J.; Shao, J.; Ou, Z.; Wenbo, E.; Koszarna, B.; Gryko, D. T.; Kadish, K. M. *Inorg. Chem.* **2006**, *45*, 2251-2265.

28. Ou, Z.; Shen, J.; Shao, J.; Wenbo, E.; Galezowski, M.; Gryko, D. T.; Kadish, K. M. *Inorg. Chem.* **2007**, *46*, 2775-2786.

29. Nardis, S.; Stefanelli, M.; Mohite, P.; Pomarico, G.; Tortora, L.; Manowong, M.; Chen, P.; Kadish, K. M.; Fronczek, F. R.; McCandless, G. T.; Smith, K. M.; Paolesse, R. *Inorg. Chem.* **2012**, *51*, 3910-3920.

30. Inisan, C.; Saillard, J.-Y.; Guilard, R.; Tabard, A.; Le Mest, Y. *New J. Chem.* **1998**, *22*, 823-830.

31. Kadish, K. M.; Chen, P.; Enakieva, Y. Y.; Nefedov, S. E.; Gorbunova, Y. G.; Tsivadze, A. Y.; Bessmertnykh-Lemeune, A.; Stern, C.; Guilard, R. *J. Electroanal. Chem.* **2011**, *656*, 61-71.

32. Storm, C. B.; Teklu, Y. *J. Amer. Chem. Soc.* **1972**, *94*, 1745-7.

33. *Porphyrins: Excited States and Dynamics*; Gouterman, M.; Rentzepis, P. M.; Straub, K. D., Eds.; American Chemical Society: New York, **1987**; Vol. 321.

34. Ding, T.; Harvey, J. D.; Ziegler, C. J. *J. Porphyrins Phthalocyanines* **2005**, *9*, 22-27.

35. Gross, Z.; Galili, N.; Simkhovich, L.; Saltsman, I.; Botoshansky, M.; Blaeser, D.; Boese, R.; Goldberg, I. *Org. Lett.* **1999**, *1*, 599-602.

36. Simkhovich, L.; Goldberg, I.; Gross, Z. *J. Inorg. Biochem.* **2000**, *80*, 235-238.

37. Paolesse, R.; Nardis, S.; Venanzi, M.; Mastroianni, M.; Russo, M.; Fronczek, F. R.; Vicente, M. G. H. *Chem. - Eur. J.* **2003**, *9*, 1192-1197.

38. Palummo, M.; Hogan, C.; Sottile, F.; Bagala, P.; Rubio, A. *J. Chem. Phys.* **2009**, *131*, 084102/1-084102/7.

39. De Luca, G.; Romeo, A.; Scolaro, L. M.; Ricciardi, G.; Rosa, A. *Inorg. Chem.* **2009**, *48*, 8493-8507.

40. Kelly, C. P.; Cramer, C. J.; Truhlar, D. G. *J. Phys. Chem. B* **2006**, *110*, 16066-16081.

41. Bard, A. J.; Faulkner, L. R. *Electrochemical Methods: Fundamentals and Applications*; Wiley: New York, **2001**.

42. Krishtalik, L. I.; Alpatova, N. M.; Ovsyannikova, E. V. *J. Electroanal. Chem.* **1992**, *329*, 1-8.

43. Tsierkezos, N. G. *J. Solution Chem.* **2008**, *37*, 1437-1448.

CHAPTER FOUR

β-Nitro Derivatives of Iron Corrolates

4.1 Introduction

Among the earliest examples of synthetic porphyrinoid macrocycles to be compared to the parent porphyrins are the corroles (Scheme 4-1), which were reported for the first time in the 1960s by Johnson and Kay.[1] Although these macrocycles have been studied for many decades, it is only recently that several research groups have focused their attention on these compounds,[2-9] taking advantage of the significant advances achieved with respect to new synthetic protocols leading to triarylcorroles in high yield.[10,11]

One reason for this recent interest in corroles and metallocorroles is the peculiar behavior exhibited by these macrocycles,[10,12-14] which are endowed with an interesting reactivity profile due in large part to the lower symmetry of the contracted ring which, in the case of peripheral functionalization, may lead to unexpected products[10] and unexpected regioselectivity.[10,15] In addition to this synthetic aspect, there is also the corrole's intriguing coordination chemistry, characterized by the so-called "non-innocent" behavior of the macrocyclic ligand.[16,17]

Many features particular to the corroles can be largely attributed to the structure of the macrocycle, which is a trianionic ligand, having three inner core amine protons within a contracted tetrapyrrolic ring. These characteristics lead, on one hand, to a stabilization of the central metal ion in a formally higher oxidation state than for similar porphyrins and, on the other hand, to a facile oxidation of the macrocyclic ring, giving π-cation radical species that exhibits an intramolecular ligand to metal charge transfer band. This feature sometimes makes it difficult to elucidate the electronic structure of metallocorroles, but at the same time it opens up interesting opportunities for both the functionalization and the further exploitation of metallocorrole derivatives.

In this regard, we have recently shown that a nitration reaction carried out on an iron triarylcorrolate[18] confirmed the noninnocence[16,17] of the macrocyclic ligand in these complexes. With this and previous results in mind, we decided to extend our initial study of the nitration reaction to other iron triarylcorrolates in order to investigate the scope of the synthetic method. Since our hypothesis was based on involvement of a corrole π-cation radical substrate[17-19] which would undergo nucleophilic attack by the nitrite ion, we wished to evaluate how different meso-aryl substituents would affect formation of the reactive species and also the yield of the reaction. For this reason, both electron-withdrawing and electron-donating groups were introduced onto the substrates of the nitration reaction (Scheme 4-1).

A second important aspect of this project was to understand how nitro substituents introduced at the β-pyrrole and/or meso-phenyl positions of the macrocycle would influence both the redox potentials and the site of electron transfer in the synthesized compounds. This is examined in the present study where we report electrochemical and spectroscopic characterization of the synthesized iron nitro complexes in CH_2Cl_2.[20]

4.2 Results and Discussion

4.2.1 Synthetic Details

The free-base triarylcorroles (H_3TArC) 1-6 were prepared according to published procedures.[10,13,21-23] The iron complexes were then prepared following two similar procedures, referred to as Method A and Method B, which differ from each other by the amount of iron chloride in the nitration reaction medium.

Method A. H_3TArC (1 mmol) and $FeCl_2$ (20 mmol) were dissolved in DMF (30 mL), and the resulting mixture was heated to reflux; water was added to precipitate the product

Scheme 4-1. Nitration of triarylcorroles.

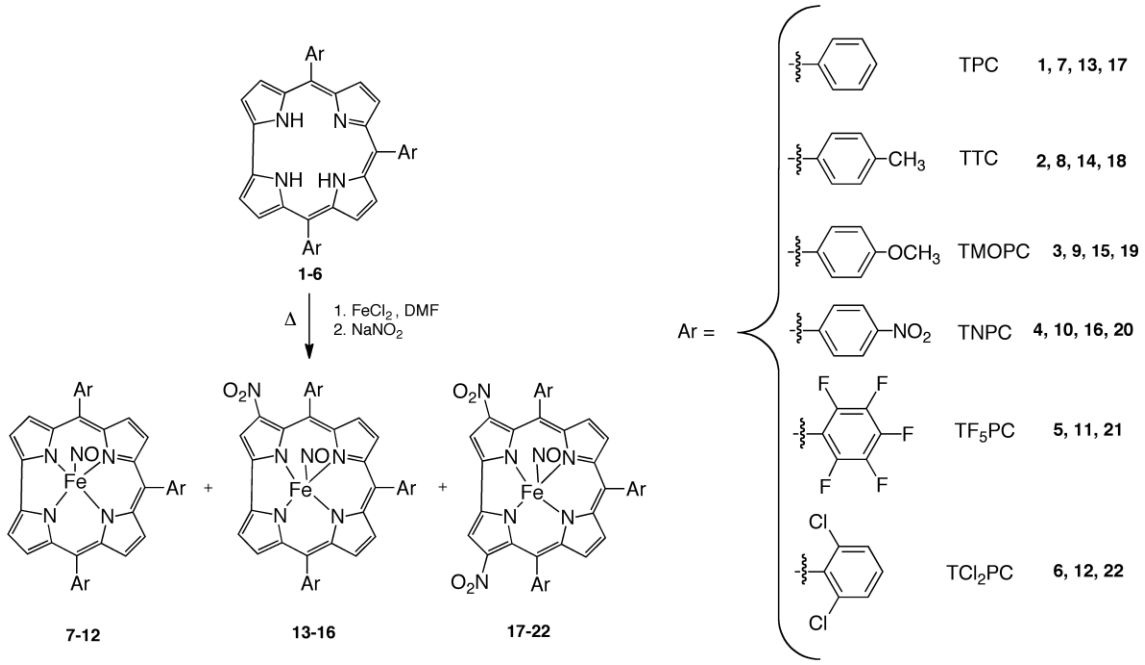

after formation of the complex was evidenced by UV-vis spectrophotometry and TLC. The precipitate was then filtered, dissolved in CH_2Cl_2, and dried over anhydrous Na_2SO_4, and after evaporating the solvent under vacuum, the residue was used without further purification for the nitration reaction. For this purpose, the iron complex was dissolved in DMF, and $NaNO_2$ (150 mmol) was added. The progress of the reaction was monitored by TLC and UV vis spectrophotometry, following the disappearance of the starting material. After precipitation by addition of water and filtration, the crude mixture was dissolved in CH_2Cl_2 and dried over anhydrous Na_2SO_4, and the solvent was evaporated. Purification by chromatography on a silica gel column using CH_2Cl_2 (or $CHCl_3$ for TNPC and TF_5PC) as eluent, followed by recrystallization from CH_2Cl_2/MeOH (1:2), afforded the desired compounds.

Method B. H_3TArC (1 mmol) was dissolved in DMF (30 mL); $FeCl_2$ (5 mmol) was added, and the resulting solution was refluxed for 90 min. During this period the color changed from purple to brown, indicating formation of the corresponding iron complex, which was confirmed by UV-vis spectrophotometry. $NaNO_2$ (150 mmol) was then added to the hot solution and the progress of the reaction monitored by TLC and UV-vis spectrophotometry. After allowing the reaction to proceed for 45 to 120 min (the exact time depending on the specific starting corrole), water was added and the precipitate was collected after filtration. The subsequent reaction workup was performed as described in Method A. The yields of the products, for each of the two described methods, are listed in Table 4-1.

We have now modified the initially reported protocol,[18] with the aim of using the free-base corrole as starting material, thus avoiding the need for purification of an intermediate iron corrole complex. Following the procedure described in Method A, we obtained all three products indicated in Scheme 4-1, while with Method B synthesis of the dinitrocorrole was optimized as a unique reaction product.

The reaction yields, calculated with respect to the starting free-base corrole, are comparable with those obtained from the published protocol. Method A, which allowed for isolation of the three different reaction products (Scheme 4-1), enabled the possibility to carry out an electrochemical and spectroscopic characterization of these derivatives, thus providing additional information on the mechanism for the nitration reaction.

Although the reaction yields depend on the method used (A or B), some general trends can be observed from Table 4-1: electron-releasing groups present on the meso-phenyl rings of triarylcorroles (**2** and **3**) induced higher yields of β-nitro substituted derivatives than those obtained with corroles bearing electron-withdrawing substituents (**4** and **5**), probably due to

Table 4-1. Yields of Iron Nitrosyl Corrole Products (data taken from ref 20).

H_3TArC	method	time (min)	TArCFe-NO (yield %)	(NO_2)TArCFeNO (yield %)	$(NO_2)_2$TArCFeNO (yield %)	$[(NO_2)_2TArCFe]_2O$ (yield %)
1	A	120	10%	12%	27.8%	
	B	45		trace	27.5%	
2	A	120	9%	11%	26%	
	B	45			28%	
3	A	120	14%	17%	27%	
	B	45	-	-	36%	
4	A	75	10.7%	12%	17.2%	
	B	40			5%	-
5	A	90	5%	Mixture		9.2%
	B	90			5.8%	9%
6	A	45	trace		32.6%	
	B	25			22.6%	

the more facile formation of a corrole π-cation radical, which is the proposed intermediate necessary for the success of the reaction. Furthermore, for the nitration of **2** and **3** we were able to isolate all three nitrosyl complexes, while with corroles bearing electron-withdrawing substituents (**4** and **5**), we observed a more rapid disappearance of the starting material, and only in the case of **4** all the complete product series was obtained. A different behavior was observed in the case of **6**, because for this corrole the reaction always led to the isolation of a unique product, the difunctionalized corrole **22**, which was isolated in 32.6% yield in the case of Method A.

The difference in reactivity is even more evident in the case of **5**, where formation of the μ-oxo dimer **24** was observed as the major reaction product. Labilization of the nitrosyl ligand with consequent formation of the μ-oxo dimer was earlier observed in the formation of **23**[18] upon slow crystallization of **18**. The process is faster in the case of the pentafluorophenylcorrole than for the triphenylcorrole complex, and the Fe(III) nitrosyl mono- and dinitrocorroles were isolated in only trace amounts.

A plausible explanation for this behavior can lie in how the *meso* aromatic ring substituents affect the lability of the axial Fe−NO bond; this labilization can facilitate formation of a corrole π-cation radical, which then undergoes nucleophilic attack by a nitrite ion. Electron-withdrawing groups have been reported to increase the NO stretching frequencies, ν_{NO}, of the coordinated ligand,[24] evidencing a slight reduction of the bond strength between the metal center and the nitrosyl ligand and consequently supporting a labilization of the coordinated nitrosyl group.

^{1}H NMR characterization of **24** confirmed the proposed structure. The ^{1}H NMR spectrum of **21** exhibits a characteristic singlet (2H) at 8.98 ppm and two doublets at 7.86

and 7.75 ppm (two protons each); in the spectrum of the μ-oxo dimer, the two doublets at 6.88 and 6.96 ppm are identified as the proton signals of the pyrroles B and C, while the singlet at 7.94 ppm is attributed to β-pyrrolic protons at the 2- and 18- positions vicinal to the nitro groups. The overall shielding of the macrocycle signals associated with μ-oxo dimer formation is in good agreement with data reported for the unsubstituted iron complexes of **5**.[25] Similar spectral behavior is observed for **23**, which was prepared by stirring **18** in a CH_2Cl_2/CH_3OH solution.

Crystals suitable for X-ray characterization of **1**7 were obtained, thereby allowing an elucidation of the structure, which is illustrated in Figure 4-1.

There are two independent Fe corroles in the crystal structure (Figure 4-1), each with an almost identical corrole framework (in terms of bond lengths and angles) and angles of the linear nitrosyl group located at the axial position of the corrole, which had a 5-coordinate square pyramid environment. All of the respective $Fe{-}N_{nitrosyl}$ bond lengths, 1.651 (2) Å and 1.652 (2) Å; N−O bond lengths for each nitrosyl ligand, 1.165 (3) Å and 1.160 (3) Å; Fe−N−O bond angles, 178.9 (2)° and 177.9 (2)°; and the average $N_{nitrosyl}{-}Fe{-}N_{pyrrole}$ bond angle, 103.6°, which ranges between 102.4 (1)° and 104.5 (1)°, are comparable to other previously reported crystal structures for nitrosyl iron corrole complexes.[26-29] Similarities can also be observed with crystallographic data published for other iron-metalated complexes of triarylcorroles[18,25,27-31] in regards to the "domed conformation" and the $Fe{-}N_{pyrrole}$ bond length, with a minimum of 1.903 (2) Å, a maximum of 1.931 (2) Å, and an average of 1.915 Å, of this square pyramidal compound.

The planarities of the four pyrrole nitrogen atoms in the two independent molecules in the crystal structure of **17** are not quite identical (the root-mean-square deviation of least-

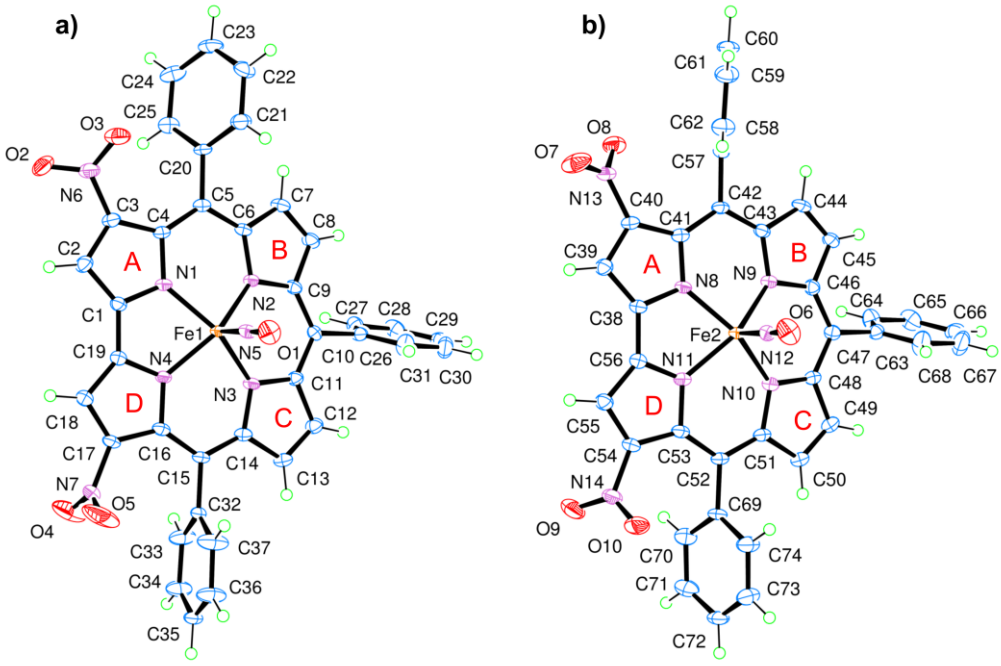

Figure 4-1. Structures of two independent Fe corroles **17**, a) Fe1 complex and b) Fe2 complex, in the unit cell are shown in approximately the same orientation to show how the respective substituents differ in orientation (taken from ref 20).

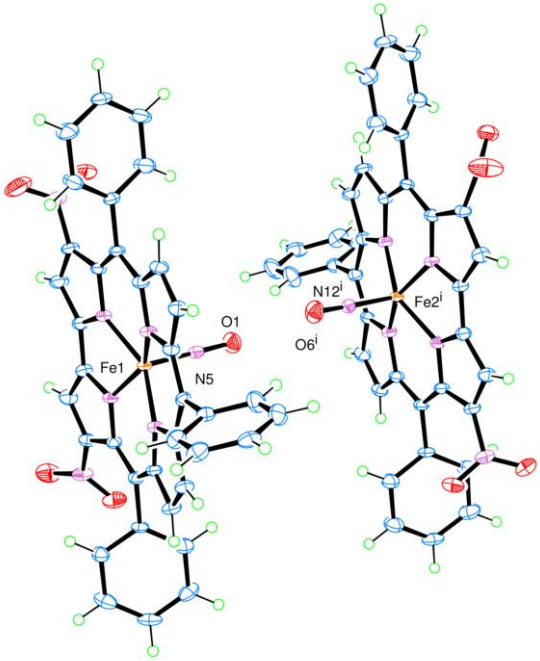

Figure 4-2. The packing relationship between Fe1 corrole and Fe2^{i} corrole related by the symmetry code: (i) −x+1, −y, −z+1. The orientation of each complex's axial nitrosyl ligands are pointed towards each other with a short intermolecular O1•••O6^{i} distance of 2.897 (3) Å (taken from ref 20).

squares planes for N1, N2, N3, N4 and N8, N9, N10, N11 are 0.0061 Å and 0.0243 Å, respectively). Out of these respective planes of the pyrrole nitrogens, the Fe atomic site deviate toward the axial nitrosyl ligand by approximately the same distance (i.e., a deviation of 0.456 (1) Å for Fe1 and 0.444 (1) Å for Fe2). The characteristic tilt of the pyrrole subunits is also noted with the deviations of the pyrrolic nitrogen atoms which buckle on the same side as the axial nitrosyl ligand and are located above a fitted plane of the *β*-pyrrole carbons (average nitrogen atomic site deviation of 0.17 Å from the two respective least-squares planes of C2, C3, C7, C8, C12, C13, C17, C18 and C39, C40, C44, C45, C49, C50, C54, C55). Using the standard A, B, C, D labels for identification of the corrole five-membered rings (as shown in Figure 4-1), a range of dihedral angles between neighboring pyrrole groups, 1.5(2)-14.4(2)°, is observed in the calculations based on the refined model, with the largest dihedral angle occurring for both independent iron corroles between pyrrole A and B.

The most interesting packing relationship in the crystal structure is between the two different Fe complexes, Fe1 corrole and Fe2 corrole (shown in Figure 4-2), where the closest Fe2 corrole is located in the adjacent unit cell and related by the symmetry code (i) $-x + 1$, $-y$, $-z + 1$. The reason for this interest lies in the orientation of the axial nitrosyl ligands of each complex, which are pointed toward each other and have a short intermolecular $O1\cdots O6^{i}$ distance of 2.897 (3) Å without any traces of residual electron densities in between the two oxygen atomic sites.

Method B was shown to be more selective from a preparative point of view, leading to the isolation of a 3,17-dinitrated compound as the major product. In no case did we observe formation of the unsubstituted nitrosyl iron corrole complex, while only trace amounts of the mononitro derivative **13** was obtained. In particular, for **1** and **3**, along with the 3,17-

dinitrocorrole major product, it was possible to collect traces of the 2,17-dinitro compound, together with small amounts of a compound compatible with an asymmetrical trinitrocorrole as characterized by the presence of three singlets (1H each) in the ^{1}H NMR spectrum; however, the small amount of product obtained did not allow us to completely characterize this product.

It is interesting to note that a similar one-pot method has already been published for the preparation of an iron nitrosyl octaalkylcorrole;[26] the authors reported the formation of this complex by adding the required amount of sodium nitrite to a refluxing pyridine/MeOH mixture of the corrole and iron chloride. In this case, the failure to observe formation of β-nitro derivatives can be attributed to the presence of pyridine as the reaction solvent; pyridine leads to the formation of a Fe(III)−bispyridinium complex having no π-cation radical character and thereby making the complex unreactive toward nucleophilic attack and further avoiding the β-functionalization observed when DMF is used as the solvent.

4.2.2 Electrochemistry and Spectroelectrochemistry

Six iron corroles were chosen as representative to electrochemically investigate the effect of nitration on the overall oxidation/reduction mechanisms and site of each electron transfer. The addition of a NO_2 group at one or two β-pyrrole positions of the corrole macrocycle or on the three meso-phenyl groups of the triarylcorrole would be expected to shift all redox potentials toward more positive values (easier reductions and harder oxidations),[32,33] but it was not clear what would be the magnitude of the potential shift for each added electronwithdrawing NO_2 group in the case of the iron nitrosyl derivatives, nor was it clear how the addition of multiple NO_2 groups to a given corrole might affect the site of electron transfer which could occur at the central metal ion, at the conjugated π-ring

system of the macrocycle, and/or at the $C_6H_4NO_2$ groups of the triarylcorrole in the case of compounds **10**, **16**, and **20**.

Chart 4-1. Structures of the electrochemically investigated compounds.

Group A: $(NO_2)_x$(TMOPC)FeNO series (x = 0, 1, 2)

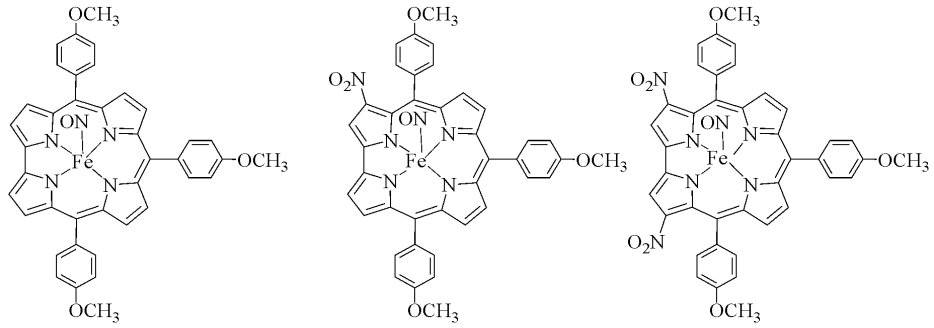

9 **15** **19**

Group B: $(NO_2)_x$(TNPC)FeNO series (x = 0, 1, 2)

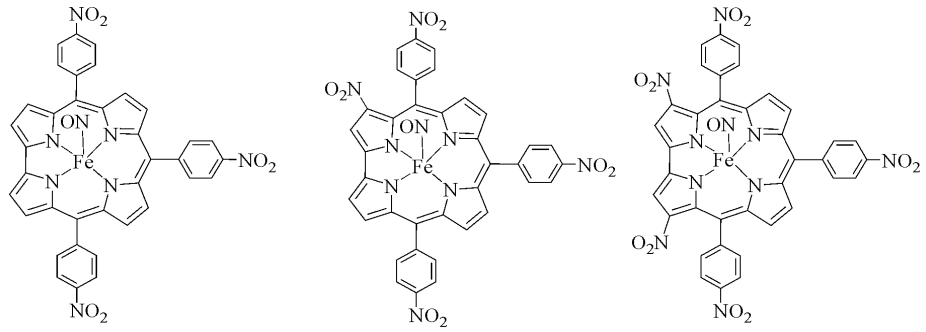

10 **16** **20**

In order to elucidate these points, two series of corroles were selected for electrochemical and spectroelectrochemical characterization in the nonbonding solvent CH_2Cl_2. The first, labeled as Group A in Chart 4-1, is comprised of compounds **9**, **15**, and **19** and represents triarylcorroles having a paramethoxyphenyl substituent at the three meso-positions of the corrole and zero, one, and two NO_2 groups at the β-pyrrole position of the macrocycle; the second group of corroles which were electrochemically characterized is labeled as Group B in Chart 4-1 and possesses three (**10**), four (**16**), or five electron

withdrawing NO_2 (**20**) substituents, three on the meso-phenyl groups of the triarylcorrole and 0, 1, or 2 at the β-pyrrole positions of the macrocycle. Thus, the six compounds in Chart 4-1 have 0, 1, 2, 3, 4, or 5 NO_2 substituents, respectively.

Cyclic voltammograms for five of the six corroles in Chart 4-1 are shown in Figures 4-3 and 4-4, and a summary of measured halfwave and peak potentials is given in Table 4-2. The reductions and oxidations of compounds **9**, **15**, and **19** are both illustrated in Figure 4-3, while only the reductions are shown for the two Group B compounds in Figure 4-4.

As seen from the cyclic voltammograms and table of potentials, the addition of one or two nitro substituents to the β-pyrrole positions of the macrocycle leads to similar positive shifts in $E_{1/2}$ for the first metal centered reduction and the first oxidation. For example, the $Fe^{III/II}$ transition of $(NO_2)_x$(TMOPC)FeNO is located at $E_{1/2}$ = -0.35 V for compound **9** (x = 0), while **15** (x = 1) is reduced at at $E_{1/2}$ = -0.16 V and **19** (x = 2) at $E_{1/2}$ = +0.04 V. A plot of $E_{1/2}$ vs the number of NO_2 groups on the macrocycle is linear with a slope of 0.02 V and a correlation coefficient of 0.996. A linear relationship between $E_{1/2}$ and the number of NO_2 groups on the macrocycle is also seen for the metal-centered reductions of $(NO_2)_x$(TNPC)FeNO, and exactly the same magnitude of shift in $E_{1/2}$ with added NO_2 groups (200 mV/group) is obtained for the Fe(III)/Fe(II) reactions of compounds **10**, **16**, and **20**. This linear free energy relationship is shown in Figure 4-5 and is identical to that reported for three Cu(III) corroles having almost the same structures as compounds **9**, **15**, and **19**.[34]

Figure 4-5, which compares substituent effects for the Fe(III) and Cu(III) corroles containing NO_2 substituents at the 3 and 17 positions of the macrocycle, also includes data on a series of Ge(IV) corroles,[35] which are structurally similar to the Group A compounds in

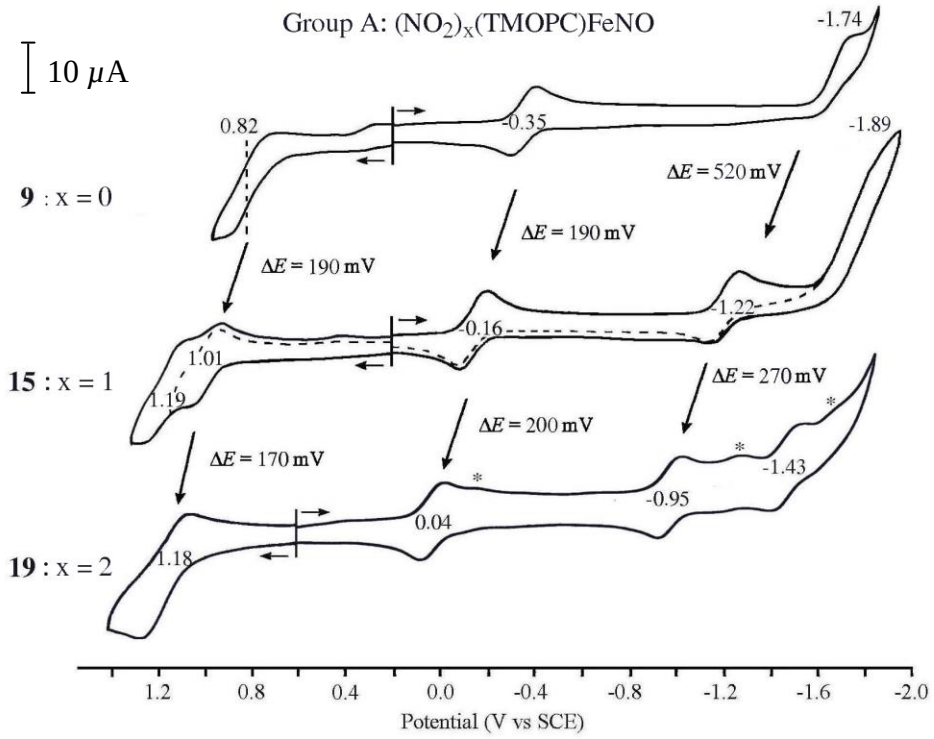

Figure 4-3. Cyclic voltammograms of (TMOPC)FeNO **9**, 3-NO_2(TMOPC)FeNO **15** and 3,17-$(NO_2)_2$(TMOPC)FeNO **19** in CH_2Cl_2 containing 0.1 M TBAP. The reduction peaks of **19** marked by asterisks are mostly likely due to Fe species with an unknown sixth axial ligand.

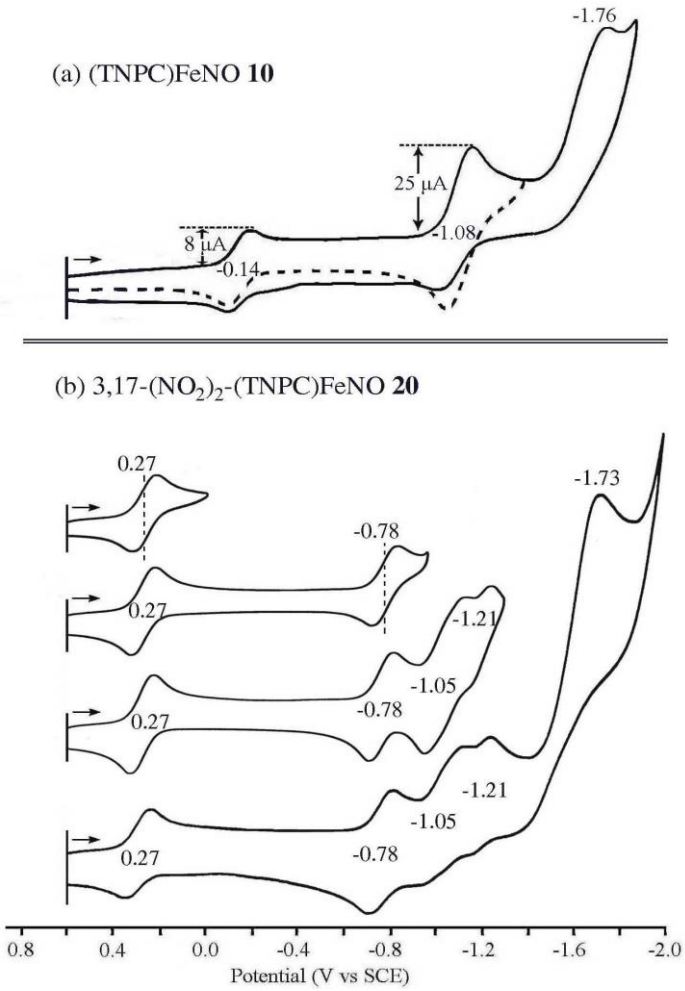

Figure 4-4. Cyclic voltammograms of (TNPC)FeNO **10** and 3,17-$(NO_2)_2$(TNPC)FeNO **20** in CH_2Cl_2 containing 0.1 M TBAP.

Table 4-2. Half-Wave or Peak Potentials (V vs. SCE) of Investigated Iron Corroles in CH_2Cl_2, 0.1 M TBAP.

		oxidation		reduction				
	cpd no.	2nd	1st	metal (Fe^{3+}/Fe^{2+})		macrocycle		
group A	9	0.82[a]	0.82[a]	-0.35		-1.74[b]		
	15	1.19	1.01	-0.16		-1.22	-1.89[b]	
	19	1.18[a]	1.18[a]	0.04		-0.95	-1.43	
group B	10	1.18[b]	0.97	-0.14		-1.08[a]	-1.76[b]	
	16	1.48[b]	1.18	0.05		-1.05	-1.38	
	20	1.46[b]	1.32	0.27	-0.78	-1.05	-1.21	-1.73
$C_6H_5NO_2$						-1.08[c]		

[a]Overlapping. [b]Peak potential at a scan rate of 0.1 V/s. [c]Data taken from ref 41.

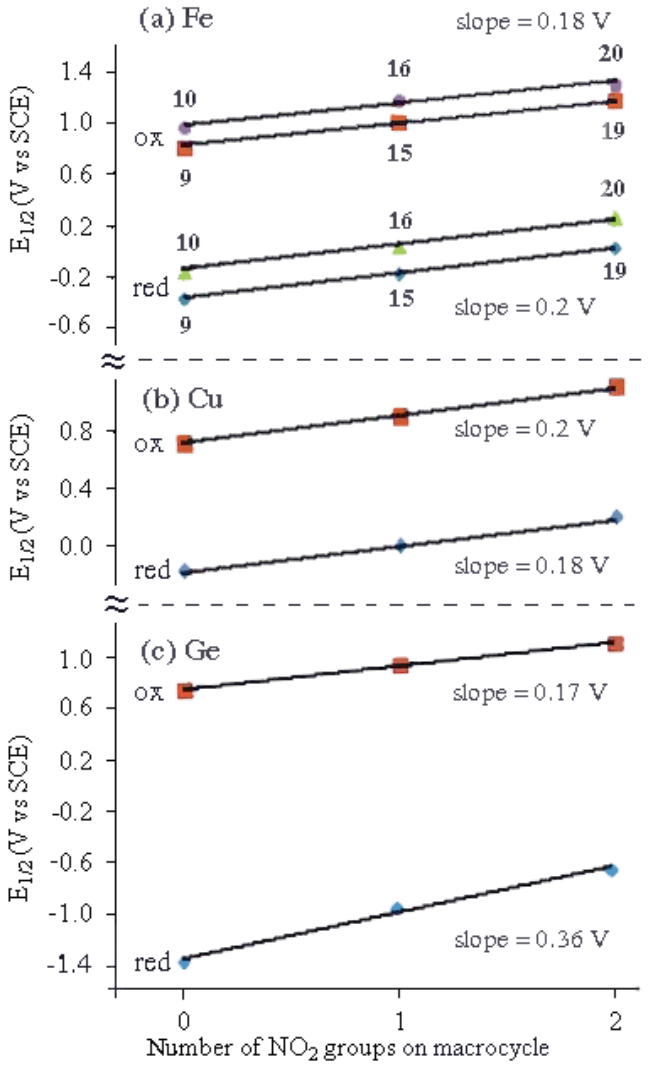

Figure 4-5. Correlation between the number of nitro groups on the corrole macrocycle and $E_{1/2}$ for the first reduction and the first oxidation of (a) $(NO_2)_x$(TNPC)Fe^{III}NO (**10**, **16** and **20**) and $(NO_2)_x$(TMOPC)Fe^{III}NO (**9**, **16** and **19**) in CH_2Cl_2, (b) $(NO_2)_x$TtBuPCorrCu in PhCN and (c) $(NO_2)_x$TPCorrGe^{IV}(OCH_3) in CH_2Cl_2. Data for the Cu(III) and Ge(III) compounds were taken from refs 34 and 35.

Chart 4-1. For this series of compounds, only macrocycle-centered reactions occur, and the first reduction and first oxidation generate the Ge(IV) corrole π-anion and π-cation radicals, respectively. For the compounds in Chart 4-1, the ~200 mV shift in $E_{1/2}$ per each nitro group at the 3 and 17 positions of the macrocycle is larger than the 70-80 mV shift in $E_{1/2}$ for each nitro group at the meso-phenyl position of the triarylcorroles. This difference in substituent effect can best be seen by comparisons of the $Fe^{III/II}$ reduction potentials for **9** and **10** ($\Delta E_{1/2}$ = 0.21 V), **15** and **16** ($\Delta E_{1/2}$ = 0.21 V), and **19** and **20** ($\Delta E_{1/2}$ = 0.23 V). This decreased substituent effect for *meso*-phenyl substituents is as expected and consistent with data in the literature for other porphyrins, corroles, and related macrocycles.[32-34,36-39] In summary, the largest substituent effect occurs for NO_2 groups at the β-pyrrole positions of the corrole macrocycle and the smallest for NO_2 substituents at the para-phenyl groups of the triarylcorrole.

In contrast to what is seen for the Group A compounds, the redox behavior of the Group B compounds differs substantially. This is because the electrode reactions of **10**, **16**, and **20** involve not only the central metal ion and conjugated macrocycle but also the electroactive $C_6H_4NO_2$ group[40] on each *meso*-position of the triarylcorrole. The reduction of nitrobenzene in CH_2Cl_2 is located at $E_{1/2}$ = -1.08 V,[41] and exactly the same half-wave potential is seen for reduction of the *meso*-$C_6H_4NO_2$ groups on (TNPC)FeNO **10** where the current is approximately three times that of the preceding Fe(III)/Fe(II) reaction (see voltammogram in Figure 4-4a). This result is consistent with a one-electron addition in the first step and three overlapping one-electron transfers in the second where the overall reduction processes can be described as shown by Eqs 4-1 and 4-2. A single multielectron reduction of *meso*-$C_6H_4NO_2$ groups has previously been reported for copper triarylcorroles[42]

as well as for tetraphenylporphyrins having the same electroactive substituents at the four *meso*-positions of the macrocycle.[37,38]

$$(TNPC)Fe^{III}(NO) + e \rightleftharpoons [(TNPC)Fe^{II}(NO)]^- \qquad E_{1/2} = -0.14 \text{ V} \qquad (4\text{-}1)$$

$$[(TNPC)Fe^{II}(NO)]^- + 3e \rightleftharpoons [(TNPC)Fe^{II}(NO)]^{4-} \qquad E_{1/2} = -1.08 \text{ V} \qquad (4\text{-}2)$$

The fact that only a single reduction peak is seen for the overall three electron conversion of $[(TNPC)Fe^{II}(NO)]^-$ to $[(TNPC)Fe^{II})(NO)]^{4-}$ (Eq 4-2) is consistent with a lack of any interaction between the three *meso*-$C_6H_4NO_2$ groups of the corrole, each of which is reduced by one electron at the same potential of $E_{1/2}$ = -1.08 V vs SCE. This is not the case for **16** and **20** where the three one-electron reductions of $C_6H_4NO_2$ each occur at separate half-wave potentials as illustrated in Figure 4-4b for the case of 3,17-$(NO_2)_2$(TNPC)FeNO **20**. For this compound, three reversible one electron reductions are seen at $E_{1/2}$ = -0.78, -1.05, and -1.21 V and the first four reductions can be described by Eqs 4-3 to 4-6.

$$(NO_2)_2(TNPC)Fe^{III}(NO) + e \rightleftharpoons [(NO_2)_2(TNPC)Fe^{II}(NO)]^- \qquad E_{1/2} = 0.27 \text{ V} \qquad (4\text{-}3)$$

$$[(NO_2)_2(TNPC)Fe^{II}(NO)]^- + e \rightleftharpoons [(NO_2)_2 (TNPC)Fe^{II})(NO)]^{2-} \qquad E_{1/2} = -0.78 \text{ V} \qquad (4\text{-}4)$$

$$[(NO_2)_2(TNPC)Fe^{II}(NO)]^{2-} + e \rightleftharpoons [(NO_2)_2 (TNPC)Fe^{II})(NO)]^{3-} \qquad E_{1/2} = -1.05 \text{ V} \qquad (4\text{-}5)$$

$$[(NO_2)_2(TNPC)Fe^{II}(NO)]^{3-} + e \rightleftharpoons [(NO_2)_2 (TNPC)Fe^{II})(NO)]^{4-} \qquad E_{1/2} = -1.21 \text{ V} \qquad (4\text{-}6)$$

The site of the electron transfer for each redox reaction can be assigned on the basis of thin-layer UV-vis and FT-IR spectroelectrochemistry. For example, the first oxidation of **15** involves an Fe^{III}/Fe^{III} π-cation radical process as confirmed by thin-layer UV-vis spectroelectrochemistry. As shown in Figure 4-6a, the controlled potential reduction of **15** at 1.10 V in CH_2Cl_2 results in a loss of the Soret band intensity at 431 nm and the appearance of absorptions between 600 and 900 nm, which are characteristic of a corrole π-ratio radical.

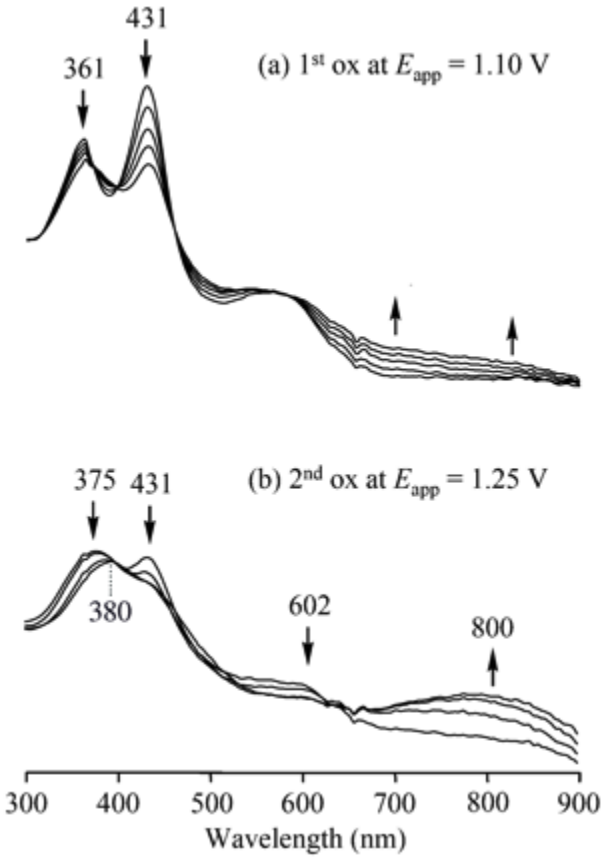

Figure 4-6. Thin-layer UV-vis spectral changes of **15** during the first and the second oxidation in CH_2Cl_2, 0.2 M TBAP.

Shifting the applied potential from 1.10 to 1.25 V then leads to a species, the UV-visible spectrum of which has a broad band at 650-900 nm and a weak band in the Soret region at 380 nm (see Figure 4-6b). Electrogenerated Fe^{IV} corroles have been characterized by a Soret band at 372-381 nm,[43] and the second oxidation of **15** is assigned as a metal-centered process to give an FeIV π-corrole radical.

UV-visible spectral changes monitored during the first one-electron reduction of the six corroles in Chart 4-1 are illustrated in Figure 4-7. A previous spectroelectrochemical study of Cu(III) corroles with Group A type structures showed the presence of quite distinctive absorption bands for the singly reduced, formally Cu(II), forms of the compound containing one or two NO_2 substituents on the macrocycle, and this is also the case for the four examined iron-nitrosyl corroles bearing the same substitution pattern (**15**, **16**, **19**, and **20**).

The UV-visible spectra of the neutral corroles in Group A all possess a split Soret band at 366-431 nm and a weak intensity visible band at 531-591 nm. The Soret band is located at 366 and 416 nm for **9**, at 359 and 431 nm for **15**, and at 347 and 423 nm for **19**. This contrasts with spectra for the neutral Group B corroles, which have a single Soret band at 383 to 403 nm and one or two visible bands at 540-611 nm (see Figure 4-7).

A comparison of spectra for the singly reduced iron nitrosyl corroles in CH_2Cl_2 (Figure 4-7) with those of related singly reduced Cu(III) corroles in PhCN (Figure 5 in ref 34) shows almost the same evolution of spectral shape upon going from the corroles with no nitro substituents at the β-pyrrole position (compounds **9** and **10**) to derivatives with one or two NO_2 groups at the 3 or 3,17 positions of the macrocycle (compounds **15**, **16**, **19**, and **20**). The spectrum of singly reduced **9** and **10** suggests formation of an Fe(II) nitrosyl corrole product,

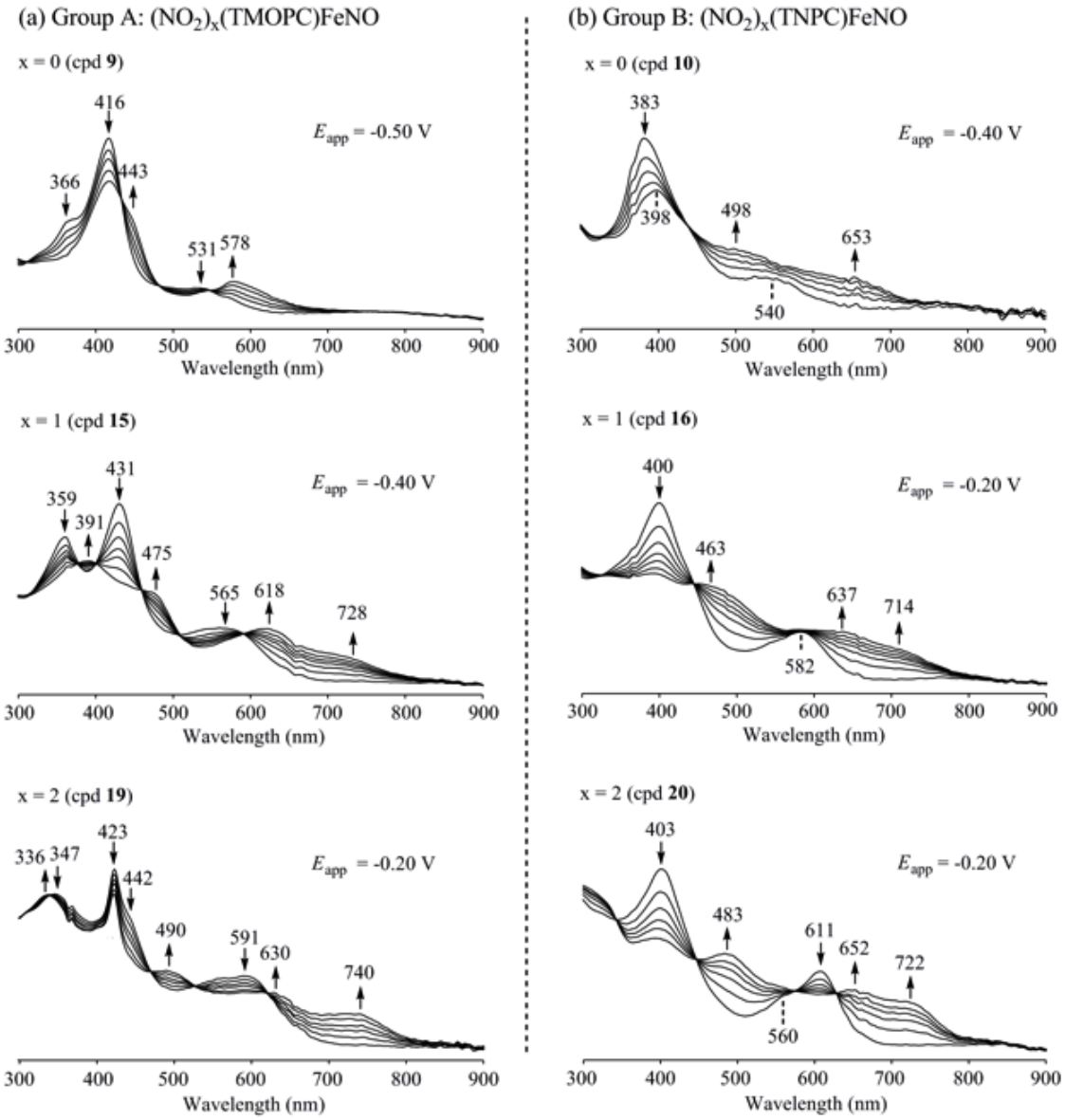

Figure 4-7. UV-visible changes recorded during the first reduction of (a) $(NO_2)_x$(TMOPC)FeNO (Goup A) and (b) $(NO_2)_x$(TNPC)FeNO (Group B) in CH_2Cl_2, 0.1 M TBAP.

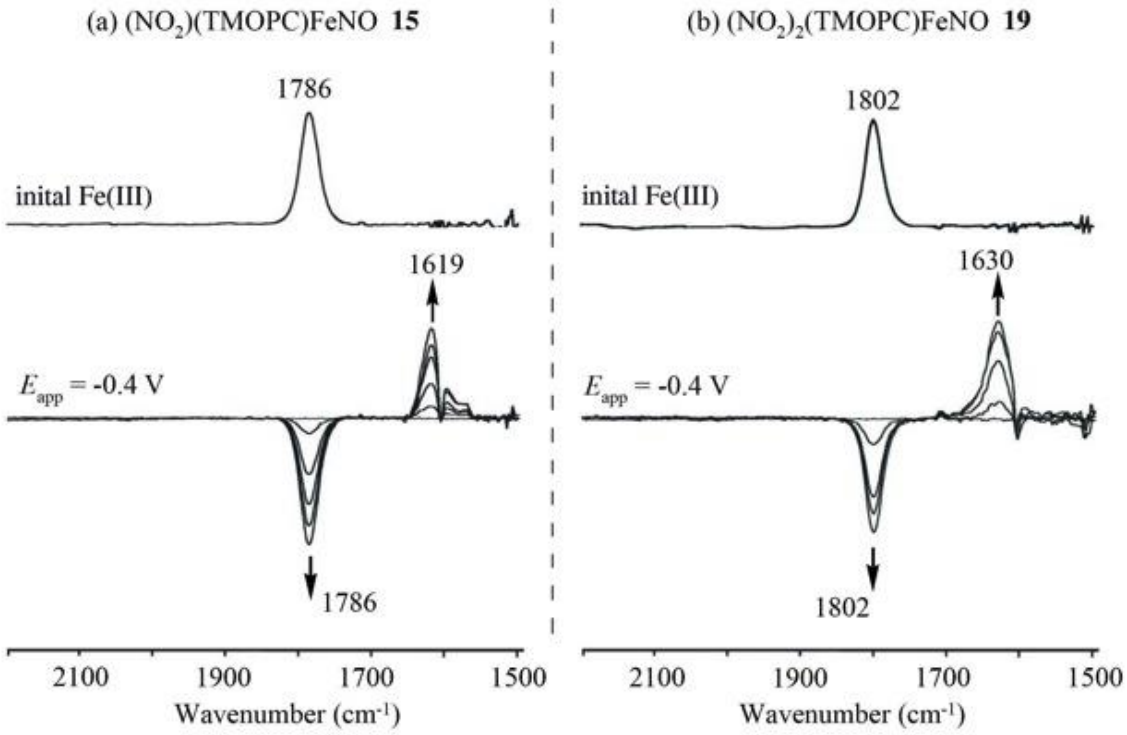

Figure 4-8. Thin-layer IR spectral changes during the first one-electron reduction of (a) **15** and (b) **19** in CH_2Cl_2, 0.1 M TBAP. The applied potentials are indicated in the figure.

and this assignment may also be true for the other four compounds, each of which possess two strong absorptions between 600 and 750 nm. It should be noted that the spectrum of singly reduced **15** has bands at 475, 618, and 728 nm as compared to 463, 637, and 714 nm for singly reduced **16**, with both species lacking a major absorption in the Soret region of the spectrum. A similar spectral shape is also seen for singly reduced **19** and **20**. Compound **19**, after reduction, has bands at 490, 630, and 740 nm, as compared to singly reduced **20**, which has bands at 483, 652, and 722 nm. Again, the overall shapes of the UV-visible spectra are quite similar to those for singly reduced Cu(III) corroles having nitro groups at the same β pyrrole positions of corrole macrocycle.

To further investigate the site of electron transfer, FT-IR spectroelectrochemistry was used to monitor the NO stretching vibrational bands during the first reduction of compounds **15** and **19** in CH_2Cl_2. The relevant spectroelectrochemical data are shown in Figure 4-8 before and after reduction at an applied potential of -0.4 V. As seen in the Figure, the neutral corroles exhibit well-defined NO bands at 1786 (**15**) cm^{-1} and 1802 (**19**), while the singly reduced forms of the compounds have bands at 1619 (**15**) and 1630 (**19**) cm^{-1}. The latter is consistent with what has been reported for other Fe^{II} corroles that exhibit a NO band at 1585-1760 cm^{-1}.[26]

Attempts to determine the NO stretching frequencies of the singly oxidized corroles were less successful due to the rapid loss of NO, which occurs after conversion to the Fe(IV) form of the compounds. When an oxidizing potential of 1.1 V was applied to a solution of **15**, a new weak transient band appeared at 1813 nm^{-1}, consistent with the initial formation of an Fe(III) corrole π-cation radical,[26] but when an oxidizing potential of 1.25 V was applied to the solution, the 1813 cm^{-1} band disappeared, indicating complete loss of the nitrosyl axial

ligand during the second oxidation of **15**. Compound **19** undergoes an overlapping two electron abstraction in the first oxidation (see Figure 4-3), and the NO seems to be lost during this process.

4.3 Summary

We report here an efficient synthetic protocol for the preparation of β-nitro substituted iron corroles, obtained by reaction of the starting triarylcorrole iron chloride complex with $NaNO_2$ in DMF. By tuning the reaction conditions, it is possible to obtain both the 3-nitro and the 3,17-dinitro derivatives in satisfying yields. The scope of the reaction is quite general, and nitro-substituted iron corroles can be obtained with a wide range of triarylcorroles, although in some cases the corresponding μ-oxo dimer, instead the nitrosyl iron complex, is obtained as the reaction side product. The π-cation radical nature of the iron corrole complex can be confidently assigned considering the reactive species, which undergoes nucleophilic attack by nitrite ion, leading to the β-nitro functionalized product.

A detailed study of electrochemistry and spectroelectrochemistry of β-nitro-substituted iron corroles is also presented, elucidating the site of electron transfer and the influence of the peripheral nitro groups. The results obtained provide novel insights on these species, showing that the effect of the nitro substituents on the redox behavior is similar to what is observed for analogous copper(III) corroles having the same substitution pattern.

4.4 References

1. Johnson, A. W.; Kay, I. T. *J. Chem. Soc.* **1965**, 1620-9.
2. Andrioletti, B.; Rose, E. *J. Chem. Soc., Perkin Trans. 1* **2002**, 715-716.
3. Paolesse, R.; Mandoj, F.; Marini, A.; Di Natale, C. In *Encyclopedia of Nanoscience and Nanotechnology*; Nalwa, H., Ed.; American Science Publishers: Valencia, CA, **2004**.
4. He, C.-L.; Ren, F.-L.; Zhang, X.-B.; Han, Z.-X. *Talanta* **2006**, *70*, 364-369.
5. Barbe, J.-M.; Canard, G.; Brandes, S.; Guilard, R. *Chem. - Eur. J.* **2007**, *13*, 2118-2129, S2118/1-S2118/3.
6. Gatto, E.; Malik, M. A.; Di Natale, C.; Paolesse, R.; D'Amico, A.; Lundstrom, I.; Filippini, D. *Chem. - Eur. J.* **2008**, *14*, 6057-6060.
7. Gross, Z.; Aviv-Harel, I. *Chem. Eur. J.* **2009**, *15*, 8382-8394.
8. Kanamori, A.; Catrinescu, M.-M.; Mahammed, A.; Gross, Z.; Levin, L. A. *J. Neurochem.* **2010**, *114*, 488-498.
9. Kupershmidt, L.; Okun, Z.; Amit, T.; Mandel, S.; Saltsman, I.; Mahammed, A.; Bar-Am, O.; Gross, Z.; Youdim, M. B. H. *J. Neurochem.* **2010**, *113*, 363-373.
10. Paolesse, R. *Synlett* **2008**, 2215-2230.
11. Lemon, C. M.; Brothers, P. J. *J. Porphyrins Phthalocyanines* **2011**, *15*, 809-834.
12. Gryko, D. T.; Fox, J. P.; Goldberg, D. P. *J. Porphyrins Phthalocyanines* **2004**, *8*, 1091-1105.
13. Nardis, S.; Monti, D.; Paolesse, R. *Mini-Rev. Org. Chem.* **2005**, *2*, 355-374.
14. Aviv-Harel, I.; Gross, Z. *Coord. Chem. Rev.* **2011**, *255*, 717-736.

15. Saltsman, I.; Mahammed, A.; Goldberg, I.; Tkachenko, E.; Botoshansky, M.; Gross, Z. *J. Am. Chem. Soc.* **2002**, *124*, 7411-7420.

16. Ghosh, A.; Wondimagegn, T.; Parusel, A. B. J. *J. Am. Chem. Soc.* **2000**, *122*, 5100-5104.

17. Walker, F. A.; Licoccia, S.; Paolesse, R. *J. Inorg. Biochem.* **2006**, *100*, 810-837.

18. Stefanelli, M.; Nardis, S.; Tortora, L.; Fronczek, F. R.; Smith, K. M.; Licoccia, S.; Paolesse, R. *Chem. Commun.* **2011**, *47*, 4255-4257.

19. Ye, S.; Tuttle, T.; Bill, E.; Simkhovich, L.; Gross, Z.; Thiel, W.; Neese, F. *Chem. - Eur. J.* **2008**, *14*, 10839-10851.

20. Nardis, S.; Stefanelli, M.; Mohite, P.; Pomarico, G.; Tortora, L.; Manowong, M.; Chen, P.; Kadish, K. M.; Fronczek, F. R.; McCandless, G. T.; Smith, K. M.; Paolesse, R. *Inorg. Chem.* **2012**, *51*, 3910-3920.

21. Gross, Z.; Galili, N.; Saltsman, I. *Angew. Chem., Int. Ed.* **1999**, *38*, 1427-1429.

22. Paolesse, R. In *The Porphyrin Handbook*; Kadish, K. M., Smith, K. M., Guilard, R., Eds.; Academic Press: New York, **2000**; Vol. 2, p 201-232.

23. Gryko, D. T. *J. Porphyrins Phthalocyanines* **2008**, *12*, 906-917.

24. Wehman, P.; Borst, L.; Kamer, P. C. J.; van Leeuwen, P. W. N. M. *J. Mol. Catal. A: Chem.* **1996**, *112*, 23-36.

25. Simkhovich, L.; Mahammed, A.; Goldberg, I.; Gross, Z. *Chem. - Eur. J.* **2001**, *7*, 1041-1055.

26. Autret, M.; Will, S.; Van Caemelbecke, E.; Lex, J.; Gisselbrecht, J.-P.; Gross, M.; Vogel, E.; Kadish, K. M. *J. Am. Chem. Soc.* **1994**, *116*, 9141-9149.

27. Simkhovich, L.; Goldberg, I.; Gross, Z. *Inorg. Chem.* **2002**, *41*, 5433-5439.

28. Joseph, C. A.; Lee, M. S.; Iretskii, A. V.; Wu, G.; Ford, P. C. *Inorg. Chem.* **2006**, *45*, 2075-2082.

29. Broering, M.; Milsmann, C.; Ruck, S.; Koehler, S. *J. Organomet. Chem.* **2009**, *694*, 1011-1015.

30. Simkhovich, L.; Galili, N.; Saltsman, I.; Goldberg, I.; Gross, Z. *Inorg. Chem.* **2000**, *39*, 2704-2705.

31. Nardis, S.; Paolesse, R.; Licoccia, S.; Fronczek, F. R.; Vicente, M. G. H.; Shokhireva, T. K.; Cai, S.; Walker, F. A. *Inorg. Chem.* **2005**, *44*, 7030-7046.

32. Kadish, K. M.; Royal, G.; Van Caemelbecke, E.; Gueletti, E. In *The Porphyrin Handbook*; Kadish, K. M., Smith, K. M., Guilard, R., Eds.; Academic Press: San Diego, CA, **2000**; Vol. 9, p 1-419.

33. Kadish, K. M.; Van Caemelbecke, E.; Royal, G. In *The Porphyrin Handbook*; Kadish, K. M., Smith, K. M., Guilard, R., Eds.; Academic Press: San Diego, CA, **2000**; Vol. 8, p 1-97.

34. Stefanelli, M.; Mandoj, F.; Mastroianni, M.; Nardis, S.; Mohite, P.; Fronczek, F. R.; Smith, K. M.; Kadish, K. M.; Xiao, X.; Ou, Z.; Chen, P.; Paolesse, R. *Inorg. Chem.* **2011**, *50*, 8281-8292.

35. Mastroianni, M.; Zhu, W.; Stefanelli, M.; Nardis, S.; Fronczek, F. R.; Smith, K. M.; Ou, Z.; Kadish, K. M.; Paolesse, R. *Inorg. Chem.* **2008**, *47*, 11680-11687.

36. Ozette, K.; Battioni, P.; Leduc, P.; Bartoli, J.-F.; Mansuy, D. *Inorg. Chim. Acta* **1998**, *272*, 4-6.

37. Schiavon, M. A.; Iwamoto, L. S.; Ferreira, A. G.; Iamamoto, Y.; Zanoni, M. V. B.; Assis, M. d. D. *J. Braz. Chem. Soc.* **2000**, *11*, 458-466.

38. Ghosh, A.; Halvorsen, I.; Nilsen, H. J.; Steene, E.; Wondimagegn, T.; Lie, R.; van Caemelbecke, E.; Guo, N.; Ou, Z.; Kadish, K. M. *J. Phys. Chem. B* **2001**, *105*, 8120-8124.

39. Bachmann, J.; Nocera, D. G. *J. Am. Chem. Soc.* **2005**, *127*, 4730-4743.

40. Lund, H. In *Cathodic Reduction of Nitro and Related Compounds*; 4th ed.; Lund, H., Hammerich, O., Eds.; Marcel Dekker, Inc.: New York, **2001**, p 379-409.

41. Kadish, K. M.; Wenbo, E.; Sintic, P. J.; Ou, Z.; Shao, J.; Ohkubo, K.; Fukuzumi, S.; Govenlock, L. J.; McDonald, J. A.; Try, A. C.; Cai, Z.-L.; Reimers, J. R.; Crossley, M. J. *J. Phys. Chem. B* **2007**, *111*, 8762-8774.

42. Bhattacharya, D.; Singh, P.; Sarkar, S. *Inorg. Chim. Acta* **2010**, *363*, 4313-4318.

43. Van Caemelbecke, E.; Will, S.; Autret, M.; Adamian, V. A.; Lex, J.; Gisselbrecht, J.-P.; Gross, M.; Vogel, E.; Kadish, K. M. *Inorg. Chem.* **1996**, *35*, 184-92.

CHAPTER FIVE

Synthesis and Characterization of *bis*-[PcRu(CO)][$Ru_2(ap)_4(C{\equiv}CC_5H_4N)_2$]

5.1 Introduction

Diruthenium complexes with a paddlewheel structure have been used as building blocks for the synthesis of supramolecular assemblies in the field of molecular electronics, in part because of their interesting magnetic and redox properties.[1-7] Most diruthenium complexes of this type contain four anionic bridging ligands and are formulated as $Ru_2(L)_4^+$ or $Ru_2(L)_4Cl$ but other neutral and charged ligands can be added at the vacant axial positions of the compounds.[8-10] Substitutions can also be made at any or all of the equatorial positions on $Ru_2L_4^{+}$[11,12] in order to examine any magnetic and electronic interactions which might exist between the central diruthenium unit and other electroactive or non-electroactive parts of the molecule.

One group of previously synthesized diruthenium compounds are the σ-alkynyl derivatives[13-20] which are particularly attractive for the construction of organometallic molecular wires. One such σ-alkynyl diruthenium compound is $Ru_2(ap)_4(C{\equiv}CC_5H_4N)_2$, where ap = 2-anilinopyridinate anion.[20] This diruthenium(III,III) derivative is of interest because the two external pyridine groups on the molecule are able to coordinate with metal complexes, such as previously shown for $[Ru_2(form)_4(C{\equiv}CC_5H_4N)_2][Re(CO)_3L]$ and $[Ru_2(dpf)_4(C{\equiv}CC_5H_4N)_2][Re(CO)_3L]$, where form = *N,N′*-di-*p*-tolylformamidinate ion, dpf = *N,N′*–diphenylformamidinate ion and L = 4,4′-bis(*tert*-butyl)-2,2′-bipyridine.[21]

Metallophthalocyanines (MPcs) are well known for their intense color, redox activity and high thermal stability.[22-24] Moreover, the optical and redox properties of phthalocyanines can be tuned by changing the central metal and/or the substituents either at the peripheral or at the axial position of the macrocycle.[24,25] Owing to their chemical versatility and their optoelectronic properties, these synthetic porphyrin analogues play a major role in the field

of molecular electronics and are used as potential photosensitizers in solar technologies and photodynamic treatment of cancer.[26-28] Their potential applications also include analytical sensors for industry, environment, and medicine.[26,29]

Numerous electron donor-acceptor conjugates containing Pc building blocks have been designed and studied in the context of molecular devices.[30-33] For preparing some of these hybrids, we and others have used phthalocyanines bearing a Ru(II) ion within their central cavity.[34-36] Such metallomacrocycles form stable and rigid architectures through metal coordination of pyridine derivatives.[37-39] thus making them ideal candidates for coordination with the diruthenium compound discussed above, namely $[Ru_2(ap)_4(C{\equiv}CC_5H_4N)_2]$.

In this chapter, we report the synthesis and characterization of a tetraruthenium complex **3** (Chart 5-1) consisting of one $[Ru_2(ap)_4(C{\equiv}CC_5H_4N)_2]$ **1** unit linked to the two ruthenium(II) centers of two ruthenium phthalocyanines **2**. The investigated compound is represented as *bis*-[PcRu(CO)]$[Ru_2(ap)_4(C{\equiv}CC_5H_4N)_2]$ **3**. For phthalocyanine **2**, single ligation at the Ru(II) center is assured due to the presence of the strongly ligating, π-acceptor carbonyl ligand at one of the two axial Ru(II) coordination sites. This should direct the diruthenium unit **1** to the opposite Pc axial coordination site.[34,35,40,41] In order to determine whether there was any electronic interaction among the metal centers, the electrochemical and UV-visible spectroelectrochemical properties of the tetraruthenium triad **3** were investigated and compared to those of $Ru_2(ap)_4(C{\equiv}CC_5H_4N)_2$ **1** and PcRu(CO) **2** under similar solution conditions.

Chart 5-1. Structures of the investigated compounds.

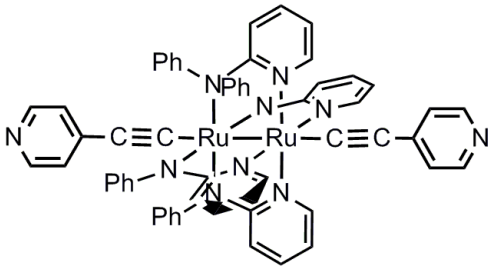

1

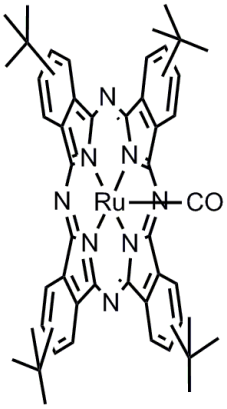

2

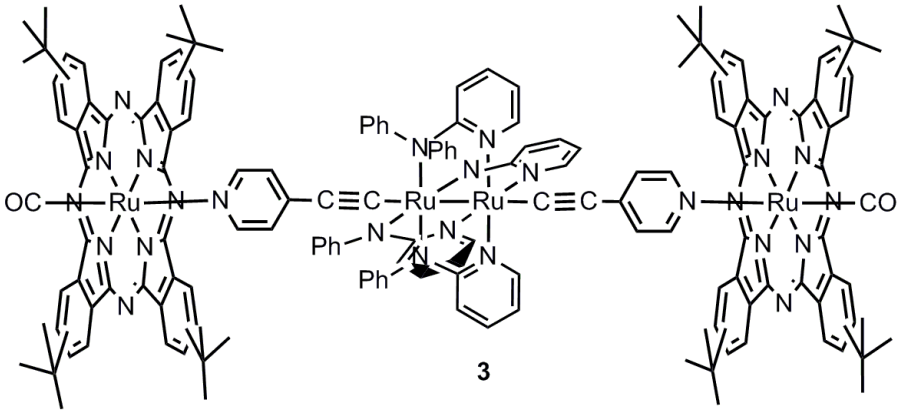

3

5.2 Results and discussion

5.2.1 Synthetic details

Bis-[PcRu(CO)][$Ru_2(ap)_4(C{\equiv}CC_5H_4N)_2$][42] **3** was synthesized by our collaborators at the Autonomous University of Madrid. $[Ru_2(ap)_4(C{\equiv}CC_5H_4N)_2]$[20] **1** and PcRu(CO)[34] **2** were synthesized according to procedures in the literature.

Most unsubstituted MPcs have limited solubility in organic solvents. In this respect, the PcRu(CO) **2** was provided with four peripheral *tert*-butyl groups in order to increase the solubility properties, reduce the aggregation in solution and provide σ-donor features.[25] *Bis*-

[PcRu(CO)][$Ru_2(ap)_4(C{\equiv}CC_5H_4N)_2$] **3** was assembled in 66% yield by treatment of the diruthenium complex **1** with two equivalents of the phthalocyanine **2** in chloroform at room temperature. The purification of **3** was carried out by gel permeation chromatography. The structure of **3** was confirmed by mass spectrometry (see Figure 5-1), as well as UV-visible and IR spectroscopies (see Figure 5-2). Tetraruthenium complex **3** showed its isotopic signature in MS (ESI-TOF) as an intense peak at *m/*z = 1405-1412, corresponding to $[M]^{2+}$, in addition to a very weak peak at *m/*z = 2819 corresponding to $[M]^{+}$. A loss of the phthalocyanine unit on **3** was observed as a weak peak at *m/z* = 1950 along with the phthalocyanine and diruthenium fragments at *m/z* = 866 and 1084, respectively.

Moreover, the IR spectrum of **3** displays features corresponding to both the Pc and diruthenium fragments. The spectrum is dominated by the $\nu_{C=O}$ stretching band at 1973 cm^{-1} corresponding to the Pc unit.[34] Typical of a ruthenium acetylide complex, an intense $\nu_{C{\equiv}C}$ stretching band appears at 2061 cm^{-1}.[43]

5.2.2 Electrochemistry of $Ru_2(ap)_4(C{\equiv}CC_5H_4N)_2$ 1

As shown in Figure 5-3, $Ru_2(ap)_4(C{\equiv}CC_5H_4N)_2$ **1** exhibits two reversible reductions and a single reversible oxidation in CH_2Cl_2 containing 0.1 M TBAP for a scan rate of 0.1 V/s. The $E_{1/2}$ values for all processes are similar to those reported by Kadish et al.[20] The two reductions at $E_{1/2}$ = -0.49 and -1.41 are assigned to the $Ru_2^{6+/5+}$ and $Ru_2^{5+/4+}$ processes while the oxidation at $E_{1/2}$ = 0.70 V is attributed to the $Ru_2^{6+/7+}$ process. These assignments were made on the basis of what has been reported for related (3,1) or (4,0) derivatives of $Ru_2(L)_4(C{\equiv}CC_6H_5)_2$ where L is an ap or substituted ap bridging ligand.[19,20] These compounds have been shown to undergo either three or four metal-centered processes,

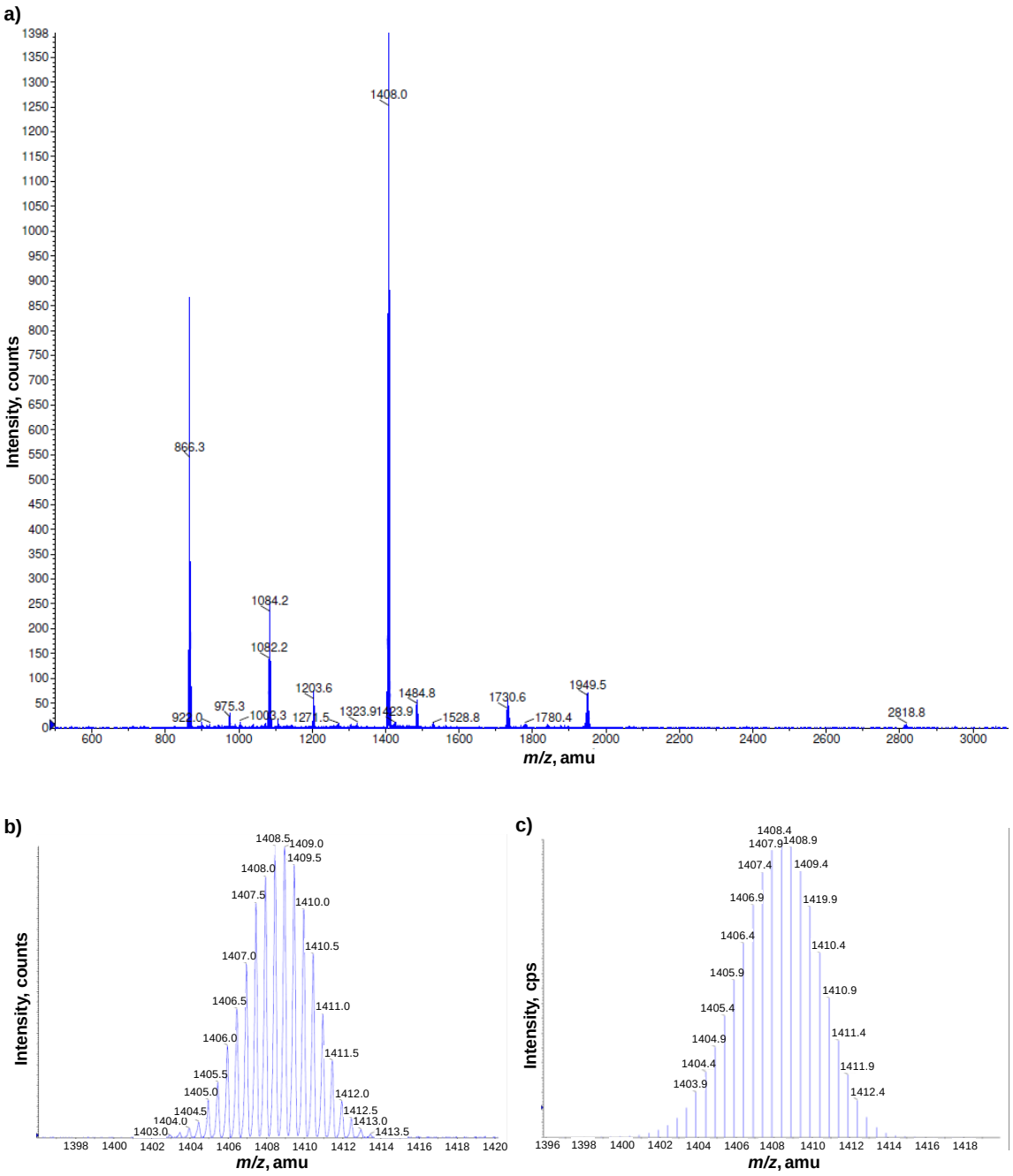

Figure 5-1. Mass spectrum (a) of compound **3**. Experimental (b) and calculated (c) isotopic distribution for $[C_{156}H_{140}N_{26}Ru_4O_2]^{2+}$ (Resolution = 10000) (taken from ref 42).

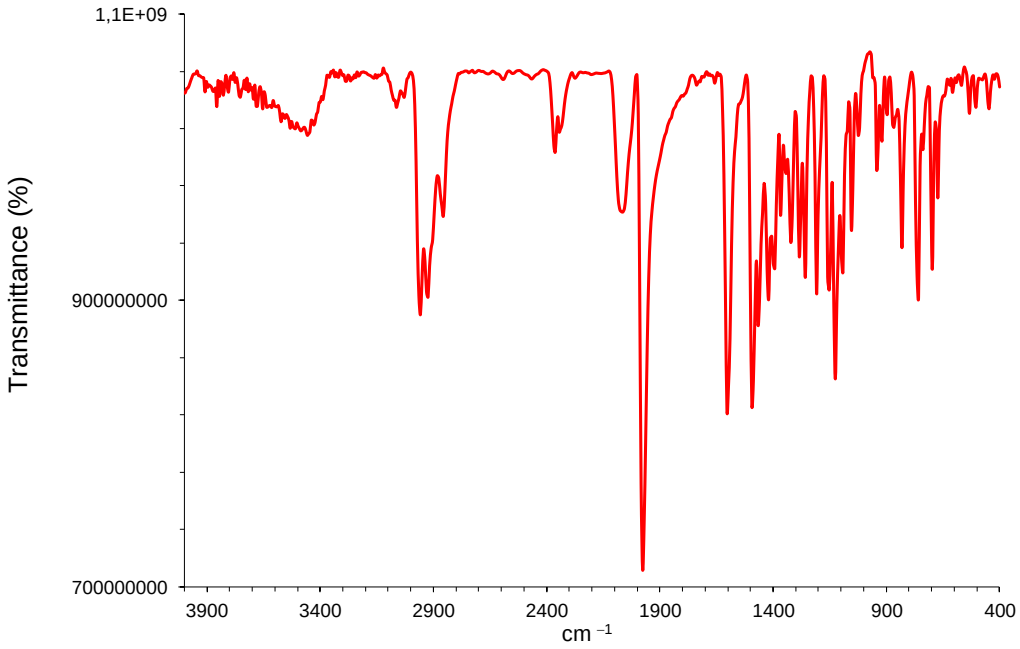

Figure 5-2. IR spectrum of compound **3** in the solid state (taken from ref 42).

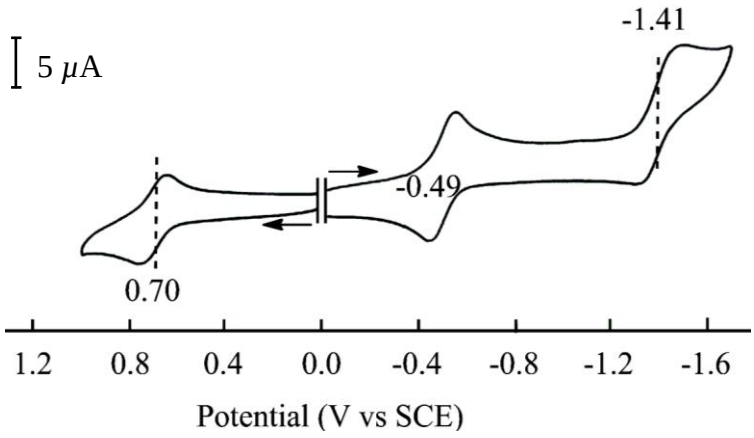

Figure 5-3. Cyclic voltammogram of $Ru_2(ap)_4(C{\equiv}CC_5H_4N)_2$ **1** in CH_2Cl_2 containing 0.1 M TBAP at a scan rate of 0.1 V/s.

yielding a stepwise conversion between compounds with Ru_2^{8+}, Ru_2^{7+}, Ru_2^{6+}, Ru_2^{5+}, or Ru_2^{4+} cores as shown by Eqs 5-1 to 5-4.

$$(L)_4Ru_2^{6+} + e^- \rightleftarrows (L)_4Ru_2^{5+} \quad (5\text{-}1)$$

$$(L)_4Ru_2^{5+} + e^- \rightleftarrows (L)_4Ru_2^{4+} \quad (5\text{-}2)$$

$$(L)_4Ru_2^{6+} \rightleftarrows (L)_4Ru_2^{7+} + e^- \quad (5\text{-}3)$$

$$(L)_4Ru_2^{7+} \rightleftarrows (L)_4Ru_2^{8+} + e^- \quad (5\text{-}4)$$

Table 5-1 summarizes half-wave potentials for the metal-centered processes of $Ru_2(ap)_4(C{\equiv}CC_6H_5)_2$ along with data for $Ru_2(ap)_4(C{\equiv}CC_5H_4N)_2$ **1** and *bis*-[PcRu(CO)][$Ru_2(ap)_4(C{\equiv}CC_5H_4N)_2$] **3** under the same solution conditions. The potential separation between the first reduction and first oxidation of **1** (1.19 V) is also close to the HOMO-LUMO gaps of (3,1) $Ru_2(L)_4(C{\equiv}CC_6H_5)_2$ which ranges from 1.13 to 1.26 V. The first reduction of **1** ($E_{1/2}$ = -0.49 V) is 50 mV less negative than the first reduction of $Ru_2(ap)_4(C{\equiv}CC_6H_5)$ ($E_{1/2}$ = -0.54 V) and this can be accounted for by the fact that the two pyridyl groups decrease the electron density on the diruthenium unit to a greater extent than the two phenyl groups.

5.2.3 Electrochemistry of PcRu(CO) 2

PcRu(CO) **2** undergoes two reductions and two oxidations but only the first reduction and first oxidation are reversible in CH_2Cl_2, as shown in Figure 5-4. All four redox processes of PcRu(CO) have been assigned to processes on the phthalocyanine ring.[40,41] To further investigate the solvent effect on the oxidation or reduction potentials of **2**, electrochemical studies were carried out in PhCN and pyridine containing 0.1 M TBAP. In these solvents, both reductions become reversible. The first reduction shifts in a positive direction by 90 mV upon going from CH_2Cl_2 to PhCN and by 140 mV upon going from CH_2Cl_2 to pyridine. The

Table 5-1. Half-wave potentials (V vs SCE) for redox processes involving the metal-metal bonded Ru_2 unit of $Ru_2(ap)_4(C{\equiv}CC_6H_5)_2$, $Ru_2(ap)_4(C{\equiv}CC_5H_4N)_2$ **1** and *bis*-[PcRu(CO)][$Ru_2(ap)_4(C{\equiv}CC_5H_4N)_2$] **3** in CH_2Cl_2, containing 0.1 M TBAP.

Compound	$Ru_2^{7+/6+}$	$Ru_2^{6+/5+}$	$Ru_2^{5+/4+}$
$Ru_2(ap)_4(C{\equiv}CC_6H_5)_2$[a]	0.55	-0.54	-1.67
$Ru_2(ap)_4(C{\equiv}CC_5H_4N)_2$	0.70	-0.49	-1.41
bis-[PcRu(CO)][$Ru_2(ap)_4(C{\equiv}CC_5H_4N)_2$]	~ 0.74	-0.49	-1.37

[a] Data taken from ref 20

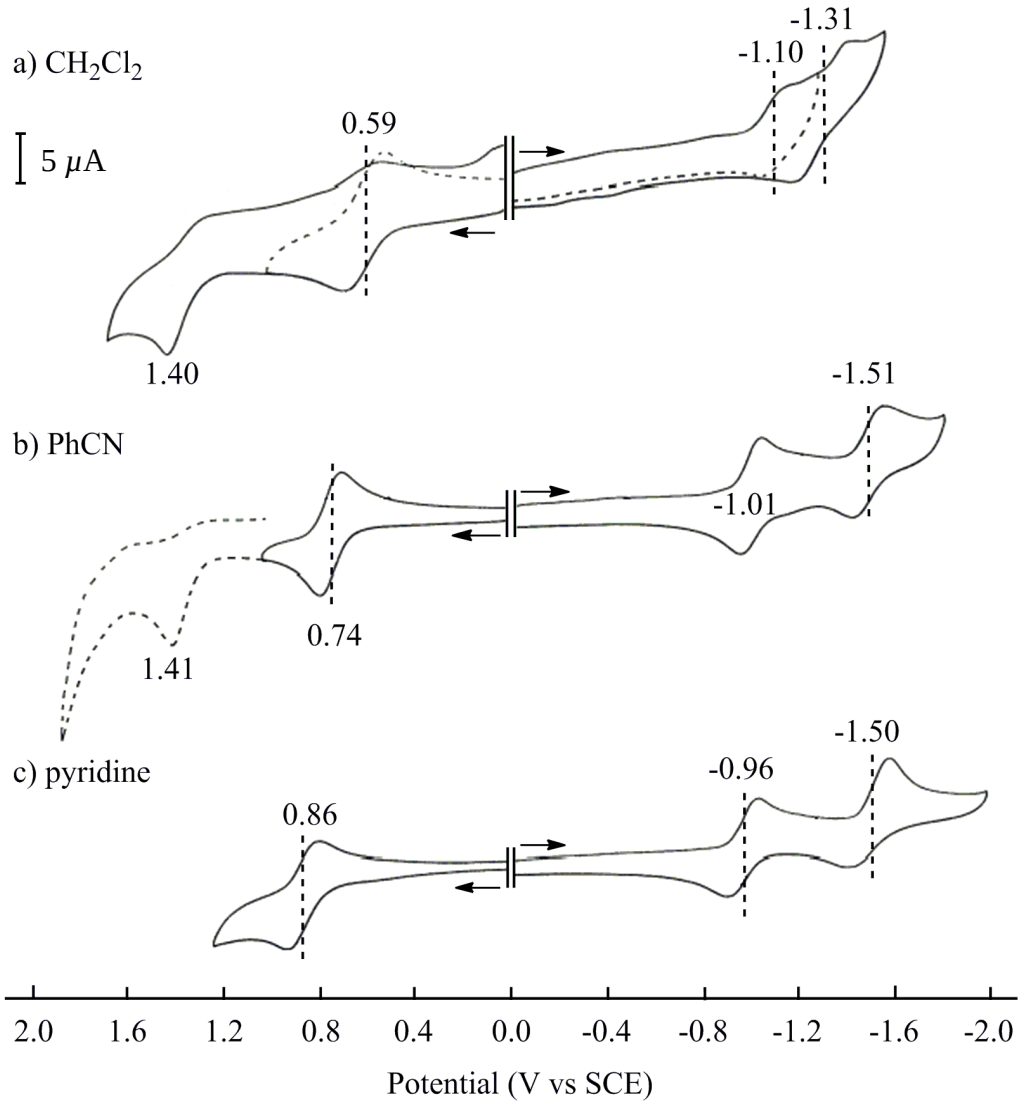

Figure 5-4. Cyclic voltammograms of PcRu(CO) **2** in a) CH_2Cl_2, b) PhCN and c) pyridine containing 0.1 M TBAP at a scan rate of 0.1 V/s.

second reduction shifts cathodically by about 200 mV upon going from CH_2Cl_2 to PhCN or pyridine. The first oxidation potential also depends on the solvent, as evidenced by the fact that the first oxidation occurs at 0.74 V in PhCN and 0.86 V in pyridine.

The electrochemical data of **2** in PhCN and pyridine suggest that one solvent molecule binds to PcRu(CO) to form PcRu(CO)(S) (where S = PhCN or pyridine). In addition, the potential difference of 1.75 V and 1.82 V between the first reduction and the first oxidation processes of PcRu(CO) in PhCN and pyridine, respectively are similar to those of related six-coordinate ruthenium(II) phthalocyanine derivatives,[35,39,44] thus further suggesting the presence of a solvent molecule trans to CO in both PhCN and pyridine and the formulation PcRu(CO)(S) for the compound in these two solvents.

5.2.4 Electrochemistry of *bis*-[PcRu(CO)][$Ru_2(ap)_4(C{\equiv}CC_5H_4N)_2$] 3

Bis-[PcRu(CO)][$Ru_2(ap)_4(C{\equiv}CC_5H_4N)_2$] **3** exhibits eight redox processes in CH_2Cl_2, containing 0.1 M TBAP (see Figure 5-5), four of which are attributed to the dimetal unit of the compound and four to the macrocycle of the two linked PcRu(CO) groups. The first and the third reductions of **3**, at $E_{1/2}$ = -0.49 and -1.37 V, are assigned to the $Ru_2^{6+/5+}$ and $Ru_2^{5+/4+}$ processes (Eq 5-1 and 5-2) based on the fact that the first reduction of the triad occurs at the same potential as the $Ru_2^{6+/5+}$ couple of the unlinked compound **1** ($E_{1/2}$ = -0.49 V) while the third reduction of **3** is shifted anodically by only 40 mV with respect to the $Ru_2^{5+/4+}$ process of **1** ($E_{1/2}$ = -1.41 V). The tetraruthenium complex **3** also exhibits an irreversible oxidation at E_{pa} = 1.22 V which has a peak current height similar to that of the first and third reduction processes, suggesting that this oxidation can also be attributed to the $Ru_2^{7+/8+}$ process of the dimetal unit (Eq 5-4). A second oxidation is not observed for $Ru_2(ap)_4(C{\equiv}CC_5H_4N)_2$ **1** in the absence of linked PcRu(CO) but several studies on related $Ru_2(L)_4(C{\equiv}CC_6H_5)_2$ derivatives

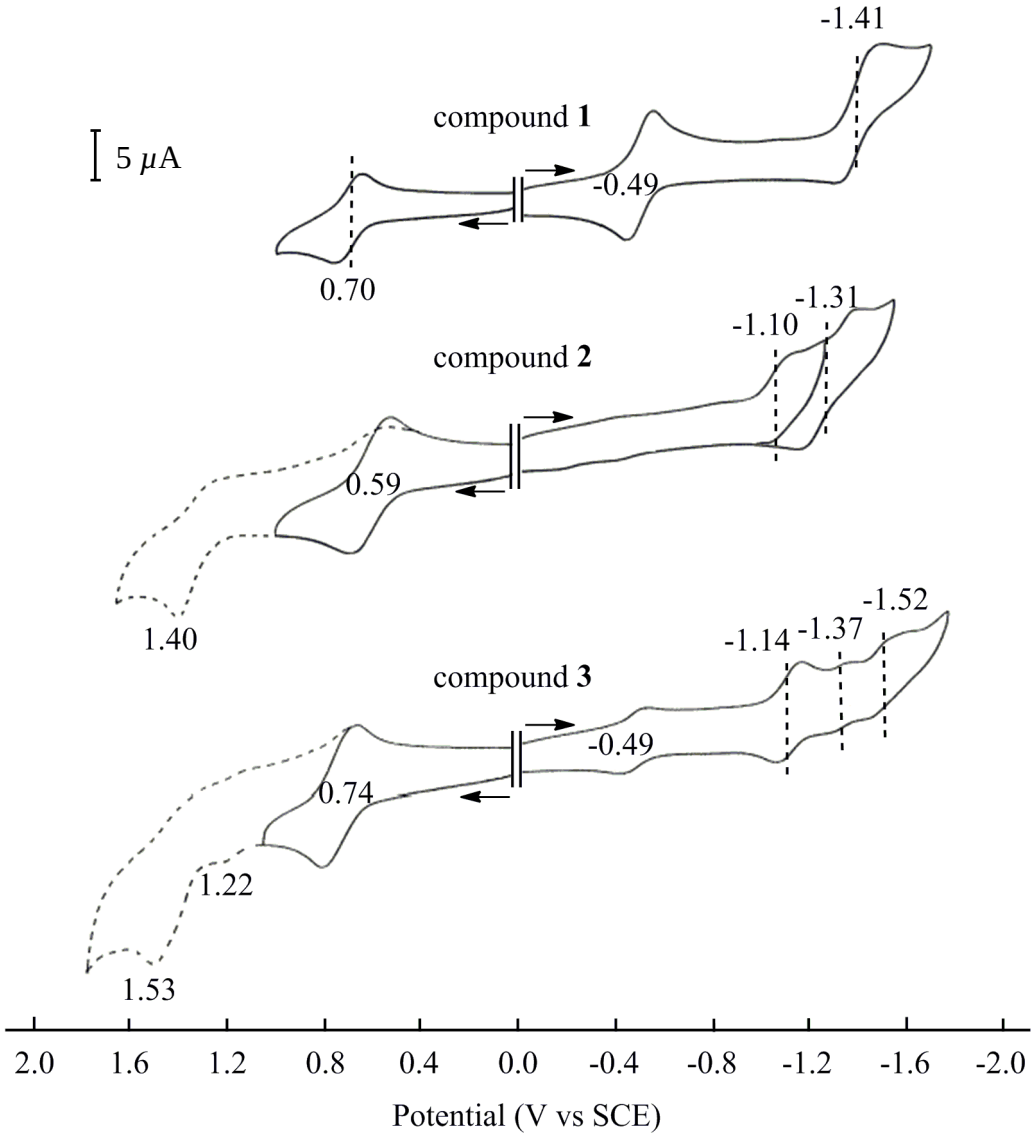

Figure 5-5. Cyclic voltammograms of $Ru_2(ap)_4(C{\equiv}CC_5H_4N)_2$ **1**, PcRu(CO) **2** and *bis*-[PcRu(CO)][$Ru_2(ap)_4(C{\equiv}CC_5H_4N)_2$] **3** in CH_2Cl_2 containing 0.1 M TBAP.

have reported the $Ru_2^{7+/8+}$ electrode process to occur in nonaqueous media.[19]

The second and fourth reductions of **3** at $E_{1/2}$ = -1.14 and -1.52 V have higher peak current heights than the first or third reductions (see Figure 5-5) and these are assigned to electron additions at the macrocycles of the two linked phthalocyanines. The first oxidation of **3** has a peak current height higher than that obtained by adding the peak current heights for the first and second reductions of the same compound and this apparent three electron transfer process is assigned to overlapping oxidations of both the diruthenium unit ($Ru_2^{6+/7+}$) and the two PcRu(CO) groups of **3**. Finally, the third oxidation of **3** at E_{pa} = 1.53 V is irreversible in CH_2Cl_2, 0.1 M TBAP and occurs at a potential close to the second oxidation of unlinked PcRu(CO) (1.40 V) under the same solution conditions, thus suggesting that this process of **3** involves the second ring-centered oxidation of the two linked PcRu(CO) groups. No clear re-reduction processes are observed on the reverse sweep (see dashed line in Figure 5-5), indicating that the third oxidation of **3** is followed by one or more chemical processes, and probable decomposition of the tetraruthenium compound.

As discussed above, the electrode processes of **3** can be assigned to either the diruthenium part of the triad or the π ring system of the two linked PcRu(CO) groups. However, the redox potentials at which these processes occur do not match exactly the corresponding processes observed for compounds **1** and **2**, thus suggesting some electronic communication between the diruthenium and PcRu(CO) units in **3**. Indeed, the $Ru_2^{6+/5+}$ process of compound **3** is expected to yield an increase in electron density on the dimetal unit, but this electron density is shifted towards the two PcRu(CO) groups, thus shifting negatively the $E_{1/2}$ value for the first electron addition to the π ring system of PcRu(CO) in

compound **3** as compared to reduction of PcRu(CO) in the unlinked phthalocyanine,i.e. -1.14 vs -1.10 (CH_2Cl_2) or -0.96 (pyridine).

Half-wave potentials for the ring-centered processes of PcRu(CO) **2** and *bis*-[PcRu(CO)][$Ru_2(ap)_4(C{\equiv}CC_5H_4N)_2$] **3** are summarized in Table 5-2. Here, we compare values in two different solvents but the choice of pyridine, instead of CH_2Cl_2, for the first reduction of PcRu(CO) is based on the fact that this compound exists as PcRu(CO)(py) in this solvent and that the Pc unit in **3** is also coordinated to the dimetal unit via the pyridine group. At the same time, the $Ru_2^{5+/4+}$ process of compound **3** (third reduction) becomes slightly positively shifted with respect to the same electrode process of compound **1** (-1.37 vs -1.41 V). Once a second electron is added to the diruthenium unit of **3** (the $Ru_2^{5+/4+}$ process), the electron density should again be shifted towards the PcRu(CO) part of the molecule, and make the second electron addition to PcRu(CO) much more difficult than for unlinked PcRu(CO). However, this is not the case because the last reduction of **3** ($E_{1/2}$ = -1.52 V) occurs at almost the same potential as the corresponding process of **2** ($E_{1/2}$ = -1.50 V) in pyridine, 0.1 M TBAP. It should be noted, however, that the peak for the fourth reduction of compound **3** is broad and not as well-defined as the second reduction of PcRu(CO) in pyridine, 0.1 M TBAP (see Figure 5-4c). This perhaps indicates that compound **3** partially dissociates upon addition of a second electron to the diruthenium unit (the $Ru_2^{5+/4+}$ process in Eq 5-2).

Table 5-2. Half-wave potentials (V vs SCE) involving the first reduction and first oxidation of the phthalocyanine macrocycle of PcRu(CO) **2** and *bis*-[PcRu(CO)][$Ru_2(ap)_4(C{\equiv}CC_5H_4N)_2$] **3**.

Compound	Solvent	$[PcRu(CO)]^{0/+}$	$[PcRu(CO)]^{0/-}$
PcRu(CO)	pyridine	0.86	-0.96
PcRu(CO)	CH_2Cl_2	0.59	-1.10
bis-[PcRu(CO)][$Ru_2(ap)_4(C{\equiv}CC_5H_4N)_2$]	CH_2Cl_2	0.74	-1.14

5.2.5 UV-visible Spectroscopy

The UV-visible spectra of **2** and **3** in CH_2Cl_2 are shown in Figure 5-6. PcRu(CO) **2** exhibits intense Q- and Soret bands at 651 and 296 nm, respectively. Both transitions are attributed to a $\pi \rightarrow \pi^*$ transition of the macrocycle. The Q- and Soret bands have side bands of lower intensity at 588 and 345 nm, respectively. An additional shoulder peak is also seen near 684 nm. As shown in Figure 5-6b, the insertion of the dimetal unit between the two PcRu(CO) rings does not yield significant changes in the UV-visible spectrum. The tetraruthenium complex **3** is characterized by Q- and Soret band absorptions at 648 and 302 nm, respectively as well as side bands of lower intensity at 587 and 347 nm. Noteworthy, the molar absorptivity of all the phthalocyanine bands in **3** is about twice that of the corresponding monomer **2**. There is also a small shoulder peak on the side of the 302 nm band and a small absorption band close to 400 nm (see * in Figure 5-6b). These features are attributed to the diruthenium unit. Indeed, $Ru_2(ap)_4(C{\equiv}CC_5H_4N)_2$ in CH_2Cl_2 exhibits an intense band around 300 nm and a small absorption feature at 407 nm (data not shown).

5.2.6 UV-visible Spectroelectrochemistry of *bis*-[PcRu(CO)][$Ru_2(ap)_4(C{\equiv}CC_5H_4N)_2$] 3

Figure 5-7a shows the UV-visible spectral changes obtained upon reduction of **3** in CH_2Cl_2, 0.1 M TBAP while Figure 5-7b illustrates the UV-visible spectral changes upon oxidation of **3** under the same solution conditions. During the first reduction, there are no significant spectral changes, consistent with the redox process involving the diruthenium unit of the compound. Upon oxidation of **3**, the four bands of the compound (at 347, 587, 623 and 648 nm) decrease in intensity with the loss of intensity being more significant for the 648 nm band. At the same time, two new bands also appear at 545 and 718 nm. The Q-band at (648 nm) has been attributed to a $\pi \rightarrow \pi^*$ transition of the macrocycle,[39] and a significant change

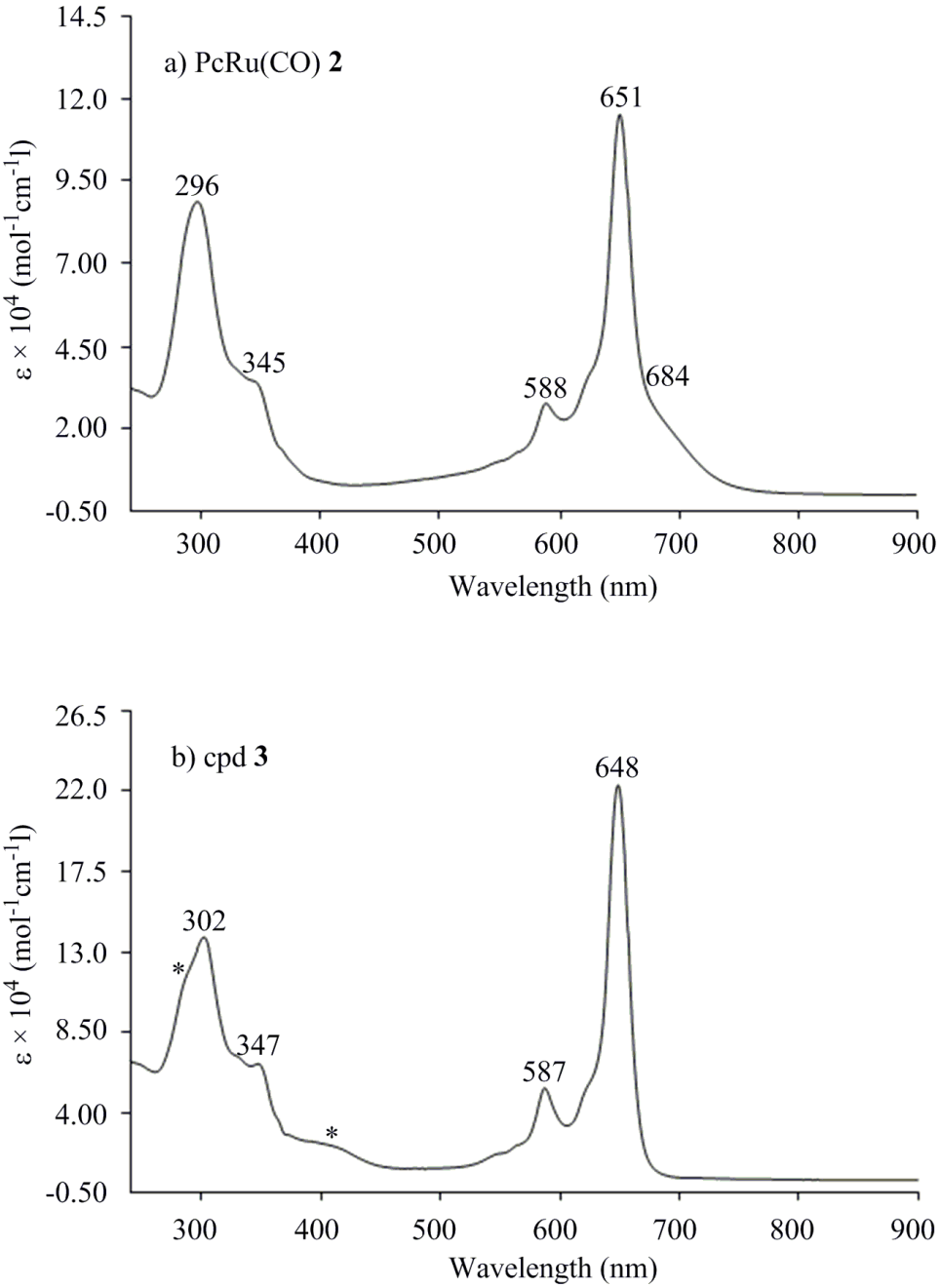

Figure 5-6. UV-visible spectra of a) PcRu(CO) **2** and b) *bis*-[PcRu(CO)][$Ru_2(ap)_4(C{\equiv}CC_5H_4N)_2$] **3** in CH_2Cl_2.

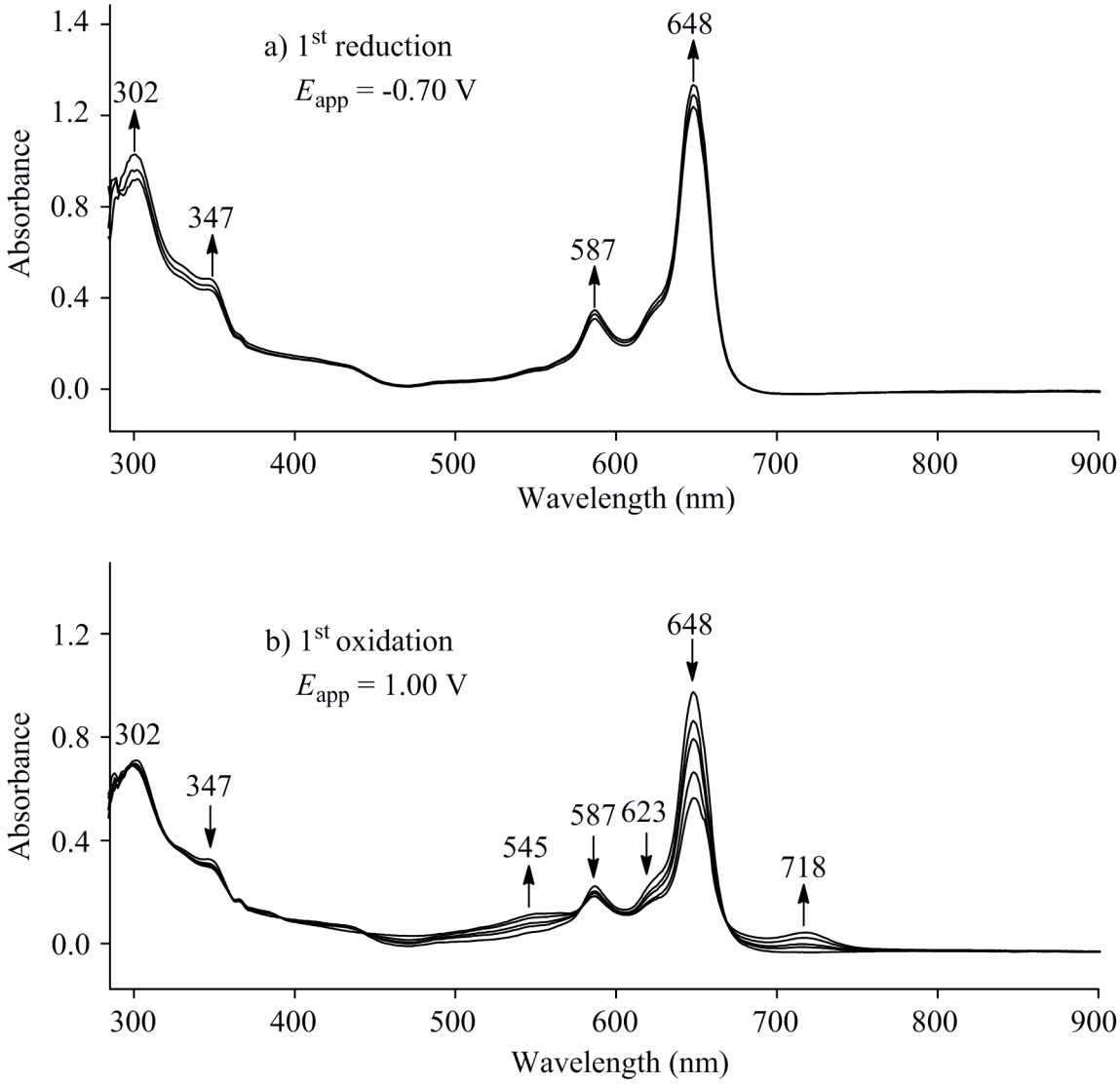

Figure 5-7. UV-visible spectral changes during a) the first reduction and b) the first oxidation of *bis*-[PcRu(CO)][$Ru_2(ap)_4(C{\equiv}CC_5H_4N)_2$] **3** in CH_2Cl_2 containing 0.1 M TBAP.

in intensity of this absorption band is consistent with the first oxidation of **3** involving the macrocycles of the two linked PcRu(CO). A third electron is abstracted from the $Ru_2(ap)_4(C{\equiv}CC_5H_4N)_2$ group at the same potential but the UV-visible spectral changes for this process are minimal when compared to the changes associated with oxidation of the phthalocyanine macrocycle.

5.2.7 Infrared Spectra of *bis*-[PcRu(CO)][$Ru_2(ap)_4(C{\equiv}CC_5H_4N)_2$] 3

Table 3 summarizes ν_{CO} bands in CH_2Cl_2 solution containing 0.1 M TBAP for the neutral, singly reduced and singly oxidized *bis*-[PcRu(CO)][$Ru_2(ap)_4(C{\equiv}CC_5H_4N)_2$] **3**. The shift in ν_{CO} from the neutral to the singly oxidized complex **3** is 30 cm^{-1} which is comparable to the difference in the CO vibration between Ru(TPP)(CO)(py) (1943 cm^{-1}) and $[Ru(TPP)(CO)(py)]^+$ (1970 cm^{-1}) under the same experiment conditions where the oxidation occurs at the porphyrin π ring system.[45] This is also the case for *bis*-[PcRu(CO)][$Ru_2(ap)_4(C{\equiv}CC_5H_4N)_2$] **3** and consistent with electrochemical and spectroscopic data that the first oxidation involves a loss of an electron on the ruthenium phthalocyanine unit of **3**. However, the CO vibration is only shifted by 8 cm^{-1} upon the reduction. This observation can be accounted for by the fact that the first reduction occurs at the diruthenium part of **3** as discussed earlier in the thesis thus the increase in negative charge on **3** would not have significant effect on the CO vibration.

5.3 Summary

A tetra-metallic complex *bis*-[PcRu(CO)][$Ru_2(ap)_4(C{\equiv}CC_5H_4N)_2$] **3** was synthesized by linking two phthalocyanines to the axial coordination sites of the diruthenium unit. This complex was quite stable and could be isolated and purified by gel permeation chromatography. The combination of IR and UV-visible spectroscopy along with cyclic

voltammetry was used to study and elucidate the electron-transfer processes of **3**. Electrochemical and spectroscopic data show a weak interaction within the subunits.

Table 5-3. ν_{CO} values (cm^{-1}) for neutral, singly reduced and singly oxidized *bis*-[PcRu(CO)][$Ru_2(ap)_4(C{\equiv}CC_5H_4N)_2$ **3** in CH_2Cl_2 containing 0.1 M TBAP.

Singly oxidized [**3**]$^{+a}$	Neutral [**3**]	Singly reduced [**3**]$^{-b}$
2006	1976	1968

[a] oxidation occurs at both the dimetal and PcRu(CO) units.
[b] reduction occurs at the dimetal unit.

5.4 References

1. Xu, G.-L.; Zou, G.; Ni, Y.-H.; DeRosa, M. C.; Crutchley, R. J.; Ren, T. *J. Am. Chem. Soc.* **2003**, *125*, 10057-10065.
2. Shi, Y.; Yee, G. T.; Wang, G.; Ren, T. *J. Am. Chem. Soc.* **2004**, *126*, 10552-10553.
3. Xu, G.-L.; DeRosa, M. C.; Crutchley, R. J.; Ren, T. *J. Am. Chem. Soc.* **2004**, *126*, 3728-3729.
4. Szuchmacher, B. A.; Ren, T.; Parish, D. A.; Trammell, S. A.; Moore, M. H.; Kushmerick, J. G.; Xu, G.-L.; Deschamps, J. R.; Pollack, S. K.; Shashidhar, R. *J. Am. Chem. Soc.* **2005**, *127*, 10010-10011.
5. Xu, G.-L.; Crutchley, R. J.; DeRosa, M. C.; Pan, Q.-J.; Zhang, H.-X.; Wang, X.; Ren, T. *J. Am. Chem. Soc.* **2005**, *127*, 13354-13363.
6. Wang, C.-F.; Zuo, J. L.; Ying, J.-W.; Ren, T.; You, X.-Z. *Inorg. Chem.* **2008**, *47*, 9716-9722.
7. Kosaka, W.; Yamamoto, N.; Miyasaka, H. *Inorg. Chem.* **2013**, *52*, 9908-9914.
8. Zhang, L.; Xi, B.; Po-Chun, L. I.; Choudhuri, M. M. R.; Crutchley, R. J.; Updegraff, J. B.; Protasiewicz, J. D.; Ren, T. *Inorg. Chem.* **2009**, *48*, 5187-5194.
9. Cai, X.-M.; Zhang, X.-Y.; Savchenko, J.; Cao, Z.; Ren, T.; Zuo, J.-L. *Organometallics* **2012**, *31*, 8591-8597.
10. Cummings, S. P.; Savchenko, J.; Fanwick, P. E.; Kharlamova, A.; Ren, T. *Organometallics* **2013**, *32*, 1129-1132.
11. Boyd, D. A.; Cao, Z.; Song, Y.; Wang, T.-W.; Fanwick, P. E.; Crutchley, R. J.; Ren, T. *Inorg. Chem.* **2010**, *49*, 11525-11531.

12. Boyd, D. A.; Crutchley, R. J.; Fanwicka, P. E.; Ren, T. *Inorg. Chem.* **2010**, *49*, 1322-1324.

13. Ren, T. *Organometallics* **2005**, *24*, 4854-4870.

14. Xi, B.; Ren, T. *C. R. Chimie* **2009**, *12*, 321-331.

15. Cummings, S. P.; Cao, Z.; Fanwick, P. E.; Kharlamova, A.; Ren, T. *Inorg. Chem.* **2012**, *51*, 7561-7568.

16. Bear, J. L.; Han, B.; Huang, S.; Kadish, K. M. *Inorg. Chem.* **1996**, *35*, 3012-21.

17. Bear, J. L.; Han, B.; Wu, Z.; Van Caemelbecke, E.; Kadish, K. M. *Inorg. Chem.* **2001**, *40*, 2275-2281.

18. Kadish, K. M.; Wang, L.-L.; Thuriere, A.; Giribabu, L.; Garcia, R.; Van Caemelbecke, E.; Bear, J. L. *Inorg. Chem.* **2003**, *42*, 8309-8319.

19. Kadish, K. M.; Phan, T. D.; Wang, L.-L.; Giribabu, L.; Thuriere, A.; Wellhoff, J.; Huang, S.; Van Caemelbecke, E.; Bear, J. L. *Inorg. Chem.* **2004**, *43*, 4825-4832.

20. Nguyen, M.; Phan, T.; Van Caemelbecke, E.; Kajonkijya, W.; Bear, J. L.; Kadish, K. M. *Inorg. Chem.* **2008**, *47*, 7775-7783.

21. Zuo, J.-L.; Herdtweck, E.; Kuehn, F. E. *J. Chem. Soc., Dalton Trans.* **2002**, 1244-1246.

22. *The Porphyrin Handbook*; Kadish, K. M.; Smith, K. M.; Guilard, R., Eds.; Academic Press: San Diego, CA, **2003**; Vol. 15-20.

23. Rio, Y.; Rodriguez-Morgade, M. S.; Torres, T. *Org. Biomol. Chem.* **2008**, *6*, 1877-1894.

24. Nemykin, V. N.; Lukyanets, E. A. In *Handbook of Porphyrin Science*; Kadish, K. M., Smith, K. M., Guilard, R., Eds.; World Scientific Publishing Co. Pte. Ltd.: Singapore, **2010**; Vol. 3, p 1-323.

25. Li, R.; Zhang, X.; Zhu, P.; Ng, D. K. P.; Kobayashi, N.; Jiang, J. *Inorg. Chem.* **2006**, *45*, 2327-2334.

26. Walter, M. G.; Rudine, A. B.; Wamser, C. C. *J. Porphyrins Phthalocyanines* **2010**, *14*, 759-792.

27. Sergeeva, N. N.; Senge, M. O. In *CRC Handbook of Organic Photochemistry and Photobiology (3rd Edition)*Griesbeck, A., Oelgemöller, M., Ghetti, F., Eds.; CRC Press: Boca Raton, FL, **2012**; Vol. 1, p 831-879.

28. Ragoussi, M.-E.; Ince, M.; Torres, T. *Eur. J. Org. Chem.* **2013**, *2013*, 6475-6489.

29. Trogler, W. C. *Struct. Bonding (Berlin, Ger.)* **2012**, *142*, 91-118.

30. Satake, A.; Kobuke, Y. *Org. Biomol. Chem.* **2007**, *5*, 1679-1691.

31. Ohkubo, K.; Fukuzumi, S. *J. Porphyrins Phthalocyanines* **2008**, *12*, 993-1004.

32. Bottari, G.; de la Torre, G.; Guldi, D. M.; Torres, T. *Chem. Rev.* **2010**, *110*, 6768-6816.

33. Bottari, G.; Trukhina, O.; Ince, M.; Torres, T. *Coord. Chem. Rev.* **2012**, *256*, 2453-2477.

34. Rodriguez-Morgade, M. S.; Torres, T.; Atienza-Castellanos, C.; Guldi, D. M. *J. Am. Chem. Soc.* **2006**, *128*, 15145-15154.

35. Spaenig, F.; Lopez-Duarte, I.; Fischer, M. K. R.; Martinez-Diaz, M. V.; Baeuerle, P.; Torres, T.; Guldi, D. M. *J. Mater. Chem.* **2011**, *21*, 1395-1403.

36. Jacobs, R.; Stranius, K.; Maligaspe, E.; Lemmetyinen, H.; Tkachenko, N. V.; Zandler, M. E.; D'Souza, F. *Inorg. Chem.* **2012**, *51*, 3656-3665.

37. Webb, S. J.; Sanders, J. K. M. *Inorg. Chem.* **2000**, *39*, 5912-5919.

38. Mak, C. C.; Bampos, N.; Darling, S. L.; Montalti, M.; Prodi, L.; Sanders, J. K. M. *J. Org. Chem.* **2001**, *66*, 4476-4486.

39. Rawling, T.; McDonagh, A. *Coord. Chem. Rev.* **2007**, *251*, 1128-1157.

40. Rodriguez-Morgade, M. S.; Plonska-Brzezinska, M. E.; Athans, A. J.; Carbonell, E.; de Miguel, G.; Guldi, D. M.; Echegoyen, L.; Torres, T. *J. Am. Chem. Soc.* **2009**, *131*, 10484-10496.

41. Jimenez, A. J.; Grimm, B.; Gunderson, V. L.; Vagnini, M. T.; Krick, C. S.; Rodriguez-Morgade, M. S.; Wasielewski, M. R.; Guldi, D. M.; Torres, T. *Chem. - Eur. J.* **2011**, *17*, 5024-5032, S5024/1-S5024/9.

42. Manowong, M.; Van Caemelbecke, E.; Rodríguez-Morgade, M. S.; Bear, J. L.; Kadish, K. M.; Torres, T. *J. Porphyrins and Phthalocyanines* **2014**, *18*, 1-9.

43. McDonagh, A. M.; Deeble, G.; Hurst, S.; Chifuentes, M. P.; Humphrey, M. G. *J. Chem. Educ.* **2001**, *78*, 232-234.

44. Rawling, T.; McDonagh, A. M.; Colbran, S. B. *Inorg. Chim. Acta* **2008**, *361*, 49-55.

45. Brown, G. M.; Hopf, F. R.; Ferguson, J. A.; Meyer, T. J.; Whitten, D. G. *J. Amer. Chem. Soc.* **1973**, *95*, 5939-42.

CHAPTER SIX

The Effect of Axial Ligands on the Spectroscopic and Electrochemical Properties of a Diruthenium Compound

6.1 Introduction

The structural, electrochemical, and spectroscopic properties of numerous diruthenium complexes with a Ru_2^{5+} core and a paddle-wheel structure have been reported in the literature[1-27] since the first synthesis and physical characterization of $Ru_2(OAc)_4Cl$ (OAc = acetate anion) by Stephenson and Wilkinson in 1966.[28] The majority of investigated Ru_2^{5+} complexes have contained an axially bound chloride anion and are formulated in their neutral form as Ru_2L_4Cl or $Ru_2(OAc)_x(L)_{4-x}Cl$ (x = 1-4), where L is a symmetrical or unsymmetrical anionic bridging ligand.[1,6,8,16,18,19,21,24-26,29,30]

Four redox reactions are generally observed for these types of diruthenium compounds in nonaqueous solvents such as CH_2Cl_2, benzonitrile (PhCN), or acetonitrile (CH_3CN). The electrode reactions are almost always reversible and correspond to one-electron additions or one-electron abstractions at the dimetal unit as described in Eqs 1-4.

$$Ru_2^{5+} + e^- \rightleftarrows Ru^{4+} \quad (6\text{-}1)$$

$$Ru_2^{4+} + e^- \rightleftarrows Ru^{3+} \quad (6\text{-}2)$$

$$Ru_2^{5+} \rightleftarrows Ru^{6+} + e^- \quad (6\text{-}3)$$

$$Ru_2^{6+} \rightleftarrows Ru^{7+} + e^- \quad (6\text{-}4)$$

The $E_{1/2}$ values for reduction and oxidation of the diruthenium unit will depend upon the type and number of anionic bridging ligands as well as upon the type and number of axial ligands which could be anionic or neutral. For example, the $E_{1/2}$ for reduction of $Ru_2(F_5ap)_4Cl$ in CH_2Cl_2 was reported as -0.35 V,[23] where F_5ap = 2-(2,3,4,5,6-pentafluoroanilino)pyridinate anion, while $Ru_2(ap)_4Cl$ is reduced at -0.87 V vs SCE[17] under the same solution conditions, a difference of more than 500 mV with changes in substituents on the ap bridging ligands (where ap = 2-anilinopyridinate anion). Likewise, the $E_{1/2}$ for

reduction of $Ru_2(ap)_4CN$ is located at -0.73 V, while $[Ru_2(ap)_4(CN)_2]^-$ is reduced at -1.24 V in the same solvent,[31] again a difference of more than 500 mV in $E_{1/2}$ for the $Ru^{5+/4+}$ process with change of axial ligands.

Changes in the type of axial ligand, while maintaining the same number and type of bridging ligands, will affect not only the redox potentials as described above, but may also lead in some cases to a change in electronic configuration and/or chemical reactivity of the diruthenium complexes in their various dimetal oxidation[13,32,33] states. Indeed, $Ru_2(dpf)_3(OAc)(BF_4)$, where dpf = *N*,*N*′-diphenylformamidinate anion, was shown to exist as a quantum admixture of spins, whereas $Ru_2(dpf)_3(OAc)Cl$, which contains axially bound Cl^- instead of BF_4^- as the counterion, exists only in an S =1 spin state.[13] The reaction of CO with $Ru_2(dpf)_3(OAc)(BF_4)$ was shown to afford the mono-CO adduct, $[Ru_2(dpf)_3(OAc)(CO)]^+$ after replacement of BF_4^- by CO, whereas no reaction at all is seen between $Ru_2(dpf)_3(OAc)Cl$ and carbon monoxide which does not bind to the Ru_2^{5+} form of the compound.[32]

In earlier studies from our laboratory we have reported how systematic changes in the bridging ligands would affect redox potentials of the dimetal unit,[8,17,34] and we have now turned our attention to systematically investigating the effect of neutral and anionic axial ligands on the redox potentials of a series of Ru_2^{5+} compounds with the same four anionic bridging ligands. The investigated diruthenium compounds are represented as $Ru_2(dpb)_4X$, $[Ru_2(dpb)_4X_2]^-$ and $[Ru_2(dpb)_4]^+$ (dpb = diphenylbenzamidinate anion), where X is a neutral or negatively charged axial ligand or a solvent molecule.[35] The redox reactions given by Eqs 6-1 to 6-4 were examined in CH_2Cl_2 and PhCN containing a variety of added anions, and the

products of each electron addition or electron abstraction were characterized by cyclic voltammetry combined with thin-layer UV-visible and IR spectroelectrochemistry.

6.2 Results and Discussion

6.2.1 Synthesis

$Ru_2(dpb)_4Cl$ (**1**) was synthesized by reaction of $Ru_2(OAc)_4Cl$ with molten dpb bridging ligand. Subsequent recrystallization in CH_2Cl_2 yielded the pure complex **1**.

The electrosynthesis of $Ru_2(dpf)_4(CO)$ under a CO atmosphere was first reported by Bear and Kadish[36] and a few years later, the chemical synthesis of $[Ru_2(dpf)_3(OAc)(CO)]BF_4$ was reported by Barral et. al.[32] In the present study, $Ru_2(dpb)_4(CO)$ (**2**) was prepared by reduction of $Ru_2(dpb)_4Cl$ using $NaBH_4$ and CH_2Cl_2 as solvent. CO gas was then passed through the solution to yield **2** which was purified by recrystallization in a hexane/acetone solvent mixture.

$Ru_2(dpb)_4(NO)$ (**3**) was synthesized by a chemical reaction of deaerated $Ru_2(dpb)_4Cl$ in CH_2Cl_2 saturated with nitric oxide; the excess NO was then removed by purging with nitrogen. Subsequent purification by recrystallization yielded pure samples of $Ru_2(dpb)_4(NO)$ (**3**).

The molecular structures of **2** and **3** are shown in Figure 6-1, whereas the crystallographic data are tabulated in Table 6-1 and selected metric parameters are listed in Table 6-2. In both complexes as well as in $Ru_2(dpf)_4(NO)$, atom Ru1 is in a distorted octahedral environment ligating to four N atoms in the equatorial plane, to the second Ru atom in one apical position and to a C or N atom in the other. The coordination environment of atom Ru2 is distorted octahedral with one vacant apical position, rendering this metal

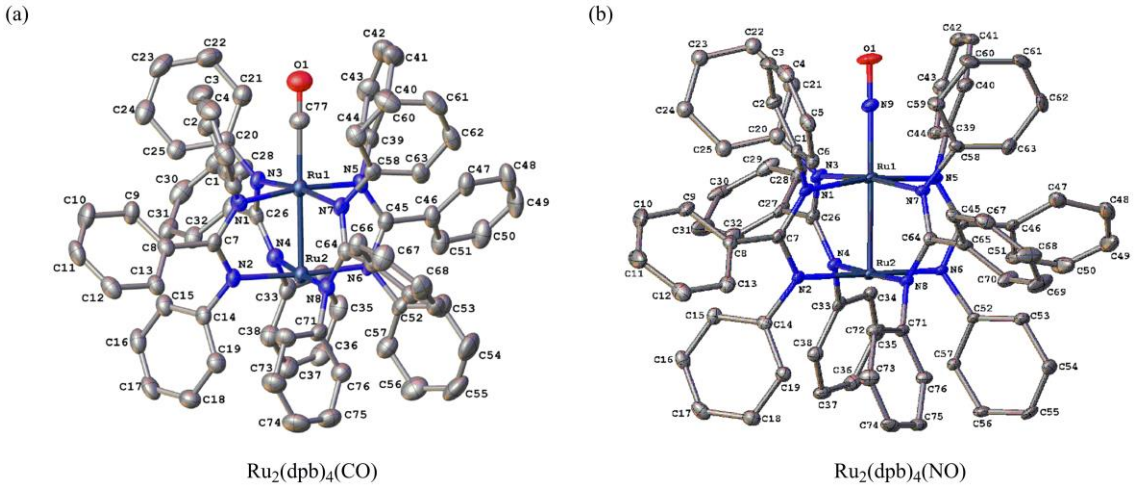

Figure 6-1. Molecular structures of (a) $Ru_2(dpb)_4(CO)$ **2-A** and (b) $Ru_2(dpb)_4(NO)$ **3**. The H atoms have been omitted for clarity (taken from ref 35).

Table 6-1. Crystal Data and Data Collection and Processing Parameters for Compounds **2** and **3** (data taken from ref 35).

Compounds	$Ru_2(dpb)_4(CO)$ (**2**)	$Ru_2(dpb)_4(NO)$ (**3**)
mol formula	$C_{77}H_{60}N_8ORu_2$	$C_{78}H_{64}Cl_4N_9ORu_2$[a]
Space group	$P\bar{4}c2$	$P2_1/n$
cell constant		
a (Å)	24.540(8)	13.9376(17)
b (Å)	24.540(8)	26.624(3)
c (Å)	40.500(13)	19.344(2)
α (deg)	90	90
β (deg)	90	91.940(2)
γ (deg)	90	90
V (Å ^{3})	24389(14)	7173.7(15)
Z	13.63	4
ρ_{calcd} (Mg/m^3)	1.221	1.377
μ (mm^{-1})	3.779	0.621
λ(Cu Kα) (Å)	1.54178	1.54178
temp (K)	100 (1)	100 (1)
R (F_o)[b]	0.0457	0.0726
Rw (F_o)[c]	0.0414	0.0498

[a] with unidentified solvent. [b] $R = \sum ||F_o| - |F_c||/\sum|F_o|$. [c] $R_w = [\sum_w(|F_o| - |F_c|)^2/\sum_w|F_o|^2]^{1/2}$.

Table 6-2. Selected Bond Lengths (Å) and Bond Angles (deg) of Compound **2** and **3** along with those of $Ru_2(dpf)_4(CO)$ and $Ru_2(dpf)_4(NO)$ (data taken from ref 35).

	$Ru_2(dpb)_4(CO)$ (**2**)	$Ru_2(dpb)_4(NO)$ (**3**)	$Ru_2(dpf)_4(CO)$[c]	$Ru_2(dpf)_4(NO)$[d]
Ru-Ru	2.4789(8)	2.4119(5)	2.5544(8)	2.444(13)
Ru1-N_L[a]	2.074(14)[b]	2.08(2)	2.069(3)	2.065
Ru2-N_L[a]	2.027(8)[b]	2.017(19)[b]	2.028(3)	2.024
Ru-L_{ax}[a]	1.939(4)	1.824(4)	1.913(10)	1.809(11)
Y-O[a]	1.117(5)	1.166(5)	1.148(11)	1.142(12)
Ru-Ru-L_{ax}	179.35(12)	179.29(12)	180.00	180.00
Ru-Y-O	178.4(4)	178.5(4)	180.00	180.00
d(Ru1/N4)[b]	0.154(2)	0.1484(17)	0.177	0.166
d(Ru2/N4)[b]	-0.069(2)	-0.0144(16)	-0.068	-0.027

[a] Nitrogen of the bridging ligand (N_L), L = dpb or dpf. L_{ax} = axial ligand (CO or NO), Y = C or N
[b] Average values. d(Ru/N4)-displacement of the Ru atom from the plane defined by the 4 coordinated nitrogen atoms. [c] Ref 36. [d] Ref 41.

center five-coordinate. The Ru–Ru bond distances in **2** and **3** measure 2.4789(8) and 2.4119(5) Å. These bonds are shorter than the Ru–Ru bond distances in the corresponding dpf complexes. This trend is consistent with the fact that metal-metal bond distances in diruthenium complexes usually greatly depend on the type of equatorial ligands. The Ru–Ru bond lengths of all complexes in Table 6-2 are within the expected ranges of Ru–Ru bond distances in diruthenium complexes. In addition, the Ru–CO bond distances are appreciably longer than the Ru–NO bond lengths and the change in Ru-L_{ax} (L_{ax} = CO or NO) bond distance is larger for the dpf complex. The Ru-Ru-L_{ax} bond angles of diruthenium complexes in Table 6-2 are all close to 180°. The bond angles are slightly different from each other for the dpb complexes with values of 178.4° or 178.5°, but are identical to each other for the dpf complexes with a value of 180°.

All Ru-N distances are typical. In all three compounds atom Ru2 is displaced from the plane defined by the four coordinated N atoms toward the CO or NO ligand by ~0.15 Å, whereas atom Ru2 is displaced in the opposite direction from its equatorial plane to a smaller extent (<0.07 Å). The coordination and geometry of the dpb ligand in **2**, **3**, and the dpf ligand in $Ru_2(dpf)_4(NO)$ are instructive to examine. The Ph rings on the N atom coordinated to Ru1 should form a much larger dihedral angle with the NCN chelating plane of the ligand than the Ph rings on the N atoms bonded to Ru2 in order to accommodate the carbonyl or nitrosyl ligands on one side of the complex and to compensate the absence of an apical ligand on the other. The respective angles for **2**, **3** and $Ru_2(dpf)_4(NO)$ span 76(3)°, 75(3)° and 78.1° at the Ru1 site and 68(5)°, 65(4)°, and 45.2° at the Ru2 end. The pairwise differences in the angle values in the same complexes are not statistically significant for **2**, probably statistically significant for **3**, and statistically significant for $Ru_2(dpf)_4(NO)$. Values closer to 90° are

observed when the Ph ring must accommodate an additional ligand, and closer to 45° when the sixth ligand is absent. The magnitude of the angles may probably serve as indicators for the possible presence of carbonyl, nitrosyl, or monoatomic ligands in the case of positional disorder (and partial occupancy) of these ligands. The idealized paddlewheel geometries of the complexes (C_{4v} or 4mm symmetry) are not observed because the chelating NCN planes of the dpb and dpf ligands are not coplanar with atoms Ru1 and Ru2. Thus, the paddlewheel assembly is replaced with a near C_4 (or 4 symmetry) propeller-like arrangement of the ligands about the Ru-Ru four-fold axis. All ligands are tilted in the same direction relative to the Ru-Ru bond. The average N-Ru1-Ru2-N torsion angles in these three compounds are 13.9(5)°, 13.2(6)°, and 14.7°, illustrating consistent tilts of the "propeller blades".

6.2.2 UV-visible Spectroscopy of $Ru_2(dpb)_4Cl$ in CH_2Cl_2 and PhCN

The UV-visible spectrum of $Ru_2(dpb)_4Cl$ in neat CH_2Cl_2 is shown in Figure 6-2a while spectra of the same compound in CH_2Cl_2 solutions containing 0.1 M TBAX where X = ClO_4, Cl^- or F^- are displayed in Figures 6-2b, 6-2c, and 6-2d, respectively. Three different UV-visible spectral patterns are observed in Figures 6-2b, 6-2c, and 6-2d, thus suggesting that each solution contains a different coordinated form of the diruthenium complex.

The spectrum in neat CH_2Cl_2 (Figure 6-2a) exhibits a 778 nm band also seen in the solution containing 0.1 M $TBAClO_4$ (Figure 6-2b) and a 715 nm band which is seen in the solution containing 0.1 M TBACl (Figure 6-2c). This suggests that the Ru_2^{5+} complex in neat CH_2Cl_2 (Figure 6-2a) exists as a mixture of two forms, $Ru_2(dpb)_4Cl$ and $[Ru_2(dpb)_4]^+$. The spectrum in Figure 6-2c has a strong 715 nm band which suggests that $Ru_2(dpb)_4Cl$ is the most likely form of the diruthenium compound in CH_2Cl_2 containing 0.1 M TBACl while

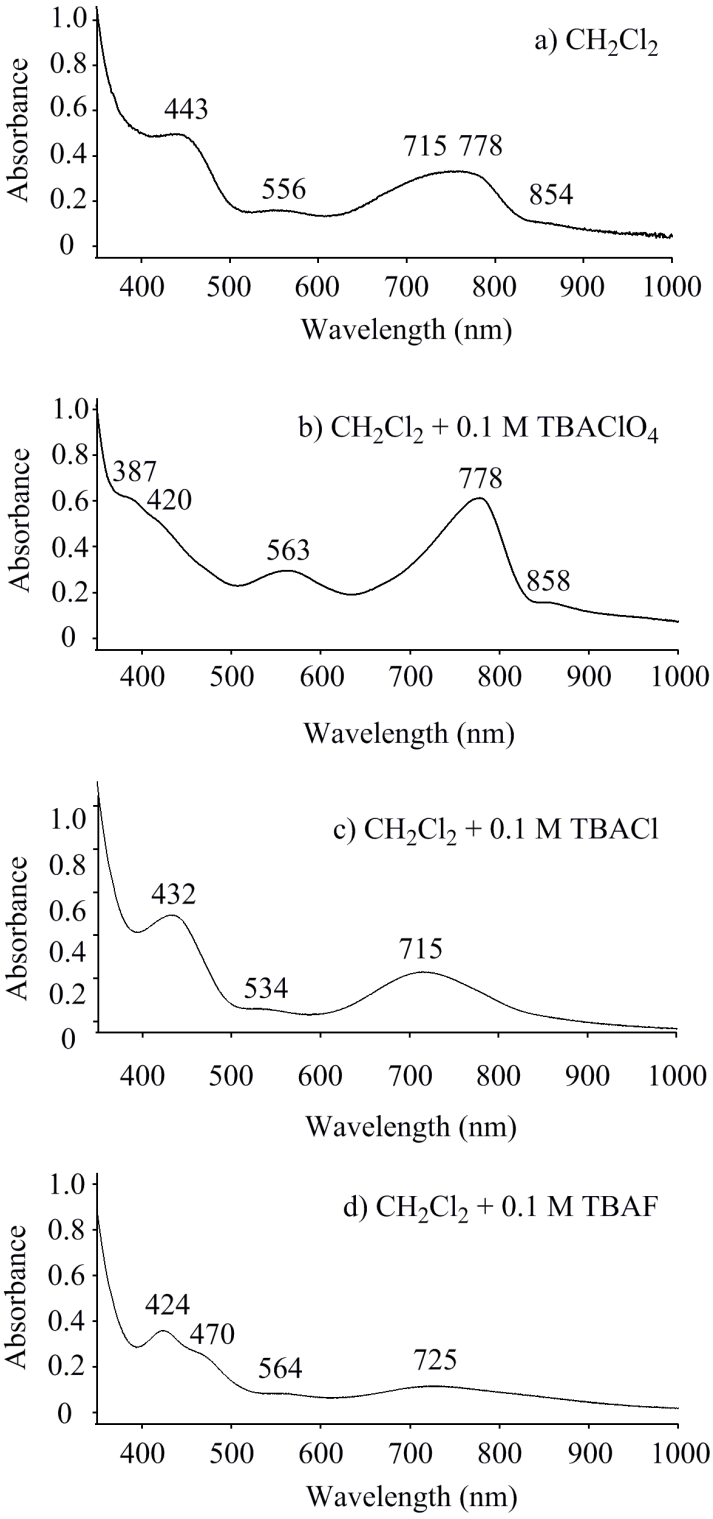

Figure 6-2. UV-visible spectra of 1.0×10^{-4} M $Ru_2(dpb)_4Cl$ in a) neat CH_2Cl_2 and in CH_2Cl_2 containing 0.1 M TBAX where X is b) ClO_4^-, c) Cl^- and d) F^-.

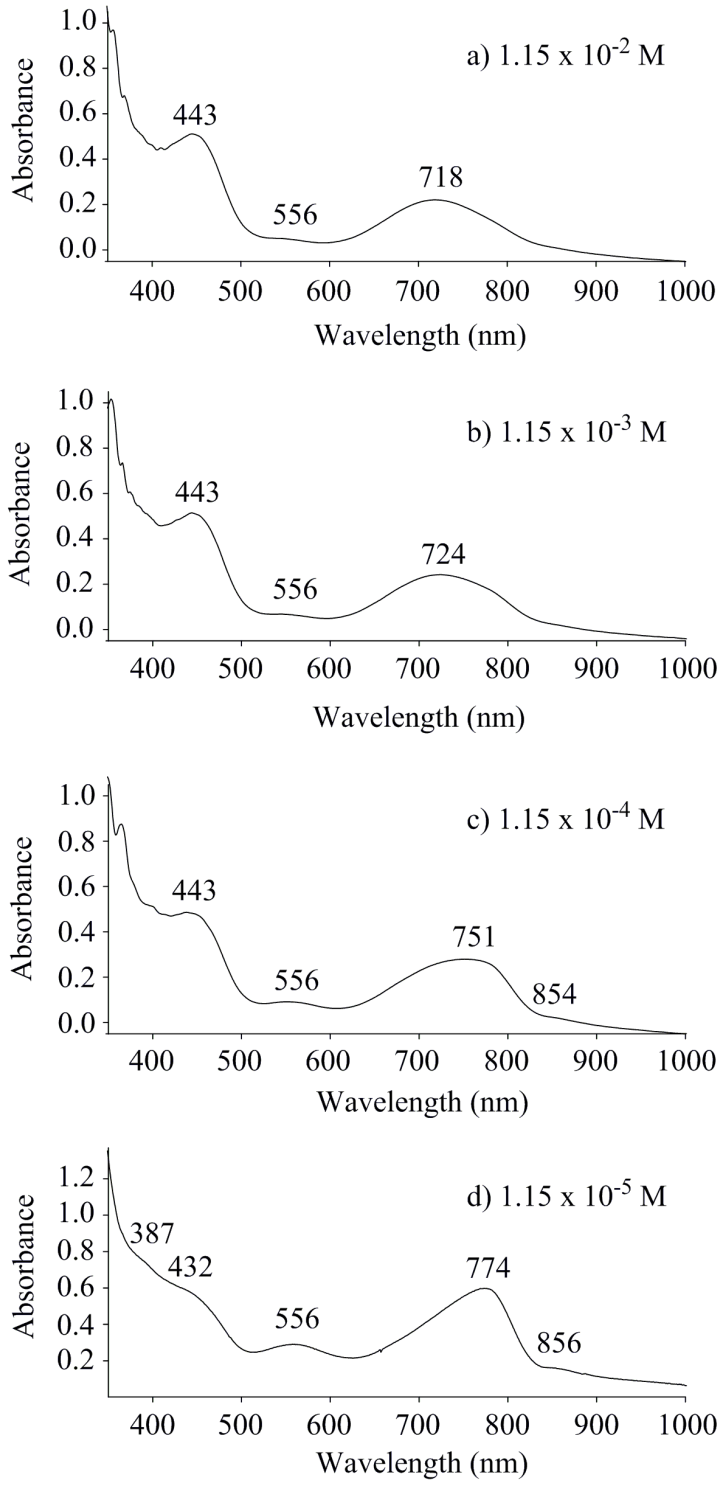

Figure 6-3. UV-visible spectra of $Ru_2(dpb)_4Cl$ in neat CH_2Cl_2 at various concentrations a) 1.15×10^{-2} M, b) 1.15×10^{-3} M, c) 1.15×10^{-4} M and d) 1.15×10^{-5} M.

the spectrum in Figure 6-2b has a strong 778 nm band indicating that $[Ru_2(dpb)_4]^+$ is the most likely form of the diruthenium compound in CH_2Cl_2 containing 0.1 M $TBAClO_4$.

The data in Figure 6-2 suggest the presence of an equilibrium involving $Ru_2(dpb)_4Cl$ and $[Ru_2(dpb)_4]^+$ in neat CH_2Cl_2 (Eq 6-5), and this was confirmed by monitoring the UV-visible spectra of $Ru_2(dpb)_4Cl$ at four different concentrations in CH_2Cl_2 where the cell path lengths were varied from 0.01 to 10 cm as the diruthenium concentration was decreased. These results are shown in Figure 6-3.

$$Ru_2(dpb)_4Cl \quad \rightleftarrows \quad [Ru_2(dpb)_4]^+ + Cl^- \qquad (6\text{-}5)$$

According to Eq 6-5, a higher concentration of $Ru_2(dpb)_4Cl$ in CH_2Cl_2 should favor the chloride associated form of the complex, whereas a lower concentration of the diruthenium compound should favor a dissociation of the chloride ion from the Ru_2^{5+} unit. This is indeed what is observed in Figure 6-3. The UV-visible spectrum of 1.15×10^{-2} M $Ru_2(dpb)_4Cl$ (Figure 6-3a) resembles the UV-visible spectrum in Figure 6-2c where the compound is proposed to exist as $Ru_2(dpb)_4Cl$ in solution, whereas the UV-visible spectrum of 1.15×10^{-5} M $Ru_2(dpb)_4Cl$ in CH_2Cl_2 (Figure 6-3d) has bands at 556, 774, and 856 nm and resembles the UV-visible spectrum in Figure 6-2b (λ_{max} = 563, 778, and 858 nm) where the diruthenium complex is proposed to exist as $[Ru_2(dpb)_4]^+$ in solution.

As seen in Figure 6-2d, the spectrum in CH_2Cl_2 containing 0.1 M TBAF exhibits an absorption band at 470 nm, a spectral feature not found in the other UV-visible spectra depicted in Figures 6-2a, 6-2b, or 6-2c. Hence, the observation of a 470 nm band would suggest the presence of $Ru_2(dpb)_4F$ and/or possibly $[Ru_2(dpb)_4F_2]^-$ in solution. However, the 470 nm band is not seen in the UV-visible spectrum of $Ru_2(dpb)_4F$, a compound *in situ*

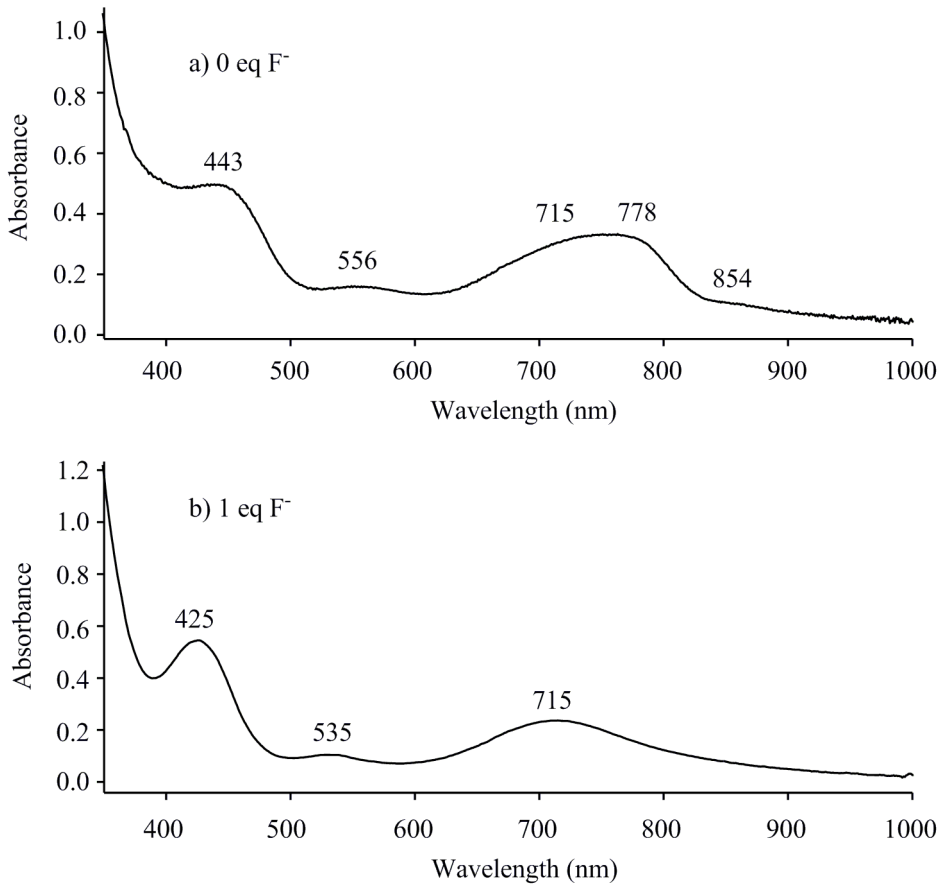

Figure 6-4. UV-visible spectra of 1.0×10^{-4} M $Ru_2(dpb)_4Cl$ in CH_2Cl_2 with a) 0 eq F^- and b) 1 eq F^-.

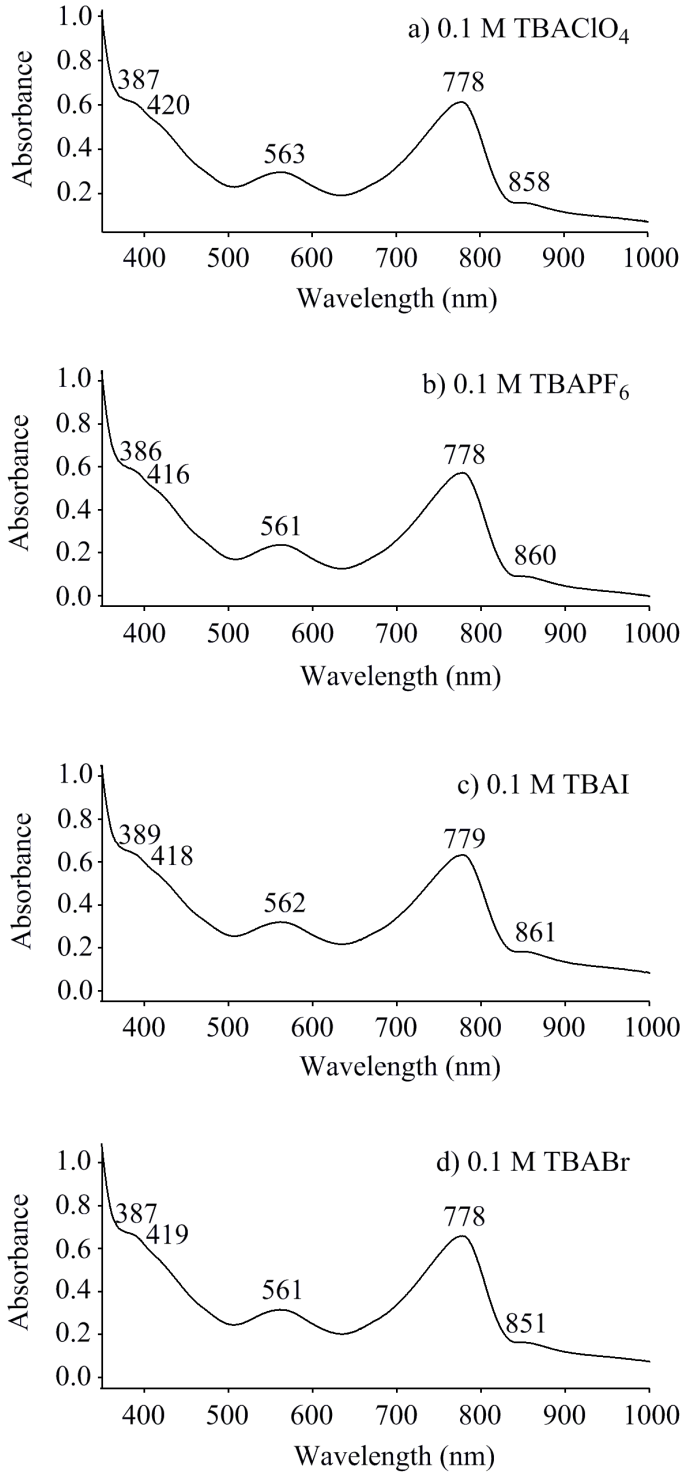

Figure 6-5. UV-visible spectra of $Ru_2(dpb)_4Cl$ (1.0×10^{-4} M) in CH_2Cl_2 containing 0.1 M TBAX where X is a) ClO_4^-, b) PF_6^-, c) I^-, and d) Br^-.

generated by adding 1 eq of F^- to a CH_2Cl_2 solution of $Ru_2(dpb)_4Cl$ (see Figure 6-4). Hence, this absorption band in Figure 6-2d is most likely attributed to the bis-fluoride adduct $[Ru_2(dpb)_4F_2]^-$.

The UV-visible spectrum of $Ru_2(dpb)_4Cl$ in CH_2Cl_2 containing 0.1 M $TBAClO_4$ (Figure 6-5a) has the same spectral features as the spectra in Figures 6-5b, 6-5c, and 6-5d, and this strongly suggests a dissociation of Cl^- from $Ru_2(dpb)_4Cl$ when excess PF_6^-, I^-, or Br^- is present in CH_2Cl_2. Hence, the spectroscopically detectable species in CH_2Cl_2 solutions with these anions is proposed to be the cationic species $[Ru_2(dpb)_4]^+$.

Figure 6-6 compares the UV-visible spectrum of $Ru_2(dpb)_4Cl$ in neat PhCN (—) with the spectrum in neat CH_2Cl_2 (- - -). In both solvents multiple bands are seen between 400 and 900 nm with the major differences being in the intensity and positions of the absorptions between 400 and 600 nm. For example, a relatively intense 559 nm band occurs in PhCN as compared to a weak 556 nm band in CH_2Cl_2. In addition, the first absorption band in CH_2Cl_2 appears at 443 nm as compared to 424 nm in PhCN. These spectral differences suggest a possible coordination of PhCN to the diruthenium unit in PhCN and this was confirmed by a spectrally monitored titration of $Ru_2(dpb)_4Cl$ in CH_2Cl_2 with PhCN (Figure 6-7).

When small aliquots of PhCN were added to a CH_2Cl_2 solution of $Ru_2(dpb)_4Cl$ containing 0.1 M $TBAClO_4$, the 778 nm band decreased in intensity and blue-shifted to 761 nm while, at the same time, a new band grows in at 424 nm (Figure 6-7a). The final UV-visible spectrum after addition of 1000 eq PhCN exhibits absorption bands at 424, 558, and 761 nm and is virtually the same as the UV-visible spectrum of $Ru_2(dpb)_4Cl$ in neat PhCN (solid line in Figure 6-6).

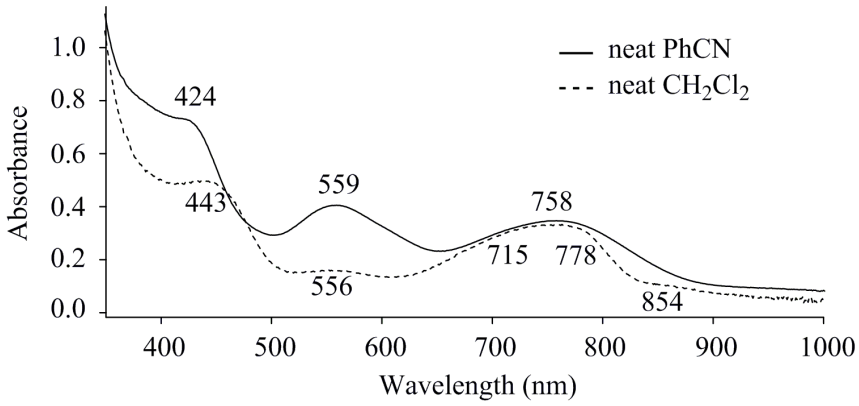

Figure 6-6. UV-visible spectra of $Ru_2(dpb)_4Cl$ (1.0×10^{-4} M) in neat CH_2Cl_2 and neat PhCN.

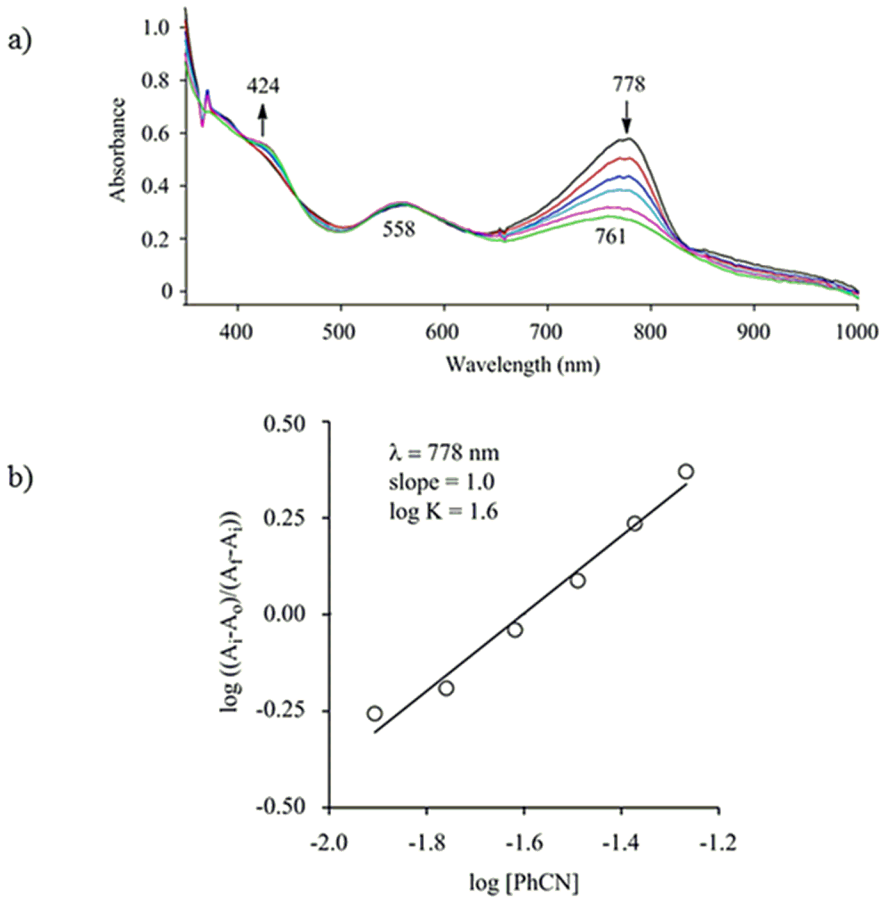

Figure 6-7. a) UV-visible spectral changes upon addition of PhCN to $Ru_2(dpb)_4Cl$ in CH_2Cl_2, 0.1 M $TBAClO_4$ and b) Hill plot constructed from the UV-visible spectra in the different solutions.

The exact number of PhCN molecules bound to the Ru_2^{5+} species was ascertained using a Hill plot (Figure 6-7b). As shown in this figure, a linear relationship with a slope of 1.00 is obtained, hence suggesting the coordination of one and only one PhCN molecule to the diruthenium unit in its Ru_2^{5+} form. The PhCN bound compound is formulated as $[Ru_2(dpb)_4(PhCN)]^+$ in neat PhCN and a log K = 1.6 was estimated for the ligand addition reaction (see Eq 6-6) on the basis of the Hill plot.

$$[Ru_2(dpb)_4]^+ + PhCN \rightleftarrows [Ru_2(dpb)_4(PhCN)]^+ \qquad (6\text{-}6)$$

Figures 6-8b shows UV-visible spectrum of $Ru_2(dpb)_4Cl$ in PhCN containing 0.1 M $TBAClO_4$, while Figure 6-8a shows the UV-visible spectrum of the compound in neat PhCN. There is no significant difference between the spectra in Figures 6-8a and 6-8b, therefore implying that the Ru_2^{5+} complex can be formulated as $[Ru_2(dpb)_4(PhCN)]^+$ under both solution conditions (with and without 0.1 M $TBAClO_4$ as supporting electrolyte).

In summary, the various forms of $Ru_2(dpb)_4Cl$ in CH_2Cl_2 containing 0.1 M TBAX when X = ClO_4^-, Cl^-, or F^- and in PhCN with or without $TBAClO_4$ are given in Scheme 6-1.

6.2.3 Electrochemistry in CH_2Cl_2

Cyclic voltammograms of $Ru_2(dpb)_4Cl$ in CH_2Cl_2 containing 0.1 M TBAX where X = ClO_4^-, Cl^-, or F^- are shown in Figure 6-9a, 6-9b, and 6-9c. As depicted in Scheme 6-1, the major diruthenium form of $Ru_2(dpb)_4Cl$ in CH_2Cl_2, 0.1 M $TBAClO_4$ is assigned as $[Ru_2(dpb)_4]^+$ with a dissociated chloride ion. Under these solution conditions, the cyclic voltammogram exhibits two reduction processes on the cathodic (negative) scan which are

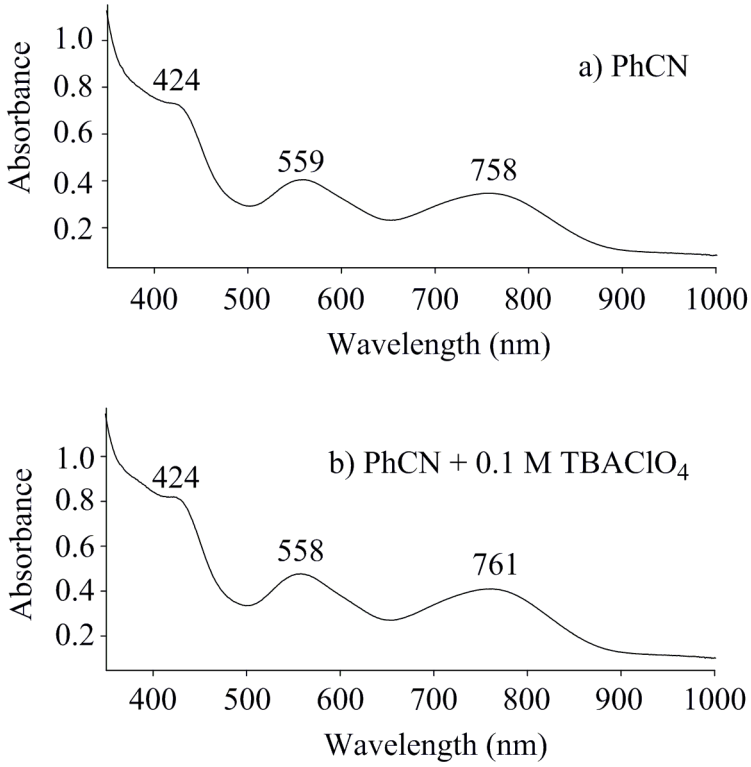

Figure 6-8. UV-visible spectra of $Ru_2(dpb)_4Cl$ (1.0×10^{-4} M) in a) neat PhCN and b) PhCN containing 0.1 M $TBAClO_4$.

Scheme 6-1. Diruthenium species formed from $Ru_2(dpb)_4Cl$ in solutions containing different anions (X).

(a) CH_2Cl_2

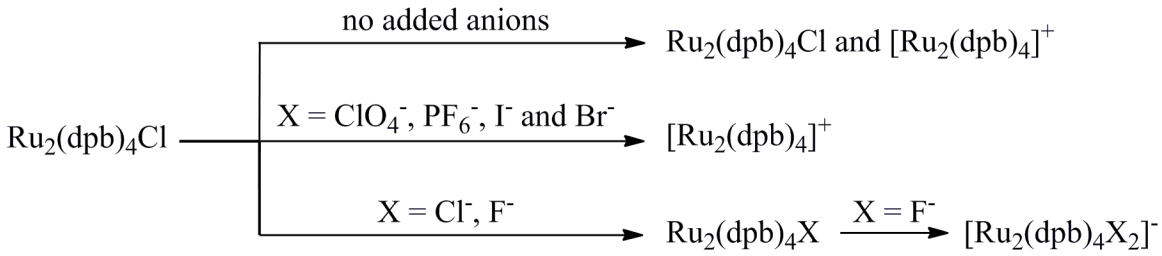

(b) PhCN

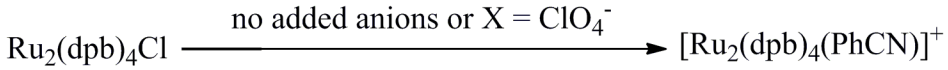

labeled as I and II and two oxidation processes on the anodic (positive) scan which are labeled as III and IV (see Figure 6-9a). The first reversible reduction at $E_{1/2}$ = -0.26 V (Process I) and the second irreversible reduction at E_{pc} = -1.80 V (Process II) are assigned to the $Ru_2^{5+/4+}$ and $Ru_2^{4+/3+}$ processes of $[Ru_2(dpb)_4]^+$ on the basis of previously reported electrochemical behavior for numerous related $Ru_2(L)_4Cl$ complexes with a variety of different anionic bridging ligands, L.[18,34,37-39]

The irreversible second reduction of $[Ru_2(dpb)_4]^+$ in CH_2Cl_2 has a much higher peak current than the first reduction at room temperature but the two reductions at -70°C are reversible and exhibit the same peak current height at $E_{1/2}$ = -0.27 and -1.64 V (see Figure 6-10). This is consistent with two stepwise one-electron additions. The difference between the electrochemical behavior at room temperature and that at low temperature is attributed to a chemical reaction involving the electrogenerated Ru_2^{3+} form of the compound and the CH_2Cl_2 solvent, as has been shown in the case of related Ru_2^{5+} complexes.[1]

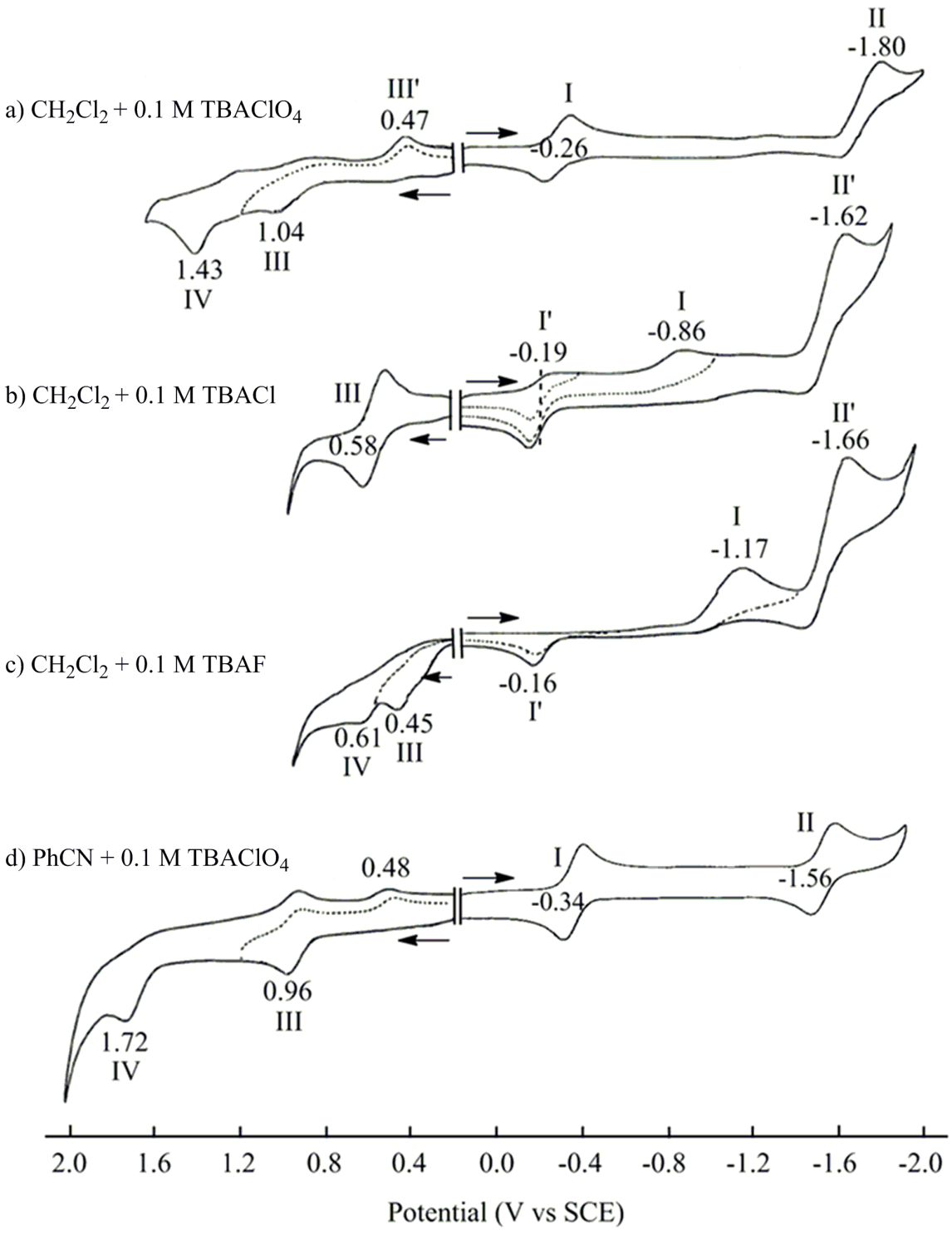

Figure 6-9. Cyclic voltammograms of $Ru_2(dpb)_4Cl$ in CH_2Cl_2 containing a) 0.1 M $TBAClO_4$, b) 0.1 M TBACl and c) 0.1 M TBAF or d) in PhCN containing 0.1 M $TBAClO_4$.

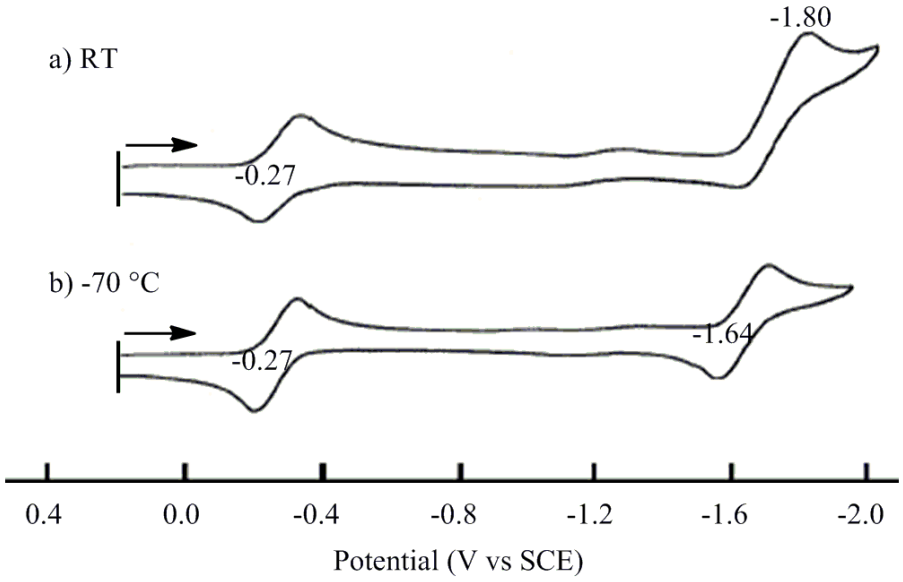

Figure 6-10. Cyclic voltammograms of $Ru_2(dpb)_4Cl$ in CH_2Cl_2 containing 0.1 M $TBAClO_4$ at a) room temp and b) -70 °C.

The irreversible oxidation processes III and IV of $[Ru_2(dpb)_4]^+$ in Figure 6-9a are located at peak potentials of 1.04 and 1.43 V for a scan rate of 0.1 V/s. Process III is coupled with a reduction peak located at E_{pc} = 0.47 V (Process III′) for a scan rate of 0.1 V/s. This process is assigned to reduction of a species that is not initially present in solution but is generated at the electrode surface, after the oxidation process III.

The most probable form of the electroactive species being re-reduced on the return scan at 0.47 V in Figure 6-9a is a chloride bound Ru_2^{6+} species, and we therefore propose the electrochemical EC mechanism shown in Scheme 6-2 to explain the oxidative behavior of $[Ru_2(dpb)_4]^+$. Since no major anodic (oxidation) process appears on positive potential sweeps prior to 1.04 V, Process III is assigned to the initial oxidation of $[Ru_2(dpb)_4]^+$ in solution, which is the major form of the diruthenium compound in CH_2Cl_2 containing 0.1 M $TBAClO_4$ as indicated by the spectroscopic data (see Figure 6-2b). The *in situ* generated one-electron oxidized dimetal compound, $[Ru_2(dpb)_4]^{2+}$, will undergo a rapid reaction with the free Cl^- ion present in solution (due to the initial dissociation of Cl^- from $Ru_2(dpb)_4Cl$) to yield $[Ru_2(dpb)_4Cl]^+$, which is then reduced on the return negative potential sweep to $Ru_2(dpb)_4Cl$ via Process III′ at a peak potential of +0.47 V for a scan rate of 0.1 V/s.

Scheme 6-2. The overall electron transfer mechanism for oxidation of $Ru_2(dpb)_4Cl$ in CH_2Cl_2, 0.1 M $TBAClO_4$.

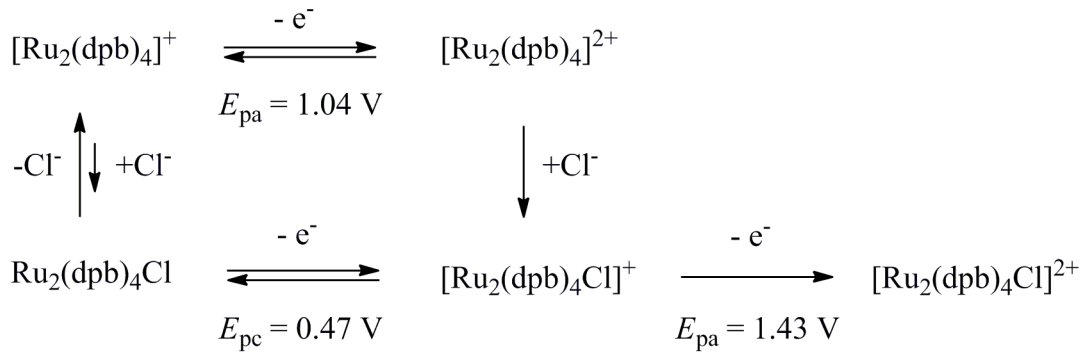

As shown in Scheme 6-2, the singly oxidized Ru_2^{6+} species formed after addition of Cl^- is formulated as $[Ru_2(dpb)_4Cl]^+$ and undergoes a one-electron oxidation at E_{pa} = 1.43 V for a scan rate of 0.1 V/s (Process IV in Figure 6-9a). This reaction is 960 mV more positive than the potential for conversion of $[Ru_2(dpb)_4Cl]^+$ to $Ru_2(dpb)_4Cl$ (0.47 V), a result consistent with the observation that the potential gap between the reversible two oxidations of most $Ru_2(L)_4Cl$ complexes is usually close to 1.0 V.[17] Process IV is irreversible, thus suggesting that the electrogenerated Ru_2^{7+} species, $[Ru_2(dpb)_4Cl]^{2+}$, is unstable on the cyclic voltammetry timescale.[17,40]

As shown in Figures 6-9b and 6-9c, different redox behavior is seen when using TBACl or TABF as supporting electrolyte. The major diruthenium species in solutions of 0.1 M TBACl is formulated as $Ru_2(dpb)_4Cl$. The cyclic voltammogram in this case exhibits three electrode processes labeled as I′, I, and II′ on the cathodic potential sweep, whereas only one electrode process (Process III) is seen on the anodic potential sweep (Figure 6-9b). Process I′ in Figure 6-9b occurs at a potential close to that for the peak assigned to Process I in Figure 6-9a, and thus is attributed to the one-electron reduction of $[Ru_2(dpb)_4]^+$. Process I, at -0.86 V, in Figure 6-9b has no corresponding peak in Figure 6-9a and is assigned to the one-electron reduction of the chloride-bound Ru_2^{5+} compound $Ru_2(dpb)_4Cl$. It may appear odd that Process I′ is assigned to a diruthenium species not initially present in solution. However, the potential difference between Processes I′ and I in Figure 6-9b is fairly large (670 mV), and this would be the driving force for a dissociation of Cl^- from $Ru_2(dpb)_4Cl$ to give the more easily reducible $[Ru_2(dpb)_4]^+$ during the negative potential scan. A similar "potential driven" dissociation of Cl^- was shown to occur for $Ru_2(dpf)_4Cl$ during electroreduction in CH_2Cl_2 containing 0.1 M $TBAClO_4$.[40]

Process I is irreversible and coupled with Process I′ on the return potential sweep, as shown by the dashed line in Figure 6-9b. This result suggests that the one-electron reduced form of $Ru_2(dpb)_4Cl$, i.e. $[Ru_2(dpb)_4Cl]^-$, undergoes a rapid dissociation of Cl^- on the cyclic voltammetry timescale to yield $Ru_2(dpb)_4$, which is then reoxidized via process I′ as shown in Scheme 6-3. As for the case of $Ru_2(dpb)_4Cl$ in CH_2Cl_2, 0.1 M $TBAClO_4$ (Figure 6-9a), the electrogenerated $Ru_2(dpb)_4$ complex present at the electrode surface after Process I and loss of Cl^- undergoes an additional irreversible reduction at E_{pc} = -1.62 V to give $[Ru_2(dpb)_4]^-$ (Process II′ for a scan rate of 0.1 V/s). Finally, the single well-defined oxidation at $E_{1/2}$ = 0.58 V (Figure 6-9b) is assigned to the reversible conversion of $Ru_2(dpb)_4Cl$ to $[Ru_2(dpb)_4Cl]^+$. Scheme 6-3 summarizes all of the electron transfer reactions involving $Ru_2(dpb)_4Cl$ in CH_2Cl_2, 0.1 M TBACl.

Scheme 6-3. Redox reactions of $Ru_2(dpb)_4Cl$ in CH_2Cl_2, 0.1 M TBACl.

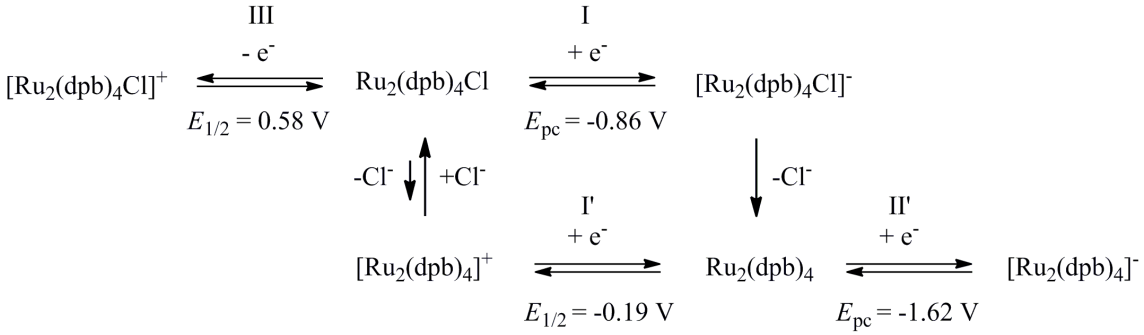

A fluoride ion will bind more strongly to Ru_2^{5+} than a chloride ion, and this is reflected in the cyclic voltammogram of $Ru_2(dpb)_4Cl$ in CH_2Cl_2 containing 0.1 M TBAF as supporting electrolyte (Figure 6-9c). There are two reduction processes (labeled as I and II′) on the cathodic potential sweep from 0.0 to -2.0 V and two oxidations (labeled as III and IV) on the

anodic potential sweep from 0.0 to +1.0 V. No electrode reaction assigned to $[Ru_2(dpb)_4]^+$ is observed on the initial sweep, thus suggesting that the fluoride ion remains tightly bound.

The spectroscopic data described earlier in this dissertation shows that the diruthenium complex exists as a mixture of $Ru_2(dpb)_4F$ and $[Ru_2(dpb)_4F_2]^-$ in CH_2Cl_2, 0.1 M TBAF (see Scheme 6-1), and the first reduction peak I at -1.17 V in Figure 6-9c is therefore proposed to involve overlapping reduction processes of $Ru_2(dpb)_4F$ and $[Ru_2(dpb)_4F_2]^-$. These two diruthenium forms of the compound bear a different charge, i.e. 0 for $Ru_2(dpb)_4F$ and -1 for $[Ru_2(dpb)_4F_2]^-$, which would suggest a large difference in the reduction potentials between the mono and bis-adducts. However, the fact that only one reduction is observed can be rationalized if $[Ru_2(dpb)_4F_2]^-$ is converted to $Ru_2(dpb)_4F$ prior to electron transfer. Alternatively, it may be that the second fluoride ion might bind more weakly to the diruthenium core as compared to the first fluoride ion and thus both reduction potentials might be similar to each other. Evidence for this possibility is given by the fact that only one equivalent of F^- is needed to completely convert $Ru_2(dpb)_4Cl$ into $Ru_2(dpb)_4F$ (Figure 6-4), whereas about 1000 eq of F^- must be added to solution in order to obtain $[Ru_2(dpb)_4F_2]^-$ (Figure 6-2d).

The irreversible reduction Process I in Figure 6-9c is located at E_{pc} = -1.17 V and the compound formed at the electrode surface during this process is reoxidized via process I′ at E_{pa} = -0.16 V, as shown by the dashed line on the return sweep. It should be noted that process I′ is not observed on the voltammogram in Figure 6-9c when the potential scan was reversed prior to process I (data not shown). The reoxidation Process I′ in Figures 6-9b and 6-9c have virtually the same E_{pa} values which is not so different from the E_{pc} of Process I in Figure 6-9a and in all three cases these reactions correspond to the $Ru_2^{5+/4+}$ processes of

$[Ru_2(dpb)_4]^+$. Therefore, one can propose that the reduced forms of $Ru_2(dpb)_4F$ and $[Ru_2(dpb)_4F_2]^-$ both undergo a rapid dissociation of the fluoride anion(s) to yield $Ru_2(dpb)_4$, which is then reoxidized via process I′ and further reduced via process II′.

As mentioned above, two electrode reactions are seen on the positive potential scan in Figure 6-9c. The first oxidation (process III) is attributed to the $Ru_2^{5+/6+}$ process of $[Ru_2(dpb)_4F_2]^-$, whereas the second oxidation (process IV) is attributed to the $Ru_2^{5+/6+}$ form of $Ru_2(dpb)_4F$. This assignment is based on the fact that $Ru_2(dpb)_4Cl$ in CH_2Cl_2, 0.1 M TBAF exists as a mixture of $Ru_2(dpb)_4F$ and $[Ru_2(dpb)_4F_2]^-$ (as shown in Scheme 6-1) and that process IV occurs at a potential close to process III in Figure 6-9b, an electrode reaction attributed to the $Ru_2^{5+/6+}$ form of $Ru_2(dpb)_4Cl$.

6.2.4 Electrochemistry in PhCN

A cyclic voltammogram of $Ru_2(dpb)_4Cl$ in PhCN containing 0.1 M $TBAClO_4$ is shown in Figure 6-9d. On the basis of the UV-visible data discussed in a previous section of the dissertation, we proposed that $Ru_2(dpb)_4Cl$ predominantly exists as $[Ru_2(dpb)_4(PhCN)]^+$ under these solution conditions. As shown in Figure 6-9d, two major reductions (I and II) and two major oxidations (III and IV) are seen in the cyclic voltammogram of $Ru_2(dpb)_4Cl$ under these solution conditions. Processes I and II are both reversible on the cyclic voltammetry timescale. Process I is assigned to the $Ru_2^{5+/4+}$ reaction of $[Ru_2(dpb)_4(PhCN)]^+$ and would give as a reduction product $Ru_2(dpb)_4(PhCN)$, $Ru_2(dpb)_4(PhCN)_2$, or $Ru_2(dpb)_4$ depending upon the ability of PhCN to coordinate to the Ru_2^{4+} form of the compound. This point was elucidated by investigating the electrochemistry of $Ru_2(dpb)_4Cl$ in CH_2Cl_2/PhCN mixtures with different concentrations of PhCN and constructing plots of $E_{1/2}$ vs log[PhCN]

for each redox process. These plots are shown in Figure 6-11 and can be divided into three regions as a function of log[PhCN].

As the concentration of PhCN increases in the CH_2Cl_2/PhCN mixtures, $E_{1/2}$ of the $Ru_2^{5+/4+}$ process remains the same in region A or region C, but shifts towards more negative values with a slope of -57 mV in region B (Figure 6-11a). Likewise, an increase in PhCN concentration in the CH_2Cl_2/PhCN mixtures does not produce a large change in $E_{1/2}$ of the $Ru_2^{4+/3+}$ process in region A or region B, but yields a shift of $E_{1/2}$ towards more positive values with a slope of 65 mV in region C (see Figure 6-11b).

The electrode reactions shown in Scheme 6-4 can explain the features of the plots of $E_{1/2}$ vs log[PhCN] in Figure 6-11. In this scheme, the diruthenium complex is shown only by its core for simplicity. The $Ru_2(dpb)_4Cl$ complex exists as $[Ru_2(dpb)_4]^+$ in region A of low PhCN concentrations and is formulated as Ru_2^{5+} in Scheme 6-4, while the $Ru_2(dpb)_4Cl$ complex exists as $[Ru_2(dpb)_4(PhCN)]^+$ in regions B and C of higher PhCN concentrations and is formulated as $Ru_2^{5+}(PhCN)$ in Scheme 6-4. The PhCN molecule dissociates from the complex upon conversion of Ru_2^{5+} to Ru_2^{4+} in region B, but the solvent molecule remains coordinated after reduction in region C. This assignment is consistent with the fact that the plot of $E_{1/2}$ (1^{st} red) vs log[PhCN] is linear with a slope of -57 mV in region B but has a $\Delta E_{1/2}/\Delta$log[PhCN] value of 0 mV in region C. The $Ru_2^{4+/3+}$ process occurs without gain or loss of PhCN in both regions A and B whereas in region C (where the Ru_2^{4+} species predominantly exists as $Ru_2(dpb)_4(PhCN)$), one additional PhCN molecule binds to the Ru_2^{3+} product of the reaction, suggesting a formulation of $[Ru_2(dpb)_4(PhCN)_2]^-$ (shown as $Ru_2^{3+}(PhCN)_2$ in Scheme 6-4) in this region of PhCN concentration. This assignment of

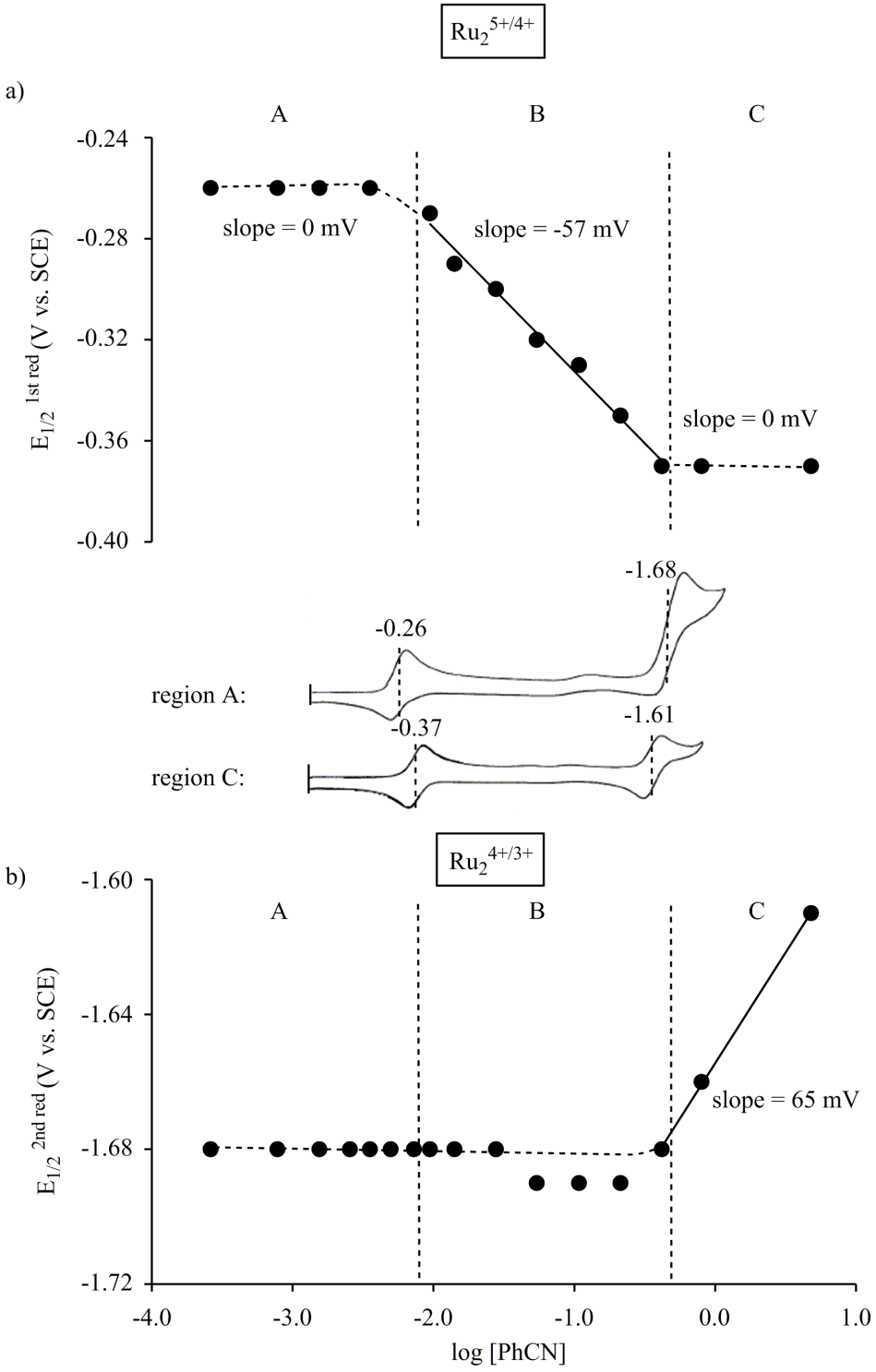

Figure 6-11. Plot of $E_{1/2}$ *vs* log[PhCN] for a) the $Ru_2^{5+/4+}$ and b) $Ru_2^{4+/3+}$ processes of $Ru_2(dpb)_4Cl$ in CH_2Cl_2, 0.1 M $TBAClO_4$ containing small aliquots of PhCN.

PhCN coordination is consistent with the fact that the plot of $E_{1/2}$ (2^{nd} red) vs log[PhCN] is linear with a slope of +65 mV in region C, while $E_{1/2}$ remains virtually invariant with change in PhCN concentration in both regions A and B.

Scheme 6-4. The overall electron transfer mechanism of $Ru_2(dpb)_4Cl$ in CH_2Cl_2/PhCN, 0.1 M $TBAClO_4$ mixtures, where the regions A, B, and C are shown in Figure 6-11.

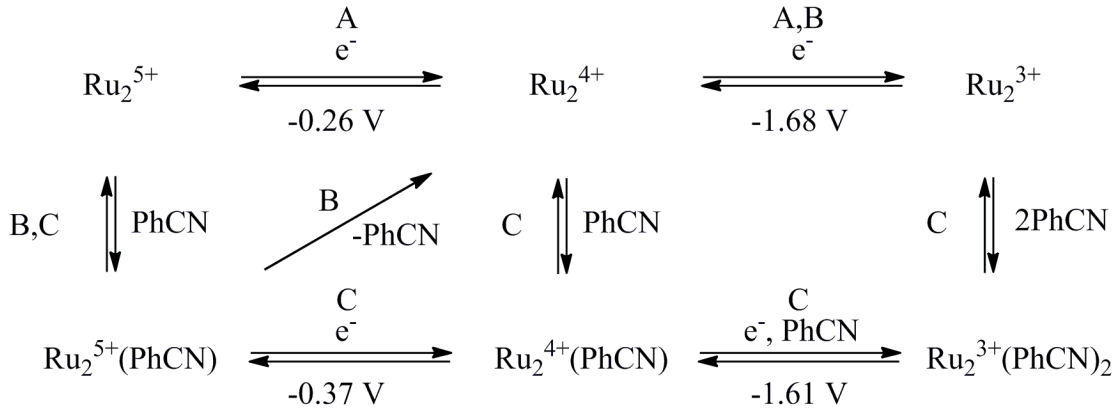

The data in Figure 6-11 were also used to evaluate the binding constants (K_1, K_2, and β_2) for the reactions illustrated by Eqs 6-7 to 6-9 and were found to be approximately $10^{1.6}$, $10^{-0.06}$, and $10^{1.1}$, respectively.

$$[Ru_2^{5+}(dpb)_4]^+ + PhCN \rightleftarrows [Ru_2^{5+}(dpb)_4(PhCN)]^+ \qquad \log K_1 = 1.6 \qquad (6\text{-}7)$$

$$Ru_2^{4+}(dpb)_4 + PhCN \rightleftarrows Ru_2^{4+}(dpb)_4(PhCN) \qquad \log K_2 = -0.06 \qquad (6\text{-}8)$$

$$[Ru_2^{3+}(dpb)_4]^- + 2PhCN \rightleftarrows [Ru_2^{3+}(dpb)_4(PhCN)_2]^- \qquad \log \beta_2 = 1.1 \qquad (6\text{-}9)$$

6.2.5 UV-visible Characterization of Electrogenerated Ru_2^{4+} and Ru_2^{6+} Complexes

The addition of one electron to $Ru_2(dpb)_4Cl$ can lead to four, five, or six coordinate singly reduced Ru_2^{4+} products, depending on the nature of added anions in solution as well as the solvent. The UV-visible spectral changes which occur during the $Ru_2^{5+/4+}$ and $Ru_2^{5+/6+}$

processes were monitored by thin-layer spectroelectrochemistry in CH_2Cl_2 and PhCN containing 0.1 M $TBAClO_4$, examples of which are shown in Figure 6-12. As seen in this figure, the absorption bands of $Ru_2(dpb)_4Cl$ in CH_2Cl_2, 0.1 M $TBAClO_4$, which are initially located at 420, 563, and 778 nm, decrease in intensity while new bands for the singly reduced Ru_2^{4+} grow in at 488 and 858 nm as the reaction proceeds (Figure 6-12a). Different spectral changes are seen in PhCN, 0.1 M $TBAClO_4$ where a new absorption band at 487 nm appears during the $Ru_2^{5+/4+}$ process and no new band at 858 nm is detected for the Ru_2^{4+} forms of $Ru_2(dpb)_4Cl$ under these solution conditions.

The products of the $Ru_2^{5+/4+}$ process are proposed to be $Ru_2(dpb)_4$ in CH_2Cl_2 and $Ru_2(dpb)_4(PhCN)$ in PhCN. The assignment of one bound solvent molecule to Ru_2^{4+} in PhCN is consistent with the electrochemical results obtained in CH_2Cl_2/PhCN mixtures (see Scheme 6-4).

The UV-visible spectral changes during the $Ru_2^{5+/6+}$ process of $Ru_2(dpb)_4Cl$ are also solution dependent as illustrated in Figure 6-12b. In CH_2Cl_2, the Ru_2^{6+} species is characterized by bands at 493, 563, and 860 nm while two major bands at 576 and 815 nm are present in PhCN. The data in Figure 6-12b therefore suggests a different degree of solvent coordination for the Ru_2^{6+} form of the compound in PhCN and CH_2Cl_2, i.e. $[Ru_2(dpb)_4Cl]^+$ in CH_2Cl_2 and $[Ru_2(dpb)_4Cl(PhCN)]^+$ in PhCN. There are well-defined isobestic points for the $Ru_2^{5+/6+}$ process in both solvents, thus indicating the absence of spectral intermediates during these electron transfer processes.

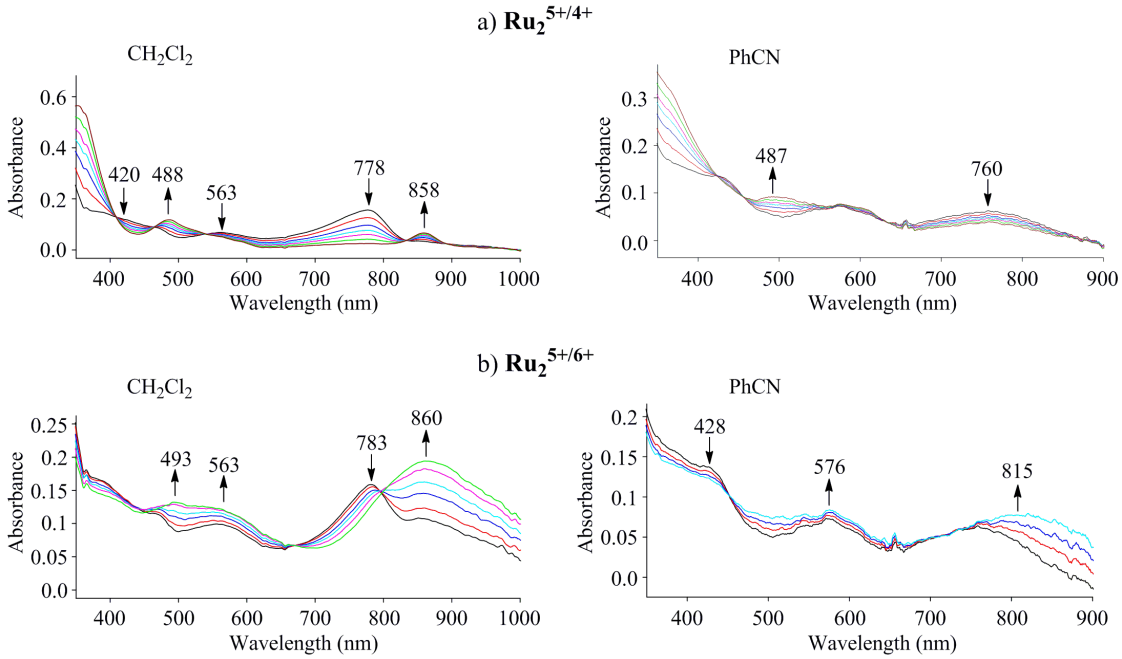

Figure 6-12. UV-visible spectral changes of $Ru_2(dpb)_4Cl$ during the a) $Ru_2^{5+/4+}$ and b) $Ru_2^{5+/6+}$ processes in CH_2Cl_2 and PhCN containing 0.1 M $TBAClO_4$

6.2.6 Electrochemistry of $Ru_2(dpb)_4(CO)$ and $Ru_2(dpb)_4Cl$ under CO

Cyclic voltammograms of $Ru_2(dpb)_4(CO)$ in CH_2Cl_2 containing 0.1 M $TBAClO_4$ under N_2 and under CO are shown in Figure 6-13a. Under both solution conditions, the compound exhibits a reversible one-electron reduction at ~ -1.25 V and a reversible one-electron oxidation at 0.11 V vs SCE. Under N_2, there is also a reversible one-electron oxidation at 1.07 V and a reduction at -1.71 V which has much smaller peak current as compared to the other redox processes. Under a CO atmosphere the reduction at -1.71 V is not observed for $Ru_2(dpb)_4(CO)$ and the first oxidation at 1.07 V is followed by a second irreversible oxidation at E_{pa} = 1.34 V for a scan rate of 0.1 V/s.

The effect of dissolved CO gas on the cyclic voltammograms of $Ru_2(dpb)_4(CO)$ in CH_2Cl_2, 0.1 M $TBAClO_4$ can be compared to the effect of this gas on the cyclic voltammograms of $Ru_2(dpf)_4(CO)$[36] under similar solution conditions. The latter compound was shown to exhibit a single reversible reduction at $E_{1/2}$ = -1.17 V under N_2 as compared to two reductions at -1.07 and -1.79 V under CO. There was also a single reversible oxidation at 0.28 V for $Ru_2(dpf)_4(CO)$[36] as compared to a reversible oxidation at 0.11 V for $Ru_2(dpb)_4(CO)$ under N_2 or CO (Figure 6-13a). Thus, $Ru_2(dpb)_4(CO)$ is easier to oxidize and harder to reduce than $Ru_2(dpf)_4(CO)$ under N_2 by 170 and 90 mV, respectively. In addition, $Ru_2(dpf)_4(CO)$ undergoes a second reduction under CO that is not observed for $Ru_2(dpb)_4(CO)$ (see Figure 6-13a) under similar experimental conditions. The first reduction of $Ru_2(dpf)_4(CO)$ was assigned to the $Ru_2^{4+/3+}$ process while the first oxidation was attributed to $Ru_2^{4+/5+}$. A second one-electron oxidation of $Ru_2(dpb)_4(CO)$ is assigned to the $Ru_2^{5+/6+}$ electrode reaction. This process was not reported for $Ru_2(dpf)_4(CO)$ under CO.

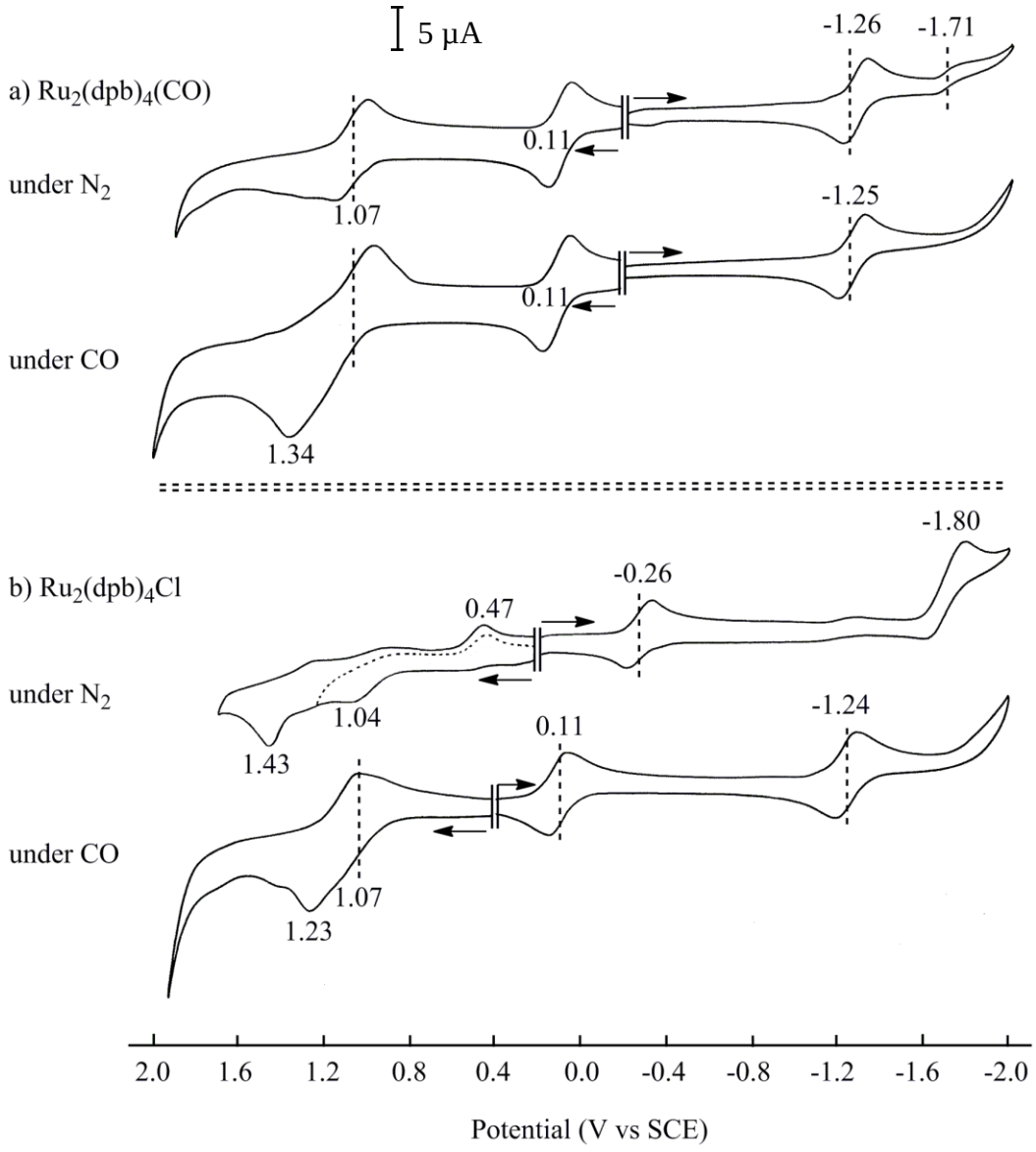

Figure 6-13. Cyclic voltammograms of a) $Ru_2(dpb)_4(CO)$ and b) $Ru_2(dpb)_4Cl$ in CH_2Cl_2 containing 0.1 M $TBAClO_4$ under an N_2 or CO atmosphere.

The "minor" reduction process at -1.71 V in Figure 6-13a may involve an electrode reaction of the CO dissociated species, $Ru_2(dpb)_4$, based on the fact that the $Ru_2(dpb)_4/[Ru_2(dpb)_4]^-$ process of $Ru_2(dpb)_4Cl$ occurs at a similar potential (E_{pc} = -1.80 V) in CH_2Cl_2, 0.1 M $TBAClO_4$ (see top cyclic voltammogram in Figure 6-13b). This dissociation reaction would be slowed down under CO which would shift the equilibrium towards the CO bound species and a redox process assigned to the unligated species would no longer be observed in the cyclic voltammogram at a scan rate of 0.1 V/s (see lower cyclic voltammogram in Figure 6-13a).

Evidence for the strong binding of a CO axial ligand to the Ru_2^{5+} form of $Ru_2(dpb)_4$ is shown in Figure 6-13b which compares cyclic voltammograms of $Ru_2(dpb)_4Cl$ under N_2 and after bubbling of CO gas through the solution. The conversion of $Ru_2(dpb)_4Cl$ to a CO bound species is rapid and the cyclic voltammogram of the *in situ* generated product is virtually identical to that of the chemically generated and structurally characterized mono-CO diruthenium species in Figure 6-13a. Both compounds exhibit well-defined redox processes at 0.11 and ~ -1.25 V and the main difference between the redox active species in Figure 6-13a and Figure 6-13b under CO is that the *in situ* generated CO containing species exists in a Ru_2^{5+} oxidation state and is also associated with a Cl^- counteranion. Evidence for this assignment is given by the IR spectroelectrochemical results described in the following sections.

6.2.7 IR Spectroelectrochemistry of $Ru_2(dpb)_4(CO)$ and $Ru_2(dpb)_4Cl$ under CO

The same two compounds in Figure 6-13 were investigated under a CO atomosphere by thin-layer IR spectroelectrochemistry in order to characterize the CO vibration of the neutral compounds as well as the reduced and oxidized forms of the diruthenium species

under the application of an applied potential. The use of thin-layer IR spectroelectrochemistry to monitor CO adducts of diruthenium compounds is described in earlier publications.[36,38,41,42]

The infrared spectrum for the Ru_2^{4+} complex $Ru_2(dpb)_4(CO)$ in CH_2Cl_2, 0.1 M $TBAClO_4$ is characterized by a CO stretching vibration band at ν_{CO} = 1924 cm^{-1}, while that of the electrochemically generated Ru_2^{5+} and Ru_2^{3+} species exhibit ν_{CO} vibrations at 2013 and 1845/1834 cm^{-1} respectively, as shown in Figure 6-14a. The oxidized form of $Ru_2(dpb)_4(CO)$ under N_2 may be formulated as $[Ru_2(dpb)_4(CO)]^+$. The reduced form of $Ru_2(dpb)_4(CO)$ under N_2 exists as a mixture of mono and bis-CO adducts, that are respectively formulated as $[Ru_2(dpb)_4(CO)]^-$ and $[Ru_2(dpb)_4(CO)_2]^-$. The former compound is proposed to have a CO stretching vibration at 1834 cm^{-1} whereas the latter compound is proposed to have a CO stretching vibration at 1845 cm^{-1}. The presence of two forms of CO adducts for the Ru_2^{3+} forms of the compound and their CO stretching vibration assignment is based on the fact that under a CO atmosphere, the Ru_2^{3+} species is characterized by only one CO stretching vibration at 1845 cm^{-1} (see Figure 6-15). Indeed, under these latter experimental conditions, only the bis-CO adduct, namely $[Ru_2(dpb)_4(CO)_2]^-$ would be expected to be formed during the Ru_2^{4+}/Ru_2^{3+} process of $Ru_2(dpb)_4(CO)$ under a CO atmosphere. As shown in Scheme 6-5, under N_2, the bis-CO adduct $[Ru_2(dpb)_4(CO)_2]^-$ is proposed to be obtained via a reaction between singly reduced $[Ru_2(dpb)_4(CO)]^-$ and CO gas released during dissociation from the initial complex as described in Figure 6-13a. This then yields $[Ru_2(dpb)_4(CO)_2]^-$ (ν_{co} = 1845 cm^{-1}) in addition to the original Ru_2^{3+} complex, $[Ru_2(dpb)_4(CO)]^-$ (ν_{co} = 1834 cm^{-1}), thus giving two IR bands in the spectrum of the singly reduced species. The shifts in the CO

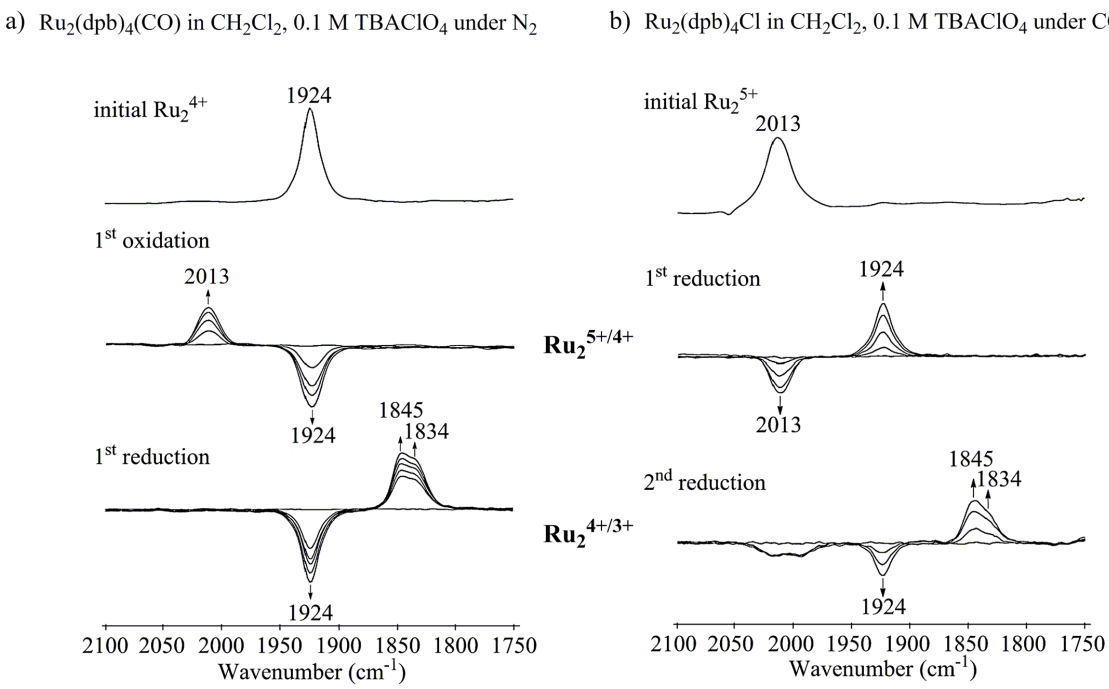

Figure 6-14. IR spectrum of a) $Ru_2(dpb)_4(CO)$ under N_2 and b) $Ru_2(dpb)_4Cl$ under CO in the absence of an applied potential (initial compounds) and during the first one-electron oxidation or reduction.

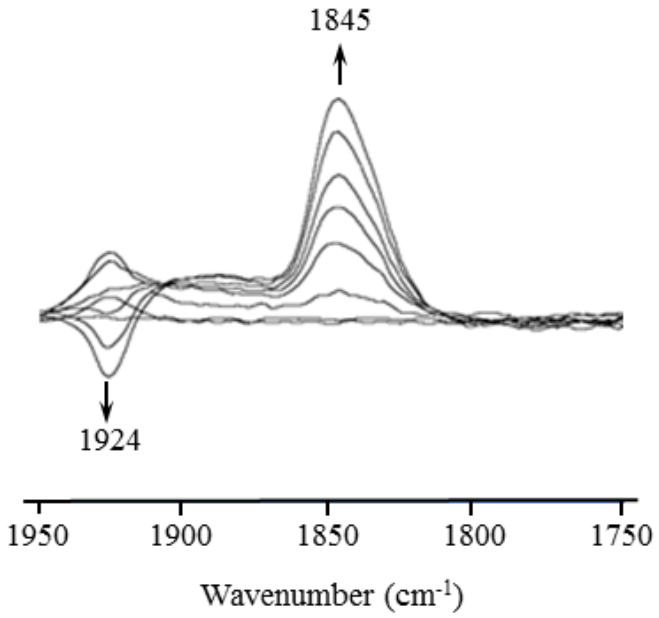

Figure 6-15. Time resolved IR spectral changes during the first controlled potential reduction of $Ru_2(dpb)_4(CO)$ at -1.60 V in CH_2Cl_2, 0.1 M $TBAClO_4$ under CO.

stretching vibration upon going from $Ru_2(dpb)_4(CO)$ to $[Ru_2(dpb)_4(CO)]^+$ or $Ru_2(dpb)_4(CO)$ to $[Ru_2(dpb)_4(CO)]^-$/$[Ru_2(dpb)_4(CO)_2]^-$ are similar to shifts in ν_{CO} seen after the one-electron oxidation and one-electron reduction of $Ru_2(dpf)_4(CO)$ in CH_2Cl_2 under N_2.[36]

Scheme 6-5. Reductions of $Ru_2(dpb)_4(CO)$ under N_2.

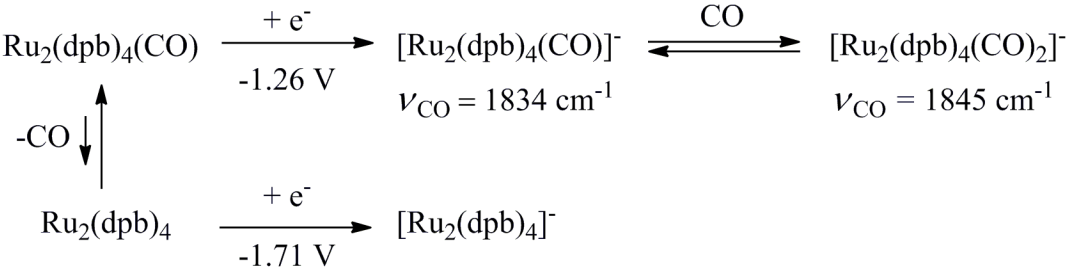

Figure 6-14b illustrates the measured CO stretching frequencies of the neutral and singly reduced forms of $Ru_2(dpb)_4Cl$ in CH_2Cl_2 containing 0.1 M $TBAClO_4$ after bubbling CO through the solution. There are no characteristic CO stretching vibrations for $Ru_2(dpb)_4Cl$ under N_2 but after replacing N_2 by CO, the $Ru_2(dpb)_4Cl$ in solution is converted to a species which exhibits a single CO stretch at 2013 cm^{-1} (Figure 6-14b), thus suggesting the coordination of one CO molecule to the Ru_2^{5+} form of the compound.

The 2013 cm^{-1} band for $Ru_2(dpb)_4Cl$ under CO is at exactly the same position as the ν_{CO} vibration of singly oxidized $Ru_2(dpb)_4(CO)$ in CH_2Cl_2 (Figure 6-14a). As discussed in an earlier section of the dissertation, $Ru_2(dpb)_4Cl$ dissociates to give $[Ru_2(dpb)_4]^+$ and Cl^- in CH_2Cl_2 containing 0.1 M $TBAClO_4$ under N_2 and the product of CO binding under a CO atmosphere is therefore proposed to be $[Ru_2(dpb)_4(CO)]^+$.

The first reduction of $Ru_2(dpb)_4Cl$ under CO occurs at $E_{1/2}$ = +0.11 V (Figure 6-13b) and under the application of an applied reduction potential, the ν_{CO} band at 2013 cm^{-1} disappears and is replaced by a strong ν_{CO} band at 1924 cm^{-1} (middle spectrum in Figure 6-

14b). The same value of ν_{CO} is seen for the Ru_2^{4+} form of structurally characterized $Ru_2(dpb)_4(CO)$ (top spectrum in Figure 6-14a). Finally, the reduction of $Ru_2(dpb)_4(CO)$ under N_2 (Figure 6-14a) or $Ru_2(dpb)_4Cl$ under CO (Figure 6-14b) at an applied potential of -1.50 V in the thin-layer IR cell leads to an almost identical IR spectrum for the Ru_2^{3+} species, which is characterized by ν_{CO} bands at 1845 and 1834 cm^{-1}.

We have shown in an earlier section of the dissertation that $Ru_2(dpb)_4Cl$ exists in CH_2Cl_2 (with no $TBAClO_4$ added) as a mixture of $[Ru_2(dpb)_4]^+$ and $Ru_2(dpb)_4Cl$, where the proportion of the two forms of the compound is concentration dependent. The IR spectrum of $Ru_2(dpb)_4Cl$ under a CO atmosphere in CH_2Cl_2 without any added $TBAClO_4$ is shown in Figure 6-16a and exhibits two CO stretching bands, a major band at 2013 and a less intense band at 1993 cm^{-1} which appears as a shoulder. This suggests the presence of two Ru_2^{5+} CO adducts in solution. The band at 2013 cm^{-1} is assigned to the ν_{CO} of $[Ru_2(dpb)_4(CO)]^+$ while the band at 1993 cm^{-1} is most likely due to $Ru_2(dpb)_4Cl(CO)$. As shown in Scheme 6-1, only $[Ru_2(dpb)_4]^+$ exists in a CH_2Cl_2, 0.1 M $TBAClO_4$ solution, and under these solution conditions only $[Ru_2(dpb)_4(CO)]^+$ should be present in solution under a CO atmosphere. This is indeed the case as shown in Figure 6-16b. $Ru_2(dpb)_4Cl(CO)$ would be expected to have a higher electron density on the Ru_2^{5+} dimetal unit than does $[Ru_2(dpb)_4(CO)]^+$, because of the axially bound Cl^- anion.

Interestingly, the present work shows that CO reacts with $Ru_2(dpb)_4Cl$, a result that differs from what has previously been reported for other ap or substituted ap derivatives.[38] It also differs from $Ru_2(dpf)_3(OAc)Cl$,[32] which showed no evidence for the CO binding to the compound in its Ru_2^{5+} oxidation state. The lack of reactivity between CO and

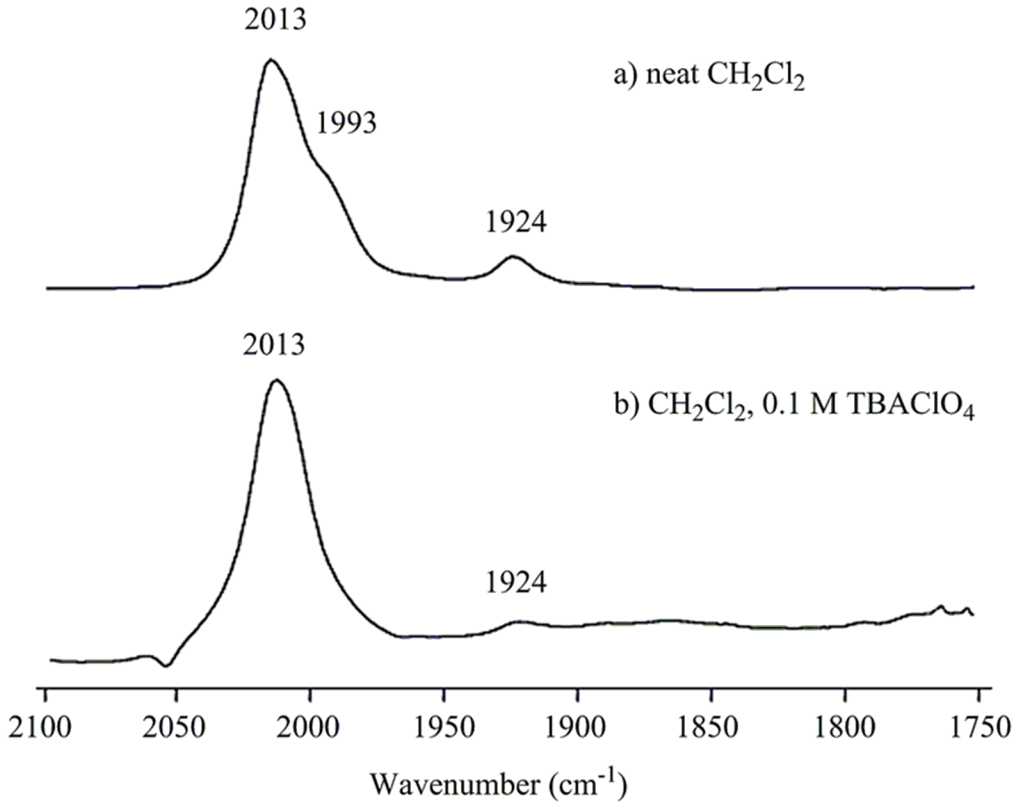

Figure 6-16. IR spectra of $Ru_2(dpb)_4Cl$ under a CO atmosphere in a) neat CH_2Cl_2 and b) CH_2Cl_2, 0.1 M $TBAClO_4$.

$Ru_2(dpf)_3(OAc)Cl$ was explained by the fact that the chloride anion inhibited the axial binding of CO to the dimetal unit.

6.2.8 Electrochemistry and IR Spectroelectrochemistry of $Ru_2(dpb)_4(NO)$

$Ru_2(dpb)_4(NO)$ in CH_2Cl_2, 0.1 M $TBAClO_4$ exhibits two one-electron reversible reductions and a single one-electron reversible oxidation (see Figure 6-17a).The reductions are located at $E_{1/2}$ = -0.04 and-1.52 V while the oxidation is seen at $E_{1/2}$ = 1.46 V. A related Ru_2^{3+} derivative, $Ru_2(dpf)_4(NO)$,[41] was previously characterized by two reversible reductions at $E_{1/2}$ = 0.06 and -1.24 V, but no oxidations were reported. Both reductions of $Ru_2(dpf)_4(NO)$ were assigned to metal-centered processes generating diruthenium complexes with formal oxidation states of Ru_2^{2+} and Ru_2^{1+}, respectively and the same assignment is given in the case of $Ru_2(dpb)_4(NO)$. The currently investigated dpb NO derivative is more difficult to reduce by 100-280 mV, consistent with the stronger donor character of the dpb ligand.

The neutral and singly reduced forms of $Ru_2(dpb)_4(NO)$ were characterized by thin-layer IR spectroelectrochemistry and an example of which is shown in Figure 6-17b. The infrared spectrum of neutral $Ru_2(dpb)_4(NO)$ in CH_2Cl_2 containing 0.1 M $TBAClO_4$ exhibits an ν_{NO} at 1778 cm^{-1}. This value is close to the measured ν_{NO} of $Ru_2(dpf)_4(NO)$ at 1786 cm^{-1} and $[Ru_2(dpf)_4(NO)_2]^+$ at 1788 cm^{-1}, both of which are examples of Ru_2^{3+} complexes.[41] This 8-10cm^{-1} difference in ν_{NO} between the dpb and dpf derivatives can be accounted for by an increased electron density on the dimetal unit in $Ru_2(dpb)_4(NO)$ which would lead to a stronger π back-donation to the antibonding π^* orbital of the NO axial ligand, thus causing the NO vibration band to shift to a lower frequency. As shown in Figure 6-17b, the ν_{NO} value of $Ru_2(dpb)_4(NO)$ at 1778 cm^{-1} shifts to 1706 cm^{-1} upon addition of one electron. This 72

cm^{-1} shift in the NO stretching vibration is comparable to the 71-74 cm^{-1} shifts reported for the one-electron reduction of $Ru_2(dpf)_4(NO)$ or $Ru_2(Fap)_4(NO)Cl$. A summary of electrochemical and IR spectral data of the dpb diruthenium complexes along with data for the dpf diruthenium complexes is given in Table 6-3.

6.3 Summary

Three diruthenium complexes were synthesized with Cl, CO, or NO axial ligands and are characterized as to their electrochemical and spectroscopic properties. Different forms of diruthenium complexes are formed in a solution of $Ru_2(dpb)_4Cl$ depending on the type of anion as well as the solvent. For example, a dissociation of Cl^- from $Ru_2(dpb)_4Cl$ is seen when ClO_4^-, PF_6^-, I^-, or Br^- is present in CH_2Cl_2, while $Ru_2(dpb)_4Cl$ is the most likely form of the diruthenium compound in CH_2Cl_2 containing Cl^- anion. Axial coordination of PhCN was found when $Ru_2(dpb)_4Cl$ was dissolved in PhCN containing ClO_4^- anion and formation constants for the coordination of PhCN to the Ru_2^{5+}, Ru_2^{4+} and Ru_2^{3+} forms of the compound were calculated. The investigated diruthenium compounds show a greater number of redox processes than the analogous diruthenium derivatives with a dpf bridging ligand, due to a stronger electron donating character of the dpb ligand.

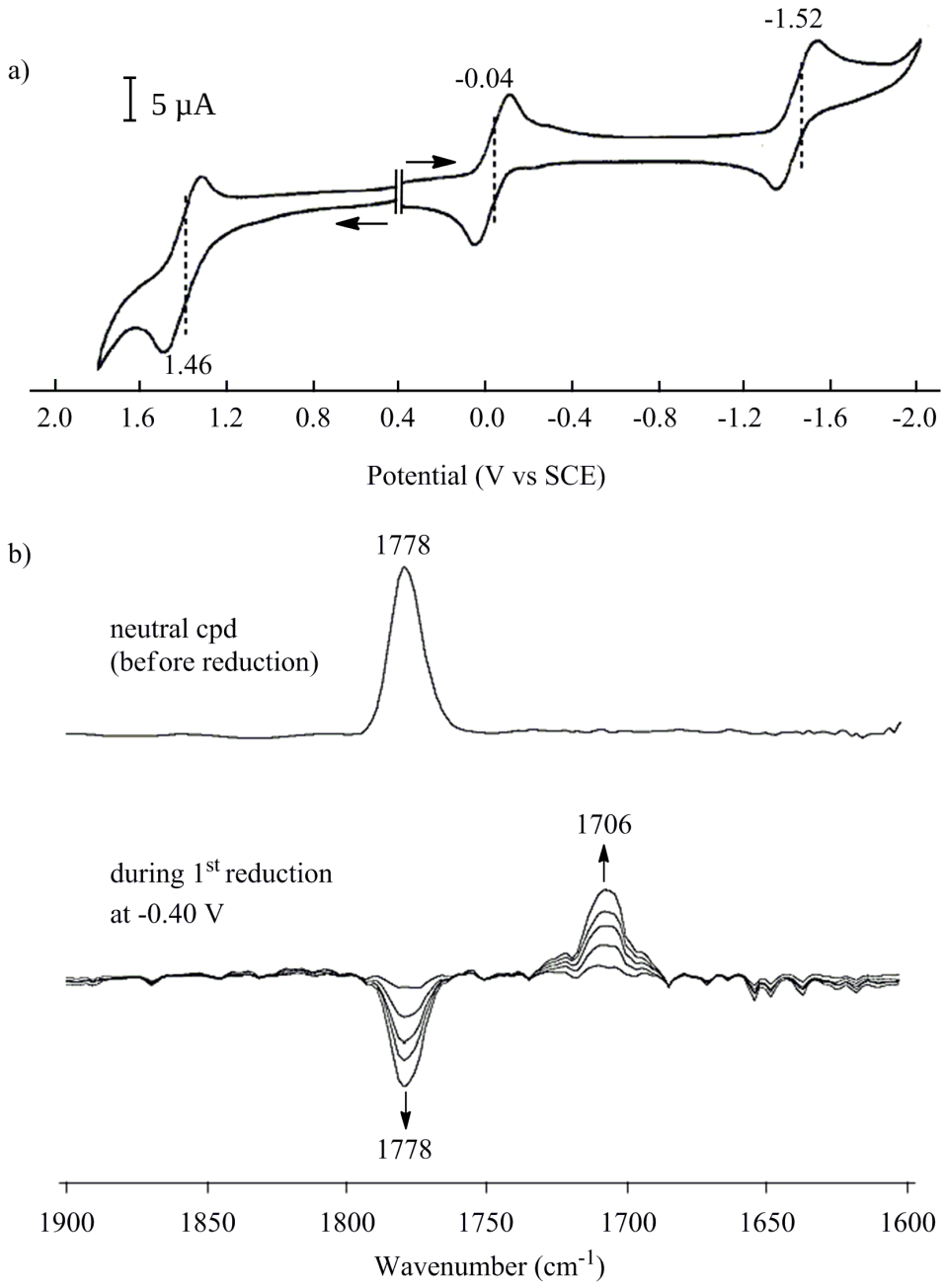

Figure 6-17. a) Cyclic voltammogram in CH_2Cl_2, 0.1 M $TBAClO_4$ and b) IR spectrum of $Ru_2(dpb)_4(NO)$ in the same solution before and after controlled potential reduction by one electron at -0.40 V.

Table 6-3. Summary of Electrochemical and IR Spectral Data of Diruthenium Complexes.

compd	oxidn state	axial ligand	stretching frequency, cm^{-1}		$E_{1/2}$ of Ru_2 (V vs SCE)[a]					ref
			ν_{CO}	ν_{NO}	6+/5+	5+/4+	4+/3+	3+/2+	2+/1+	
$Ru_2(dpb)_4Cl$	Ru_2^{5+}	Cl^-	1993[b]		0.58	-0.19	-1.62[c]			tw
$[Ru_2(dpb)_4]^+$	Ru_2^{5+}		2013[b]		1.04[c]	-0.26	-1.80[c]			tw
$[Ru_2(dpb)_4(PhCN)]^+$	Ru_2^{5+}	PhCN			0.96[c,d]	-0.34[d]	-1.56[d]			tw
$[Ru_2(dpb)_4(CO)]^+$	Ru_2^{5+}	CO	2013							tw
$Ru_2(dpb)_4(CO)$	Ru_2^{4+}	CO	1924		1.07	0.11	-1.26			tw
$[Ru_2(dpb)_4(CO)]^-$	Ru_2^{3+}	CO	1834, 1845							tw
$Ru_2(dpb)_4(NO)$	Ru_2^{3+}	NO		1778			1.46	-0.04	-1.52	tw
$[Ru_2(dpb)_4(NO)]^-$	Ru_2^{2+}	NO		1706						tw
$Ru_2(dpf)_4Cl$	Ru_2^{5+}	Cl^-			0.54	-0.64[c]				40
$[Ru_2(dpf)_4(CO)]^+$	Ru_2^{5+}	CO	2019							36
$Ru_2(dpf)_4(CO)$	Ru_2^{4+}	CO	1929			0.28	-1.17			36
$[Ru_2(dpf)_4(CO)]^-$	Ru_2^{3+}	CO	1840							36
$Ru_2(dpf)_4(NO)$	Ru_2^{3+}	NO		1786				0.06	-1.24	41
$[Ru_2(dpf)_4(NO)]^-$	Ru_2^{2+}	NO		1712						41

[a] in CH_2Cl_2, 0.1 M TBAP; [b] in CH_2Cl_2 under CO; [c] Peak potential at the scan rate of 0.1 V/s; [d] in PhCN, 0.1 M TBAP; tw = this work.

6.4 References

1. Ngubane, S.; Kadish, K. M.; Bear, J. L.; Van Caemelbecke, E.; Thuriere, A.; Ramirez, K. P. *Dalton Trans.* **2013**, *42*, 3571-3580.
2. Cummings, S. P.; Savchenko, J.; Fanwick, P. E.; Kharlamova, A.; Ren, T. *Organometallics* **2013**, *32*, 1129-1132.
3. Villalobos, L.; Cao, Z.; Fanwick, P. E.; Ren, T. *J. Chem. Soc., Dalton Trans.* **2012**, *41*, 644-650.
4. Santos, R. L. S. R.; van Eldik, R.; de Oliveira Silva, D. *Inorg. Chem.* **2012**, *51*, 6615-6625.
5. Delgado, P.; Gonzalez-Prieto, R.; Jimenez-Aparicio, R.; Perles, J.; Priego, J. L.; Torres, R. M. *Dalton Transactions* **2012**, *41*, 11866-11874.
6. Boyd, D. A.; Cao, Z.; Song, Y.; Wang, T.-W.; Fanwick, P. E.; Crutchley, R. J.; Ren, T. *Inorg. Chem.* **2010**, *49*, 11525-11531.
7. Fan, Y.; Fanwick, P. E.; Ren, T. *Polyhedron* **2009**, *28*, 3654-3658.
8. Kadish, K. M.; Garcia, R.; Phan, T.; Wellhoff, J.; Van Caemelbecke, E.; Bear, J. L. *Inorg. Chem.* **2008**, *47*, 11423-11428.
9. Castro, M. A.; Roitberg, A. E.; Cukiernik, F. D. *Inorg. Chem.* **2008**, *47*, 4682-4690.
10. Kaim, W.; Sarkar, B. *Coord. Chem. Rev.* **2007**, *251*, 584-594.
11. Barral, M. C.; Gallo, T.; Herrero, S.; Jiménez-Aparicio, R.; Torres, M. R.; Urbanos, F. *Chem.--Eur. J.* **2007**, *13*, 10088-10095.
12. Barral, M. C.; Gonzalez-Prieto, R.; Jimenez-Aparicio, R.; Priego, J. L.; Torres, M. R.; Urbanos, F. A. *Eur. J. Inorg. Chem.* **2006**, 4229-4232.

13. Barral, M. C.; Herrero, S.; Jiménez-Aparicio, R.; Torres, M. R.; Urbanos, F. A. *Angew. Chem. Int. Ed.* **2005**, *44*, 305-307.

14. Angaridis, P. In *Multiple Bonds Between Metal Atoms*; 3rd ed.; Cotton, F. A., Murillo, C. A., Walton, R. A., Eds.; Springer Science and Business Media Inc.: New York, **2005**.

15. Aquino, M. A. S. *Coord. Chem. Rev.* **2004**, *248*, 1025-1045.

16. Miyasaka, H.; Izawa, T.; Sugiura, K.; Yamashita, M. *Inorg. Chem.* **2003**, *42*, 7683-7690.

17. Kadish, K. M.; Wang, L.-L.; Thuriere, A.; Van Caemelbecke, E.; Bear, J. L. *Inorg. Chem.* **2003**, *42*, 834-843.

18. Kachi-Terajima, C.; Miyasaka, H.; Ishii, T.; Sugiura, K.-i.; Yamashita, M. *Inorg. Chim. Acta* **2002**, *332*, 210-215.

19. Campos-Fernández, C. S.; Ouyang, X.; Dunbar, K. R. *Inorg. Chem.* **2000**, *39*, 2432-2433.

20. Ren, T. *Coord. Chem. Rev.* **1998**, *175*, 43-58.

21. Cotton, F. A.; Yokochi, A. *Inorg. Chem.* **1998**, *37*, 2723-2728.

22. Aquino, M. A. S. *Coord. Chem. Rev.* **1998**, *170*, 141-202.

23. Bear, J. L.; Li, Y.; Han, B.; Van Caemelbecke, E.; Kadish, K. M. *Inorg. Chem.* **1997**, *36*, 5449-5456.

24. McCarthy, H. J.; Tocher, D. A. *Inorg. Chim. Acta* **1989**, *158*, 1-2.

25. Chakravarty, A. R.; Cotton, F. A. *Inorg. Chim. Acta* **1986**, *113*, 19-26.

26. Chakravarty, A. R.; Cotton, F. A.; Tocher, D. A. *Inorg. Chem.* **1985**, *24*, 2857-2861.

27. Malinski, T.; Chang, D.; Feldmann, F. N.; Bear, J. L.; Kadish, K. M. *Inorg. Chem.* **1983**, *22*, 3225-3233.

28. Stephenson, T. A.; Wilkinson, G. *J. Inorg. Nucl. Chem.* **1966**, *28*, 2285-2291.

29. Campos-Fernández, C. S.; Thomson, L. M.; Galán-Mascarós, J. R.; Ouyang, X.; Dunbar, K. R. *Inorg. Chem.* **2002**, *41*, 1523-1533.

30. McCarthy, H. J.; Tocher, D. A. *Polyhedron* **1992**, *11*, 13-20.

31. Bear, J. L.; Chen, W.-Z.; Han, B.; Huang, S.; Wang, L.-L.; Thuriere, A.; Van Caemelbecke, E.; Kadish, K. M.; Ren, T. *Inorg. Chem.* **2003**, *42*, 6230-6240.

32. Barral, M. C.; Herrero, S.; Jiménez-Aparicio, R.; Torres, M. R.; Urbanos, F. A. *J. Organomet. Chem.* **2008**, *693*, 1597-1604.

33. Barral, M. C.; Gallo, T.; Herrero, S.; Jiménez-Aparicio, R.; Torres, M. R.; Urbanos, F. A. *Inorg. Chem.* **2006**, *45*, 3639-3647.

34. Kadish, K. M.; Nguyen, M.; Van Caemelbecke, E.; Bear, J. L. *Inorg. Chem.* **2006**, *45*, 5996-6003.

35. Manowong, M.; Han, B.; McAloon, T. R.; Shao, J.; Guzei, I. A.; Ngubane, S.; Van Caemelbecke, E.; Bear, J. L.; Kadish, K. M. *submitted to Inorg. Chem.* **2014**.

36. Kadish, K. M.; Han, B.; Shao, J.; Ou, Z.; Bear, J. L. *Inorg. Chem.* **2001**, *40*, 6848-6851.

37. Chen, W.-Z.; Protasiewicz, J. D.; Davis, S. A.; Updegraff, J. B.; Ma, L.-Q.; Fanwick, P. E.; Ren, T. *Inorg. Chem.* **2007**, *46*, 3775-3782.

38. Kadish, K. M.; Phan, T. D.; Giribabu, L.; Shao, J.; Wang, L.-L.; Thuriere, A.; Van Caemelbecke, E.; Bear, J. L. *Inorg. Chem.* **2004**, *43*, 1012-1020.

39. Kadish, K. M.; Wang, L.-L.; Thuriere, A.; Giribabu, L.; Garcia, R.; Van Caemelbecke, E.; Bear, J. L. *Inorg. Chem.* **2003**, *42*, 8309-8319.

40. Bear, J. L.; Han, B.; Huang, S.; Kadish, K. M. *Inorg. Chem.* **1996**, *35*, 3012-3021.

41. Han, B.; Shao, J.; Ou, Z.; Phan, T. D.; Shen, J.; Bear, J. L.; Kadish, K. M. *Inorg. Chem.* **2004**, *43*, 7741-7751.

42. Bear, J. L.; Wellhoff, J.; Royal, G.; Van Caemelbecke, E.; Eapen, S.; Kadish, K. M. *Inorg. Chem.* **2001**, *40*, 2282-2286.

CHAPTER SEVEN

Structural and Electrochemical Studies of Copper(I) Complexes with Diethoxyphosphoryl-1,10-Phenanthrolines

7.1 Introduction

1,10-Phenanthroline complexes of transition metals have played a key role in a large number of recent studies and have been extensively studied by researchers working in photochemistry and photophysics,[1] electrochemistry,[2] biochemistry,[3] and supramolecular and material science.[4] The major interest of these complexes essentially stems from their relevance to solar energy conversion, sequence-selective DNA cleavage, and fine chemical production by catalytic reactions. Surprisingly, advances in the various application areas are still limited by the synthesis of functionalized 1,10-phenanthroline ligands. Commercially available 2,9-dimethyl-1,10-phenanthroline (neocuproine) is often used to attach additional functional groups to a phenanthroline moiety via reactions involving methyl substituents.[3b] However, for a wide range of applications, a direct functionalization of the heteroaromatic ring is needed.[3b,5]

Recently we reported convenient conditions for the introduction of diethoxyphosphoryl substituents into the 1,10-phenanthroline backbone in the presence of palladium catalysts and synthesized a novel family of mono- and diphosphonate derivatives **1a-f** (Chart 7-1).[6]

Chart 7-1. Structures of diethoxyphosphoryl-substituted 1,10-phenanthrolines **1a-f**.

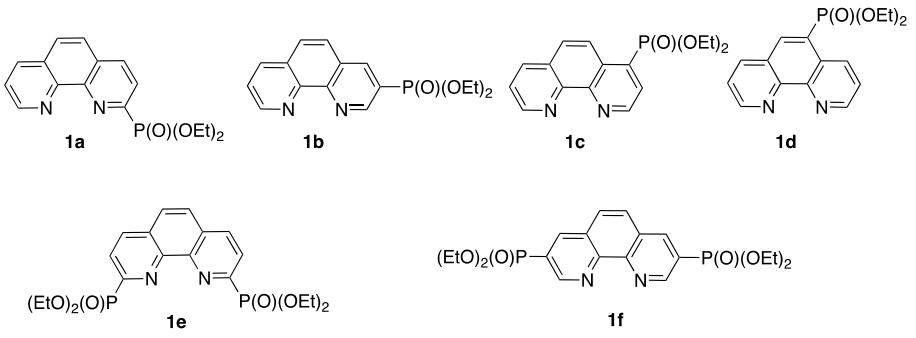

This is an unusual series of functionalized 1,10-phenanthrolines for which all positional isomers are readily available and can be used for systematic studies of the influence of electronic and steric factors on physico-chemical properties of 1,10-phenanthroline complexes. These ditopic ligands should be promising for the development of novel supramolecular photoactive materials and catalysts working in organic medium and water. Moreover, supported catalysts based on these ligands are simple to prepare since organophosphonates can be readily incorporated into inorganic matrices or grafted onto preformed inorganic supports.[7]

In this dissertation, the complexation of copper(I) ions by these ligands were investigated.[8] The Cu(I) phenanthroline complexes are of interest in various fields of research. Indeed, they are efficient catalysts for an impressive range of carbon—carbon and carbon— heteroatom bond forming reactions.[9] These compounds are also good candidates to develop bio-inspired Cu-catalysed oxidation[10] and sulfimidation[11] reactions. Moreover, studies of redox processes involving simple copper(I)–O2 complexes are useful to mimic the action of Cu-containing metalloenzymes.[12] The copper phenanthroline complexes are key derivatives for biochemical applications[13] and show antibacterial[14] and antitumor[3c] activities. In addition, their photochemical and photophysical properties have been widely studied.[15] With this in mind, we report here a series of homoleptic and heteroleptic copper(I) complexes with phosphorus substituted phenanthroline ligands **1a**-**f**. Their solid-state structures were resolved and their solution behavior was studied by different spectroscopic methods and electrochemistry. The results of our studies should contribute to a better understanding of the photophysical[15] and catalytic[16] properties of these complexes and are important for a rational development of functional hybrid materials based on 1,10-

phenanthroline complexes for various applications, including light harversting systems and catalysis.[17]

7.2 Results and Discussion

7.2.1 Ligand Synthesis

The target ligands **1a-f** were prepared using the Hirao reaction from aryl halides **2a-f** according to a procedure recently described by our groups.[6] Remarkably, both chlorides and bromides reacted smoothly under these conditions, the chlorides being better suited as starting compounds for the synthesis of 2- or 4-substituted phenanthrolines due to their low cost. Products were obtained in good yields (65-90%) after purification by column chromatography.

Scheme 7-1. Synthesis of ligands **1a-f**.

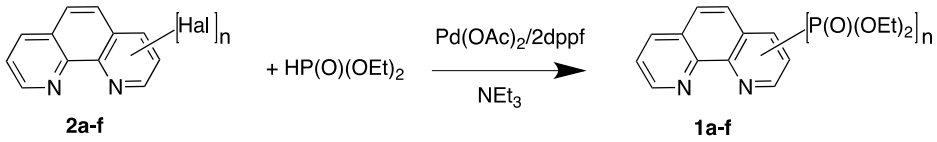

2a: Hal = 2-Cl; **2b**: Hal = 3-Br; **2c**: Hal = 4-Cl; **2d**: Hal = 5-Br;
2e: Hal = 2,9-Cl; **2f:** Hal = 3,8-Br

7.2.2 Synthesis of Copper(I) Complexes

The coordination affinity of (diethoxyphosphoryl)-phenanthrolines **1a-f** was not significantly influenced by the presence of the electron-withdrawing phosphorus substituent and their reactivity towards copper(I) derivatives was similar to that of the parent phenanthroline **1g** and independent on the number and the position of the diethoxyphosphoryl groups, with only one exception, that being the sterically bulky 2,9-diphosphonate **1e**.

Indeed, the reaction of isomeric phosphonates **1a-d** and **1f** with $Cu(PPh_3)_3Br$ in chloroform afforded $Cu(\mathbf{1a\text{-}d,f})(PPh_3)Br$ in 63-82% yields which is similar to that of 1,10-phenanthroline (**1g**) (Scheme 7-2). However, the bulky diphosphonate ligand **1e** failed to react under these conditions.

The complexes **3a**, **3c, 3d**, **3f**, and **3g** were air stable in the solid state and in different organic solvents. Complex **3b** was also stable under most conditions, but a slow oxidation was observed in chloroform/methanol, leading to a blue solution of a copper(II) complex during attempts to grow crystals for X-ray analysis.

Scheme 7-2. Synthesis of heteroleptic Cu(I) complexes **3a-d**, **3f**, and **3g**.

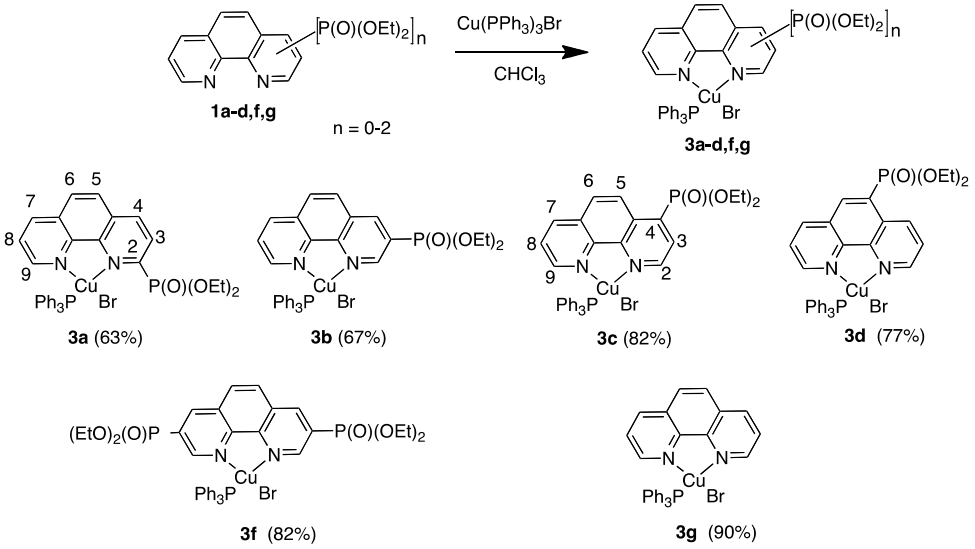

The synthesized complexes were initially characterized by MALDI-MS analysis and gave data consistent with the expected formula. Preliminary information on the structure of these complexes was obtained using IR spectroscopy because the PO stretching vibrations (ν = 1240-1270 cm^{-1}) in aryl phosphonates is sensitive to variation in the environment and a

bathochromic shift of ν =30-80 cm^{-1} occurs upon hydrogen-bond formation or coordination to a metal ion.[18] Only one ν(P=O) band at ν = 1239-1269 cm^{-1} was observed in the IR spectra of **3a-d** and **3f**, indicating that the PO group is not coordinated to the copper(I) ion.

The homoleptic bis-chelates [Cu(**1a-c**)$_2$]PF_6 (**4a-c**) were readily obtained by the reaction of [Cu(MeCN)$_4$]PF_6 with the mono-substituted phenanthrolines **1a-c** in CH_2Cl_2 solution. Steric hindrance of the 2-isomer **1a** did not significantly influence the product yield (Scheme 7-3). Under these conditions, the bulky ligand **1e** also reacted smoothly giving [Cu(**1e**)$_2$]PF_6 (**4e**) in 87% yield.

Scheme 7-3. Synthesis of homoleptic Cu(I) complexes **4a-c** and **4e**.

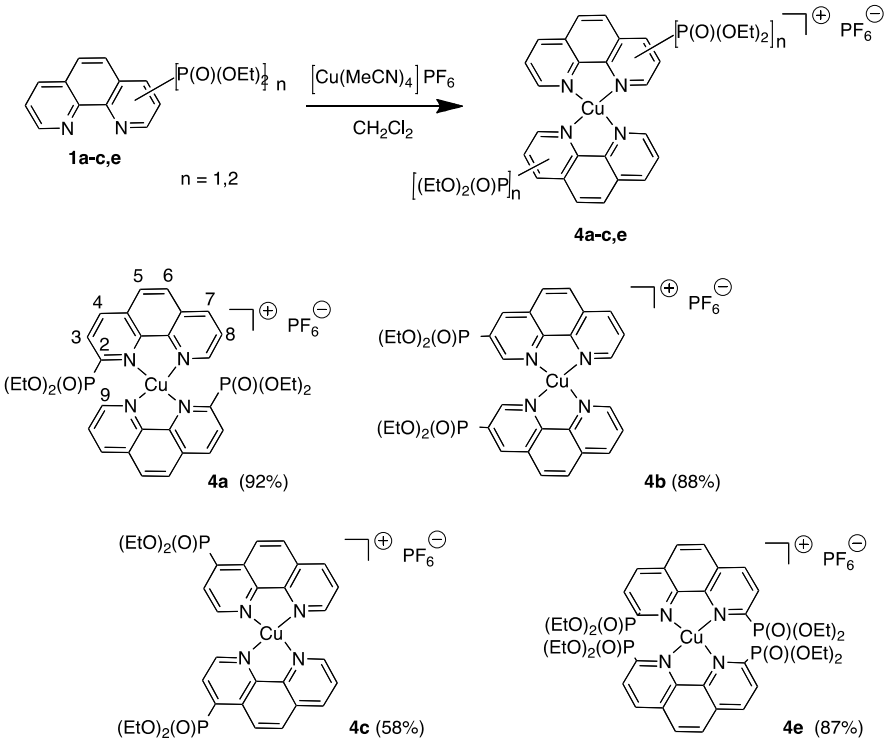

The complexes **4a-c** and **4e** are air-stable in the solid state and in CH_2Cl_2 or methanol solutions but slowly decompose in $CHCl_3$. MALDI-MS of **4a-c** and **4e** gave data corresponding to the expected composition with ligand to metal ratio of 2:1.

The complexes were also characterized by IR spectroscopy indicating that the phenanthroline chelators were coordinated to the copper(I) ion only by two nitrogen atoms and the phosphoryl groups are not bound to the copper center.

7.2.3 Crystal Structure

HSAB theory classifies Cu(I) as a soft acid and the preference of copper(I) ions for soft donor ligands such as phosphines, thiols, or chelating diimine ligands (2,2'-bipyridine, 1,10-phenanthroline) is well established. However, the copper(I) ion can accommodate both soft and hard donors in its coordination sphere in the solid state and in solution.[19] Phosphine oxides are suitable ligands to form such copper(I) complexes as was demonstrated for diphenylphosphinoethane and diphenylphosphinomethane monoxides,[20] 1,1'-bis(diphenylphosphino)ferrocene dioxide[21] and 6-(4-diethylmethylphosphonatephenyl)-2,2'-bipyridine.[22] It was of interest to compare the coordination mode of diethoxyphosphoryl-1,10-phenanthrolines in various copper(I) complexes.

Crystal structures of the copper(I) complexes were determined by single crystal X-ray diffraction. Crystallographic data for **3a**, **3c**, **3d**, **3f**, **4a**, and **4e** are represented in Table 1.

In the heteroleptic complexes **3a**, **3c**, **3d**, and **3f**, the four-coordinated copper (I) ion adopts a distorted tetrahedral geometry (Figure 7-1). The chelators **1a**, **1c**, **1d**, and **1f** exhibit bidentate coordination of the copper(I) atom by two nitrogen atoms and the inner-coordination sphere is completed by a bromine and a phosphorus atom of the triphenylphosphine ligand.

Table 7-1. Crystal data for **3a**, **3c**, **3d**, **3f**, **4a** and **4e** (data taken from ref 8).

	3a	**3c**	**3d**
Empirical formula	$C_{34}H_{32}BrCuN_2O_3P_2$	$C_{34}H_{32}BrCuN_2O_3P_2$	$C_{38}H_{42}BrCuN_2O_4P_2$
Formula weight	722.00	722.00	796.12
T/K	115	115	115
Crystal system	monoclinic	monoclinic	monoclinic
Space group	$P2_1/c$	$P2_1/c$	$P2_1/c$
a/Å	13.9612(6)	9.0943(3)	8.9662(2)
b/Å	14.0230(6)	14.9473(5)	13.7514(3)
c/Å	18.8623(8)	22.9609(6)	29.6049(6)
α/°	90	90	90
β/°	120.887(3)	96.2310(10)	97.3220(10)
γ/°	90	90	90
V/Å^3	3169.1(2)	3102.76(17)	3620.45(13)
Z	4	4	4
ρ_{calc}mg/mm^3	1.513	1.546	1.461
m/mm^{-1}	2.089	2.133	1.838
F(000)	1472.0	1472.0	1640.0
Crystal size/mm^3	0.15 × 0.06 × 0.05	0.35 × 0.15 × 0.12	0.25 × 0.05 × 0.05
2*Θ* range for data collection	7.288 to 54.894°	4.49 to 54.934°	4.058 to 54.998°
Index ranges	$-18 \le h \le 18$, $-15 \le k \le 18$, $-24 \le l \le 24$	$-11 \le h \le 11$, $-19 \le k \le 19$, $-28 \le l \le 29$	$-11 \le h \le 11$, $-17 \le k \le 17$, $-38 \le l \le 38$
Reflections collected	12333	28262	15409
Independent reflections	7021 [*R*(int) = 0.0629]	7077 [*R*(int) = 0.0663]	8248 [*R*(int) = 0.0340]
Data/restraints/ parameters	7021/0/233	7077/0/390	8248/22/417
Goodness-of-fit on F^2	1.166	1.160	1.103
Final *R* indexes [I>=2σ (I)]	R_1 = 0.1045, wR_2 = 0.2434	R_1 = 0.0667, wR_2 = 0.1727	R_1 = 0.0563, wR_2 = 0.1009
Final *R* indexes [all data]	R_1 = 0.1500, wR_2 = 0.2723	R_1 = 0.0768, wR_2 = 0.1788	R_1 = 0.0757, wR_2 = 0.1104
Largest diff. peak/hole /e Å^{-3}	1.58/-1.03	1.26/-0.94	1.27/-2.16

Table 7-1. Crystal data for **3a**, **3c**, **3d**, **3f**, **4a** and **4e** (continued).

	3f	**4a**	**4e**
Empirical formula	$C_{38}H_{41}BrCuN_2O_6P_3$	$C_{32}H_{34}Cu\ F_6N_4O_6P_3$	$C_{41}H_{54}Cl_2CuF_6N_4O_{12}P_5$
Formula weight	858.09	841.08	1198.17
T/K	115	115	115
Crystal system	triclinic	monoclinic	monoclinic
Space group	*P*-1	*C*2/c	$P2_1/c$
a/Å	9.6822(4)	17.3850(7)	15.7069(5)
b/Å	11.3919(4)	12.4191(4)	21.2043(7)
c/Å	18.5870(8)	17.2407(11)	17.2286(6)
α/°	95.640(2)	90	90
β/°	98.783(2)	113.715(2)	114.662(2)
γ/°	104.948(2)	90	90
V/Å^3	1937.07(14)	3408.0(3)	5214.7(3)
Z	2	4	4
ρ_{calc}mg/mm^3	1.471	1.639	1.526
m/mm^{-1}	1.766	0.866	0.757
F(000)	880.0	1720.0	2464.0
Crystal size/mm^3	0.3 × 0.15 × 0.15	0.3 × 0.1 × 0.07	0.25 × 0.25 × 0.15
2*Θ* range for data collection	5.31 to 72.28°	5.162 to 57.842°	4.786 to 65.794°
Index ranges	$-16 \le h \le 15$, $-18 \le k \le 18$, $-30 \le l \le 30$	$-23 \le h \le 23$, $-16 \le k \le 16$, $-23 \le l \le 23$	$-23 \le h \le 23$, $-32 \le k \le 32$, $-26 \le l \le 26$
Reflections collected	128080	36106	152981
Independent reflections	18159 [*R*(int) = 0.0708]	4497 [*R*(int) = 0.0768]	19458 [*R*(int) = 0.0759]
Data/restraints/ parameters	18159/12/468	4497/12/217	19458/10/677
Goodness-of-fit on F^2	1.019	1.051	1.041
Final *R* indexes [I>=2σ (I)]	R_1 = 0.0397, wR_2 = 0.0788	R_1 = 0.0744, wR_2 = 0.1738	R_1 = 0.0459, wR_2 = 0.1080
Final *R* indexes [all data]	R_1 = 0.0776, wR_2 = 0.0908	R_1 = 0.1013, wR_2 = 0.1938	R_1 = 0.0758, wR_2 = 0.1242
Largest diff. peak/hole /e Å^{-3}	0.90/-0.82	2.73/-2.53	1.19/-1.15

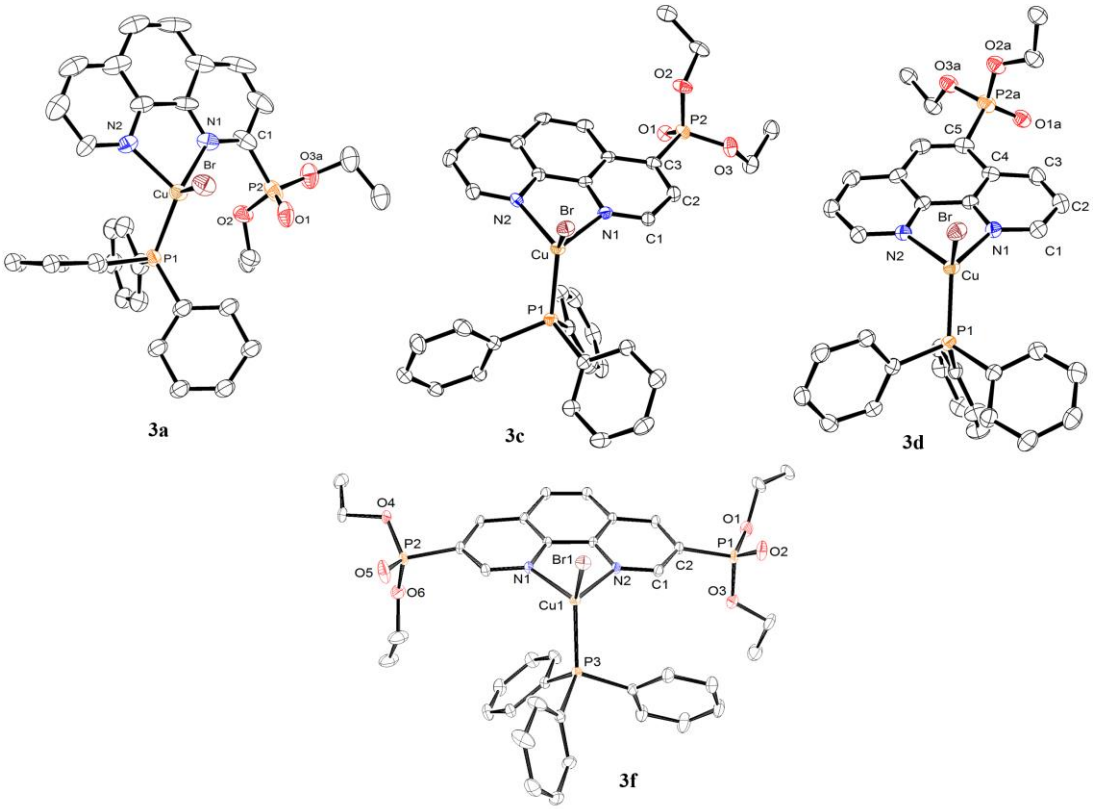

Figure 7-1. ORTEP[23] views of compound **3a**, **3c**, **3d**, and **3f**. Thermal ellipsoids are drawn at 50% probability. Solvent molecules, disordered parts and hydrogen atoms are not shown for clarity (taken from ref 8).

The selected bond lengths and angles reported in Table 7-2 lie in the usual ranges and are comparable with those for Cu(phen)(PPh_3)Br (**3g**)[24] except for complex **3a**, which bears a bulky diethoxyphosphoryl substituent in the α position of the phenanthroline ligand.

For this compound the angles between N1–Cu–P1 and N2–Cu–Br are significantly different from those of the other studied complexes. This difference in the orientation of the phosphorus and bromine atoms is shown in Figure 7-2. When the phenanthroline rings of **3a** and **3c** are overlaid, the distances between corresponding heteroatoms are 0.651 and 0.762 Å for the phosphorus and bromine atoms, respectively.

Another interesting feature of all the studied compounds is related to the Cu–N distances which are similar and range from 2.077 to 2.1236 Å, independent of the number and location of the electron-withdrawing substituents.

The molecular packing for complex **3a** is significantly different from that of the other complexes. As shown in Figure 7-3, **3c**, **3d**, and **3f** form dimers in which two phenanthroline moieties are almost parallel and their interplanar distance is equal to 3.3 Å in all the studied compounds indicating efficient π-stacking interactions. The middle ring of each phenanthroline ligand overlaps in a face-to-face mode with the alternated alignment of carbon atoms. In complex **3a**, the diethoxyphosphoryl group in the α position disturbs this π-stacking and the heteroaromatic residues associate via edge-to-face C–H ….π-interactions.

ORTEP views of bis-chelates **4a** and **4e** are represented in Figure 7-4. Once again, the bulky diethoxyphosphoryl group in the α position significantly influences the geometry of the copper(I) ion.

Table 7-2. Selected bonds lengths (Å) and angles (°) in **3a**, **3c**, **3d**, **3f**, and **3g** (data taken from ref 8).

bond length or angle	**3a**	**3c**	**3d**	**3f**	**3g** CCDC BEQLAK[24]
Br-Cu	2.4490(11)	2.4096(8)	2.4359(6)	2.3812(2)	2.4436(10)
Cu-N1	2.1003(15)	2.119(4)	2.077(3)	2.0980(12)	2.079(3)
Cu-N2	2.1087(16)	2.077(4)	2.088(3)	2.1236(12)	2.104(2)
Cu-P1	2.1793(15)	2.1958(14)	2.1823(10)	2.1880(4)	2.1856(12)
N1-Cu-N2	79.75(6)	79.88(17)	79.98(12)	79.35(5)	79.89(10)
N1-Cu-P1	135.33(6)	113.16(12)	125.43(9)	109.74(4)	123.76(8)
N2-Cu-P1	112.28(6)	119.39(12)	118.69(9)	113.35(4)	118.59(8)
N1-Cu-Br	106.93(5)	111.06(12)	106.88(9)	109.12(3)	102.96(8)
N2-Cu-Br	96.93(5)	107.52(12)	109.67(9)	110.78(3)	105.84(8)
P1-Cu-Br	113.55(5)	119.24(4)	112.00(3)	125.051(13)	118.63(3)

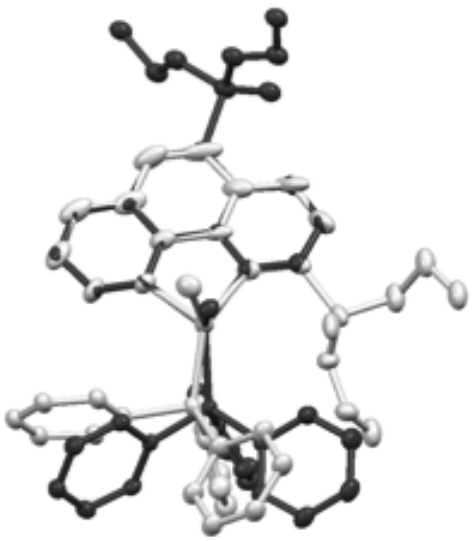

Figure 7-2. Overlay of **3a** (grey) and **3c** (black) (taken from ref 8).

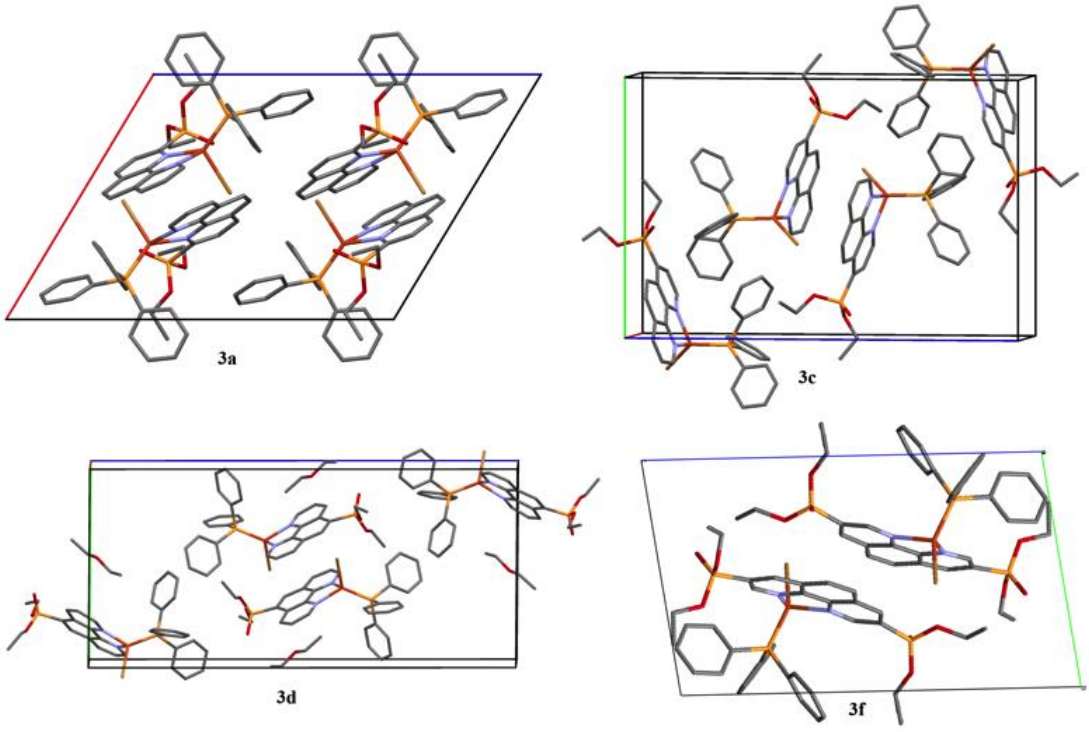

Figure 7-3. Views of crystal packing in **3a**, **3c**, **3d**, and **3f** (taken from ref 8).

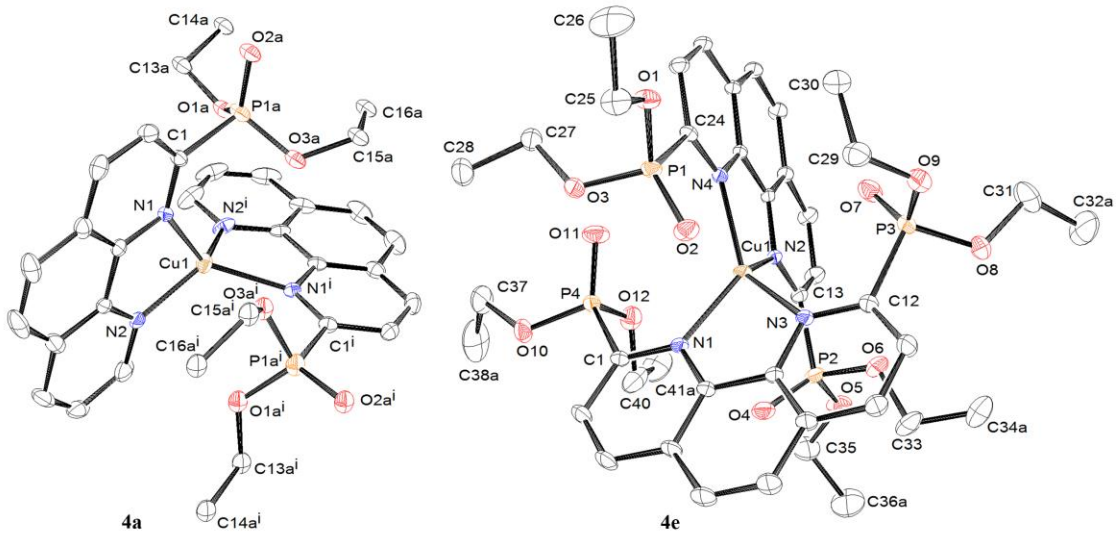

Figure 7-4. ORTEP[23] views of compound **4a** and **4e**. Thermal ellipsoids are drawn at 50% probability. Solvent molecules, disordered groups and hydrogen atoms are not shown for clarity (taken from ref 8).

The copper(I) ion is in a tetrahedral environment with small distortion from T_d symmetry in both complexes **4a** and **4e**. This geometry is unusual for copper(I) bis-chelates where a distorted seesaw geometry (C_{2v}) for the metal center is generally observed. The selected bond lengths and angles are given in Table 7-3.

In complex **4a**, two Cu—N distances of each ligand molecule are similar to each other (1.996 and 2.081 Å) and comparable to those of the complex **4e** (2.0056 - 2.0245 Å) as well as the heteroleptic complexes **3a**, **3c**, **3d**, and **3f** (Table 7-2). Two stereoisomeric molelules of **4a** co-crystallyzed in one unit cell.

It is also interesting to compare molecular packing for complexes **4a** and **3a** which contain the same bulky α-(diethoxyphosphoryl)phenanthroline ligand (Figures 7-3 and 7-5). In contrast to **3a** described above, the 1,10-phenanthroline rings of adjacent molecules are parallel in the racemic compound **4a** and are predisposed for π-π stacking. However, a steric hindrance induced by the diethoxyphosphoryl substituent prohibits stacking interactions, as indicated by the value of the interplanar distance between these fragments which is close to 6.9 Å. Surprisingly, in the crystal of complex **4e**, where the ligand bears two bulky substituents in the α position, this interplanar spacing was decreased up to 3.3 Å testifying an efficient π-π stacking of the 1,10-phenanthroline rings (Figure 7-5).

Thus, the phosphoryl group of diethoxyphosphoryl-substituted phenanthrolines is non-coordinated in all the currently studied complexes including those where the structures allow a chelation and facilitate the coordination, e.g. ligands **1a** and **1e**.

Table 7-3. Selected bonds lengths (Å) and angles (°) in **4a** and **4e** (data taken from ref 8).

bond length or angle	**4a**	bond length or angle	**4e**
Cu-N1	2.081(3)	Cu-N1	2.0056(14)
Cu-N2	1.996(3)	Cu-N2	2.0089(14)
$N1^{i}$-Cu-N1	124.29(17)	Cu-N3	2.0245(14)
N2-Cu-N1	82.50(13)	Cu-N4	2.0118(14)
N2-Cu-$N1^{i}$	122.49(12)	N1-Cu-N2	113.16(12)
$N2^{i}$-Cu-N1	122.49(12)	N1-Cu-N3	119.39(12)
$N2^{i}$-Cu-$N1^{i}$	82.50(13)	N1-Cu-N4	111.06(12)
N2-Cu-$N2^{i}$	128.4(2)	N2-Cu-N3	107.52(12)
		N2-Cu-N4	119.24(4)
		N4-Cu-N3	125.96(6)

Symmetry code (i) 1-x,y,3/2+z.

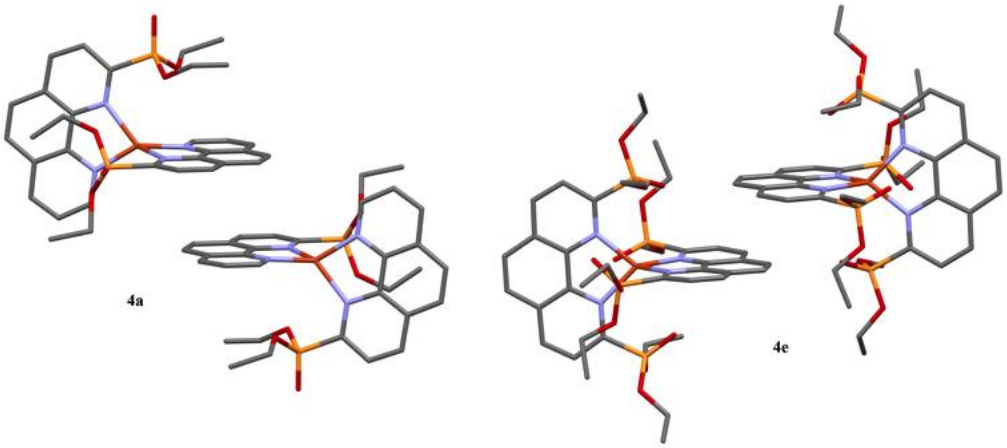

Figure 7-5. View of phenanthroline ring stacking in **4a** and **4e** (taken from ref 8).

7.2.4 Electrochemistry and Spectroelectrochemistry

Six heteroleptic Cu(I) phenanthroline complexes, **3a**-**d**, **3f**, and **3g** (Scheme 7-2), and three bis-phenanthroline Cu(I) complexes, **4a**, **4b**, and **4e** (Scheme 7-3), were investigated to elucidate how changes in the number and location of $P(O)(OEt)_2$ substituents on the bound phenanthroline ligand(s) would affect redox potentials and the overall oxidation/reduction mechanisms. The measured half-wave or peak potentials for oxidation and reduction of each Cu(I) complex in CH_2Cl_2 or PhCN containing 0.1 M TBAP are summarized in Table 7-4, which includes data for three reference compounds, unsubstituted phenanthroline, triphenylphosphine, and bromide ion (added in the form of TBABr). The site of electron transfer for each electrode reaction is also given in Table 7-4, with assignments being based on the measured potentials and previous assignments of electron transfer site given in the literature[25] for related compounds.

7.2.4.1 Electrochemistry of Heteroleptic Derivatives

The investigated mono-phenanthroline complexes **3a**-**d**, **3f**, and **3g** undergo multiple redox reactions. Examples of cyclic voltammograms for three of the six characterized heteroleptic complexes are shown in Figure 7-6, along with the three reference compounds, phenanthroline, PPh_3 and TBABr.

As seen in this figure, the unsubstituted phenanthroline group is electrochemically inactive over the investigated range of potentials (-2.0 to +2.0 V vs SCE), while PPh_3 and Br^- are oxidized in one and two irreversible electron transfer steps, respectively. Compounds **3a**, **3f** and **3g** also undergo similar irreversible redox processes associated with PPh_3 and/or Br^- oxidations, although as described below, this depends on the solvent. There are also

Table 7-4. Half-wave or peak potentials (V vs SCE) and proposed site of electron transfer for redox reactions of the investigated compounds (see Schemes 7-2 and 7-3 for Structures).

Solvent	Cpd	Oxidation				Reduction	
		Br^-(2)	PPh_3	Br^- (1)	Cu^I/Cu^{II}	Cu^I/Cu^0	Phenanthroline
CH_2Cl_2	**3a**	1.45[a]	1.25[a]	0.85[a]	0.35	-1.41[c]	
	3b		1.20[a]		0.67,[a] 0.17[c]	-1.28[c]	
	3c		1.20[a]		0.67,[a] 0.11[c]	-1.26	
	3d		1.20[a]		0.65,[a] 0.07[c]	-1.42[c]	
	3f		1.25[a]		0.70,[a] 0.24[c]	-1.10	-1.60[c]
	3g		1.18[a]		0.34,[a, b] 0.10[c]	-1.60[c]	
	PPh_3		1.26[a]		--	--	
	TBABr	1.25[a]		0.84[a]	--	--	
	4a				0.32	-1.46[b]	
	4b				0.48	-1.40[b]	-1.57
	4e				0.49	-1.45[b]	-1.89[c, d]
PhCN	**3a**	1.40[a]	1.15[a]	1.00[a]	0.33	-1.32	-1.86
	3b	1.38[a]	1.10[a]	1.10[a]	0.60,[a] 0.14[c]	-1.22	-1.72[c]
	3c	1.37[a]	1.14[a]	1.14[a]	0.63,[a] 0.10[c]	-1.24	-1.73[c]
	3d	1.35[a]	1.13[a]	0.96[a]	0.58,[a] 0.09[c]	-1.38[b]	
	3f	1.50[a]	1.23[a]	1.00[a]	0.64,[a] 0.23[c]	-1.08	-1.46
	3g	1.38[a]	1.08[a]	0.90[a]	0.36,[a, b] 0.05[c]	-1.50	
	PPh_3		1.26[a]		--	--	
	TBABr	1.40[a]		0.80[a]	--	--	
	4a				0.32	-1.34	-1.80[d]
	4b				0.33	-1.30[c]	-1.51, -1.76
	4e				0.83,[a] 0.39[c]	0.84[c]	-1.21, -1.59,[c] -1.68[d]

[a]E_{pa} at a scan rate of 0.1 V/s. [b]Show a split peak at E_{pa} = 0.56 - 0.60 V (see Figure 7-6). [c]E_{pc} at a scan rate of 0.1 V/s. [d]Overlapping of several one-electron processes.

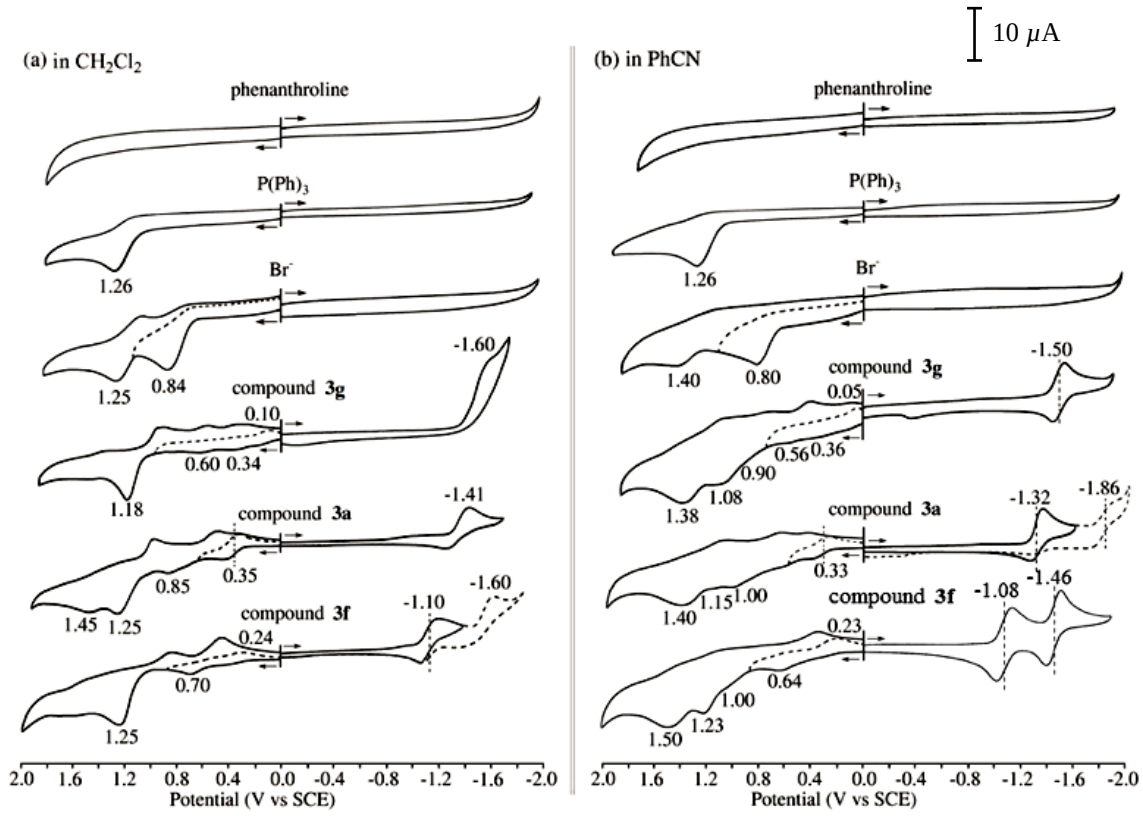

Figure 7-6. Cyclic voltammograms of phenanthroline, Ph_3P, Br^- (in the form of TBABr) and compounds **3a**, **3f** and **3g** in (a) CH_2Cl_2 and (b) PhCN containing 0.1 M TBAP at a scan rate of 0.1 V/s.

electrode reactions involving the substituted phenanthroline ligands on **3a** and **3f** as well as metal-centered reactions involving reduction or oxidation of the Cu(I) ion.

The reversibility and potentials of the Cu^{I}/Cu^{0} and Cu^{I}/Cu^{II} reaction also vary with changes in the solvent, temperature, and potential scan rate, as well as with the number and location of $P(O)(OEt)_2$ substituents on the phenanthroline ligand.

The Cu^{I}/Cu^{II} process is reversible only in the case of compound **3a**, while all but one or two of the six heteroleptic compounds in Scheme 7-2 show reversible Cu^{I}/Cu^{0} reductions in PhCN (**3d** is the only exception) and CH_2Cl_2 (see Table 7-4 where **3b** and **3d** are both irreversibly reduced). The expected influence of electron-withdrawing $P(O)(OEt)_2$ group on the potential values can be seen only for some reduction processes. For example, the Cu^{I}/Cu^{0} reaction of **3g** (which has no $P(O)(OEt)_2$ groups, see Scheme 7-2), is located at $E_{1/2}$ = -1.50 V in PhCN while **3b** (which has one $P(O)(OEt)_2$ group) is reduced at $E_{1/2}$ = -1.22 V and **3f** (which possesses two $P(O)(OEt)_2$ groups) is reduced at $E_{1/2}$ = -1.08 V. Thus, addition of the first electron-withdrawing $P(O)(OEt)_2$ group to **3g** leads to a 280 mV positive shift of $E_{1/2}$ (for compound **3b**), while addition of a second group (to give compound **3f**) results in a smaller 100 mV positive shift in potential.

Figure 7-7 illustrates the effect of temperature and scan rate on the redox behavior of complex **3c** in CH_2Cl_2. With the exception of slow scan rates (0.05 V/s), the reduction of Cu^{I} to Cu^{0} is reversible. However, at longer times (slower scan rates) all of the ligands dissociate after generation of Cu^{0} and when this occurs, the overall Cu^{I}/Cu^{0} reduction becomes irreversible.

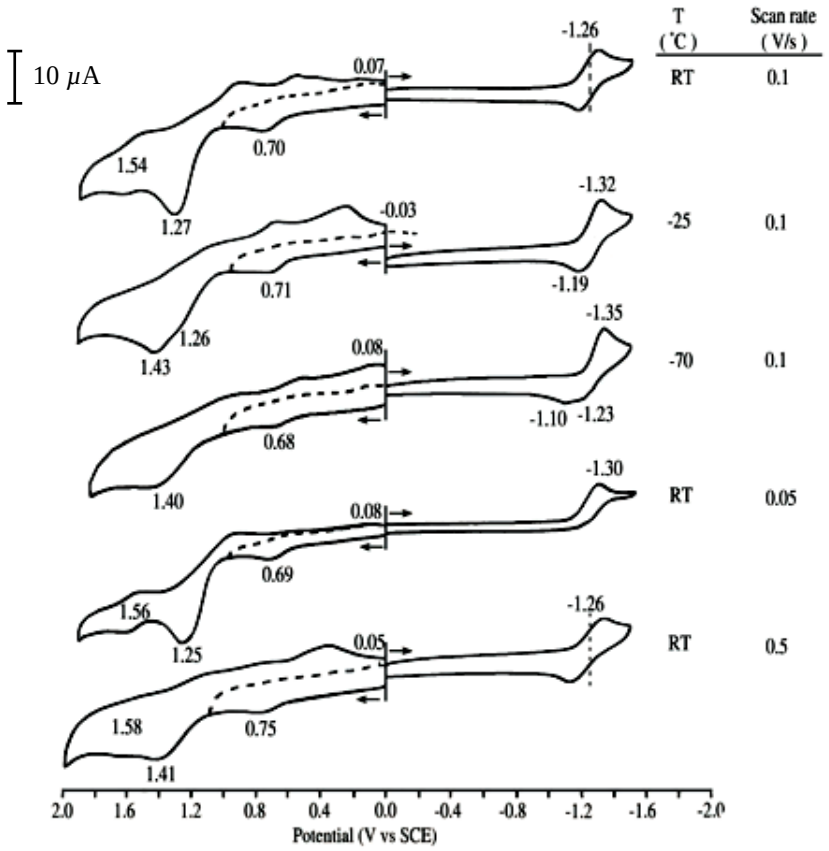

Figure 7-7. Cyclic voltammograms of compound **3c** in CH_2Cl_2 containing 0.1 M TBAP at the indicated temperature and scan rate.

Interestingly, the number of electroreductions depends upon the presence or absence of an $P(O)(OEt)_2$ group on the phenanthroline ligand. Compound **3g**, which lacks a $P(O)(OEt)_2$ substituent (see Scheme 7-2), exhibits no reductions beyond the Cu^I/Cu^0 process at $E_{1/2}$ = -1.50 V, while compounds **3a**, **3b**, and **3c**, all contain a single $P(O)(OEt)_2$ substituent and exhibit one additional reduction at -1.72 to 1.86 V. Compound **3f** has two $P(O)(OEt)_2$ substituents and in both CH_2Cl_2 and PhCN a second reversible reduction is observed following the Cu^I/Cu^0 process, these reactions occurring at $E_{1/2}$ = -1.60 V and $E_{1/2}$ = -1.46 V, respectively. Since $P(O)(OEt)_2$ is electrochemically inert,[26] as is unsubstituted phenanthroline (see top CV in Figure 7-6), the second electron addition to compounds **3a-c** and **3f** at negative potentials are proposed to occur at the benzene rings containing the electron-withdrawing $P(O)(OEt)_2$ groups. A similar reduction process is seen for free ligands containing one or two $P(O)(OEt)_2$ groups and has been reported for benzene with one or two electron-withdrawing groups (e.g. CN, NO_2, Br and CO_2Me).[27]

As mentioned above, the unsubstituted phenanthroline exhibits no oxidations, while triphenylphosphine shows one oxidation (E_{pa} = 1.26 V) and Br^- exhibits two oxidations. These latter reactions occur at E_{pa} = 0.80 V and E_{pa} =1.40 V in PhCN and at E_{pa} = 0.84 V and E_{pa} =1.25 V in CH_2Cl_2. Thus, the first oxidation peaks of **3b-d**, **3f** and **3g** at E_{pa} = 0.34-0.70 V and $E_{1/2}$ = 0.35 V for **3a** in CH_2Cl_2 are assigned to a Cu^I/Cu^{II} process which is coupled with a re-reduction at E_{pc} = 0.07-0.24 V on the return sweep. Among the investigated mono-phenanthroline complexes, only compound **3a** exhibits a reversible Cu^I/Cu^{II} couple while the other five mono-phenanthroline complexes show non-coupled oxidation and re-reduction peaks due to the presence of a coupled chemical reactions, probably related to a change in the type of metal ion ligand coordination[25b,25d,28] and/or the number of bound ligands after

electron transfer.[29] The further oxidations of **3a-d**, **3f** and **3g** (at E_{pa} = 0.85-1.45 V in CH_2Cl_2 or E_{pa} = 0.90-1.50 V in PhCN) are then attributed to the presence of Br^- and PPh_3 in solutions of these compounds. In CH_2Cl_2, a Br^- oxidation can be detected only for **3a** (at E_{pa} = 0.85 V and E_{pa} = 1.45 V), suggesting that a Br^- is not coordinated to the Cu(I) ion center of this complex, even in CH_2Cl_2 solution. This behavior and the value of potential of Cu^I/Cu^{II} process are consistent with a decomposition of **3a** to give the bis-phenanthroline complex corresponding to **4a**, with uncoordinated Br^-. This complex could be formed after triphenylphosphine dissociation, followed by further ligand exchange reactions (Eq 7-1). The structure of the second product was tentatively assigned to a known compound, $Cu_2(PPh_3)_3Br_2$.[30]

$$\underset{\textbf{3a}}{4Cu(\textbf{1a})(PPh_3)Br} \rightleftharpoons 2[Cu(\textbf{1a})_2]Br + Cu_2(PPh_3)_3Br_2 + PPh_3 \qquad (7\text{-}1)$$

The fact that Br^- oxidation is not observed in CH_2Cl_2 for compounds **3b-d**, **3f**, and **3g** suggests that bromide is not dissociated from the Cu(I) ion in the non-binding solvent CH_2Cl_2. However, this is not the case in PhCN, where two oxidations assigned to Br^- are observed for **3a-d**, **3f**, and **3g** after probable ligand displacement by PhCN (Eq 7-2).

$$\underset{\textbf{3c}}{Cu(\textbf{1c})(PPh_3)Br} + PhCN \rightleftharpoons [Cu(\textbf{1c})(PPh_3)(PhCN)]^+ + Br^- \qquad (7\text{-}2)$$

7.2.4.2 Electrochemistry of Homoleptic Complexes

The electrochemical behavior of compounds **4a**, **4b**, and **4e** in CH_2Cl_2 and PhCN is shown in Figure 7-8 and the assigned electron transfer sites for each electrode reaction are given in Table 7-4. Compounds **4a**, **4b**, and **4e** do not possess a Br^- or PPh_3 ligand and only a single reversible Cu^I/Cu^{II} process is observed for these compounds in CH_2Cl_2.

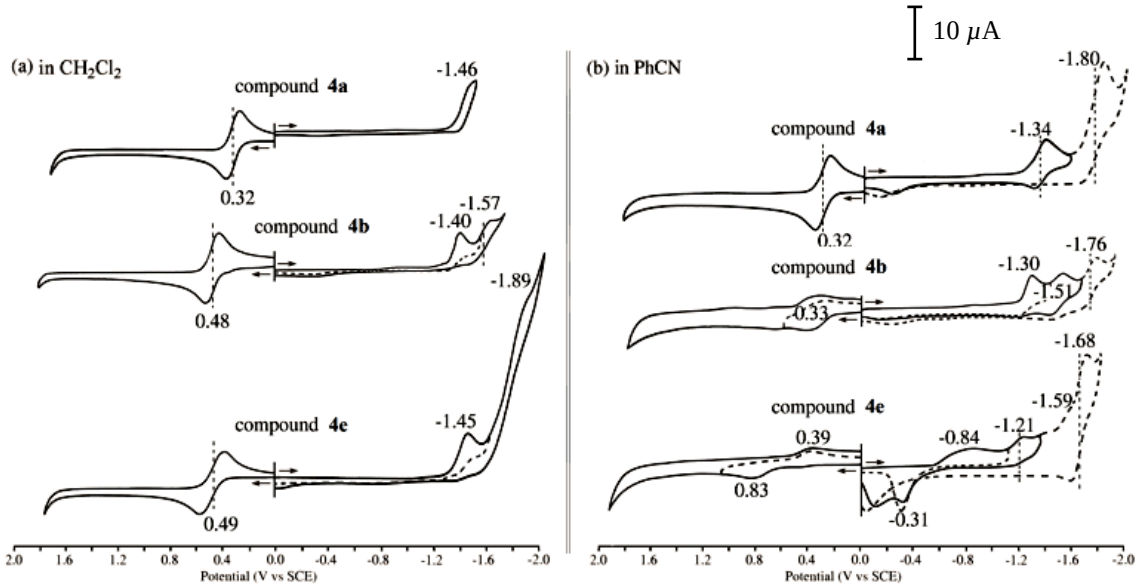

Figure 7-8. Cyclic voltammograms of **4a**, **4b** and **4e** in (a) CH_2Cl_2 and (b) PhCN containing 0.1 M TBAP at a scan rate of 0.1 V/s.

One exception to the reversible Cu^{I}/Cu^{II} reaction is seen for compound **4e** which exhibits a broad and ill-defined oxidation peak in PhCN. The oxidation and re-reduction peaks are located at E_{pa} = 0.83 V and E_{pc} = 0.39 V and the overall shape of the current-voltage curve is similar to that of the mono-phenanthroline compounds discussed earlier. The behavior of **4e** in PhCN suggests that one of the two bound phenanthroline ligands dissociates from Cu(I) prior to electron transfer.

The Cu^{I}/Cu^{0} reductions of **4a**, **4b**, and **4e** are irreversible and located at E_{pc} = -1.40 to -1.46 V in CH_2Cl_2 for a scan rate of 0.1 V/s. The same process of **4a** and **4b** are quasi-reversible in PhCN and located at $E_{1/2}$ or E_{pc} = -1.30 to -1.34 V. Compound **4e** shows an irreversible Cu^{I}/Cu^{0} reduction at E_{pc} = -0.84 V in PhCN and exhibits a "stripping-like" anodic peak at E_{pa} = -0.31 V. This is consistent with Cu^{0} plating onto the electrode upon reduction and being stripped off upon re-oxidation.

An irreversible reduction of the $P(O)(OEt)_2$ substituted phenanthroline ligands on **4b** and **4e** can be detected in CH_2Cl_2, respectively at $E_{1/2}$ = -1.57 V (**4b**) and E_p = -1.89 V (**4e**) for a scan rate of 0.1 V/s, while reversible ligand-centered reductions are observed in PhCN for the three investigated bis-phenanthroline compounds (see Table 7-4). The cyclic voltammograms in PhCN (Figure 7-8b) show, in some cases, two separated ligand-centered reductions, and in others, an overlapping of multiple electron transfers are observed.

7.2.4.3 Spectroelectrochemistry

The investigated copper complexes were also characterized and examined by thin-layer spectroelectrochemistry under the same solution conditions in order to confirm the proposed redox processes using ligand-centered π-π* transitions (IL) and the metal-to-ligand charge

transfer (MLCT).[31] Examples of the UV-visible spectral changes obtained during controlled redox processes of **3f** and **4b** in CH_2Cl_2 are given in Figures 7-9 and 7-10.

The spectrum of the neutral **3f** in CH_2Cl_2 containing 0.1 M TBAP is dominated by a two strong near UV bands at λ_{max} = 232 and λ_{max} = 273 nm. There is also a shoulder at λ_{max} = 295 nm as well as a weak broad visible band near λ_{max} = 450 nm. Absorption in the UV and visible regions can be attributed to IL and MLCT transitions, respectively.

During the first oxidation of **3f**, the Cu(I) ion is oxidized to Cu(II). As shown in Figure 7-9a, the broad visible MLCT band near λ_{max} = 450 nm and the shoulder at λ_{max} = 295 nm, both disappear and a new shoulder appears near λ = 313 nm, while the intensity of the λ_{max} = 273 nm IL band slightly decreases and the λ_{max} = 232 nm IL band shifts to λ_{max} = 228 nm. The final spectrum for Cu(II) complexes is characterized by bands at λ_{max} = 228, 277 and 313 nm.

Switching the controlled potential to E_{app} = 1.40 V gave the spectral changes shown in Figure 7-9b. At this potential, the PPh_3 ligand and the Br^- counteranion should both be oxidized but there is almost no change in the spectra. This might be explained by the fact that the UV-visible spectrum of **3f** is dominated by IL of phenanthroline fragment (see above). Thus, changing the electronic states of PPh_3 or Br^- does not significantly affect the UV-visible spectrum of the molecule.

Figure 7-9c shows spectral changes for the Cu^I/Cu^0 reduction of **3f** at a controlled potential of E_{app} = -1.30 V. The broad visible band of the neutral compound blue shifts from 450 to 396 nm, while a slight decrease in absorbance is seen at λ_{max} = 273 nm and λ_{max} = 295 nm. Switching the applied potential to E_{app} = -1.70 V (Figure 7-9d) shows an obvious

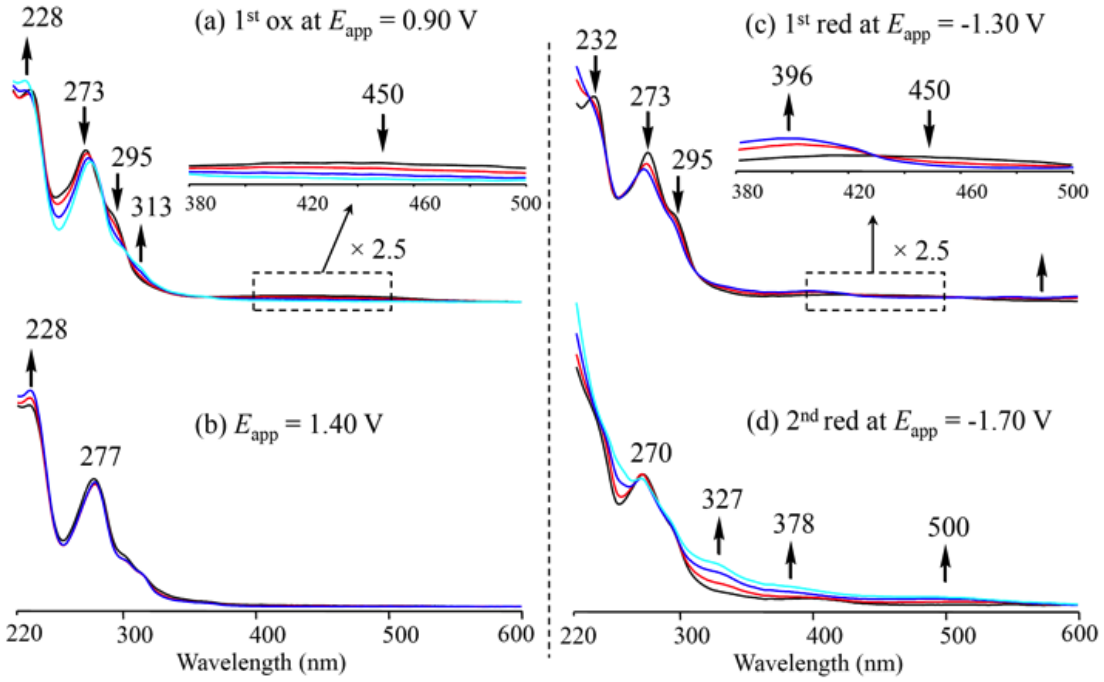

Figure 7-9. UV-visible spectral changes of **3f** during indicated redox potentials in CH_2Cl_2 containing 0.1 M TBAP.

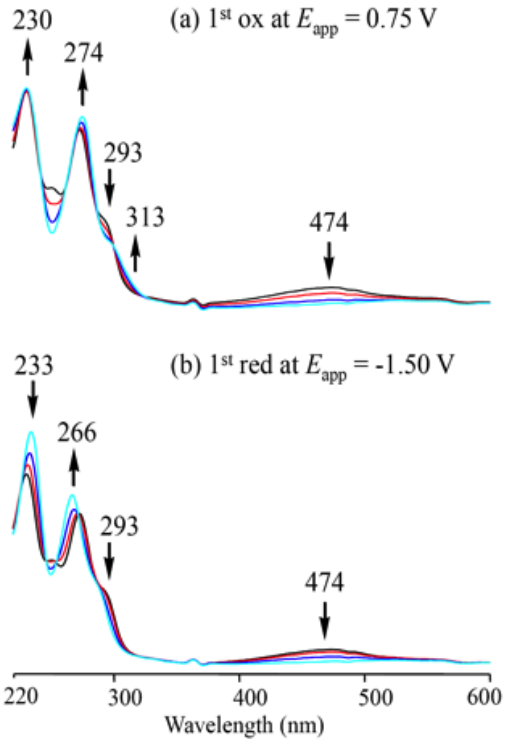

Figure 7-10. UV-visible spectral changes of **4b** during indicated redox potentials.

increase in intensity of the bands at λ_{max} = 327, 378, and 500 nm. The second reduction of **3f** occurs at the substituted phenanthroline ring. This reduction results in a change of the electronic states of the phenanthroline ligand and the spectral changes are assigned as resulting upon formation of the substituted phenanthroline π-anion radical.[31b]

Figure 7-10a shows the spectral changes which occur during the Cu^{I}/Cu^{II} oxidation of the bis-phenanthroline compound **4b** in CH_2Cl_2. The initial broad visible band at λ_{max} = 474 nm decreases upon formation of Cu(II) and this compound has bands at λ_{max} = 230, 274 and 313 nm, similar to the spectrum of the Cu(II) mono-phenanthroline compound **3f**. At an applied reducing potential of E_{app} = -1.50 V (Figure 7-10b), the broad visible band of **4b** at λ_{max} = 474 nm disappears and no new visible bands are seen. This is different from the spectra of the Cu^0 species obtained in the case of **3f**, probably due to a rapid ligand dissociation in the case of **4b**. The cyclic voltammograms of **3f** and **4b** in CH_2Cl_2 (see Figures 7-6 and 7-8) also suggest this occurrence.

Thus, systematic electrochemical and spectroelectrochemical studies of copper(I) complexes with diethoxyphosphoryl-1,10-phenanthrolines have shown that the steric hindrance of the metal center is a key factor for the overall oxidation/reduction process. Bulky and weakly coordinating ligands dissociate quite readily leading to irreversible behavior of the systems. The ligand dissociation may proceed in copper(I) complexes and/or during redox processes leading to the change of coordination properties of the metal center. Interestingly, the electronic influence of the electron-withdrawing diethoxyphosphoryl substituent on the redox potentials is rather limited whereas steric effects of this substituent located in the *α* position are much more pronounced and observed for the studied complexes in both series.

To gain a deeper insight into the behavior of the newly synthesized complexes in solution, detailed multinuclear NMR studies were undertaken, supplemented by UV-vis absorption and high-resolution electrospray ionisation mass spectrometry (ESI/MS) investigations.

7.2.4.4 Structural Determination in Solution

The solution behavior of homoleptic and heteroleptic complexes is rather different because all of the ligands at the copper(I) center are involved in ligand exchange reactions. Moreover, in each series the solution speciation is dependent upon the location of the phosphorus substituent on the phenanthroline backbone and the nature of the solvent.

In the ESI/MS spectra of the bis-chelate complexes **4a**-**c**, the major peaks are attributed to the loss of the hexafluorophosphate counterion $[\mathbf{4}\text{-}PF_6]^+$ {m/z = 695.123}. Small peaks corresponding to the consecutive loss of hexafluorophosphate and one phenanthroline ligand $[\mathbf{4}\text{-}PF_6\text{-}\mathbf{1}]^+$ {m/z = 379.026} and the peaks of free ligands $[\mathbf{1}+Na]^+$ {m/z = 339.087} are also observed for compounds **4a**,**b**. In the spectrum of **4e**, the intensities of the corresponding peaks $[\mathbf{4e}\text{-}PF_6\text{-}\mathbf{1e}]^+$ and $[\mathbf{1e}+Na]^+$ are higher as compared to $[\mathbf{4e}\text{-}PF_6]^+$, indicating that ligand dissociation is favored by the steric hindrance of the copper(I) center.

Additional structural information can be extracted from the ^1H and ^{31}P NMR spectra of complexes **4a**-**c** and **4e** because all of the expected signals are observed as distinct and often as sharp signals.

The number and splitting patterns of the proton resonances point out the presence of only one major species in the studied CD_2Cl_2 and $CDCl_3$ solutions. Binding of the copper(I) ion induces pronounced spectral changes in the ^1H NMR spectra of the ligands **1a**-**c** and **1e**, especially in the low field region, reflecting coordination of the phenanthroline moiety to the

copper(I) ion by two nitrogen atoms. In the aliphatic region, proton resonances of the ethoxy groups were shifted upfield (by more than $\Delta\delta$ = 0.7 ppm for CH_2 resonances and $\Delta\delta$ = 0.4 ppm for CH_3 signals) only in the spectra of **4a** and **4e** bearing α-diethoxyphosphoryl substituent, thus indicating the presence of a second phenanthroline ligand on the metal center. Another piece of evidence is provided by two characteristic $ABPX_3$ spin systems corresponding to the ethoxy groups in **4a**. The corresponding resonances of **4b**, **4c** are more simple and resemble those of the free ligands having two equivalent ethoxy groups. This simplification could be related to a rapid ligand exchange.

Thus, according to NMR data and in agreement with the solid state and electrochemical studies for **4a** and **4e**, mononuclear bis-chelate species exist in the CD_2Cl_2 or $CDCl_3$ solutions for the complexes **4a-c** and **4e**. However, these complexes seem to be labile at room temperature.

To gain a deeper insight into the ligand exchange reactions, complexes **4a** and **4e** were mixed together at different ratios, dissolved in CD_2Cl_2 and the solutions studied by ^1H and ^{31}P NMR spectroscopies. The spectra were recorded at room temperature just after dissolution of the compounds. Three sets of narrow signals attributed to the homoleptic complexes **4a**, **4e** and the mixed-ligand species [Cu(**1a**)(**1e**)]PF_6 (**4g**) were observed in the spectra, indicating a rapid ligand exchange (Eq 7-3).

$$\underset{\textbf{4a}}{[Cu(\textbf{1a})_2]PF_6} + \underset{\textbf{4e}}{[Cu(\textbf{1e})_2]PF_6} \rightleftharpoons \underset{\textbf{4g}}{2[Cu(\textbf{1a})(\textbf{1e})]PF_6} \qquad (7\text{-}3)$$

The intensity of the NMR signals was independent of the time and more than a 2.5-fold excess of **4e** over **4a** was needed for quantitative formation of the heteroleptic complex **4g**

from **4a**. This result indicates that complex **4a** is more stable and the ligand dissociation is favored in sterically bulky complex **4e** compared to **4a**.

When the spectra of **4a** and **4e** were recorded in a coordinating solvent such as CD_3CN, only in the case of **4a** was the bis-chelate a major species. In the spectrum of the bulky complex **4e**, two sets of sharp signals were observed in an 8:1 ratio. The minor signals are attributed to the expected bis-chelate. Signals of the major set are only slightly deshielded compared to those of the free ligand and are ascribed to a mixture of the heteroleptic chelate **5e** and the free ligand **1e** being in a rapid equilibrium (Eq 7-4).

$$\underset{\textbf{4e}}{[Cu(\textbf{1e})_2]PF_6} + 2CD_3CN \rightleftharpoons \underset{\textbf{5e}}{[Cu(\textbf{1e})(CD_3CN)_2]PF_6} + \textbf{1e} \qquad (7\text{-}4)$$

This behavior is in a good accordance with the electrochemical data obtained for **4e** in PhCN described above. As seen in Scheme 7-3, two substituted phenanthroline ligands with bulky $P(O)(OEt)_2$ groups closely surround the Cu(I) ion in the complex **4e**. One would expect a steric repulsion between two phenanthroline ligands, leading to the replacement of one phenanthroline ligand by two smaller solvent molecules. This ligand exchange could occur in the binding solvent CD_3CN but not in the non-binding solvent CD_2Cl_2.

The solution behavior of Cu(**1a-d**,**f**)(PPh_3)Br (**3a-d** and **3f**) was more complicated. In the ESI/MS spectra of **3a-d** and **3f** obtained from CH_2Cl_2/methanol solutions, the expected peaks corresponding to the loss of bromide ions [**3a-d**,**f**-Br]$^+$ {m/z = 641.117 for **3a-d** and m/z = 777.145 for **3f**} were observed for all compounds. However, additional peaks attributed to [Cu(**1a-d**,**f**)$_2$]$^+$ ions {m/z = 695.123 for **3a-d** and m/z = 967.180 for **3f**} also appeared indicating that more than one species could exist under the solution conditions. The

intensity of the peaks was dependent of the ligand and decreased when the spectra were recorded in the presence of triphenylphosphine.

However, according to the ^{1}H and ^{31}P NMR data, the mononuclear heteroleptic species Cu(**1b-d**,**f**)(PPh_3)Br were prevalent in $CDCl_3$ or CD_2Cl_2 solutions. The splitting pattern of triphenylphosphine closely resembled that observed for Cu(PPh_3)$_3$Br in these solvents, indicating that this ligand was coordinated to the copper(I) ion. All expected resonances of the 1,10-phenanthroline ligand were well-resolved and largest chemical shift variations were observed for the α protons which were shielded due to ring current effects of the phenyl substituents on triphenylphosphine ligand. On the other hand, proton resonances assigned to the diethoxyphosphoryl substituent were pretty much the same as in the free ligands, indicating that this group was not coordinated to the metal center.

In contrast, the ^{1}H NMR spectrum of the sterically bulky **3a** in CD_2Cl_2 at 300 K consisted of a poorly resolved set of signals, which prevented structure determination. A decrease of temperature to 250 K resulted in a resolution gain, showing the presence of two compounds in the studied solution. The spectral data of the major compound are consistent with the formula Cu(**1a**)(PPh_3)Br. The non-equivalence of the ethoxy groups induced by the presence of the stereogenic metal center indicates that the ligand exchange reactions are slow on the NMR timescale at this temperature. The structure of the minor complex [Cu(**1a**)$_2$]Br (about 7%) was determined using an authentic sample of [Cu(**1a**)$_2$]PF_6 (**4a**). This complex could be formed after triphenylphosphine dissociation, followed by further ligand exchange reactions (Eq 7-1). Once again, a good agreement was observed between the electrochemical behavior described above and the NMR data.

According to the variable-temperature ^{1}H NMR data, the exchange between **3a** and **4a** is slow even at room temperature, although an increase in temperature leads to the broadening of all proton resonances due to other ligand exchange reactions.

^{1}H NMR spectra of the heteroleptic complexes recorded in methanol-d_4 indicate that the ligand exchange proceeds easily in this coordinating solvent. In the case of **3c** in methanol-d_4, the broad signals are only slightly shifted compared to those in CD_2Cl_2 and are markedly different from those of [Cu(**1c**)$_2$]PF_6 (**4c**). A gradual temperature decrease from 300 to 210 K resulted in a significant evolution of the spectrum (Figure 7-11).

Two sets of narrow signals were observed for the phenanthroline ligand at low temperature. They were quite similar to each other and are attributed to Cu(**1c**)(PPh_3)Br (**3c**) and [Cu(**1c**)(PPh_3)(CD_3OD)]Br (**6c**) (Eq 7-5).

$$\underset{\textbf{3c}}{\text{Cu(}\mathbf{1c}\text{)(PPh}_3\text{)Br}} + \text{CD}_3\text{OD} \rightleftharpoons \underset{\textbf{6c}}{\text{[Cu(}\mathbf{1c}\text{)(PPh}_3\text{)(CD}_3\text{OD)]Br}} \qquad (7\text{-}5)$$

When the temperature was increased, the corresponding phenanthroline protons coalesce into broad lines indicating that the bromine replacement by a methanol molecule is rapid at room temperature. Consistent with this behavior, the two phosphorus signals of the diethoxyphosphoryl group observed at 250 K in the ^{31}P NMR spectrum collapsed into a broad signal at δ = 13.1 ppm at room temperature, while the phosphorus resonance of the triphenylphosphine ligand at δ = –2 ppm was significantly broadened over all examined temperature ranges.

Chemical shifts of the phenanthroline protons for the major species of compound **3a** in methanol-d_4 are in good agreement with those of [Cu(**1a**)$_2$]PF_6. The minor compound

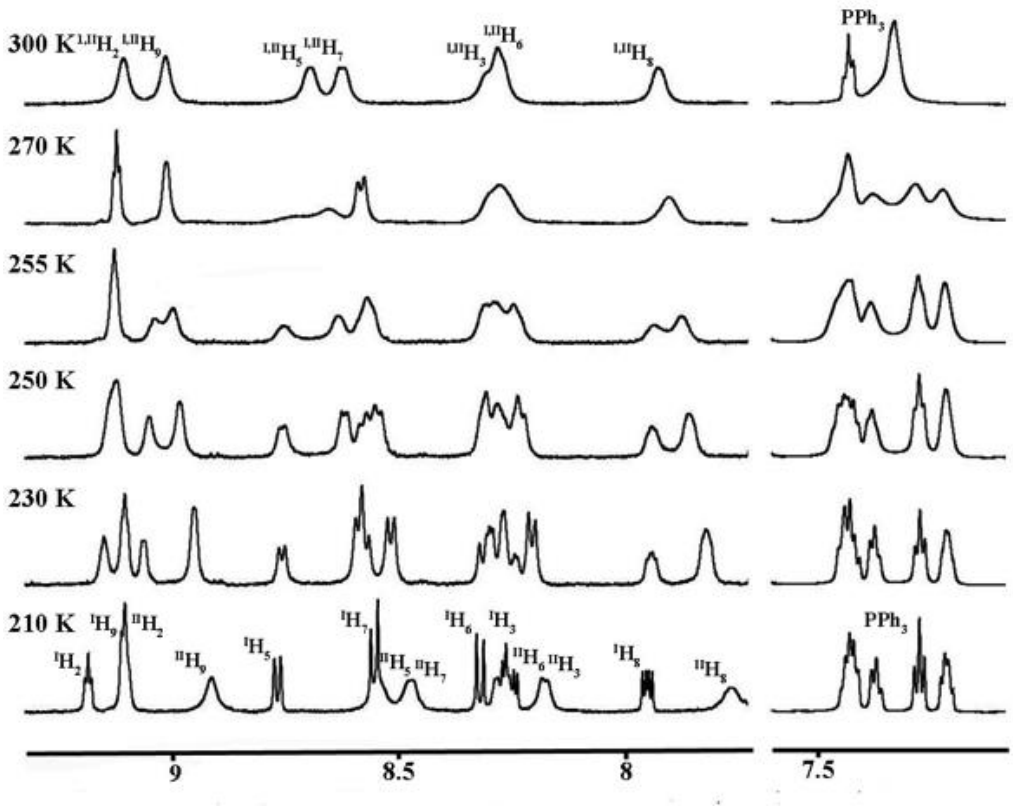

Figure 7-11. Variable-temperature ^{1}H NMR spectra of **3c** in methanol-d_4. Atom numbering is displayed in Scheme 7-2. Two sets of resonances corresponding to complexes **3c** and **6c** are noted as ^{I}H and ^{II}H (data taken from ref 8).

observed as a set of broad signals is tentatively assigned to Cu(**1a**)(PPh_3)Br taking into account the splitting pattern of $PO(OEt)_2$ protons and chemical shifts of the phenanthroline ligand.

The ratio of two complexes in this solvent is significantly different from that in CD_2Cl_2 and the homoleptic bis-chelate is a major species (above 70%). Cooling the solution of **3a** to 230 K afforded narrow sets of proton resonances, as was observed in CD_2Cl_2. As shown in Figure 7-12, the exchange between the homoleptic and heteroleptic complexes is slow even at room temperature but the mixed ligand complex is involved in ligand dissociation reactions (a possible process can involve bromine substitution by a methanol molecule as represented for **3c** in Eq 7-5). Interestingly, the chemical shifts and splitting pattern of triphenylphosphine in this solution resemble that for a pure sample of PPh_3 and look much different from that of $Cu(PPh_3)_3Br$, indicating a weak binding of this ligand to the copper(I) ion.

Thus, the heteroleptic (diethoxyphosphoryl)phenanthroline complexes **3a-d** and **3f** are labile in solution with a binding solvent replacing a bromine in the inner-coordination sphere of the metal center. The copper(I) complexes with α-substituted phenanthrolines easily dissociate, even in non-binding solvents such as CH_2Cl_2 and $CDCl_3$. The disproportion reactions affording less sterically hindered species are observed under these solution conditions as displayed, for example, by Eq 7-1.

It has to be noted that a good agreement between NMR and electrochemical studies was observed in both binding and non-binding solvents, indicating a key influence of the ligand dissociation from copper(I) complexes on the overall oxidation/reduction process of the studied complexes.

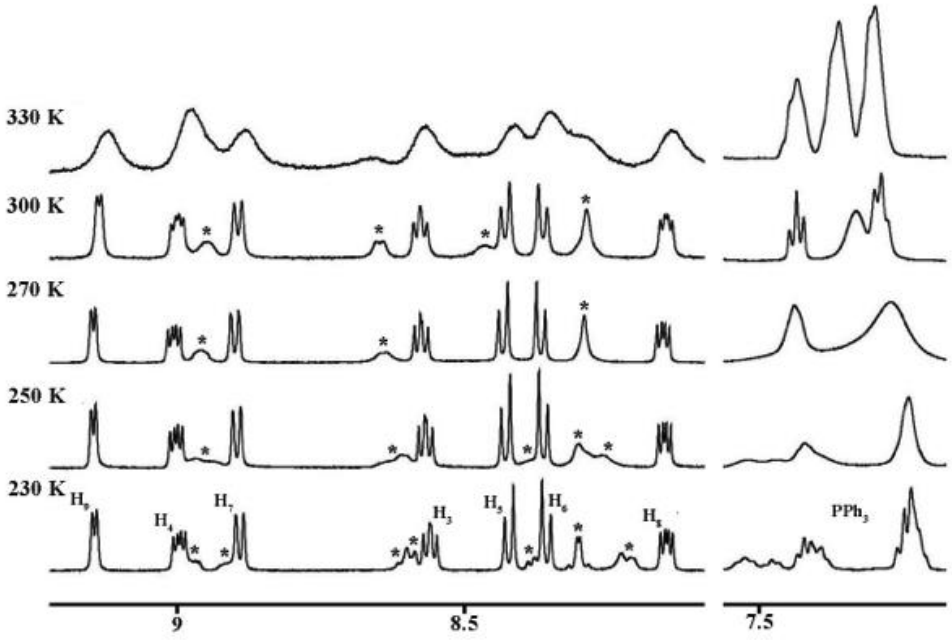

Figure 7-12. Variable-temperature ^{1}H NMR spectra of **3a** in methanol-d_4. Atom numbering for a major solution species **4a** is displayed in Scheme 7-3. The signals of a minor species showing a dynamic behavior are marked by * (see text for further explanation, data taken from ref 8).

Electronic absorption spectra of **3a-d**, **3f**, **4a-c** and **4e** are in line with the behavior of known compounds similar to those investigated in the current study. The intense ligand-centered bands at λ_{max} = 230-280 nm are typical of the π-π* transitions of the phenanthroline ligands, with the molar absorption coefficients being on the order of ε = 25000-75000 $dm^3mol^{-1}cm^{-1}$.[1e] The bands lying in the visible spectral region at λ_{max} = 340-520 nm are much weaker (ε =1400-8500 dm^3 $mol^{-1}cm^{-1}$) than those in the UV part of the spectra and are assigned to MLCT absorptions.[15d,32] Indeed, copper(I) is characterized by a d^{10} electronic configuration and exhibits a low oxidation potential while phenanthroline is a good π* electron acceptor.

The emissive properties of the homoleptic copper(I) complexes **4a-c** and **4e** were studied to compare these derivatives with emissive copper(I) complexes bearing 2,9-dialkyl substituted phenanthroline ligands. However, the emission bands in CH_2Cl_2 at room temperature were barely detectable. This suggests an active role of the diethoxyphosphoryl groups in fluorescence quenching. Fluorescence quenching was earlier reported for bis(phenanthroline)copper(I) complexes with appended substituents bearing nitrogen or oxygen atoms.[33,34]

The above described solution behavior of the copper(I) complexes **3a-d**, **3f**, **4a-c**, and **4e** clearly points out how steric hindrance around the metal center influences the ligand exchange reactions, showing that the solution behavior of the copper(I) complexes is hardly predictable. This behavior of copper(I) complexes could also be one of the reasons why the choice of experimental conditions for catalytic reactions is much more difficult for Cu-catalyzed coupling reactions as compared to reactions that are catalyzed by palladium complexes.[16]

7.3 Summary

In summary, two series of diethoxyphosphoryl-substituted 1,10-phenanthroline copper(I) complexes bearing only phenanthroline ligands or one phenanthroline and one triphenylphosphine ligand were obtained and characterized in the solid state and in solution. In all complexes phenanthroline ligands donate to the metal centers four electrons of two nitrogen atoms. The diethoxyphosphoryl group is not coordinated to the metal center and influences structural parameters and the solution behavior of the complexes mainly by steric effects. These complexes are labile in solution and the solution equilibria were studied by NMR spectroscopy and electrochemistry. All ligands at the copper(I) center can be involved in the ligand exchange reactions and solution speciation determined both by the nature of solvent and the location of the phosphorus substituent on the phenanthroline backbone. The binding solvent can replace a bromine atom, the triphenylphosphine and even the phenanthroline ligand in the inner-coordination sphere of the metal center. Copper(I) complexes with α-substituted phenanthrolines easily dissociate, even in non-binding solvents such as CH_2Cl_2 and $CDCl_3$. The disproportion reactions affording less sterically hindered species are observed under these solution conditions. These studies demonstrate the interest of diethoxyphosphoryl-substituted 1,10-phenanthroline copper(I) complexes for catalysis. Indeed, these readily available air-stable complexes may be useful for a search of efficient catalytic systems for various copper(I)-catalyzed reactions. Currently, efforts are underway to show their efficiency in different catalytic transformations and to immobilize these catalysts on a titania support.

7.4 References

1. a) Juris, A.; Balzani, V.; Barigelletti, F.; Campagna, S.; Belser, P.; Von Zelewsky, A. *Coord. Chem. Rev*. **1988**, *84*, 85–277.; b) Armaroli, N. *Photochem. Photobiol. Sci*. **2003**, *2*, 73–87.; c) Bossert, J.; Daniel, C. *Coord. Chem. Rev*. **2008**, *252*, 2493–2503.; d) Chen, Z.-N.; Fan, Y.; Ni, J. *Dalton Trans*. **2008**, 573–581.; e) Accorsi, G.; Listorti, A.; Yoosaf, K.; Armaroli, N. *Chem. Soc. Rev*. **2009**, *38*, 1690–1700.; f) Kiran, A. J.; Lee, H. W.; Kumar, H. C. S.; Rudresha, B. J.; Bhat, B. R.; Yeom, D. I.; Kim, K.; Rotermund, F. *J. Opt.* (Bristol, U. K.) **2010**, *12*, 035211.; g) Costa, R. D.; Tordera, D.; Orti, E.; Bolink, H. J.; Schonle, J.; Graber, S.; Housecroft, C. E.; Constable, E. C.; Zampese, J. A. *J. Mater. Chem*. **2011**, *21*, 16108–16118.
2. a) Schmittel, M.; Ammon, H.; Wöhrle, C. *Chem. Ber*. **1995**, *128*, 845–850.; b) Sugihara, H.; Hiratani, K. *Coord. Chem. Rev*. **1996**, *148*, 285–299.; c) García, C.; Ferraudi, G.; Lappin, A. G.; Isaacs, M. *Inorg. Chim. Acta* **2012**, *386*, 73–82.
3. a) Sigman, D. S.; Landgraf, R.; Perrin, D. M.; Pearson, L. In *Metal Ions in Biological Systems* Sigel, A.; Sigel, H., Ed.; Marcel Dekker: New York, **1996**, vol. 33, pp. 485–513.; b) Bencini, A.; Lippolis, V. *Coord. Chem. Rev*. **2010**, *254*, 2096–2180.; c) Starosta, R.; Stokowa, K.; Florek, M.; Król, J.; Chwiłkowska, A.; Kulbacka, J.; Saczko, J.; Skała, J.; Jeżowska-Bojczuk, M. *J. Inorg. Biochem*. **2011**, *105*, 1102–1108.
4. a) Catalano, V. J.; Bennett, B. L.; Yson, R. L.; Noll, B. C. *J. Am. Chem. Soc*. **2000**, *122*, 10056–10062.; b) Masar, M. S.; Mirkin, C. A.; Stern, C. L.; Zakharov, L. N.; Rheingold, A. L. *Inorg. Chem*. **2004**, *43*, 4693–4701.; c) Colasson, B. X.; Sauvage, J. P. *Inorg. Chem*. **2004**, *43*, 1895–1901.; d) Chen, C. Y.; Lu, H. C.; Wu, C. G.;

Chen, J. G.; Ho, K. C. *Adv. Funct. Mater*. **2007**, *17*, 29–36.; e) Masar, M. S.; Gianneschi, N. C.; Oliveri, C. G.; Stern, C. L.; Nguyen, S. T.; Mirkin, C. A. *J. Am. Chem. Soc*. **2007**, *129*, 10149–10158.; f) Balzani, V.; Credi, A.; Venturi, M. *Molecular Devices and Machines. Concepts and Perspectives for the Nanoworld.* 2nd ed.; Wiley–VCH: Weinheim, **2008**.; g) Terry, T. J.; Dubois, G.; Murphy, A.; Stack, T. D. P. *Angew. Chem. Int. Ed.* **2007**, *46*, 945–947.; h) Ishi–i, T.; Hirashima, R.; Tsutsumi, N.; Amemori, S.; Matsuki, S.; Teshima, Y.; Kuwahara, R.; Mataka, S. *J. Org. Chem*. **2010**, *75*, 6858–6868.; i) De, S.; Mahata, K.; Schmittel, M. *Chem. Soc. Rev*. **2010**, *39*, 1555–1575.

5. Luman, C. R.; Castellano, F. N. In *Comprehensive Coordination Chemistry*, McCleverty, J. A.; Meyer, T. J.; Lever, A. B. P., Ed.; Elsevier: Oxford, **2004**, vol. 1, pp. 25–39.

6. Mitrofanov, A.; Bessmertnykh Lemeune, A.; Stern, C.; Guilard, R.; Gulyukina, N.; Beletskaya, I. *Synthesis* **2012**, *44*, 3805–3810.

7. a) Alberti, G. *Acc. Chem. Res*. **1978**, *11*, 163–170.; b) Vermeulen, L. A. *Prog. Inorg. Chem*. **1997**, *44*, 143–166.; c) Kalyanasundaram, K.; Grattzel, M. *Coord. Chem. Rev*. **1998**, *177*, 347–414.; d) Kong, D.; Li, Y.; Ross, J. H., Jr.; Clearfield, A. *Chem. Commun*. **2003**, 1720–1721.; e) Clearfield, A.; Alloys, J. *Compd*. **2006**, *418*, 128–138.

8. Mitrofanov, A.; Manowong, M.; Bessmertnykh-Lemeune, A.; Brandes, S.; Rousselin, Y.; Guilard, R.; Chen, P.; Kadish, K. M.; Goulioukina, N.; Beletskaya, I. *Eur. J. Inorg. Chem.* **2014**, in press.

9. a) Gujadhur, R. K.; Bates, C. G.; Venkataraman, D. *Org. Lett*. **2001**, *3*, 4315–4317.; b) Bates, C. G.; Saejueng, P.; Murphy, J. M.; Venkataraman, D. *Org. Lett.* **2002**, *4*, 4727–4729.; c) Kelkar, A. A.; Patil, N. M.; Chaudhari, R. V. *Tetrahedron Lett.* **2002**, *43*, 7143–7146.; d) Allen, D. V.; Venkataraman, D. *J. Org. Chem*. **2003**, *68*, 4590–4593.; e) Bates, C. G.; Saejueng, P.; Doherty, M .Q.; Venkataraman, D. *Org. Lett*. **2004**, *6*, 5005–5008.; f) Gruijters, B. W. T.; Broeren, M. A. C.; van Delft, F. L.; Sijbesma, R. P.; Hermkens, P. H. H.; Rutjes, F. P. J. T. *Org. Lett*. **2006**, *8*, 3163–3166.; g) Fazal, A.; Al–Fayez, S.; Abdel–Rahman, L. H.; Seddigi, Z. S.; Al–Arfaj, A. R.; Ali, B. E.; Dastageer, M. A.; Gondal, M. A.; Fettouhi, M. *Polyhedron* **2009**, *28*, 4072–4076.; h) Bagley, M. C.; Lin, Z.; Pope, S. J. A. *Chem. Commun*. **2009**, 5165–5167.; i) Cain, M. F.; Hughes, R. P.; Glueck, D. S.; Golen, J. A.; Moore, C. E.; Rheingold, A. L. *Inorg. Chem*. **2010**, *49*, 7650–7662.; j) Das, B.; Salvanna, N.; Reddy, G. C.; Balasubramanyam, P. *Tetrahedron Lett*. **2011**, *52*, 6497–6500.

10. Chelucci, G.; Iuliano, A.; Muroni, D.; Saba, A. *J. Mol. Catal. A: Chem*. **2003**, *191*, 29–33.

11. Giribabu, L.; Singh, S. P.; Patil, N. M.; Kantam, M. L.; Gupte, S. P.; Chaudhari, R. V. *Synth. Commun*. **2008**, *38*, 619–625.

12. Lei, Y.; Anson, F. C. *Inorg. Chem*. **1995**, *34*, 1083–1089.

13. a) Mahadevan, S.; Palaniandavar, M. *Inorg. Chem*. **1998**, *37*, 3927–3934.; b) Yang, Z.-S.; Yu, J.-S.; Chen, H.-Y. *Electroanalysis* **2002**, 14, 747–752.

14. Starosta, R.; Florek, M.; Król, J.; Puchalska, M.; Kochel, A. *New J. Chem*. **2010**, *34*, 1441–1449.

15. a) Scaltrito, D. V.; Thompson, D. W.; O'Callaghan, J. A.; Meyer, G. J. *Coord. Chem. Rev.* **2000**, *208*, 243–266.; b) Armaroli, N. *Chem. Soc. Rev*. **2001**, *30*, 113–124.; c) Zhang, Q.; Zhou, Q.; Cheng, Y.; Wang, L.; Ma, D.; Jing, X.; Wang, F. *Adv. Funct. Mater*. **2006**, *16*, 1203–1208.; d) Lavie-Cambot, A.; Cantuel, M.; Leydet, Y.; Jonusauskas, G.; Bassani, D. M.; McClenaghan, N. D. *Coord. Chem. Rev*. **2008**, *252*, 2572–2584.; e) Starosta, R.; Puchalska, M.; Cybinska, J.; Barys, M.; Mudring, A. V. *Dalton Trans*. **2011**, *40*, 2459–2468.

16. Beletskaya, I. P.; Cheprakov, A. V. *Organometallics* **2012**, *31*, 7753–7808.

17. Kaeser, A.; Mohankumar, M.; Mohanraj, J.; Monti, F.; Holler, M.; Cid, J.-J.; Moudam, O.; Nierengarten, I.; Karmazin-Brelot, L.; Duhayon, C.; Delavaux-Nicot, B.; Armaroli, N.; Nierengarten, J.-F. *Inorg. Chem*. **2013**, *52*, 12140–12151.

18. Bellamy, L. J. In *The Infrared Spectra of Complex Molecules*.; Wiley & Sons: New York, **1962**.

19. a) Saravanabharathi, D.; Nethaji, M.; Samuelson, A. G. *Proc. Indian Acad. Sci., Chem. Sci***. 2002**, *114*, 347–356.; b) Yeh, W.-Y.; Liu, Y.-C.; Peng, S.-M.; Lee, G.-H. *Inorg. Chim. Acta* **2005**, *358*, 1987–1992.; c) Chen, W.-T.; Luo, Z.-G.; Wang, Y.-F.; Zhang, X.; Fu, H.-R. *Inorg. Chim. Acta* **2014**, *414*, 1–7.

20. Saravanabharathi, D.; Nethaji, M.; Samuelson, A. G. *Polyhedron* **2002**, *21*, 2793–2800.

21. Pilloni, G.; Corain, B.; Degano, M.; Longato, B.; Zanotti, G. *J. Chem. Soc., Dalton Trans.* **1993**, 1777–1778.

22. Cao, Q.-Y.; Gan, X.; Fu, W.-F.; Anorg, Z. *Allg. Chem.* **2007**, *633*, 176–179.

23. Farrugia, L. *J. Appl. Crystallogr*. **1997**, *30*, 565.

24. Jin, Q. H.; Xin, X. L.; Zhu, F. J. *Acta Crystallogr., Sect. C* **1999**, *C55*, IUC9900107.

25. a) Eggleston, M. K.; McMillin, D. R.; Koenig, K. S.; Pallenberg, A. J. *Inorg. Chem.* **1997**, *36*, 172–176.; b) Rader, R. A.; McMillin, D. R.; Buckner, M. T.; Matthews, T. G.; Casadonte, D .J.; Lengel, R. K.; Whittaker, S. B.; Darmon, L. M.; Lytle, F. E. *J. Am. Chem. Soc.* **1981**, *103*, 5906–5912.; c) Hadjikakou, S. K.; Akrivos, P. D.; Karagiannidis, P.; Papadopoulos, N. *Polyhedron* **1995**, *14*, 2999–3003.; d) Accorsi, G.; Armaroli, N.; Duhayon, C.; Saquet, A.; Delavaux-Nicot, B.; Welter, R.; Moudam, O.; Holler, O.; Nierengarten, J.-F. *Eur. J. Inorg. Chem*. **2010**, 164–173.

26. Ackerman, B.; Jordan, T. A.; Eddy, C. R.; Swern, D. *J. Am. Chem. Soc*. **1956**, *78*, 4444–4447.

27. a) Sertel, M.; Yildiz, A.; Gambert, R.; Baumgaertel, H. *Electrochim. Acta* **1986**, *31*, 1287–1292.; b) Sertel, M.; Yildiz, A.; Baumgaertel, H. *Electrochim. Acta* **1986**, *31*, 1625–1632.; c) Fox, M. A. In *Topics in Organic Electrochemistry* Fry, A. J.; Britton, W. E., Ed.; Springer Science+Business Media, LLC, **1986**, p 177–225.; d) Wagenknecht, J. H.; Eberson, L.; Utley, J. H. P. In *Organic Electrochemistry* Lund, H.; Hammerich, O.; Ed.; 4th ed., Marcel Dekker: New York, **2001**, pp. 453–471.

28. a) Barbe, J.-M.; Habermeyer, B.; Khoury, T.; Gros, C. P.; Richard, P.; Chen, P.; Kadish, K. M. *Inorg. Chem.* **2010**, 49, 8929–8940.; b) Federlin, P.; Kern, J. M.; Rastegar, A.; Dietrich-Buchecker, C.; Marnot, P. A.; Sauvage, J. P. *New J. Chem.* **1990**, 14, 9–12.

29. a) Miller, M. T.; Gantzel, P. K.; Karpishin, T. B. *Inorg. Chem*. **1999**, *38*, 3414–3422.; b) Van Meerssche, M.; Germain, G.; Declercq, J. P.; Wilputte-Steinert, L. *Cryst. Struct. Commun*. **1981**, *10*, 47–53.; c) Kadish, K. M.; Shen, J.; Fremond, L.; Chen,

P.; El Ojaimi, M.; Chkounda, M. Gros, C. P.; Barbe, J.-M.; Ohkubo, K.; Fukuzumi, S.; Guilard, R. *Inorg. Chem.* **2008**, *47*, 6726–6737.; d) Chen, P.; Lau, H.; Habermeyer, B.; Gros, C. P.; Barbe, J.-M.; Kadish, K. M. *J. Porphyrins Phthalocyanines* **2011**, *15*, 467–479.

30. Chen, J.-L.; Song, P.; Liao, J.; Wen, H.-R.; Hong, R.; Chen, Z.-N.; Chi, Y. *Inorg. Chem. Commun.* **2010**, *13*, 1057–1060.

31. a) Scaltrito, D. V.; Thompson, D. W.; O'Callaghan, J. A.; Meyer, G. J. *Coord. Chem. Rev.* **2000**, *208*, 243–266.; b) Záliš, S.; Consani, C.; El Nahhas, A.; Cannizzo, A.; Chergui, M.; Hartl, F.; Vlček, A. Jr., *Inorg. Chim. Acta* **2011**, *374*, 578–585.

32. Armaroli, N.; Accorsi, G.; Cardinali, F.; Listorti, A. In *Photochemistry and Photophysics of Coordination Compounds I, Topics in Current Chemistry* Balzani, V.; Campagna, S., Ed.; Springer: Berlin-Heidelberg, **2007**, vol. 280, pp. 69–115.

33. Everly, R. M.; Ziessel, R.; Suffert, J.; McMillin, D. R. *Inorg. Chem*. **1991**, *30*, 559–561.

34. Accorsi, G.; Armaroli, N.; Duhayon, C.; Saquet, A.; Delavaux-Nicot, B.; Welter, R.; Moudam, O.; Holler, M.; Nierengarten, J.-F. *Eur. J. Inorg. Chem*. **2010**, 164–173.